Rational design of next-generation filovirus vaccines with glycoprotein stabilization, nanoparticle display, and glycan modification

Yi-Zong Lee[1#], Yi-Nan Zhang[1#], Maddy L. Newby[2], Garrett Ward[1], Keegan Braz Gomes[3], Sarah Auclair[1], Connor DesRoberts[1], Joel D. Allen[2], Andrew B. Ward[1], Robyn L. Stanfield[1], Linling He[1], Max Crispin[2], Ian A. Wilson[1,4], and Jiang Zhu[1,3,5]*

[1]Department of Integrative Structural and Computational Biology, The Scripps Research Institute, La Jolla, CA 92037, USA

[2]School of Biological Sciences, Highfield Campus, University of Southampton, Southampton, SO17 1BJ, UK

[3]Uvax Bio, LLC, Newark, DE 19702, USA

[4]Skaggs Institute for Chemical Biology, The Scripps Research Institute, La Jolla, CA 92037, USA

[5]Department of Immunology and Microbiology, The Scripps Research Institute, La Jolla, CA 92037, USA

[#] These authors contributed equally to this work

* Corresponding author

JZ: Phone (858) 784-8157; Email: jiang@scripps.edu

ABSTRACT (200 WORD LIMIT)

Filoviruses pose a significant threat to human health with frequent outbreaks and high mortality. Although two vector-based vaccines are available for Ebola virus, a broadly protective filovirus vaccine remains elusive. In this study, we evaluate a general strategy for stabilizing glycoprotein (GP) structures of Ebola, Sudan, and Bundibugyo ebolaviruses and Ravn marburgvirus. A 3.2 Å-resolution crystal structure provides atomic details for the redesigned Ebola virus GP, and cryo-electron microscopy reveals how a pan-ebolavirus neutralizing antibody targets a conserved site on the Sudan virus GP (3.13 Å-resolution), in addition to a low-resolution model of antibody-bound Ravn virus GP. A self-assembling protein nanoparticle (SApNP), I3-01v9, is redesigned at the *N*-terminus to allow the optimal surface display of filovirus GP trimers. Following detailed *in vitro* characterization, the lymph node dynamics of Sudan virus GP and GP-presenting SApNPs are investigated in a mouse model. Compared with soluble GP trimer, SApNPs show ~112 times longer retention in lymph node follicles, up-to-28 times greater presentation on follicular dendritic cell dendrites, and up-to-3 times stronger germinal center reactions. Functional antibody responses induced by filovirus GP trimers and SApNPs bearing wildtype and modified glycans are assessed in mice. Our study provides a foundation for next-generation filovirus vaccine development.

ONE-SENTENCE SUMMARY

Filovirus glycoproteins and nanoparticles were rationally designed and characterized *in vitro* and *in vivo* to aid filovirus vaccine development.

INTRODUCTION

The first case of human infection with filovirus was documented in 1967 in Marburg and Frankfurt, Germany, where laboratory workers were infected with the subsequently named Marburg virus (MARV) by nonhuman primates (NHPs) imported from Africa (*1*). The largest filovirus outbreak in history was caused by Ebola virus (EBOV), which was first identified in 1976 in Zaire in Central Africa (*2, 3*). Approximately 28,600 cases were reported during this outbreak, which resulted in 11,325 deaths between 2013 and 2016 (*4*). Both MARV and EBOV cause viral hemorrhagic fever (VHF) in humans, with a case fatality rate of up to 90% (*5, 6*). Filoviruses can be classified into five genera, including *Ebolavirus* and *Marburgvirus (7, 8)*. The *Ebolavirus* genus comprises three pathogenic species, including EBOV, Bundibugyo virus (BDBV), and Sudan virus (SUDV), and three species that are non-pathogenic or rarely infect humans. The *Marburgvirus* genus contains a single species with two members, MARV and Ravn virus (RAVV). The single-stranded, negative-sense RNA genome of filoviruses encodes the nucleoprotein, virion proteins, glycoprotein (GP), and RNA-polymerase, among others. As a class I viral fusion protein (*9-12*), functional GP is a trimer of heterodimers responsible for filovirus attachment, entry, and membrane fusion (*13*). GP is recognized by the host immune system during natural infection (*14-16*), and thus represents the main target for the development of prophylactic vaccines and antibody therapeutics (*17-20*).

Substantial progress has been made in filovirus research (*21*). First, a greater understanding of filovirus pathogenesis and its mechanism of infection has been achieved (*22-24*). Niemann-Pick C1 (NPC1) was identified as the endosomal receptor for filovirus entry, suggesting that NPC1 inhibitors may have antiviral potential (*25-27*). Second, neutralizing antibodies (NAbs) have now been established as effective therapeutics to treat filovirus infections (*28-31*). Compared with a monoclonal antibody (mAb) cocktail, ZMapp (*32*), which showed early promise (*33*), REGN-EB3

(a three-mAb cocktail (*34*)) and mAb114 (*35*) proved to be more efficacious against EBOV in a randomized controlled trial (*36*). The 2013-2016 EBOV outbreak led to an enduring campaign for antibody discovery against filoviruses (*37*). Panels of mAbs were isolated from human survivors and immunized animals, revealing multiple sites of vulnerability on GP (*15, 16, 35, 38-53*). At the peak of this effort, the Viral Hemorrhagic Fever Immunotherapeutic Consortium analyzed 171 mAbs targeting diverse GP epitopes: base, glycan cap, fusion loop, GP1/core, GP1/head, GP1/2, heptad repeat 2 (HR2), and mucin (*54*). Third, x-ray crystallography and cryo-electron microscopy (EM) have been used to determine high-resolution structures of filovirus GP bound to the NPC1 receptor (*27*), small-molecule ligands (*55-57*), and mAbs (*15, 38, 39, 41, 42, 46, 48-51, 58, 59*). Notably, negative-stain EM (nsEM) offers a useful tool for validating GP structures and mapping mAb epitopes (*16, 40, 45-47, 52-54*). These GP complex structures have provided insights into the molecular mechanism of filovirus neutralization and facilitated the development of antibody therapeutics and vaccines (*17, 60, 61*). Fourth, two viral vector-based EBOV vaccines have been approved for human use thus far. ERVEBO (*62*) is a single-dose vaccine based on the recombinant vesicular stomatitis virus (rVSV) expressing the EBOV GP, while Zabdeno/Mvabea (*63*) utilizes a two-dose, heterologous regimen administering an Adenovirus 26 (Ad26) expressing the EBOV GP followed by a modified Vaccina Ankara (MVA) virus expressing multiple filovirus GPs. Other EBOV vaccines that utilize DNA (*64*) and viral vectors (*65-70*) have been tested in humans. Recent efforts have been directed toward mRNA, protein, and nanoparticle (NP) platforms (*71-74*).

Despite this rapid advancement, critical innovations are still needed for next-generation filovirus vaccine development (*75*). Although the correlates of protection remained unclear (*76*), an in-depth B cell analysis revealed diverse yet convergent polyclonal NAb responses induced by the rVSV-ZEBOV vaccine in a Phase 1 trial (*77*). A follow-up study elucidated how NAbs from

multiple subjects utilized the same germline genes to target the receptor binding site on GP (*78*). These results highlighted the central role of GP as a vaccine antigen for eliciting protective NAbs. For more than a decade, antibody-guided, structure-based antigen design has been the focus of vaccine development for several important targets, such as type-1 human immunodeficiency virus (HIV-1) (*79-82*) and respiratory syncytial virus (RSV) (*83*). Rational designs have been proposed for stabilization of the HIV-1 envelope (Env) (*84-86*) and RSV fusion (F) (*87-90*) proteins in their prefusion state. After preclinical assessment, many of these vaccine designs have been advanced to human trials (*91, 92*), with two products approved for RSV prevention in older adults (*93*). So far, however, only two studies reported rational designs of stabilized filovirus GP with limited *in vivo* data (*94, 95*). Most recently, Xu et al. proposed an immunofocusing GP design by engineering additional *N*-linked glycans (*73*). Notably, almost all current filovirus vaccine candidates (*96*) are based on wildtype GP with a highly variable mucin-like domain (MLD), which shields conserved NAb epitopes and facilitates immune evasion (*97, 98*). As a vaccine antigen, the MLD-deleted GP (GPΔmuc) should in principle be more effective in NAb elicitation than wildtype GP but has not been evaluated in humans. In addition to the GP form, the delivery platform may be crucial for vaccine-induced immunity. Although viral vectors appeared to be a preferable platform with the licensure of two EBOV vaccines, mRNA vaccines may provide an alternative given their widely acclaimed success in the COVID-19 vaccine campaign (*99, 100*). In the realm of protein vaccines, NPs have become an increasingly recognized delivery platform due to their virus-like size, shape, surface display, and ability to induce strong and durable NAb responses (*101-106*). Two EBOV GP-presenting NP vaccines were recently reported (*73, 95*) but have not been evaluated in animal challenge models. Finally, engineering the glycan component of vaccine candidates may prove to be an important step in their development. The enzymatic trimming of *N*-glycans was previously

shown to enhance NAb responses for influenza hemagglutinin (HA) or stem, SARS-CoV-2 spike, and HIV-1 Env vaccines (*107-110*). It is unclear whether the same strategy is applicable to filovirus GP, which is also heavily glycosylated with up to 17 glycans on the surface.

In our previous study, we stabilized EBOV GP with mutations in the $HR1_C$ bend and HR2 stalk and displayed one of two lead designs, termed GPΔmuc-WL^2P^2, on self-assembling protein nanoparticles (SApNPs) as EBOV vaccine candidates (*95*). Here, we first extended the GPΔmuc-WL^2P^2 and WL^2P^4 construct designs from EBOV to SUDV and BDBV and determined a crystal structure for EBOV GPΔmuc-WL^2P^4 at 3.2 Å-resolution. We also obtained a 3.13 Å cryo-EM model for SUDV GPΔmuc-WL^2P^4 bound to CA45 Fab. The nearly identical backbones of SUDV and EBOV GPΔmuc-WL^2P^4 suggest a widely applicable design to stabilize ebolavirus GPs. We then displayed EBOV, SUDV, and BDBV GPΔmuc-WL^2P^4 trimers on SApNPs derived from E2p and I3-01v9, the latter of which was computationally redesigned at the *N*-terminus. A similar design strategy was applied to RAVV GP, resulting in a promising trimer construct termed GPΔmuc-P^2CT. Next, we investigated the lymph node delivery and immunological responses for ebolavirus vaccines, using SUDV GPΔmuc-WL^2P^4 trimer and SApNPs as examples, at the intra-organ, intercellular, and intracellular levels in mice. Compared with soluble trimers, large SApNPs showed prolonged retention and presentation on follicular dendritic cell (FDC) dendrites and more robust and durable germinal center (GC) reactions in lymph node follicles. Lastly, we immunized mice with various filovirus GP vaccines to evaluate their antibody responses. RAVV GPΔmuc-P^2CT trimer elicited detectable cross-ebolavirus NAbs, but not vice versa. Both multivalent display and glycan modification were found to impact the immunogenicity of GP-based filovirus vaccines. Notably, increasing the mannose content of the GP glycan shield exerted a positive effect on NAb responses. These findings should facilitate future filovirus vaccine development.

RESULTS

A universal design strategy for ebolavirus GP stabilization

GPs within the *Ebolavirus* genus share considerable sequence and structural similarities (*58, 111*). These viral GPs consist of functionally conserved structural components, such as GP1, MLD, internal fusion loop (IFL), GP2, which contains the heptad repeat 1 (HR1) and HR2 regions, and transmembrane domain (TMD). Recently, we stabilized EBOV GPΔmuc with a T577P (P^2) or L579P (P^4) mutation in the $HR1_C$ bend, a W615L mutation at the neck of the HR2 stalk, and an HR2 C-terminal extension (D632 to D637) (*95*) (**Fig. 1a**). A foldon motif was appended to the HR2 stalk C-terminus in trimer but not SApNP constructs. The modified EBOV GPΔmuc trimers exhibited superior structural and thermal stability compared with the wildtype GP construct.

Here, we applied the same design principles to SUDV and BDBV GPs and characterized the two constructs, GPΔmuc-WL^2P^2 and -WL^2P^4, for all three ebolaviruses (**Fig. S1a**). Following a similar protocol (*95*), all six GPΔmuc constructs were transiently expressed in HEK293F cells and purified using two different methods. In addition to an immobilized nickel affinity (Nickel) chromatography column, pan-ebolavirus NAbs ADI-15878 (*112*) and CA45 (*113*) were produced in the immunoglobulin G (IgG) form in ExpiCHO cells and used to prepare immunoaffinity chromatography (IAC) columns. The IAC method was established in our previous study, where the mAb100 and mAb114 (*35*) columns were used to purify EBOV GP trimers and SApNPs (*95*). The IAC/Nickel-purified ebolavirus GP was then characterized by size-exclusion chromatography (SEC) on a Superdex 200 column after ADI-15878 (**Fig. 1b)** and CA45 (**Fig. S1b**) purification. All SEC profiles showed an aggregation peak around ~8 ml and a consistent trimer peak at ~11 ml, with little hint of dimer or monomer peaks. The Nickel column generated higher aggregation peaks for EBOV and SUDV GPs than both IAC columns (**Fig. S1b**). Between the two tested

broadly neutralizing antibodies (bNAbs), ADI-15878 appeared to be more effective at capturing diverse ebolavirus GPs than CA45, indicated by substantially higher ultraviolet absorbance at 280 nm (UV_{280}) for the eluted protein (**Fig. 1b** and **S1b**). Our results suggest that ADI-15878 provides a universal, tag-free IAC method for purifying ebolavirus GP. Blue native polyacrylamide gel electrophoresis (BN-PAGE) confirmed that the SEC fractions around ~11 ml were indeed GPΔmuc trimers, with bands on the native gel corresponding to their theoretical molecular weights (**Fig. 1c**). Next, differential scanning calorimetry (DSC) was used to assess the thermostability of ebolavirus GP trimers. For EBOV, while GPΔmuc-WL^2P^2 showed two denaturing states at melting temperatures (T_m) of 60.9ºC and 67.7ºC, GPΔmuc-WL^2P^4 had a widened peak with a single T_m of 64.4ºC (**Fig. 1d**), consistent with our previous findings (*95*). By comparison, all four SUDV and BDBV GPΔmuc trimers generated similar DSC curves with a single denaturing state and a narrow range of T_m values (62.9-63.6ºC). Notably, among the three ebolaviruses, SUDV GPΔmuc trimers showed the highest T_{onset} (54.8ºC and 56.0ºC), followed by EBOV and BDBV GPΔmuc trimers (50.1-54.2ºC). Based on the biochemical and biophysical data, GPΔmuc-WL^2P^4 was selected as a candidate for the pan-ebolavirus GP design and subjected to further experimental validation.

A glycan shield is utilized by the HIV-1 Env spike as a major defense mechanism to evade host NAb responses (*108*). Similarly, ebolavirus GPs have a glycan cap to shield the receptor binding site (*95*), in addition to a heavily glycosylated MLD, which is removed in GPΔmuc. Thus, glycans play a critical role in evading or mediating antibody interactions with the GP. To generate site-specific glycosylation profiles, the three ebolavirus GPΔmuc-WL^2P^4 proteins were digested with trypsin, chymotrypsin, and α-lytic protease to generate glycopeptides each containing a single *N*-linked glycan site. Site-specific composition and occupancy were determined by analyzing these glycopeptides using liquid chromatography-mass spectrometry (LC-MS), as previously described

(*108*). All glycosylation sites on the three ebolavirus GPΔmuc-WL^{2}P^4 proteins present complex-type glycans except for N563 and N257, where mixed forms were detected. Specifically, the N563 site contains ~30% of oligomannose-type glycans for EBOV and ~60% for both SUDV and BDBV, whereas the N257 site has ~15% of oligomannose-type glycans for EBOV (**Fig. 1e** and **Fig. S1c**). Due to technical limitations, accurate assessment of the glycan compositions could not be achieved for all glycosylation sites.

Negative-stain EM (nsEM) was used to characterize structures of ebolavirus GPΔmuc-WL^{2}P^4 trimers, either alone or in complex with bNAb ADI-15878 (**Fig. S1d**). For EBOV and BDBV, crystal structures of wildtype GPΔmuc trimer in complex with ADI-15878 (Protein Data Bank [PDB] IDs: 7JPH (*95*), 6EA7, and 6EA5 (*111*)) were used for fitting three-dimensional (3D) EM reconstructions, whereas for SUDV, the GPΔmuc and ADI-15878 structures obtained from two different complexes (PDB IDs: 3S88 (*58*) and 6DZM (*112*)) were fitted separately (**Fig. 1f** and **Figs. S1e-g**). Overall, the low-resolution nsEM models of three ebolavirus GPΔmuc trimers shared a three-lobed chalice shape consistent with the native-like GPΔmuc structure, albeit missing densities associated with the HR2 stalk. The nsEM models of ADI-15878-bound GPΔmuc trimer were highly similar among the three ebolaviruses, revealing an epitope formed across two GP protomers overlapping the conserved regions of the IFL and HR1 in GP2 (*47, 112*).

The antigenicity of six stabilized ebolavirus GPΔmuc trimers was assessed against pan-ebolavirus bNAbs CA45 (*46*), ADI-15878, ADI-15946 (*114*), and BDBV-289 (*51*), along with a marburgvirus NAb, MR78 (*39*). In the enzyme-linked immunosorbent assay (ELISA), the proline mutation in HR1c (P^2 or P^4) appeared to have no influence on antibody binding (**Fig. 1g** and **Fig. S1h**). Among the four pan-ebolavirus bNAbs, ADI-15946 and BDBV-289 showed the lowest binding affinity for SUDV GPΔmuc trimers, 2.5 to 6-fold weaker than those for EBOV and BDBV

GPΔmuc trimers, indicated by the half maximal effective concentration (EC_{50}). The NHP-derived bNAb, CA45, yielded 1.5- to 2.5-fold lower EC_{50} values in ELISA binding to EBOV compared with SUDV and BDBV GPΔmuc trimers. The negative control, MR78, exhibited no detectable binding to any of ebolavirus GPΔmuc trimers. The results from biolayer interferometry (BLI) were largely consistent with the ELISA data (**Fig. 1h** and **Fig. S1i**). Among the six ebolavirus GPs, CA45 bound to EBOV GPΔmuc trimers with the highest signals, whereas ADI-15946 and BDBV-289 interacted least favorably with SUDV GPΔmuc trimers. BLI showed negligible to no binding signals between ebolavirus GPΔmuc trimers and the marburgvirus NAb, MR78.

Structural characterization of ligand-free and antibody-bound ebolavirus GPΔmuc trimers

Previously, we determined the crystal structure of EBOV GPΔmuc-WL^2P^2 (*95*). Here, we sought to obtain atomic details for the more stable EBOV GPΔmuc-WL^2P^4. To this end, EBOV GPΔmuc-WL^2P^4 was transiently expressed in HEK293S cells and purified by IAC (mAb100) and SEC as previously described (*95*) (**Fig. S2a**). EBOV GPΔmuc-WL^2P^4 was crystallized under a similar condition to GPΔmuc-WL^2P^2, resulting in similar crystal packing with a P321 space group (**Table S1**). The final structure was determined at a resolution of 3.2 Å. Each asymmetric unit contained one GP protomer, with the glycan cap atop the GP1 and the belt-forming IFL of the GP2 clearly recognizable from the densities (**Fig. 2a**). Three GP1-GP2 heterodimers assembled into a chalice-shaped trimer in the crystal lattice, with three GP2 subunits forming a base that cradles the three outward-facing GP1 lobes (**Fig. S2b**). Four *N*-linked glycans, N228, N257, N563, and N618, were identified in the crystal structure. The most complete carbohydrate chain was obtained for N563 (revealing electron density for $Man_4GlcNAc_2$), which is part of the ADI-15878 epitope in HR1a (*111*), whereas a single *N*-acetylglucosamine (GlcNAc) was visible at the other three sites. EBOV GPΔmuc-WL^2P^4 showed a nearly identical backbone to GPΔmuc-WL^2P^2, with a global Cα root-

mean-square deviation (RMSD) of 0.48 Å calculated for 243 matching Cα atoms and a local Cα-RMSD of 0.68 Å for the HR1c bend after fitting the protomer structure (**Fig. 2a** and **Fig. S2c**). In GPΔmuc-WL^{2}P^4, the amine group of the K95 sidechain formed hydrogen bonds with the backbone carbonyl groups of L573 and T576 (~3.0 Å), which were absent in GPΔmuc-WL^{2}P^2. These two interprotomer hydrogen bonds stabilized the GPΔmuc-WL^{2}P^4 trimer from its center, resulting in higher thermostability compared with GPΔmuc-WL^{2}P^2. This was also supported by the EBOV GPΔmuc-WL^2 structure (PDB ID: 7JPI), which contained the K95-L573 and K95-T576 hydrogen bonds (2.7 and 2.9 Å, respectively). The structural analysis is consistent with the DSC data, where EBOV GPΔmuc-WL^{2}P^4 showed a single denaturing state with a T_m of 64.4°C (*95*).

Cryo-EM plays an important role in understanding how viral GPs interact with antibodies (*115-117*). Several cryo-EM models have been reported for EBOV and BDBV GPs (*42, 51, 112*), but only two crystal structures (*58, 118*) and no cryo-EM models are available for SUDV GP. Here, we determined a cryo-EM structure for SUDV GPΔmuc-WL^{2}P^4 in complex with CA45 Fab. The SUDV GP was transiently expressed in HEK293F cells and purified using an IAC (ADI-15878) column, prior to complexation with CA45 Fab and SEC on a Superose 6 16/600 GL column (**Fig. S2d**). The complex fraction at ~72 ml was imaged on a Krios G4 transmission electron microscope with the data processed in CryoSPARC (*119*) (see Methods) (**Fig. S2e**). A resolution of 3.13 Å was obtained for the final reconstruction, in which the SUDV GPΔmuc-WL^{2}P^4 trimer flanked by three CA45 Fabs could be recognized from the density map (**Fig. 2b**). The glycan cap and GP2 stalk only became partially visible when the density was relaxed beyond 4.0 Å (**Fig. S2e**). Crystal structures of EBOV GPΔmuc-WL^{2}P^2 (PDB ID: 7JPH) (*95*) and CA45 variable domains (PDB ID: 6EAY) (*113*) were used as the initial model for EM fitting, followed by manual refinement. The final model of SUDV GPΔmuc-WL^{2}P^4 lacking the glycan cap and GP2 stalk was superposed onto

the crystal structure of EBOV GPΔmuc-WL^{2}P^4, showing a Cα-RMSD of 0.66 Å for 154 matching Cα atoms (**Fig. S2f**, left). The three HR1$_C$ bends of SUDV GPΔmuc-WL^{2}P^4 were superposed onto those of EBOV GPΔmuc-WL^{2}P^4 and BDBV GPΔmuc (PDB ID: 7KFE) (*51*), with Cα-RMSDs of 0.34 and 0.53 Å for the 24 matching Cα atoms, respectively (**Fig. 2c**, right). Compared with the crystal structure of EBOV GPΔmuc/CA45 complex (PDB ID: 6EAY) (*113*), cryo-EM revealed a nearly identical CA45 binding mode and epitope in the SUDV GPΔmuc-WL^{2}P^4/CA45 complex, with a Cα-RMSD of 0.69 Å for 147 matching Cα atoms after superposition of a single GP/CA45 component between the two complexes (**Fig. S2f**, right). Specifically, the CA45-GP2 interface was stabilized by a backbone hydrogen bond formed between CA45 HC-Y32 and GP2-E545 (~3.3 Å) and a sidechain salt bridge between CA45 HC-D101 carboxyl and GP2-H595 imidazole groups (~4.0 Å), as well as hydrogen bonds between the CA45 LC-Y49 sidechain and GP2-N550 backbone (~3.4 Å) and between the CA45 LC-N53 sidechain and GP2-N550 backbone (~2.6 Å) (**Fig. 2c**). Although the interpretation of these interactions may be limited by the resolution of the cryo-EM structure, similar interactions were identified in the previous 3.7 Å-resolution crystal structure of EBOV GPΔmuc in complex with CA45 Fab (PDB ID: 6EAY) (**Fig. S2g**) (*113*), including those between CA45 HC-Y32 and GP2-E545 (~3.2 Å), between CA45 HC-D101 and GP2-H549 (~3.9 Å), and the same CA45 LC-GP2 pairs with nearly identical lengths.

Rational design and basic characterization of ebolavirus GPΔmuc-presenting nanoparticles

Previously, we redesigned the I3-01v9 SApNP to achieve optimal display of monomeric antigens (*120*). In the resulting I3-01v9a scaffold, the *N*-termini formed a triangle of 43.9 Å (**Fig. 3a**, left). Here, we further modified I3-01v9a to accommodate trimeric antigens with a narrow stalk, such as filovirus GPs (see Methods). After removing the first 4 amino acids (aa) of I3-01v9a, we fused a 9-aa helix to the truncated I3-01v9a *N*-terminal helix with a 4-aa turn. The resulting model was

computationally optimized first in structure and then in sequence to generate two new I3-01v9 scaffolds, termed I3-01v9b/c (**Fig. S3a**), in which the *N*-termini form a triangle of 12.9 Å (**Fig. 3a**, right). The trimeric forms of I3-01v9b/c, termed I3-01v9b/c-T, were generated by interrupting the particle-forming interface based on the structure of the aldolase (PDB ID: 1VLW) from which I3-01 was derived. Two "scaffolded" EBOV GP constructs, termed GPΔmuc-WL^{2}P^4-I3-01v9b/c-T, were designed to validate whether the I3-01v9b/c *N*-termini can accommodate the GP2 stalk (**Fig. S3b**). Both constructs were transiently expressed in HEK293S cells, purified using a mAb100 column, and analyzed by SEC (**Fig. S3c**). The trimer fractions were validated by BN-PAGE (**Fig. S3d**) before the nsEM analysis, which yielded two-dimensional (2D) classes corresponding to native-like GPΔmuc-WL^{2}P^4 trimers anchored to I3-01v9b/c-T (**Figs. S3e** and **S3f**). The GP2 stalk, although indiscernible in EM, was likely well-formed as the GPΔmuc trimer displayed the classic chalice shape (**Fig. 3b** and **Fig. S3g**). Computational modeling suggested that EBOV GPΔmuc-WL^{2}P^4-I3-01v9b would form a particle of 49.1 nm diameter measured for GP1-T269 (**Fig. 3c**).

Six SApNP constructs, with EBOV, SUDV, and BDBV GPΔmuc-WL^{2}P^4 displayed on the E2p and I3-01v9b scaffolds (**Fig. S3h**), were transiently expressed in ExpiCHO cells and purified by IAC using an ADI-15878 column and SEC using a Superose 6 increase 10/300 GL SEC column. All constructs showed a peak at ~8.7 ml corresponding to assembled protein particles (**Fig. 3d**). For EBOV and BDBV, a greater yield was noted for the GPΔmuc-WL^{2}P^4-presenting E2p SApNPs, but for SUDV, an opposite pattern was observed, with I3-01v9b showing a higher particle peak in SEC. The structural integrity of SApNPs was validated by nsEM (**Fig. 3e**). Most EM micrographs contained well-formed protein particles displaying an array of GP trimers on the outer surface. The particle size distribution was analyzed in solution using dynamic light scattering (DLS) (**Fig. 3f**). For EBOV GPΔmuc-WL^{2}P^4-presenting SApNPs, E2p and I3-01v9b were sized at 55.7 and 84.0

nm, respectively (**Fig. 3f**). The unusually large I3-01v9b "particle size" from DLS might be caused by SApNP aggregation, although this form was not frequently observed in nsEM. For SUDV and BDBV GPΔmuc-WL^{2}P^4-presenting SApNPs, the particle size was in the range of 61.1-71.9 and 51.3-53.8 nm, respectively. The notable variation in particle size might be attributed to the intrinsic structural flexibility of the glycan cap, which could have a significant impact on the measurement of hydrodynamic radius in DLS. Site-specific glycosylation profiles were generated for SUDV GPΔmuc-presenting SApNPs (**Fig. 3g** and **Fig. S3i**). An increase in oligomannose-type glycans was observed for SApNPs compared with soluble trimers. In both SUDV GPΔmuc trimers and their SApNPs, N563 carried predominantly oligomannose-type glycans (**Fig. 3g**).

The antigenicity of ebolavirus GPΔmuc-WL^{2}P^4-presenting SApNPs was assessed against the same antibody panel. In ELISA, SApNPs exhibited largely similar antibody-binding patterns to soluble trimers (**Fig. 3h** and **Fig. S3j**). For example, SUDV SApNPs bound less favorably to ADI-15946 and BDBV-289 compared with EBOV and BDBV SApNPs, with 5.0- to 16.8-fold higher EC_{50} values. SUDV GPΔmuc-WL^{2}P^4 E2p outperformed I3-01v9b with greater affinities for both bNAbs, with 1.4- to 1.9-fold lower EC_{50} values. A similar pattern was also found in SUDV GPΔmuc-WL^{2}P^4-presenting SApNPs binding to CA45, with a 2.5-fold difference in EC_{50} between the two NP scaffolds. Interestingly, an opposite trend was observed for EBOV and BDBV SApNPs, with I3-01v9b binding more tightly than E2p in most cases. BLI revealed a somewhat different antigenic profile (**Fig. 3i** and **Fig. S3k**). Most notably, SUDV and BDBV SApNPs exhibited greater signals in their binding to ADI-15878 and ADI-15946 than EBOV SApNPs, while SUDV SApNPs bound most weakly to BDBV-289 among the three ebolaviruses. For each ebolavirus GP, the binding signals against each bNAb were mostly similar between E2p and I3-01v9b, except in

316 the cases of SUDV SApNPs against CA45 and BDBV SApNPs against CA45 and BDBV-289,
317 where the difference between the two NP scaffolds was evident.

318 In this study, we displayed a stabilized GPΔmuc-WL^{2}P^4 trimer on two SApNP scaffolds,
319 E2p and a newly designed I3-01v9b, for three representative ebolaviruses. While SEC, nsEM, and
320 DLS were used to assess their purity and particle properties, which were largely comparable to our
321 HIV-1 Env trimer-presenting SApNPs (*108*), glycan and antigenic profiling revealed some unique
322 patterns associated only with SApNPs (e.g., a higher proportion of oligomannose-type glycans).

323 ***In vitro* effect of glycan modification on ebolavirus GPΔmuc trimers and SApNPs**
324 Previously, we investigated the effect of glycan modification on rationally designed HIV-1 Env
325 trimer and SApNP vaccines (*108*). Adding kifunensine (Kif) to ExpiCHO culture media, which
326 induced oligomannose-type glycosylation, neither enhanced nor reduced NAb elicitation, whereas
327 glycan trimming by endoglycosidase H (endo H) significantly improved NAb responses, indicated
328 by a high vaccine responder rate (*108*). The benefit of glycan trimming has also been reported for
329 influenza hemagglutinin (HA) and SARS-CoV-2 spike vaccines (*107, 109*). It is thus imperative
330 to examine how glycan modification may affect filovirus vaccines *in vivo*. However, these glycan-
331 modified filovirus GP immunogens first needed to be generated and characterized *in vitro*.

332 Here, we adopted a similar strategy (*108*) to generate ebolavirus GPΔmuc trimers that carry
333 either oligomannose-only glycans or a single layer of mono-*N*-acetylglucosamine (mono-GlcNAc)
334 glycans. EBOV and SUDV GPΔmuc-WL^{2}P^4 were transiently expressed in HEK293F cells in the
335 presence of Kif, which resulted in oligomannose-only glycans, and purified using an ADI-15878
336 column followed by SEC. The SEC profiles showed a trimer peak at ~10.7 ml, similar to wildtype
337 trimers (**Fig. 4a**). SEC-purified, Kif-treated GPΔmuc (e.g., 1 mg) was treated with endo H (termed
338 Kif/Endo H), which resulted in mono-GlcNAc stumps, with the enzyme removed by SEC. The

SEC profiles showed a trimer peak at ~11.1 ml and an endo H peak at ~13.9 ml (**Fig. 4a**). Sodium dodecyl sulfate (SDS)-PAGE and BN-PAGE confirmed that Kif/Endo H-treated GPΔmuc had a lower molecular weight than wildtype and Kif-treated GPΔmuc (**Fig. S4a**). DSC revealed a differential effect of glycan modification on GPΔmuc thermostability (**Fig. 4b**). The Kif-treated EBOV GPΔmuc-WL^{2}P^4 trimer displayed two denaturing states, with T_{m1} at 58.2ºC and T_{m2} at 64.3ºC. Endo H treatment further reduced T_{m1} and T_{m2} by 5.2ºC and 2.6ºC, respectively. In contrast, the Kif-treated SUDV GPΔmuc-WL^{2}P^4 trimer remained thermostable, showing the same T_m (63.6ºC) as the wildtype trimer with T_{onset} measured at 54.7ºC. Endo H treatment slightly reduced T_m to 62.6ºC and initiated unfolding at a lower T_{onset} of 48.9ºC. Antigenicity was assessed using the same antibody panel. In the ELISA (**Fig. 4c and Fig. S4b**), endo H treatment improved trimer binding to CA45, ADI-15878, and ADI-15946, which access a quaternary epitope near the base with few glycan contacts, but reduced trimer binding to BDBV-289, which targets the glycan cap, with glycans at N238 and N268 being part of the epitope. However, their differences in EC_{50} were small (1.5- to 1.9-fold) and not ebolavirus-specific. In the BLI analysis, glycan-modified trimers generated slightly higher binding signals than wildtype trimers (**Fig. 4d** and **Fig. S4c**). Glycan modification appeared to only have a modest impact on the biochemical, biophysical, and antigenic properties of stabilized ebolavirus GPΔmuc trimers except thermostability for EBOV.

We next characterized glycan-modified GPΔmuc-WL^{2}P^4-presenting SApNPs. For SUDV, both E2p and I3-01v9 SApNPs were included in this analysis, but for EBOV, only the E2p scaffold was tested due to the low yield of I3-01v9b SApNP. Notably, an N655D mutation was introduced to eliminate an *N*-glycan site at the base of the SUDV GP2 stalk that may hinder SApNP assembly. A design variant termed SUDV GPΔmuc-WL^{2}P^4-PD will be used hereafter (**Fig. S4d**). EBOV and SUDV SApNPs were transiently expressed in ExpiCHO cells with Kif and purified by IAC (ADI-

15878) and SEC. SEC-purified, Kif-treated SApNP was trimmed by endo H and further purified by SEC. The SEC profiles contained a peak at ~8.5-9.0 ml corresponding to SApNPs and, after endo H treatment, a peak at ~16.8 ml corresponding to endo H (**Fig. 4e**). The structural integrity of glycan-modified EBOV and SUDV GPΔmuc SApNPs was validated by nsEM (**Fig. 4e**). SDS-PAGE confirmed that Kif/Endo H-treated SApNPs had a lower molecular weight than Kif-treated SApNPs (**Fig. S4e**). Given the low yield of EBOV SApNPs, only SUDV SApNPs were subjected to glycan profiling and antigenic characterization. Site-specific glycan profiles confirmed that all complex glycans in SUDV GPΔmuc were now replaced by oligomannose-type glycans in the Kif-treated material (**Fig. 4f** and **Fig. S4f**). As expected, the N655 glycan was absent in the N655D mutant construct. In the ELISA (**Fig. 4g** and **Fig. S4g**), the antigenic profiles of SApNPs appeared to be largely consistent with those of trimers, with a more pronounced difference in EC_{50} between Kif and Kif/Endo H-treated materials (1.0- to 7.9-fold) observed for CA45, ADI-15878, and ADI-15946 (**Fig. 4g** and **Fig. S4g**). In the BLI analysis, all pan-ebolavirus bNAbs showed higher binding signals to Kif/Endo H-treated SApNPs, which only had a layer of mono-GlcNAc stumps on the GP trimer (**Fig. 4h** and **Fig. S4h**). In summary, these results suggested that glycan trimming may allow better antibody access to the conserved GP epitopes on the SApNP surface.

Rational design of a prefusion-stabilized RAVV GPΔmuc trimer

RAVV is one of the two known members of the *Marburgvirus* genus in the filovirus family (*39, 48*). Similar to ebolavirus GPs, RAVV GP also contains GP1 with a heavily glycosylated MLD and GP2 (**Fig. 5a**). Here, we applied a similar strategy to design a prefusion-stabilized RAVV GP trimer based on an MLD-deleted GP construct (ΔN257-T425), termed GPΔmuc. Other mutations, such as T578P and E580P (P^2 and P^4, respectively) in the HR1c bend and E631F/Q632V at the C-terminus (termed CT), were introduced to create five RAVV GP constructs: 1) GPΔTM (truncation

385 at 637), 2) GPΔmuc, 3) GPΔmuc-P^2, 4) GPΔmuc-P^4, and 5) GPΔmuc-P^2CT, all with a C-terminal
386 foldon motif and His_6 tag (**Fig. S5a**). All RAVV GP constructs were transiently expressed in
387 ExpiCHO cells and purified using a Nickel column followed by SEC. Both GPΔTM and GPΔmuc
388 constructs produced a low yield that contained multiple GP species including aggregate (~9-10
389 ml), trimer (~10.5 ml), dimer (~13.6 ml), and monomer (~14.7) (**Fig. 5b**). The P^2 mutation in HR1c
390 substantially improved the SEC profiles of various GPΔmuc constructs, showing a predominant
391 trimer peak at ~10.5 ml as well as visible dimer and monomer peaks. In contrast, the P^4 mutation
392 caused significant aggregation, indicated by a peak at ~8.63 ml (**Fig. S5b**). The GPΔmuc-P^2CT
393 construct demonstrated an optimal SEC profile, with an equivalent yield to GPΔmuc-P^2 but less
394 dimer/monomer content. MARV NAbs MR78 and MR191 (*48*), when used in IAC purification,
395 failed to capture GPΔmuc-P^2 and GPΔmuc-P^2CT (**Fig. S5c**). Nonetheless, distinct trimer bands
396 were discernible on the SDS-PAGE gel after Nickel/SEC purification (**Fig. 5c** and **Fig. S5d**). In
397 DSC, we observed two denaturing states for GPΔmuc-P^2 at 51.0ºC and 60.0ºC and three denaturing
398 states for GPΔmuc-P^2CT at 54.5ºC, 58.3ºC, and 66.6ºC (**Fig. 5d**). The CT mutation appeared to
399 improve the trimer thermostability at the cost of creating a new unfolding intermediate.

400 The lead RAVV GPΔmuc design, GPΔmuc-P^2CT, was complexed with MR78 for nsEM
401 analysis (**Fig. 5e** and **Fig. S5e**). We hypothesized that if the nsEM model, albeit at a low resolution,
402 matched the crystal structure (PDB ID: 5UQY), then it would not only validate our rational design
403 but also provide evidence for the correct presentation of a conserved neutralizing epitope. Indeed,
404 the 2D classifications showed well-formed RAVV GPΔmuc/MR78 complexes (**Fig. S5e**). The
405 crystal structure could be fitted into the nsEM density map (**Fig. 5e**, left). Notably, our nsEM
406 model also superposed well with a previous nsEM model of the RAVV GPΔmuc/MR78 complex
407 (**Fig. 5e**, right). The site-specific glycan analysis showed distinct patterns compared to ebolavirus

GPs (**Fig. 5f** and **Fig. S5f**). Specifically, four *N*-glycan sites at N94, N171, N219, and N564 were mainly oligomannose-type, whereas N190, N202, and N487 presented either oligomannose- or complex-type glycans. Two sites, N475 and N619, presented predominantly complex-type glycans. In the ELISA (**Fig. 5g** and **Fig. S5g**), RAVV GPΔmuc-P^2- and GPΔmuc-P^2CT trimers bound to MR78 and MR191 with similar EC_{50} values. The BLI data were largely consistent with the ELISA data (**Fig. 5h** and **Fig. S5h**). RAVV GPΔmuc-P^2CT was displayed on E2p and I3-01v9b SApNPs, which were assessed by nsEM following ExpiCHO expression and IAC purification (**Fig. S5i**). Protein NPs were not observed in any nsEM micrographs. Taken together, our results indicate that GPΔmuc-P^2CT provides a native-like, prefusion-stabilized design for marburgvirus GP vaccine development, but its multivalent display on SApNPs may require further optimization.

Distribution, trafficking, and retention of SUDV GPΔmuc trimers and trimer-presenting SApNPs in lymph nodes

In our previous studies, we observed a positive correlation between the thermostability of a viral antigen (i.e., T_m) to be displayed on E2p or I3-01v9 SApNPs and the retention time of resulting SApNP vaccine antigens in lymph node follicles (*108, 120, 121*). In this study, we hypothesized that SUDV GPΔmuc-presenting SApNPs may behave *in vivo* similarly to HIV-1 Env-presenting SApNPs, as their trimeric antigens exhibited comparable T_m values (~63-66°C). Following our previously established protocol (*108, 120, 121*), we immunized mice with SUDV GPΔmuc-WL^2P^4 trimer and SApNPs (both E2p and I3-01v9b included) to investigate their interaction with cellular components in lymph nodes and analyze vaccine-induced immunological responses.

To induce a robust humoral response, vaccine antigens must be transported through the lymphatic system, accumulate in lymph node follicles, and effectively engage with B cell receptors (BCRs) to stimulate B cell activation (*122-125*). We first examined the distribution of E2p and I3-

01v9b SApNPs in lymph nodes. We intradermally administered SApNPs to mice via footpads (4 footpads, 10 μg/footpad). The brachial and popliteal sentinel lymph nodes were isolated from both sides of the body of the mouse 12 h after a single-dose injection for immunohistological studies. Four NAbs, ADI-15878 (*111*), ADI-15946 (*114*), CA45 (*113*), and mAb100 (*126*), were used to stain lymph node sections for antigen detection (**Fig. S6a**). Overall, the immunostaining images from CA45 demonstrated the best signal-to-noise ratio. Based on these data, CA45 was selected to study the distribution and trafficking of SUDV GPΔmuc-based vaccines in lymph nodes. Consistent with our previous studies of SARS-CoV-2 spike (*121*), HIV-1 Env (*108*), and influenza M2ex3 (*120*) SApNPs, SUDV GPΔmuc-presenting E2p and I3-01v9b SApNPs accumulated in the centers of lymph node follicles (**Figs. 6a** and **b**, images on the left; schematics on the right).

We next assessed the trafficking and retention patterns of SUDV GPΔmuc-WL^{2}P^4 trimer and SApNPs in lymph node follicles over a period of 8 weeks after a single-dose injection (4 footpads, 10 μg/footpad) (**Fig. 6c**). Histological images showed that all SUDV immunogens were transported into lymph nodes and accumulated in the subcapsular sinus within 2 h (**Fig. 6c**). While the soluble trimer was transported into lymph node follicles within 2 h and completely cleared by 48 h, both E2p and I3-01v9b SApNPs appeared in follicles at 2 h, achieved peak accumulation at 48 h, and were retained in follicles over a period of 8 weeks (**Fig. 6c**). Next, the CA45-stained area was quantified in a time-dependent manner, demonstrating a ~112-times longer retention for the E2p and I3-01v9b SApNPs compared with the soluble trimer (**Figs. 6c** and **d**). The area under the curve (AUC) indicated that the exposure of SUDV GPΔmuc presented on the SApNP surface is 14-28 times higher than the same antigen in a soluble trimer form (**Fig. 6e**). The two large SApNPs displaying 20 GPΔmuc trimers also showed 19-33 times greater accumulation compared with the soluble GPΔmuc trimer at 48 h (**Fig. 6f**). These findings are consistent with our previous studies

(*108, 120, 121*), where individual antigens were cleared from follicles within 48 h, whereas large antigen-presenting SApNPs exhibited prolonged follicular retention lasting for 2-8 weeks. Notably, the retention time of SUDV GPΔmuc SApNPs fell in the same range as HIV-1 Env SApNPs and influenza M2ex3 SApNPs, all of which yielded a T_m value greater than 62°C, supporting our hypothesis that antigen thermostability (T_m) correlates with SApNP retention.

FDCs are resident stromal cells that form a network structure in lymph node follicles and play an essential role in antigen retention and presentation to stimulate B cell responses (*122-124, 127*). FDC networks retain soluble antigens, immune complexes, viruses, and bacteria on their surfaces and dendrites to induce GC initiation and maintenance (*128-130*). Our previous studies demonstrated that FDC networks are the major follicular components to retain SARS-CoV-2 spike, HIV-1 Env, and influenza M2ex3 SApNPs (*108, 120, 121*). To test whether this would be the case for SUDV GPΔmuc SApNPs, we isolated sentinel lymph nodes at the peak of accumulation (48 h) and subsequent timepoints (2 h to 8 weeks) after intradermal administration (**Fig. 6g** and **Figs. S6b-g**). Lymph node sections were stained with NAb CA45 (white) (*113*) for SUDV GPΔmuc, anti-CD21 antibodies (green) for FDCs, and anti-CD169 antibodies (red) for subcapsular sinus macrophages. The immunofluorescent signals of SUDV GPΔmuc SApNPs colocalized well with FDC ($CD21^+$) networks at 48 h (**Fig. 6g**), thus confirming our hypothesis.

Interaction of SUDV GPΔmuc SApNPs with FDCs and phagocytic cells in lymph nodes

FDC networks form a reservoir in lymph node follicles for antigen sequestration, alignment, and presentation to effectively crosslink BCRs, activate naive B cells, and stimulate GC reactions (*122-124, 131*). Our previous transmission electron microscopy (TEM) analysis indicated that FDC networks retained SARS-CoV-2 spike and HIV-1 Env SApNPs on their cell surface and dendrites through interactions with complement protein 3 (C3) and complement receptor 2 (CR2) (*108, 121*).

Here, we visualized the interface between FDC dendrites and B cells to understand how FDC networks present SUDV GPΔmuc SApNPs adjuvanted with aluminum phosphate (AP) to engage B cells. To this end, we injected adjuvanted E2p and I3-01v9b SApNPs into the mouse hind footpads (2 footpads, 50 μg/footpad). Fresh popliteal sentinel lymph nodes were isolated 2, 12, and 48 h after a single injection. The lymph node tissues were sectioned and processed for TEM analysis. TEM images revealed the expected, characteristic morphology of long FDC dendrites interacting with B cells in lymph node follicles (**Figs. 7a-c**). Intact SUDV GPΔmuc E2p and I3-01v9b SApNPs (round-shaped granules, yellow arrows) were aligned on FDC dendrites and B cell surfaces at all timepoints, and AP particles appeared not to colocalize with SApNPs (**Figs. 7a-c** and **Fig. S7a-f**). These results illustrated how FDC networks collect and present vaccine antigens (i.e., SUDV GPΔmuc SApNPs) and use their long dendrites to maximize interactions between antigens and BCRs. At the later timepoints (12 and 48 h), SUDV GPΔmuc SApNPs were also found to be inside endolysosomes of B cells (**Figs. S7c** and **e**).

Phagocytic cell populations, such as macrophages and dendritic cells, take up and process vaccine antigens to facilitate adaptive immune responses (*125, 132, 133*). These innate immune cells, located in the subcapsular sinus and medullary sinus of lymph nodes, can capture vaccine antigens, transport them to migrating B cells, and eventually deposit them on FDCs through a complement-dependent transport mechanism (*123, 124, 134-138*). In this study, we assessed the interaction between phagocytic cells and AP-adjuvanted SApNPs. SUDV GPΔmuc-presenting E2p and I3-01v9b SApNPs were found to be either on the surface or inside endolysosomes of phagocytic cells (**Figs. 7d** and **e** and **Figs. S7g-l**), consistent with our previous findings for SARS-CoV-2 spike and HIV-1 Env SApNPs (*108, 121*). AP particles tended to aggregate in the extracellular matrix (ECM) 2 h after the injection (**Fig. 7f** and **Fig. S7m**). Both I3-01v9b SApNPs

and AP particles were also observed inside endolysosomes of phagocytic cells at all timepoints (**Fig. 7g** and **Figs. S7n-p**). Overall, E2p and I3-01v9b SApNPs were associated with FDC networks, B cells, and phagocytic cells with a similar trend. FDC networks retained SApNPs on the cell dendrites and presented native antigens to B cells in lymph node follicles. A substantial amount of SApNPs was processed inside endolysosomes of phagocytic cells with AP adjuvant.

Assessment of GC reactions induced by SUDV GPΔmuc trimers and SApNPs in lymph nodes

In lymph node follicles, GCs are the places where B cell somatic hypermutation, selection, affinity maturation, and class switching occur (*128, 139, 140*). GC reactions lead to the formation of immune memory and development of NAb responses upon vaccination (*122, 125*). As the essential components supporting GC initiation and maintenance, FDC networks and T follicular helper (T_{fh}) cells present vaccine antigens and stimulate B cells, respectively (*141-143*). Here, we hypothesized that SUDV GPΔmuc SApNPs can be retained by FDC networks for a longer period and thus induce more robust and long-lived GC reactions in lymph node follicles compared with the soluble trimers. We first characterized GC reactions induced by I3-01v9b after a single-dose injection (4 footpads, 10 μg/footpad). Using a previously established protocol (*108, 120, 121*), vaccine-induced GC B cells ($GL7^+$, red) and T_{fh} cells ($CD4^+$ $Bcl6^+$, co-labeled with cyan and red) in lymph nodes were assessed by immunohistological analysis. Robust GCs were formed and attached to FDC networks ($CD21^+$, green), with well-organized dark zone (DZ) and light zone (LZ) compartments in B cell follicles (B220+, blue) (**Fig. 8a**, left). T_{fh} cells were observed in the LZ of GCs, sustaining the process of B cell affinity maturation (**Fig. 8a**, right). We then applied this immunohistological assessment to the SUDV GPΔmuc trimer and SApNPs (both E2p and I3-01v9b) 2, 5, and 8 weeks after a single-dose injection (**Fig. 8b** and **Figs. S8a-c**) and 2 and 5 weeks after the boost (**Fig. 8c** and **Figs. S8d** and **e**). We quantified GC reactions using two metrics: GC/FDC ratio (the frequency

of GCs associated with FDC networks) and size of GCs (occupied area in follicles) as previously described (*108, 120, 121*). All three SUDV GPΔmuc immunogens induced robust GCs, with the I3-01v9b SApNP group showing the largest GCs 2 weeks after a single-dose vaccination (**Fig. 8b** and **Fig. S8a**). While the GC/FDC ratio after a single trimer dose decreased significantly over 8 weeks, the two SApNPs induced long-lived GCs with high GC/FDC ratios (above 50%) lasting for 8 weeks (**Fig. 8b**). The sizes of GCs declined over time in both trimer and SApNP groups (**Figs. 8b** and **d**). For all vaccine groups, robust GCs were restored after the boost, and the GC/FDC ratio of the GPΔmuc trimer group remained similar (all above 75%) to the two SApNP groups (**Fig. 8c**). Overall, the two SApNPs generated larger GCs than the soluble trimer, 1.3 to 2.5 times larger after one dose (**Figs. 8b** and **d**) and 1.4 to 1.8 times larger after the boost (**Figs. 8c** and **e**).

Next, we assessed GC reactions using flow cytometry. We intradermally immunized mice with three vaccines and isolated the sentinel lymph nodes 2, 5, and 8 weeks after a single-dose injection (**Fig. 8f** and **Fig. S9**) and 2 and 5 weeks after the boost injection (**Fig. 8g**) (4 footpads, 10 μg/injection). Fresh lymph node tissues were disaggregated into a single-cell suspension and stained with an antibody cocktail. The GC reactions were quantified based on the percentage and number of GC B and T_{fh} cells (**Fig. S9**). The I3-01v9b SApNP group yielded the highest percentage and number of GC B cells 2 weeks after a single-dose injection (**Fig. 8f**), consistent with the immunohistological analysis. Among all the vaccine groups, GC B cells declined over time while T_{fh} remained steady for 8 weeks. A boost improved both the frequency and number of GC B cells and T_{fh} cells (**Fig. 8g**). Notably, GC B and T_{fh} cells induced by I3-01v9b SApNP remained at a relatively high level over 8 weeks after a boost injection. Compared with the soluble trimer, the E2p and I3-01v9b SApNPs elicited 1.8/2.4-3.3 times more GC B cells and 1.5-1.8/2.4-3.2 times more T_{fh} cells 8 weeks after the single-dose/boost injection, respectively (**Figs. 8f** and **g**). In

546 summary, the two SUDV GPΔmuc SApNPs generated more robust and long-lived GC reactions
547 than the soluble GPΔmuc trimer, leading to more potent and durable humoral immune responses.

548 **Antibody responses induced by rationally designed filovirus GPΔmuc vaccines in mice**

549 We assessed the immunogenicity of rationally designed filovirus GPΔmuc constructs, both trimers
550 and SApNPs (E2p and I3-01v9b), in mice (**Fig. 9a**). The filovirus antigen (10 μg) was adjuvanted
551 with aluminum hydroxide (AH) and a Toll-like receptor 9 (TLR9) agonist (CpG ODN 1826). Mice
552 were immunized intraperitoneally at weeks 0, 3, 9, and 15 with an interval of 6 weeks between the
553 second and third doses and the third and fourth doses. Blood serum was collected 2 weeks after
554 each immunization for serological analysis. The EBOV vaccine-induced serum binding antibody
555 (bAb) responses were determined by ELISA using an EBOV GPΔmuc-WL^{2}P^4(1TD0) antigen (**Fig.**
556 **9b** and **Figs. S10a** and **b**). Notably, the use of 1TD0, and not foldon, as the trimerization motif
557 allowed us to detect only GPΔmuc-specific bAb responses. Overall, EBOV GPΔmuc E2p SApNP
558 elicited the highest bAb titers at all four timepoints, showing 8.2- and 5.3-fold higher EC_{50} values
559 than the soluble trimer at weeks 2 and 5, respectively. All vaccine groups reached plateaued EC_{50}
560 titers after three immunizations at week 11. EBOV GPΔmuc I3-01v9b SApNP yielded an identical
561 EC_{50} titer of 182253 to its E2p counterpart at week 11, 2.5-fold higher than the EC_{50} titers elicited
562 by the soluble trimer. The sera after four vaccine doses at week 17 were assessed against a SUDV
563 GPΔmuc-WL^{2}P^4(1TD0) antigen (**Fig. 9c** and **Fig. S10c**). Similarly, EBOV GPΔmuc E2p SApNP
564 elicited the highest EC_{50} titer of 32585, which was 3.5-fold higher than the soluble trimer. Cross-
565 reactive bAb responses were also tested against a RAVV GPΔmuc-P^{2}CT(1TD0) antigen (**Fig. 9d**
566 and **Fig. S10d**). Both E2p and I3-01v9b SApNP groups demonstrated significantly higher serum
567 binding signals, indicated by absorbance at 450 nm (A450), than the soluble trimer group. Serum
568 NAb responses were evaluated using a filovirus pseudoparticle (pp) neutralization assay (*35*), with

the 50% inhibitory dilution (ID_{50}) values calculated for comparison. Here, the week-2 sera were used as a negative control in the longitudinal serum NAb analysis. None of the EBOV GPΔmuc vaccines elicited any NAb response at week 2, but ID_{50} titers were detected at weeks 5, 11, and 17 and continued to increase when tested against an EBOV-Makona pseudovirus (**Fig. 9e** and **Figs. S10e** and **f**). Consistent with the bAb titers, EBOV GPΔmuc E2p SApNP produced the highest NAb titers at all timepoints, although no statistical significance was observed in a cross-group comparison. The week-17 mouse sera were also assessed using a SUDV-Gulu pseudovirus assay (**Fig. 9f** and **Fig. S10g**). EBOV GPΔmuc E2p SApNP yielded the highest EC_{50} titer of 761 among all vaccine groups. Notably, the EBOV GPΔmuc trimer group elicited the highest EC_{50} titer of 2759 at week 17 against a BDBV-Uganda pseudovirus, which was 4.5- and 4.9-fold higher than E2p and I3-01v9b SApNPs, respectively (**Fig. 9g** and **Fig. S10h**).

We assessed SUDV vaccine-induced serum bAb responses by ELISA against a SUDV GPΔmuc-WL^2P^4(1TD0) antigen (**Fig. 9h** and **Figs. S10i** and **j**). Consistent with the bAb responses elicited by EBOV vaccines, SUDV GPΔmuc E2p SApNP yielded the highest EC_{50} titers of 871, 82910, and 307187 at weeks 2, 5 and 11, respectively, 12.4-, 4.5-, and 5.7-fold higher than the soluble trimer. The EC_{50} titers in both E2p and I3-01v9 SApNP groups plateaued after three doses at week 11, whereas the soluble trimer group reached a peak of 102959 after four doses at week 17, which was still slightly lower than the two SApNP groups. These results correlated well with the GC reactions generated by SUDV GPΔmuc trimer and SApNPs (**Fig. 8**). The week-17 sera were then evaluated against an EBOV GPΔmuc-WL^2P^4(1TD0) antigen (**Fig. 9i** and **Fig. S10k**). SUDV GPΔmuc-presenting E2p and I3-01v9b SApNPs elicited EC_{50} titers of 27290 and 25446, which were 2.6- and 2.4-fold higher than the soluble GPΔmuc trimer. We tested cross-reactive bAb responses using week-17 sera against a RAVV GPΔmuc-P^2CT(1TD0) antigen (**Fig. 9j** and

592 **Fig. S10l**). The E2p and I3-01v9b SApNP groups demonstrated significantly higher serum binding
593 signals (A450) than the soluble trimer group. Next, we assessed SUDV GPΔmuc vaccine-induced
594 autologous NAb responses in a SUDV-Gulu pseudovirus assay. Similarly, the week-2 sera were
595 used as a negative control in the longitudinal SUDV neutralization assays. None of the vaccines
596 elicited a detectable NAb response at week 2 except for one mouse in the E2p group, but the ID_{50}
597 titers were detectable at weeks 5, 11, and 17 and plateaued at week 11 after three doses (**Fig. 9k**
598 and **Figs. S10m** and **n**). Overall, SUDV GPΔmuc trimer and SApNP vaccines showed comparable
599 EC_{50} titers in the range of 1329-4628 at each timepoint after two doses. The week-17 mouse sera
600 were tested against EBOV-Makona (**Fig. 9l** and **Fig. S10o**) and BDBV-Uganda (**Fig. 9m** and **Fig.**
601 **S10p**) pseudoviruses. No statistical significance was found between the SUDV trimer and SApNP
602 groups in their cross-NAb responses, measured by ID_{50} titers, against EBOV and BDBV.

603 Lastly, we assessed RAVV GPΔmuc trimer-induced serum bAb responses in ELISA using
604 a RAVV GPΔmuc-P^2CT(1TD0) antigen (**Fig. 9n** and **Fig. S10q**). Similar to EBOV and SUDV
605 GPΔmuc trimers, RAVV GPΔmuc trimer generated a strong bAb response after two doses, with
606 the peak EC_{50} titer of 362215 at week 5. We tested cross-reactive bAb responses using week-17
607 sera against two ebolavirus antigens, EBOV GPΔmuc-WL^2P^4(1TD0) (**Fig. 9o** and **Fig. S10r**) and
608 SUDV GPΔmuc-WL^2P^4(1TD0) (**Fig. 9p** and **Fig. S10s**). Low bAb titers, indicated by absorbance
609 (A450) values, were observed for SUDV GPΔmuc in most mice. Vaccine-induced NAb responses
610 were evaluated against pseudotyped MARV-Angola and ebolaviruses using purified IgG and
611 week-17 sera, respectively (**Fig. 9q** and **Figs. S10t** and **u**). Notably, mouse IgG was purified to
612 eliminate nonspecific serum background in the MARV pseudovirus assay (**Fig. S10t**, left), and in
613 this assay, the neutralization potency was measured by the 50% inhibitory concentration (IC_{50}).
614 To summarize, the RAVV GPΔmuc trimer group yielded IC_{50} values of 30.9-148.4 μg/ml with a

geometric mean of 70.2 μg/ml when IgG was tested against MARV-Angola. To be consistent with EBOV and SUDV vaccines, RAVV GPΔmuc trimer-induced sera were tested against EBOV-Makona, SUDV-Gulu, and BDBV-Uganda in pseudovirus assays. Despite the positive signals in serum (**Fig. S10u**), IgG neutralization is likely needed to confirm this critical finding.

Antibody responses induced by glycan-modified filovirus GPΔmuc vaccines in mice

We assessed the immunogenicity of filovirus GPΔmuc vaccines with oligomannose-rich (Kif) and trimmed (Kif/endo H) glycans in mice (**Fig. 10a**). We utilized the same immunization protocol as in our previous vaccine studies (*95, 108, 144, 145*), which differed from the longer-interval (6 weeks) regimen used for wildtype GPΔmuc vaccines (**Fig. 9a**). Here, mice were immunized at weeks 0, 3, 6, and 9 with an interval of 3 weeks between two adjacent doses via the intraperitoneal route. The injection dose contained 10 μg of glycan-modified antigen formulated with 100 μl of CpG/AH adjuvant, resulting in a final volume of 200 μl. Blood serum was collected 2 weeks after each dose and the EC_{50} titers were plotted longitudinally for comparison.

We first assessed glycan-modified EBOV GPΔmuc trimer-induced serum bAb responses by ELISA against an EBOV GPΔmuc-WL^2P^4(1TD0) antigen (**Fig. 10b** and **Figs. S11a** and **b**). Among the three groups, the glycan-trimmed EBOV GPΔmuc trimer elicited the lowest EC_{50} titers at all three timepoints, while Kif-treated EBOV GPΔmuc trimer yield the highest EC_{50} titers, 212 and 42360 at weeks 2 and 5, respectively. In terms of EC_{50} titers, the Kif-treated group was 2.2- and 6.2-fold higher at week 2 and 1.2- and 2.1-fold higher at week 5 than the wildtype and trimmed groups, respectively. All trimer groups reached the peak of EC_{50} titers after three doses. Following a similar trend, the Kif-treated EBOV GPΔmuc-E2p SApNP group showed the highest bAb titers at all three timepoints (**Fig. 10c** and **Figs. S11a** and **b**). The bAb responses appeared to plateau at

week 5, with Kif-treated EBOV GPΔmuc-E2p SApNP showing the highest EC_{50} titer of 300502, 1.5- and 3.2-fold higher than its wildtype and glycan-trimmed counterparts, respectively. Wildtype and Kif-treated EBOV GPΔmuc I3-01v9 SApNPs induced comparable bAb responses, reaching peak EC_{50} titers after three doses (**Fig. 10d** and **Figs. S11a** and **b**). We next assessed NAb responses induced by glycan-modified EBOV GPΔmuc vaccines against EBOV-Makona. Overall, the Kif-treated vaccines were the best performers, while the glycan-trimmed vaccines induced the lowest NAb responses at all three timepoints (**Fig. 10e-g** and **Figs. S11c** and **d**). Specifically, Kif-treated EBOV GPΔmuc trimer yielded an ID_{50} titer of 449 at week 5, 1.5- and 1.9-fold higher than its wildtype and glycan-trimmed counterparts, respectively (**Fig. 10e**). Kif-treated EBOV GPΔmuc E2p SApNP elicited an ID_{50} titer of 1459 at week 5, 2.3- and 4.1-fold higher than its wildtype and glycan-trimmed counterparts, respectively (**Fig. 10f**). A similar pattern was noted for the I3-01v9b SApNP groups (**Fig. 10g**). Our results thus demonstrated the beneficial effect of an oligomannose-rich glycan shield on bAb and NAb responses induced by EBOV GPΔmuc vaccines.

We assessed glycan-modified SUDV GPΔmuc trimer-induced serum bAb responses by ELISA against a SUDV GPΔmuc-WL^2P^4(1TD0) antigen (**Fig. 10h** and **Figs. S11e** and **f**). At all three timepoints, Kif-treated SUDV GPΔmuc trimer elicited the highest bAb titers, whereas glycan-trimmed elicited the lowest bAb titers, similar to EBOV. Regardless of glycan modification, all vaccine groups reached peak EC_{50} titers after three doses. Kif-treated SUDV GPΔmuc trimer elicited the highest EC_{50} titers, 425 and 150326 at weeks 2 and 5, respectively. In terms of EC_{50} titers, Kif-treated SUDV GPΔmuc trimer was 6.1- and 13.3-fold higher at week 2 and 8.2- and 27.6-fold higher at week 5 than its wildtype and glycan-trimmed counterparts, respectively. Similarly, for both SUDV GPΔmuc E2p and I3-01v9b SApNPs, the Kif-treated groups showed

659 the highest bAb responses at weeks 2 and 5 (**Figs. 10i** and **j** and **Figs. S11e** and **f**). In addition, for
660 both SApNPs, Kif treatment led to plateaued EC_{50} titers after two doses at week 5, whereas the
661 wildtype and glycan-trimmed groups required three doses to reach their EC_{50} titers at week 8. Kif-
662 treated SUDV GPΔmuc E2p and I3-01v9b SApNP elicited the highest EC_{50} titers of 329358 and
663 271692 at week 5, respectively, 2.1- and 6.9-fold higher than their wildtype counterparts and 2.3-
664 and 5.7-fold higher than their glycan-trimmed counterparts, respectively. We then evaluated NAb
665 responses induced by glycan-modified SUDV GPΔmuc vaccines against SUDV-Gulu. All three
666 SUDV GPΔmuc trimer groups reached peak ID_{50} titers after three doses (**Fig. 10k** and **Figs. S11g**
667 and **h**). The Kif-treated SUDV GPΔmuc trimer group showed the highest ID_{50} titer of 3652 at week
668 5, 2.7- and 2.2-fold higher than its wildtype and glycan-trimmed counterparts, respectively (**Fig.**
669 **10k**). Three E2p SApNPs showed comparable ID_{50} titers, indicating a limited impact of glycan
670 modification on NAb responses (**Fig. 10l**). Among the I3-01v9 SApNP groups, Kif-treated I3-
671 01v9b SApNP elicited the highest ID_{50} titer of 4041 at week 8, 2.9- and 3.2-fold higher than its
672 wildtype and glycan-trimmed counterparts, respectively (**Fig. 10m**).

673 Lastly, we assessed glycan-trimmed RAVV GPΔmuc trimer-induced serum bAb responses
674 by ELISA against a wildtype RAVV GPΔmuc-P^2CT(1TD0) antigen (**Fig. 10n** and **Figs. S11i** and
675 **j**). The wildtype trimer group achieved the peak EC_{50} titer of 362215 after two doses, whereas the
676 glycan-trimmed trimer group required three doses to reach the highest EC_{50} titer, 446121. Overall,
677 no significant difference was found between the two groups at any timepoint. We also compared
678 NAb responses induced by the wildtype and glycan-trimmed RAVV GPΔmuc vaccines using
679 purified IgG against pseudotyped MARV-Angola and ebolaviruses (**Fig. 10o** and **Fig. S10k**). In
680 terms of MARV-Angola neutralization, the two trimer groups showed similar IC_{50} values in the
681 range of 25.9-191.6 μg/ml. In terms of ebolavirus neutralization, mouse IgG was tested against

682 EBOV-Makona, SUDV-Gulu, and BDBV-Uganda. Indeed, both RAVV GPΔmuc trimers elicited
683 cross-ebolavirus NAbs, with the wildtype being more effective than the glycan-trimmed trimers.
684 IgG neutralization against lymphocytic choriomeningitis virus pseudoparticles (LCMV-pps) was
685 tested in a negative control assay, in which nonspecific activity was not detected.

686 Our results illustrated the importance of NP display and glycan modification for filovirus
687 vaccine immunogenicity in a mouse model. Overall, the Kif-treated GPΔmuc SApNPs elicited the
688 strongest bAb and NAb responses. However, due to the differences in our immunization protocols
689 (e.g., injection intervals), more *in vivo* studies are needed to confirm our results. Another important
690 finding is the induction of cross-ebolavirus NAbs by RAVV GPΔmuc-P^{2}CT, shown at both serum
691 and IgG levels (**Fig. 9q** right and **Fig. 10o**), suggesting a more immunogenetic nature of this
692 marburgvirus GP and its potential as a pan-filovirus vaccine antigen.

693 **DISCUSSION**

694 Filoviruses are a major cause of lethal VHF in humans and NHPs (*5, 6*). Viral GP mediates cell
695 entry by initiating attachment and membrane fusion (*13*). Structures of filovirus GP bound to NAbs
696 from human survivors demonstrate that GP harbors neutralizing epitopes and is the main target of
697 vaccine development (*17-20*). Two vector-based EBOV vaccines are now available for human use
698 after rVSV-ZEBOV (ERVEBO) (*62*) and a two-dose formula (Zabdeno + Mvabea) (*63*) were
699 approved by the U.S. FDA in 2019 and the European Commission in 2020, respectively. However,
700 no vaccines exist to prevent VHF caused by other filoviruses. In the past decade, a structure-based
701 rational approach has emerged and proven useful in accelerating vaccine development for RSV,
702 as well as the more challenging HIV-1 (*83, 84, 86, 87*). Like other class-I viral fusion proteins,
703 filovirus GP is metastable in its wildtype form (*94, 95*). As a result, filovirus vaccines that express
704 wildtype GP may not elicit an optimal immune response. Two recent studies explored potential

causes of filovirus GP metastability and stabilized the MLD-deleted GPΔmuc trimer in a native-like conformation as vaccine antigens (*94, 95*). While native-like GP trimers remained the focus of filovirus vaccines, protein NPs began to be assessed as a more effective platform for vaccine delivery (*73, 95*). Glycan trimming was reported to improve NAb responses for influenza, HIV-1, and SARS-CoV-2 vaccines (*107-109*), suggesting a general strategy for viral GP-based vaccines. However, GP stabilization, NP display, and glycan modification have yet to be explored in a systematic manner for diverse filoviruses in the context of rational vaccine design.

We previously reported that the HR2 stalk and HR1c bend in GP2 contributed to EBOV GP metastability, and a W615L mutation and C-terminal extension (targeting HR2) in combination with a proline mutation at T577 or L579 (targeting HR1c) resulted in a stable GPΔmuc trimer that can be produced in mammalian cells with high yield and homogeneity (*95*). In the present study, we sought to extend rational GP design to SUDV and BDBV in the *Ebolavirus* genus and RAVV in the *Marburgvirus* genus to facilitate vaccine development to counter future filovirus outbreaks, as highlighted by the U.S. Biomedical Advanced Research and Development Authority (BARDA) (*75, 146, 147*). For GPs from these two filovirus genera, while the same GP2 elements (i.e., HR1c and HR2 stalk) cause metastability, solutions to stabilize these proteins appear to be different. For EBOV, SUDV, and BDBV, a comparative analysis of GPΔmuc-WL^{2}P^2 and -WL^{2}P^4 constructs revealed a more favorable thermostability profile for P^4 but little difference in trimer yield, purity, and antigenicity between P^2 and P^4. The crystal structure of EBOV GPΔmuc-WL^{2}P^4 elucidated the stabilizing effect of an interprotomer hydrogen bond (R130-A575), while the cryo-EM model of SUDV GPΔmuc-WL^{2}P^4 captured the atomic details of GP-CA45 interactions, thus confirming that GPΔmuc-WL^{2}P^4 is a general design to stabilize ebolavirus GP in a native-like conformation for immune recognition. For RAVV, the P^2 (T578P) construct showed substantially higher trimer

yield than its P^4 (E580P) counterpart, with a double mutation (E631F/Q632V) toward the base of the HR2 stalk further improving trimer stability, resulting in a GPΔmuc-P^2CT design. Notably, the W615L mutation used to stabilize ebolavirus GP was adopted from MARV GP (*95*), whereas here the E631F/Q632V mutation used to stabilize marburgvirus GP was introduced from EBOV GP, suggesting that filoviruses may have evolved distinct mechanisms to control metastability through either a widened neck (for ebolaviruses) or a charged tail (for marburgviruses) within the coiled-coil HR2 stalk. Our findings also suggest that other class-I viral GPs may contain triggers of metastability within their stalks, such as RSV fusion and SARS-CoV-2 spike proteins.

We previously focused our NP design efforts on the interior, incorporating an inner shell of locking domains and a core of helper T-cell epitopes (*95*). The resulting "multilayered" E2p and I3-01v9 SApNPs were used to present EBOV, SARS-CoV-2, HIV-1, and influenza antigens (*95, 108, 120, 144, 148*). We also observed that EBOV GP and RSV F (*95, 149*), both containing a coiled-coil stalk, but not HIV-1 Env (*86, 150*) dissociated into monomers without a C-terminal trimerization motif, suggesting that NPs with small, rigid anchoring sites may be more suitable for displaying such GP trimers with extended stalks. Compared with E2p, which has a small triangular anchoring site (9 Å) on the NP surface (*151*), I3-01v9 *N*-termini form a large spacing of 50.5 Å (*150*), which may destabilize EBOV and other filovirus GPs on the NP surface. To address this issue, we redesigned I3-01v9 using a previously created I3-01v9a variant (*120*) as the template. An *N*-terminal helix was generated and packed against the protein core *in silico*, resulting in I3-01v9b/c. When the I3-01v9b/c-T variants were used as "scaffolds" to present EBOV GPΔmuc-WL^2P^4, the resulting constructs showed native-like GP structures in EM. However, it is worth noting that while all three ebolavirus GPΔmuc-WL^2P^4 trimers were successfully displayed on E2p and I3-01v9b SApNPs, a similar attempt with RAVV GPΔmuc-P^2CT produced low yield and

751 aggregation. It is plausible that certain regions within RAVV GP might interact with the NP
752 backbone and consequently cause misfolding. Nonetheless, our results suggest that I3-01v9b/c can
753 now be used to display filovirus GP as well as other viral GPs, such as RSV F and SARS-CoV-2
754 spike, with greater trimer stability. Glycan modification adds another dimension to rational vaccine
755 design (*108*), but the biochemical, biophysical, structural, and antigenic properties must be
756 reevaluated. Here, the glycan-trimmed GPΔmuc trimers showed lower T_m values than wildtype
757 and Kif-treated oligomannose-rich GPΔmuc trimers. Similar to our previous HIV-1 study (*108*),
758 glycan trimming improved NAb epitope recognition for both trimers and SApNPs. However, the
759 improved *in vitro* antigenicity may not necessarily correlate with *in vivo* immunogenicity.

760 In recent studies, we established a vaccine strategy in which a detailed mechanistic analysis
761 was performed to characterize *in vivo* behaviors of immunogens to provide potential explanations
762 for the NAb results from vaccination (*108, 120, 121*). In the analysis of SUDV GPΔmuc vaccine
763 constructs, multivalent display of GPΔmuc trimers on SApNPs allowed stronger interactions with
764 FDC networks, B cells, and phagocytic cells in lymph nodes. The size and intrinsic thermostability
765 of SApNPs enhanced vaccine retention and presentation in lymph node follicles (over 8 weeks),
766 in addition to more robust and durable GC reactions, compared with the soluble GPΔmuc trimer.
767 The nearly identical trafficking and retention patterns observed for SApNPs presenting SUDV
768 GPΔmuc, HIV-1 Env (*108*), and influenza M2ex3 (*120*), which differ significantly in their glycan
769 profiles, confirm our previous conclusion that glycans may not be critical for the follicular
770 localization of NP vaccines in lymph nodes (*108*). Collectively, our current and previous studies
771 suggest that NP size and antigen thermostability may be determining factors in behaviors of these
772 NPs in lymph nodes (*108, 120, 121*). Mouse immunization sheds light on antibody responses to
773 various filovirus vaccines. Overall, the NAb responses tracked well with the bAb responses in the

774 longitudinal serum analysis. Among wildtype vaccines, EBOV and SUDV GPΔmuc-presenting
775 E2p SApNPs elicited the highest EC_{50} and ID_{50} titers at most timepoints, consistent with robust
776 GC reactions induced by E2p in the lymph node analysis. The two glycan modification strategies,
777 however, showed somewhat unexpected results. Glycan-trimmed trimers and SApNPs elicited the
778 lowest EC_{50} and ID_{50} titers at all timepoints, whereas Kif-treated, oligomannose-rich immunogens
779 induced the most potent bAb and NAb responses at most timepoints. This pattern was opposite to
780 that seen in the previous influenza HA/stem, SARS-CoV-2 spike, and HIV-1 Env vaccine studies,
781 in which glycan trimming improved the breadth and potency of vaccine-induced NAb responses
782 (*107-110*). Although the causes for this discrepancy remain unclear, our results suggest that there
783 may not be a general glycan strategy that fits all viral GP vaccines.

784 Our future research will focus on several directions. First, antibodies induced by GPΔmuc
785 trimers and SApNPs, both wildtype and glycan-modified, need to be isolated and mapped onto the
786 GP surface to determine how SApNP display improves NAb function, as demonstrated for SARS-
787 CoV-2 (*121*), how cross-NAbs recognize diverse GPs, and how glycan modification alters epitope
788 targeting. Second, the impact of glycan modification on vaccine-induced NAb responses requires
789 more in-depth studies. While it remains to be seen whether enriched oligomannose content can
790 improve NAb elicitation for other viral GP vaccines, approaches that produce different glycan
791 profiles may be readily tested for filovirus vaccine constructs. Non-mammalian systems, such as
792 engineered fungal (*152, 153*) and insect (*154*) cell lines, may generate shorter oligomannose-type
793 glycans with distinct glycoforms, reducing the complexity of chemical-based glycan modification.
794 Third, strategies for achieving pan-filovirus protection may warrant investigation. Although our
795 EBOV or SUDV GPΔmuc SApNPs can elicit cross-ebolavirus NAb responses, their combined use
796 with an optimized marburgvirus GP immunogen may be required to generate a pan-filovirus bNAb

response. Given the cross-ebolavirus NAb response induced by the RAVV GPΔmuc-P^{2}CT trimer, efforts may also be directed to the multivalent display of this GPΔmuc trimer on SApNPs to further improve the breadth and potency of this bNAb-like response. Lastly, filovirus challenge in mice or guinea pigs will provide critical information on protection, allowing selected vaccine constructs to be advanced to evaluation in an NHP immunization/challenge model.

METHODS

Construct design, expression, and purification of filovirus GP immunogens

For ebolaviruses, the amino acid sequences of EBOV GP (Mayinga strain, GenBank Accession: NP_066246) with a T42A substitution, SUDV GP (Gulu strain, GenBank Accession: AAU43887), and BDBV GP (R4386L strain, GenBank Accession: AYI50307) were used to design GPΔmuc trimers (**Fig. S1a**) and SApNPs (**Fig. S3h**). Of note, an N637D mutation was later introduced to the SUDV GPΔmuc-WL^{2}P^4 construct to eliminate a potential *N*-linked glycosylation site at N637 due to the enzymatic site "AS" between the GP and SApNP backbone. For marburgviruses, the amino acid sequence of RAVV GP (Ravn-87 strain, GenBank Accession: ABE27071) was used to design GPΔTM and various GPΔmuc trimers (**Fig. S5a**).

Rationally designed EBOV, SUDV, and BDBV GPΔmuc trimers were transiently expressed in HEK293F cells as previously described (*95*). Briefly, HEK293F cells were thawed and suspended in FreeStyle 293 Expression Medium (Life Technologies, Carlsbad, CA) and placed in a shaker incubator at 37°C at 135 rotations per minute (rpm) with 8% CO_2. When the cells reached a density of 2.0×10^6/ml, the cells were diluted to a concentration of 1.0×10^6/ml in 1 L of FreeStyle 293 Expression Medium for transfection using a polyethyleneimine (PEI) (Polysciences) transfection protocol. In brief, 900 μg of expression plasmid in 25 ml of Opti-MEM transfection medium (Life Technologies, Carlsbad, CA) was mixed with 5 ml of PEI-MAX

(1.0 mg/ml) in 25 ml of Opti-MEM and incubated for 30 min at room temperature. Next, the HEK293F cells were transfected with the DNA-PEI-MAX mixture and incubated in a shaker incubator at 37°C at 135 rpm with 8% CO_2. Kifunensine (10 mg/L, Tocris Bioscience) was added at the time of transfection to inhibit α-mannosidase I to generate oligomannose-type glycans. Five days after transfection, supernatants containing the target protein were harvested, clarified by centrifugation at 1126 × g for 22 min, and filtered through a 0.45 μm filter (Thermo Scientific). Ebolavirus GP was purified using an ADI-15878 antibody column except for the crystallographic analysis of EBOV GPΔmuc-WL^{2}P^4 and nsEM analysis of EBOV GPΔmuc-WL^{2}P^4-I3-01v9b/c-T, where an mAb100 antibody column was used. Ebolavirus GP was eluted three times each with 5 ml of 0.2 M glycine (pH 2.2), neutralized with 0.5 ml of 2 M Tris-Base (pH 9.0), and buffer-exchanged into phosphate-buffered saline (PBS; pH 7.2). The IAC-purified ebolavirus GP was further purified by SEC using a Superdex 200 Increase 10/300 GL column (Cytiva).

RAVV GPΔmuc trimers and all ebolavirus GPΔmuc-presenting SApNPs were produced in ExpiCHO cells (Thermo Fisher). Briefly, ExpiCHO cells were thawed and incubated in ExpiCHO Expression Medium (Thermo Fisher) in a shaker incubator at 37°C at 135 rpm with 8% CO_2. When the cells reached a density of 10×10^6/ml, ExpiCHO Expression Medium was added to adjust the cell density to 6×10^6/ml for transfection. The ExpiFectamine CHO/plasmid DNA complexes were prepared for 100-ml transfection in ExpiCHO cells following the manufacturer's instructions. Kifunensine (10 mg/L, Tocris Bioscience) was added at the time of ExpiCHO transfection to inhibit α-mannosidase I to generate oligomannose-type glycans. For these constructs, 100 μg of plasmid and 320 μl of ExpiFectamine CHO reagent were mixed in 7.7 ml of cold OptiPRO™ medium (Thermo Fisher). After the first feed on day 1, ExpiCHO cells were cultured in a shaker incubator at 33°C at 115 rpm with 8% CO_2 according to the Max Titer protocol

with an additional feed on day 5 (Thermo Fisher). Culture supernatants were harvested 13–14 days after transfection, clarified by centrifugation at 3724 × g for 25 min, and filtered using a 0.45 µm filter (Thermo Fisher). RAVV GPΔmuc trimers were purified using Ni Sepharose excel resin (Nickel, Cytiva), and the bound protein was eluted twice, each with 15 ml of 0.5 M imidazole, and then exchanged into Tris-buffered saline (TBS; pH 7.2). Ebolavirus GPΔmuc-presenting SApNPs were purified using an ADI-15878 antibody column, eluted three times each with 5 ml of 0.2 M glycine (pH 2.2), neutralized with 0.5 ml of 2 M Tris-Base (pH 9.0), and buffer-exchanged into PBS (pH 7.2). The Nickel-purified RAVV GPΔmuc trimer and all ebolavirus GPΔmuc-presenting SApNPs were further polished by SEC using a Superdex 200 Increase 10/300 GL column (Cytiva) and a Superose 6 Increase 10/300 GL column (Cytiva), respectively. Selected SEC fractions were pooled, aliquoted, and frozen in liquid nitrogen or at -80 ºC until use.

Expression and purification of neutralizing antibodies (NAbs)

Antibodies in the IgG form were transiently expressed in ExpiCHO cells (Thermo Fisher). At 12-14 days post-transfection, the cells were centrifuged at 3,724 × g for 25 min, with the supernatants filtered using a 0.45-µm filter (Millipore). IgGs were purified using protein A affinity resin (Cytiva) and eluted in 0.3 M citric acid (pH 3.0). The elution was immediately titrated to a neutral pH of 7.0 by the addition of 2 M Tris-base (pH 9.0). The eluate was concentrated and exchanged into PBS using an Amicon 10 kDa filter (Millipore). The IgG concentration was quantified by UV_{280} absorption with theoretical extinction coefficients.

Glycan trimming by endo H treatment and enzyme removal

The protocol for endo H treatment and removal was reported in our previous study (*108*). Briefly, the surface glycans of filovirus GPΔmuc trimers and SApNPs were trimmed by endoglycosidase H (Endo-Hf), a fusion of endo H and MBP (NEB, catalog no. P0703L), by mixing 1 mg of antigen

with 200 µl of 10× GlycoBuffer 3, 250 µl of endo H, and H_2O (if necessary) to make a 2 ml reaction. The mixture was incubated at room temperature (25°C) for 5 h to facilitate enzymatic processing of the GP glycans. After incubation, the mixtures were passed through a Superdex 200 increase 10/300 GL column (for trimers) and Superose 6 increase 10/300 GL column (for SApNPs) to remove the MBP-tagged endo H. Notably, to enable glycan trimming by endo H, the filovirus GPΔmuc trimers and SApNPs must be expressed in the presence of kifunensine. Previously, the amylose resin (NEB, catalog no. E8021S) was used to remove residual endo Hf from the SEC-purified HIV-1 Env trimer and SApNPs (*108*). Notably, this additional step of endo H removal was not included in the present study to preserve vaccine antigens for animal studies. The SEC-purified fractions were pooled aliquoted, and frozen in liquid nitrogen or at -80 ºC until use.

SDS-PAGE and BN-PAGE

Filovirus GPΔmuc trimers and SApNPs were analyzed by sodium dodecyl sulfate-polyacrylamide gel electrophoresis (SDS-PAGE) and blue native-polyacrylamide gel electrophoresis (BN-PAGE). The proteins were mixed with loading dye and loaded on a 10% Tris-Glycine Gel (Bio-Rad) or a 4-12% Bis-Tris NativePAGE gel (Life Technologies). For SDS-PAGE under reducing conditions, the proteins were mixed with 6× Laemmli SDS sample buffer (Thermo Scientific) and boiled for 5 min at 100°C. SDS-PAGE gels were run for 25 min at 250 V using SDS running buffer (Bio-Rad). SDS-PAGE gels were stained with InstantBlue (Abcam). For BN-PAGE, the proteins were mixed with 4× native dye and loaded on a BN-PAGE gel. The gel was run for 2–2.5 h at 150 V with NativePAGE running buffer (Life Technologies) according to the manufacturer's instructions. The BN-PAGE gels were stained using Coomassie Brilliant Blue R-250 (Bio-Rad) and destained using a solution of 6% ethanol and 3% glacial acetic acid.

Differential scanning calorimetry (DSC)

Melting temperature (T_m) and other thermal parameters of filovirus GPΔmuc trimers purified by an IAC or Nickel column followed by SEC were obtained using a MicroCal PEAQ-DSC Man instrument (Malvern). Briefly, the purified protein in PBS buffer was diluted to 0.5-5 µM. Melting was probed at a scan rate of 60°C/h from 20°C to 100°C. Data processing, including buffer correction, normalization, and baseline subtraction, was conducted using MicroCal PEAQ-DSC software. Gaussian fitting was performed using GraphPad Prism 10.3.1 software.

Site-specific glycan analysis

To generate site-specific glycan profiles, 100 µg aliquots of each antigen were denatured for 1 h in 50 mM Tris/HCl, pH 8.0 containing 6 M urea and 5 mM dithiothreitol (DTT). Next, antigen samples were reduced and alkylated by adding 20 mM iodoacetamide (IAA) and incubated for 1 h in the dark, followed by 1h of incubation with 20 mM DTT to eliminate residual IAA. The alkylated antigen samples were buffer-exchanged into 50 mM Tris/HCl, pH 8.0 using Vivaspin columns (10 kDa), and three of the aliquots were digested separately overnight using trypsin (Mass Spectrometry Grade, Promega), chymotrypsin (Mass Spectrometry Grade, Promega) or alpha lytic protease (Sigma Aldrich) at a ratio of 1:30 (w/w). The next day, the peptides were dried and extracted using an Oasis HLB µElution Plate (Waters).

The peptides were dried again, resuspended in 0.1% formic acid, and analyzed by nanoLC-electrospray ionization MS with an Ultimate 3000 HPLC (Thermo Fisher Scientific) system coupled to an Orbitrap Eclipse mass spectrometer (Thermo Fisher Scientific) using stepped higher energy collision-induced dissociation (HCD) fragmentation. Peptides were separated using an EasySpray PepMap RSLC C18 column (75 µm × 75 cm). A trapping column (PepMap 100 C18 3µM 75µM × 2cm) was used in line with liquid chromatography (LC) prior to separation with the analytical column. The LC conditions were as follows: 280-minute linear gradient consisting of 4-

912 32% acetonitrile in 0.1% formic acid over 260 minutes followed by 20 minutes of alternating 76%
913 acetonitrile in 0.1% formic acid and 4% ACN in 0.1% formic acid, used to ensure all the sample
914 had eluted from the column. The flow rate was set to 300 nl/min. The spray voltage was set to 2.7
915 kV and the temperature of the heated capillary was set to 40 °C. The ion transfer tube temperature
916 was set to 275 °C. The scan range was 375−1500 m/z. The stepped HCD collision energies were
917 set to 15%, 25%, and 45% and the MS2 for each energy was combined. Precursor and fragment
918 detection were performed using an Orbitrap at a resolution of MS^1 = 120,000 and MS^2 = 30,000.
919 The AGC target for MS1 was set to standard and injection time set to auto which involves the
920 system setting the two parameters to maximize sensitivity while maintaining cycle time. Full LC
921 and MS methodology can be extracted from the appropriate Raw file using XCalibur FreeStyle
922 software or upon request.

923 Glycopeptide fragmentation data were extracted from the raw file using Byos 4.6 (Protein
924 Metrics). The glycopeptide fragmentation data were evaluated manually for each glycopeptide;
925 the peptide was scored as true-positive when the correct b and y fragment ions were observed
926 along with oxonium ions corresponding to the glycan identified. The MS data was searched using
927 the Protein Metrics 38 insect N-glycan library. The relative amounts of each glycan at each site as
928 well as the unoccupied proportion were determined by comparing the extracted chromatographic
929 areas for different glycotypes with an identical peptide sequence. All charge states for a single
930 glycopeptide were summed. The precursor mass tolerance was set at 4 ppm and 10 ppm for
931 fragments. A 1% false discovery rate (FDR) was applied. The relative amounts of each glycan at
932 each site as well as the unoccupied proportion were determined by comparing the extracted ion
933 chromatographic areas for different glycopeptides with an identical peptide sequence. Glycans
934 were categorized according to the composition detected.

HexNAc(2)Hex(9−3) was classified as M9 to M3. Any of these structures containing a fucose were categorized as fucosylated mannose (FM). Complex-type glycans were classified according to the number of HexNAc subunits and the presence or absence of fucose. Core glycans refer to truncated structures smaller than M3. As this fragmentation method does not provide linkage information, compositional isomers are grouped.

Biolayer interferometry

Antigenic profiles of filovirus GPΔmuc trimers and SApNPs were measured using Octet RED96 (FortéBio, Pall Life Sciences) against a panel of antibodies, including five pan-ebolavirus NAbs and two marburgvirus NAbs, all in the IgG form. All assays were performed with agitation set to 1000 rpm in FortéBio 1× kinetic buffer. The final volume for all solutions was 200 µl per well. Assays were performed at 30 °C in solid black 96-well plates (Geiger Bio-One). For all antigens, 5 µg/ml antibody in 1× kinetic buffer was loaded onto the surface of anti-human Fc Capture Biosensors (AHC) for 300 s. Next, a 2-fold concentration gradient of antigen, starting at 500 nM for trimers and 10 nM for SApNPs, was used in a dilution series of six. A 60-s biosensor baseline step was applied before the analysis of association of the antibody on the biosensor to the antigen in solution for 200 s. Dissociation of the interaction was followed for 300 s. The correction of baseline drift was performed by subtracting the mean value of shifts recorded for a sensor loaded with antibody but not incubated with antigen, and for a sensor without antibody but incubated with antigen. Octet data were processed by FortéBio's data acquisition software (version 8.1). Peak signals at the highest antigen concentration were summarized in a matrix and color-coded accordingly to allow comparisons between different constructs. Experimental data for each antigen-antibody pair were fitted with the binding equations describing a 1:1 interaction, and three

datasets that showed the optimal fitting were then grouped to determine the K_{on} and K_D values. The antibody-antigen binding curve was plotted using GraphPad Prism 10.3.1 software.

Enzyme-linked immunosorbent assay (ELISA)

Costar 96-well, high-binding, flat-bottom, half-area plates (Corning) were first coated with 50 µl of PBS containing 0.1 µg of the appropriate filovirus GPΔmuc trimer or SApNP antigen protein. The plates were incubated overnight at 4 °C and then washed five times with PBST wash buffer containing PBS and 0.05% (v/v) Tween 20. Each well was then blocked for 1 h at RT with 150 µl of blocking buffer consisting of 4% w/v blotting-grade blocker (Bio-Rad) in PBS. Next, the plates washed five times with PBST wash buffer. To evaluate antibody binding to the coating antigens, antibodies were diluted in blocking buffer to a maximum concentration of 10 µg/ml followed by a 10-fold dilution series. For each antibody dilution, a total volume of 50 µl was added to the appropriate wells. For serum sample analysis, mouse sera were diluted 40-fold in blocking buffer and subjected to a 10-fold dilution series. For each sample dilution, a total volume of 50 µl was added to the wells. Each plate was incubated for 1 h at room temperature and then washed five times with PBST wash buffer. For secondary antibody binding, a 1:5000 dilution of goat anti-human IgG antibody (Jackson ImmunoResearch Laboratories) or for mouse sample analysis, a 1:3000 dilution of horseradish peroxidase (HRP)-conjugated goat anti-mouse IgG antibody (Jackson ImmunoResearch Laboratories) was prepared in PBST wash buffer, with 50 µl of diluted secondary antibody added to each well. The plates were incubated for 1 h at room temperature and then washed six times with PBST wash buffer. Lastly, the wells were developed with 50 µl of 3,3',5,5'-tetramethylbenzidine (Life Sciences) for 3-5 min before the reaction was stopped with 50 µl of 2 N sulfuric acid. The plates were then immediately read on a BioTek Synergy plate reader at a wavelength of 450 nm. EC_{50} values were then calculated from full curves using GraphPad

Prism 10.3.1 software. When OD_{450} absorbance values were lower than 0.5, the EC_{50} values were set to 10 μg/ml in **Figs. 1g**, **3h**, **4c** and **4h** to facilitate EC_{50} plotting and comparison.

Protein crystallization and data collection

EBOV GPΔmuc-WL^2P^4 was transiently expressed in HEK293S cells using the same procedure as in HEK293F cells, followed by mAb100 and SEC purification. The mAb100/SEC-purified EBOV GPΔmuc-WL^2P^4 trimer at a 9.3 mg/ml concentration was used for crystallization experiments following the sitting drop vapor diffusion method using an automated CrystalMation robotic system (Rigaku) at 20°C at The Scripps Research Institute (*155*). The reservoir solution consisted of 12% PEG-6000 (*v/v*) and 0.1 M sodium citrate-citric acid (pH 4.51). Diffraction-quality crystals were obtained after 2 weeks of incubation at 20°C. The crystal was cryoprotected with a well solution containing 25% (*v/v*) ethylene glycol, mounted on a nylon loop, and flash cooled in liquid nitrogen. Diffraction data were collected at Stanford Synchrotron Radiation Lightsource (SSRL) beamline 12-1 and processed with HKL-2000 (*156*). Diffraction data were indexed in P321.

Structure determination and refinement

The crystal structure of EBOV GPΔmuc-WL^2P^4 was determined by molecular replacement using Phaser-MR from Phenix (version 1.19.2-4158) with the coordinates of the previously reported EBOV GPΔmuc-WL^2P^2 structure (PDB ID: 7JPH) (*95*) as a search model. Polypeptide chains were manually adjusted into electron density using Coot (*157*), refined with phenix-refine (*158*), and validated using the wwPDB Validation System (*159*). Carbohydrates were further validated using Privateer in CCP4i (*160*) before and after refinement. The final data processing and refinement statistics are described in **Table S1**. All images for crystal structures shown in the figures were generated using PyMOL 2.3.4 software. Notably, due to the weak electron density, structural model was not built for residues K633-D637 in the GP2 stalk region of EBOV GPΔmuc-

WL^{2}P^4, as well as the C-terminal foldon trimerization motif, leaving an apparent gap in crystal packing when visualizing the GP structure within the electron density map.

Negative-stain electron microscopy (nsEM)

The nsEM analysis of filovirus GPΔmuc trimers, their antibody-bound complexes, and GPΔmuc-presenting SApNPs, was performed by the Core Microscopy Facility at The Scripps Research Institute. Briefly, samples were prepared at a concentration of 0.008 and 0.01 mg/ml, respectively. Carbon-coated copper grids (400 mesh) were glow-discharged, and 8 µl of each sample was then adsorbed for 2 min. Next, excess samples were removed, and grids were negatively stained with 2% uranyl formate for 2 min. Excess stain was wicked away and the grids were allowed to dry. Trimer samples were analyzed at 120 kV with a Talos L120C transmission electron microscope (Thermo Fisher), and images were acquired using a CETA 16 M CMOS camera under 73,000× magnification at a resolution of 1.93 Å/pixel and defocus of 0.5-2 µm. For SApNP samples, the images were collected under 52,000× magnification. The resulting pixel size at the specimen plane was 2.05 Å, and the defocus was set to −1.50 µm. Computational analysis of the images was performed using the high-performance computing core facility at The Scripps Research Institute. Briefly, the nsEM images were converted to the MRC format by EMAN2 (*161*) for further processing by CryoSPARC 4.3.0 (*119*). Micrographs were contrast-transfer function (CTF)-corrected by patch CTF estimation. Particles were selected using a Blob/template picker and later extracted with a box size of 130 pixels for 2D classification, with 50 and 230 Å used as the minimum and maximum particle sizes in blob picking. 3D models were generated by *ab initio* reconstruction and optimized by heterogeneous and homogeneous refinement. All nsEM and fitted structure images were generated by UCSF Chimera (*162*) and Chimera X (*163-165*).

Cryo-electron microscopy (cryo-EM) for SUDV GP-CA45 complexes

The SUDV GPΔmuc-WL^{2}P^4 construct was expressed in HEK293F cells and purified using an ADI-15878 column. The eluate was then mixed with CA45 Fab at a 1:1.5 molar ratio. The mixture was further purified using a Superose 6 Increase 10/300 GL column and the complex fractions were pooled. Cryo-EM grid preparation and image collection were performed at the UC San Diego Cryo-EM Facility. Vitrification was carried out using a Vitrobot Mark IV (FEI) equilibrated to 4ºC and 100% humidity. The Quantifoil Cu 1.2/1.3 300 grid was plasma cleaned by Solarus II (Gatan) with a mixture of Ar/O_2 for 10 s. After plasma cleaning, the grid was blotted on one side with 3.5 µl of the SUDV GPΔmuc-WL^{2}P^4/CA45 Fab complex at a concentration of 0.55 mg/ml for 4 s and then frozen in liquid ethane. The frozen grid was stored in liquid nitrogen until image collection. Cryo-EM data were collected on a Krios G4 (Thermo Fisher) operated at 200 keV with a Falcon 4 camera and Selectris-X energy filter (Thermo Fisher). Automated data collection was performed using Smart EPU software (Thermo Fisher). Images were collected under 130,000× magnification, resulting in a pixel size of 0.89 Å, with the defocus range set between -1 and -2.5 µm. All datasets were processed by CryoSPARC 3.3 software. Movie frames were aligned using "Patch Motion Correction," and CTF estimations were performed by "Patch CTF Estimation" (**Fig. S2d**). Particle picking was performed by "Blob Picking" with the particle size set to 100-350 Å, and particles were extracted using a box size of 360 pixels. After 2D classification, the selected classes were used as an input for "Template Picking" and extracted using a box size of 360 pixels. After multiple 2D classifications, 249,139 particles were selected for building 3D volume models. The function "Ab-Initio Reconstruction" in CryoSPARC was used to generate three starting reference models for "Heterologous Refinement". The particles derived from the largest cluster (163,924 particles) were used for "Homogeneous Refinement" using a focusing mask and C3 symmetry. The refined model was then subjected to "3D Classification," resulting in 10 models, of which the cluster

associated with the most complete model (41,233 particles) was used for another around of "Ab-Initio Reconstruction." The model obtained from this smaller set was further optimized using "Non-uniform Refinement" and "Local Refinement" using 163,924 particles and a focusing mask. The final GSFSC resolution was 3.13 Å, and the final structural model was built using the crystal structures of EBOV GPΔmuc-WL^{2}P^2 (PDB ID: 7JPH) (*95*) and EBOV GPΔmuc-bound CA45 Fab (PDB ID: 6EAY) (*113*) as templates. After fitting into the density map using Chimera X (*163-165*), the resulting complex underwent real-space refinement in Phenix (*158*), manual refinement by Coot (*157*), and again real-space refinement in Phenix (*158*). Statistical details of the final cryo-EM structure are shown in **Table S2**, with the coordinates and 3D density map deposited in Protein Data Bank (PDB) and Electron Microscopy Data Bank (EMDB), respectively.

Rational design of trimer-presenting I3-01v9b/c SApNP scaffolds

Previously, we redesigned the I3-01v9 scaffold to optimize the NP display of monomeric antigens (*120*). In the resulting I3-01v9a SApNP, the *N*-terminal helix was extended so that its first residue is just above the NP surface. Here, we redesigned the I3-01v9a scaffold to optimize the NP display of trimeric antigens with a long coiled-coil stalk (**Fig. S3**). First, the 11-aa *N*-terminal helix in I3-01v9a was truncated to 7 aa. Then, a 13-aa helix-turn fragment (9-aa helix + 4-aa turn, all alanine) was fused to the 7-aa *N*-terminal helix of the modified I3-01v9a such that the new 9-aa *N*-terminal helix from the fused fragment packed within the groove of two helices that are part of the I3-01 core. The 9-aa helix in this fragment was from the structure of a human transcription factor (PDB ID: 6G6L). Next, four mutations were introduced to the I3-01 core helices to remove their steric clashes with the new *N*-terminal helix. Iterative modular optimization (IMO) (*166*) was used to relax the helix-turn backbone, which was then subjected to the CONCOORD structure sampling program (*167*) to generate 1000 slightly perturbed backbone conformations. An ensemble-based

protein design program (*86, 145*) was used to predict the optimal sequence for the 9-aa *N*-terminal helix within the fragment using Cα and Cβ-based RAPDF (*168*) scoring functions. The 4-aa turn was set to "GSGS" during the protein design process. The I3-01v9b design was selected by combining data from both scoring functions, and a second design I3-01v9c was obtained by mutating the turn from "GSGS" to "GPPS" to increase its rigidity. An I3-01v9b structural model was built after further backbone relaxation using IMO with a minimum perturbation angle. The distance between the *N*-termini of the I3-01v9b/c trimer (I3-01v9b/c-T) model was 43.9 Å. EBOV GPΔmuc-WL^{2}P^4-I3-01v9b/c-T constructs (**Fig. S3b**) were designed for experimental validation with transient expression in HEK293F cells followed by structural validation by nsEM.

Dynamic Light Scattering (DLS)

Particle size distributions of ebolavirus GPΔmuc trimer-presenting SApNPs were obtained using a Zetasizer Ultra instrument (Malvern). Briefly, ADI-15878/SEC-purified SApNPs produced from ExpiCHO cells were diluted to 0.2 mg/ml in 1× PBS buffer, after which 30 µl of the prepared sample was added to a quartz batch cuvette (Malvern, catalog no. ZEN2112). Particle size was measured at 25°C using back scattering mode. Data processing was performed on the Zetasizer particle size analyzer using Ultra instrument software. The resulting particle size distribution was plotted using GraphPad Prism 10.3.1 software.

Mouse immunization and sample collection

We utilized similar mouse immunization protocols from our previous studies (*108, 120, 121*). The Association for the Assessment and Accreditation of Laboratory Animal Care (AAALAC) guidelines were followed throughout all animal experiments. The animal protocols were approved by the Institutional Animal Care and Use Committee (IACUC) of The Scripps Research Institute. Six-to-8-week-old female BALB/c mice were purchased from The Jackson Laboratory and housed

in ventilated cages in environmentally controlled rooms at 20°C with 50% humidity under a 12 h/12 h light-dark cycle. In the mechanistic analysis of vaccine transport and induced immune responses in lymph nodes, mice were intradermally inoculated via four footpads using a 29-gauge insulin needle under 3% isoflurane anesthesia with oxygen. The injection dose was 80 µl of antigen and AP adjuvant mix containing 40 µg of vaccine antigen per mouse or 10 µg per footpad. In the first immunogenicity study, mice were injected at weeks 0, 3, 9, and 15, with an extended interval of 6 weeks between the second and third doses and third and fourth doses, via the intraperitoneal (i.p.) route. In the second immunogenicity study, our standard screening regimen (*108, 120, 121, 148*) was used with mice injected at weeks 0, 3, 6, and 9 with an interval of 3 weeks. The injecting dose was 200 µl of antigen/adjuvant mix containing 10 µg of vaccine antigen and 100 µl of adjuvant including 40 µg/50 µl of CpG (oligonucleotide 1826, a TLR9 agonist from InvivoGen) adsorbed onto 50 µl of AH (InvivoGen). Blood samples were collected 2 weeks after each injection through the retro-orbital sinus using heparinized capillary tubes. Samples were spun at 12000 rpm for 10 min to separate serum (top layer) and the rest of the whole blood layer. Upon heat inactivation at 56°C for 30 min, serum was spun at 12000 rpm for 10 min to remove precipitates. For the last timepoint, the rest of the whole blood layer was diluted with an equal volume of PBS and then overlaid on 4.5 ml of Ficoll in a 15 ml SepMate tube (STEMCELL Technologies) and spun at 1200 rpm for 10 min at 20°C to separate peripheral blood mononuclear cells (PBMCs). Cells were washed once in PBS and then resuspended in 1 ml of ACK Red Blood Cell lysis buffer (Lonza). After washing with PBS, PBMCs were resuspended in 1 ml of freezing media (10% dimethyl sulfoxide [DMSO]/90% fetal calf serum [FCS]). Two weeks after the last bleed, spleens were harvested and ground against a 70-µm cell strainer (BD Falcon) to release splenocytes into a cell suspension. Splenocytes were centrifuged, washed in PBS, treated with 5 ml of ACK lysing

buffer (Lonza), and frozen with 3 ml of freezing media (10% DMSO/90% FCS). Serum samples from week 11 in the second study were purified using a CaptureSelect™ IgG-Fc (Multispecies) Affinity Matrix (Thermo Scientific) following the manufacturer's instructions. Purified IgG from individual mice was analyzed in filovirus-pp assays to determine vaccine-induced NAb responses.

Histology, immunostaining, and imaging for lymph node tissues

To study vaccine distribution, trafficking, retention, cellular interaction, and GC reactions in sentinel lymph nodes, SUDV GPΔmuc trimer and SApNPs (E2p and I3-01v9b) adjuvanted with AP were intradermally injected into four mouse footpads. A similar protocol was reported in our previous studies (*108, 120, 121*). In brief, the injection dose consisted of 80 µl of antigen and adjuvant mix that contained 40 µg of filovirus antigen (10 µg/footpad, 40 µg/mouse). Mice were euthanized at 2 h to 8 weeks after a single-dose injection. Fresh sentinel lymph nodes were collected and merged into the frozen section compound (VWR International, catalog no. 95057-838). Lymph node sample molds were merged into liquid nitrogen and stored at -80°C before shipping to The Centre for Phenogenomics (Toronto, Canada). Lymph node tissues were cut into 8 µm thick sections using a cryostat (Cryostar NX70). The primary antibody was applied on lymph node sections and incubated overnight at 4 °C. After washing with TBS containing 0.1% Tween-20 (TBST), biotin or fluorophore-conjugated secondary antibodies were utilized on the sections and tissue samples were incubated at 25 °C for 1 h. Lymph node sections were stained with NAbs ADI-15878 (*111*), ADI-15946 (*114*), CA45 (*113*), or mAb100 (*126*) (1:100) and biotinylated goat anti-human secondary antibody (Abcam, catalog no. ab7152, 1:300), followed by streptavidin-horseradish peroxidase (HRP) reagent (Vectastain Elite ABC-HRP Kit, Vector, catalog no. PK-6100) and ImmPACT diaminobenzidine (DAB; Vector, catalog no. SK-4105).

To study interactions between SUDV GPΔmuc immunogens and cellular components in lymph nodes, FDCs were labeled using anti-CD21 primary antibody (Abcam, catalog no. ab75985, 1:1800), followed by anti-rabbit secondary antibody conjugated with Alexa Fluor 555 (Thermo Fisher, catalog no. A21428, 1:200). Subcapsular sinus macrophages were labeled using anti-sialoadhesin (CD169) antibody (Abcam, catalog no. ab53443, 1:600), followed by anti-rat secondary antibody conjugated with Alexa Fluor 488 (Abcam, catalog no. ab150165, 1:200). B cells were labeled using anti-B220 antibody (eBioscience, catalog no. 14-0452-82, 1:100), followed by anti-rat secondary antibody conjugated with Alexa Fluor 647 (Thermo Fisher, catalog no. A21247, 1:200). SUDV GPΔmuc trimer and SApNP-induced GC reactions were assessed by immunohistological study. GC B cells were stained using rat anti-GL7 antibody (FITC; BioLegend, catalog no. 144604, 1:250). T_{fh} cells were stained using anti-CD4 antibody (BioLegend, catalog no. 100402, 1:100), followed by anti-rat secondary antibody conjugated with Alexa Fluor 488 (Abcam, catalog no. ab150165, 1:1000). GC cells were stained using Bcl6 antibody (Abcam, catalog no. ab220092, 1:300), followed by anti-rabbit secondary antibody conjugated with Alexa Fluor 555 (Thermo Fisher, catalog no. A21428, 1:1000). Cell nuclei were stained using 4',6-diamidino-2-phenylindole (DAPI; Sigma-Aldrich, catalog no. D9542, 100 ng/ml).

The stained lymph node tissues were scanned using an Olympus VS-120 slide scanner with a Hamamatsu ORCA-R2 C10600 digital camera. The transport of SUDV GPΔmuc trimer and SApNP immunogens and their induced GCs in lymph nodes were quantified through bright-field and fluorescent images using ImageJ software (*169*).

Electron microscopy analysis of protein nanoparticles in lymph node tissues

To assess interactions between SUDV GPΔmuc immunogens and stromal and immune cells in lymph nodes, TEM analysis was conducted by the Core Microscopy Facility at The Scripps

Research Institute (TSRI). The same protocol used for lymph node isolation, processing, and analysis was reported in our previous studies (*108, 121*). To visualize AP-adjuvanted SUDV GPΔmuc SApNPs (E2p and I3-01v9b) interacting with FDCs and phagocytic cells in lymph node tissues using TEM, mice were administered with 200 µl of antigen/adjuvant mix containing 100 µg of SUDV immunogen and 100 µl of AP adjuvant into two hind footpads or 50 µg per footpad. Fresh popliteal lymph nodes were collected 2, 12, and 48 h after a single-dose injection. Lymph node tissues were then bisected and immersed in oxygenated 2.5% glutaraldehyde and 4% paraformaldehyde in 0.1 M sodium cacodylate buffer (pH 7.4) fixative overnight at 4°C. Next, lymph node samples were fixed and stained with 0.5% uranyl acetate overnight at 4°C. Lymph node tissues were infiltrated with LX-112 (Ladd) epoxy resin and polymerized at 60 °C. Ultrathin tissue slices (70 nm) were sectioned and placed on copper grids for TEM imaging. Tissue sections were imaged at 80 kV with a Talos L120C transmission electron microscope (Thermo Fisher). TEM images were acquired with a CETA 16M CMOS camera for further analysis.

Lymph node disaggregation, cell staining, and flow cytometry

To assess vaccine-induced humoral immune responses, the frequency and number of GC B cells ($GL7^+B220^+$) and T_{fh} cells ($CD3^+CD4^+CXCR5^+PD\text{-}1^+$) were used to quantify GC reactions by flow cytometry (**Fig. S9**). The same protocol used for lymph node tissue collection, processing, and analysis was reported in our previous studies (*108, 120, 121*). In brief, mice were administered with 80 µl of antigen/adjuvant mix containing 40 µg of vaccine immunogen (10 µg/injection, 40 µg/mouse) into four footpads. The mice were euthanized 2, 5, and 8 weeks after a single-dose injection or 2 and 5 weeks after the boost. Fresh sentinel lymph nodes were isolated and immediately processed through mechanical disaggregation. Lymph node tissues were then merged in enzyme digestion solution. Upon incubation at 37°C for 30 min on a rotator, lymph node cells

were filtered through a 70 μm cell strainer to achieve a single cell suspension. Anti-CD16/32 antibody (BioLegend, catalog no. 101302, 1:50) was added to the cell samples to block the nonspecific binding of Fc receptors and kept on ice for 30 min. Next, cells were transferred to 96-well V-shaped-bottom microplates with preprepared cocktail antibodies that included Zombie NIR live/dead stain (BioLegend, catalog no. 423106, 1:100), Brilliant Violet 510 anti-mouse/human CD45R/B220 antibody (BioLegend, catalog no. 103247, 1:300), FITC anti-mouse CD3 antibody (BioLegend, catalog no. 100204, 1:300), Alexa Fluor 700 anti-mouse CD4 antibody (BioLegend, catalog no. 100536, 1:300), PE anti-mouse/human GL7 antibody (BioLegend, catalog no. 144608, 1:500), Brilliant Violet 605 anti-mouse CD95 (Fas) antibody (BioLegend, catalog no. 152612, 1:500), Brilliant Violet 421 anti-mouse CD185 (CXCR5) antibody (BioLegend, catalog no. 145511, 1:500), and PE/Cyanine7 anti-mouse CD279 (PD-1) antibody (BioLegend, catalog no. 135216, 1:500). Cells were mixed with cocktail antibodies on ice for 30 min and spun down at 400 × *g* for 10 min. Cells were then fixed with 1.6% paraformaldehyde (Thermo Fisher Scientific, catalog no. 28906) in Hank's Balanced Salt Solution (HBSS) on ice for 30 min. Next, cells were spun down at 400 × *g* for 10 min and placed in HBSS blocking solution at 4 °C. Sample events were acquired by a 5-laser AZE5 flow cytometer (Yeti, Bio-Rad) with Everest software at the Core Facility of The Scripps Research Institute. The data were analyzed using FlowJo 10 software.

Pseudovirus production and neutralization assays

A filovirus-pseudoparticle (pp) neutralization assay (*95*) was performed to assess the neutralizing activity of vaccine-induced mouse sera and purified mouse IgG. Filovirus-pps were generated by the co-transfection of HEK293T cells with envelope-deficient HIV-1 pNL4-3.lucR^{-}E^{-} plasmid (NIH AIDS reagent program: https://www.aidsreagent.org/) and an expression plasmid encoding the GP gene of an EBOV Makona (GenBank accession no. KJ660346), SUDV Gulu (GenBank

accession no. AY729654), BDBV Uganda (GenBank accession no. KR063673), or MARV Angola (GenBank accession no. DQ447653) strain at a 4:1 ratio using a Lipofectamine 3000 transfection protocol (Thermo Fisher). After 72 h, pseudoviruses were collected from the supernatant by centrifugation at 3724 × g for 10 min, aliquoted, and stored at -80°C until use. For pseudovirus neutralization assays, mouse sera starting at a dilution of 100× or purified IgG at a starting concentration of 300 µg/ml were serially diluted 3-fold and incubated with pseudoviruses at 37°C for 1 h in white solid-bottom 96-half-well plates (Corning). Next, 0.8×10^4 Huh-7 cells were added to each well and the plates were incubated at 37°C for 60-72 h. After incubation, the supernatant was removed, and cells were lysed. Luciferase reporter gene expression was quantified through the addition of Bright-Glo Luciferase substrate (Promega) according to the manufacturer's instructions. Luciferase activity in relative light units (RLU) was measured on a BioTek microplate reader with Gen 5 software. Values from experimental wells were compared against virus-containing wells, with background luminescence from a series of uninfected wells subtracted from both. Dose-response neutralization curves were then fit by nonlinear regression with constraints (0-100%) in GraphPad Prism 10.3.1 software, from which IC_{50} and ID_{50} were calculated. The same protocols were used to produce and assay pseudoparticles displaying the envelope glycoprotein of lymphocytic choriomeningitis virus (LCMV-pps) as a negative control in IgG neutralization.

Statistical analysis

Data were collected from $n = 8$ mice per group in the immunization studies and $n = 3$-5 mice per group in the mechanistic study. All ELISA and pseudovirus neutralization assays were performed in duplicate. Different vaccine constructs, and adjuvant-formulated filovirus vaccine antigens, were compared using one-way analysis of variation (ANOVA), followed by Tukey's multiple comparison *post hoc* test. Statistical significance is indicated as the following in the figures: ns

(not significant), *$p < 0.05$, **$p < 0.01$, ***$p < 0.001$, and ****$p < 0.0001$. The graphs were generated, and statistical analyses were performed using GraphPad Prism 10.3.1 software.

ACKNOWLEDGEMENTS

The authors acknowledge the facilities of the UC San Diego cryo-EM facility, part of the Goeddel Family Technology Sandbox, along with the scientific and technical assistance of Dr. Mariusz Matyszewski. We thank G. Ossetchkine, K. Duffin, M. Ganguly, and V. Bradaschia at The Centre for Phenogenomics for their expertise and technical support in immunohistology. We acknowledge K. Vanderpool, T. Fassel, and S. Henderson of the Core Microscopy Facility at The Scripps Research Institute for their expert assistance in the TEM analysis. We thank A. Saluk, B. Seegers, and B. Monteverde of the Flow Cytometry Core Facility at The Scripps Research Institute for their technical support in flow cytometry. Diffraction data were collected at the Stanford Synchrotron Radiation Lightsource (SSRL) beamlines 12-1. Use of the Stanford Synchrotron Radiation Lightsource and Stanford Linear Accelerator Center (SLAC), National Accelerator Laboratory, is supported by the U.S. Department of Energy, Office of Science, Office of Basic Energy Sciences under Contract No. DE-AC02-76SF00515. The SSRL Structural Molecular Biology Program is supported by the Department of Energy (DOE) Office of Biological and Environmental Research, and by the National Institutes of Health (NIH), National Institute of General Medical Sciences (NIGMS) (P30GM133894). The contents of this publication are solely the responsibility of the authors and do not necessarily represent the official views of NIGMS or NIH. We thank M. Arends for proofreading during the manuscript.

Funding: This work was supported by Ufovax/SFP-2018-1013 and Uvax/SFP-2020-0111 (J.Z.).

Author contributions: Project design by Y.-Z.L., Y.-N.Z., L.H., and J.Z.; protein design by J.Z.; protein expression and purification by Y.-Z.L., G.W., C.D., and L.H.; glycan analysis by

M.N., J.D.A., and M.C.; negative-stain EM and cryo-EM by Y.-Z.L., A.B.W., and J.Z.; x-ray crystallographic analysis by Y.-Z.L., R.L.S., and I.A.W; mouse immunization, lymph node isolation, immunohistology, TEM, flow cytometry, and serum ELISA by Y.-N.Z.; pseudovirus neutralization assays by G.W., K.B.G., C.D., and L.H.; manuscript written by Y.-Z.L., Y.-N.Z., M.N., K.B.G., S.A., L.H., M.C., and J.Z. All authors were asked to comment on the manuscript.

Competing interests: Dr. Jiang Zhu serves as the Co-Founder, Interim Chief Scientific Officer, Consultant, and Scientific Advisory Board member of Uvax Bio, LLC, and holds associated financial interests. Other authors declare that they have no competing interests. **Data and material availability:** All data to understand and assess the conclusions of this research are available in the main text and Supplementary Materials. Structures obtained from x-ray crystallography and cryo-EM have been deposited in the Protein Data Bank (PDB, https://www.rcsb.org/) under accession codes 9N8E and 9N8F, respectively. Cryo-EM data were deposited in the Electron Microscopy Data Bank (EMDB, https://www.ebi.ac.uk/emdb/) under accession code EMD-49127. Mass spectrometry data has been deposited in the MassIVE server (https://massive.ucsd.edu) under accession code MassIVE MSV000097145. The authors declare that the data supporting the findings of this study are available within the article and its Supplementary Information files. Source data are provided with this paper.

References:

1. W. Slenczka, in *Marburg- and Ebolaviruses: From Ecosystems to Molecules,* E. Muhlberger, L. L. Hensley, J. S. Towner, Eds. (2017), vol. 411, pp. 3-21.
2. K. M. Johnson, J. V. Lange, P. A. Webb, F. A. Murphy, Isolation and partial characterisation of a new virus causing acute haemorrhagic fever in Zaire. *Lancet* **1**, 569-571 (1977).
3. E. T. Bowen *et al.*, Viral haemorrhagic fever in southern Sudan and northern Zaire. Preliminary studies on the aetiological agent. *Lancet* **1**, 571-573 (1977).
4. C. E. M. Coltart, B. Lindsey, I. Ghinai, A. M. Johnson, D. L. Heymann, The Ebola outbreak, 2013-2016: old lessons for new epidemics. *Philos. Trans. R. Soc. B, Biol. Sci.* **372**, 20160297 (2017).
5. S. Paessler, D. H. Walker, Pathogenesis of the viral hemorrhagic fevers. *Annu. Rev. Pathol.* **8**, 411-440 (2013).
6. A. M. Marty, P. B. Jahrling, T. W. Gelsbert, Viral hemorrhagic fevers. *Clin. Lab. Med.* **26**, 345-386 (2006).
7. J. H. Kuhn *et al.*, New filovirus disease classification and nomenclature. *Nat. Rev. Microbiol.* **17**, 261-263 (2019).
8. J. H. Kuhn *et al.*, Virus nomenclature below the species level: a standardized nomenclature for filovirus strains and variants rescued from cDNA. *Arch. Virol.* **159**, 1229-1237 (2014).
9. S. C. Harrison, Viral membrane fusion. *Virol.* **479**, 498-507 (2015).
10. M. Kielian, Mechanisms of virus membrane fusion proteins. *Annu. Rev. Virol.* **1**, 171-189 (2014).
11. J. M. White, S. E. Delos, M. Brecher, K. Schornberg, Structures and mechanisms of viral membrane fusion proteins: multiple variations on a common theme. *Crit. Rev. Biochem. Mol. Biol.* **43**, 189-219 (2008).
12. S. C. Harrison, Viral membrane fusion. *Nat. Struct. Mol. Biol.* **15**, 690-698 (2008).
13. J. E. Lee, E. O. Saphire, Ebolavirus glycoprotein structure and mechanism of entry. *Future Virol.* **4**, 621-635 (2009).
14. T. R. W. Tipton *et al.*, Characterisation of the T-cell response to Ebola virus glycoprotein amongst survivors of the 2013-16 West Africa epidemic. *Nat. Commun.* **12**, 1153 (2021).
15. A. I. Flyak *et al.*, Cross-reactive and potent neutralizing antibody responses in human survivors of natural ebolavirus infection. *Cell* **164**, 392-405 (2016).
16. Z. A. Bornholdt *et al.*, Isolation of potent neutralizing antibodies from a survivor of the 2014 Ebola virus outbreak. *Science* **351**, 1078-1083 (2016).
17. X. Y. Yu, E. O. Saphire, Development and structural analysis of antibody therapeutics for filoviruses. *Pathog.* **11**, 374 (2022).
18. L. B. King, B. R. West, S. L. Schendel, E. O. Saphire, The structural basis for filovirus neutralization by monoclonal antibodies. *Curr. Opin. Immunol.* **53**, 196-202 (2018).
19. R. W. Cross, C. E. Mire, H. Feldmann, T. W. Geisbert, Post-exposure treatments for Ebola and Marburg virus infections. *Nat. Rev. Drug Discov.* **17**, 413-434 (2018).
20. B. M. Friedrich *et al.*, Potential vaccines and post-exposure treatments for filovirus infections. *Viruses* **4**, 1619-1650 (2012).
21. R. Burk *et al.*, Neglected filoviruses. *FEMS Microbiol. Rev.* **40**, 494-519 (2016).

22. S. Mahanty, M. Bray, Pathogenesis of filoviral haemorrhagic fevers. *Lancet Infect. Dis.* **4**, 487-498 (2004).
23. I. Messaoudi, G. K. Amarasinghe, C. F. Basler, Filovirus pathogenesis and immune evasion: insights from Ebola virus and Marburg virus. *Nat. Rev. Microbiol.* **13**, 663-676 (2015).
24. S. Moller-Tank, W. Maury, Ebola virus entry: a curious and complex series of events. *PLoS Pathog.* **11**, e1004731 (2015).
25. M. Cote *et al.*, Small molecule inhibitors reveal Niemann-Pick C1 is essential for Ebola virus infection. *Nature* **477**, 344-348 (2011).
26. I. Khan *et al.*, Tubeimosides are pan-coronavirus and filovirus inhibitors that can block their fusion protein binding to Niemann-Pick C1. *Nat. Commun.* **15**, 162 (2024).
27. H. Wang *et al.*, Ebola viral glycoprotein bound to its endosomal receptor Niemann-Pick C1. *Cell* **164**, 258-268 (2016).
28. A. P. Cardile, L. G. Downey, P. D. Wiseman, T. K. Warren, S. Bavari, Antiviral therapeutics for the treatment of Ebola virus infection. *Curr. Opin. Pharmacol.* **30**, 138-143 (2016).
29. O. T. Mbaya, P. Mukumbayi, S. Mulangu, Review: insights on current FDA-approved monoclonal antibodies against Ebola virus infection. *Front. Immunol.* **12**, 721328 (2021).
30. T. Hoenen, A. Groseth, H. Feldmann, Therapeutic strategies to target the Ebola virus life cycle. *Nat. Rev. Microbiol.* **17**, 593-606 (2019).
31. Y. Gao *et al.*, Effects of therapies for Ebola virus disease: a systematic review and network meta-analysis. *Lancet Microbe* **3**, E683-E692 (2022).
32. X. G. Qiu *et al.*, Reversion of advanced Ebola virus disease in nonhuman primates with ZMapp. *Nature* **514**, 47-53 (2014).
33. R. T. Davey *et al.*, A randomized, controlled trial of ZMapp for Ebola virus infection. *N. Engl. J. Med.* **375**, 1448-1456 (2016).
34. A. Markham, REGN-EB3: first approval. *Drugs* **81**, 175-178 (2021).
35. D. Corti *et al.*, Protective monotherapy against lethal Ebola virus infection by a potently neutralizing antibody. *Science* **351**, 1339-1342 (2016).
36. S. Mulangu *et al.*, A randomized, controlled trial of Ebola virus disease therapeutics. *N. Engl. J. Med.* **381**, 2293-2303 (2019).
37. E. O. Saphire, M. J. Aman, Feverish quest for Ebola immunotherapy: straight or cocktail? *Trends Microbiol.* **24**, 684-686 (2016).
38. C. D. Murin *et al.*, Structures of protective antibodies reveal sites of vulnerability on Ebola virus. *Proc. Natl. Acad. Sci. U. S. A.* **111**, 17182-17187 (2014).
39. T. Hashiguchi *et al.*, Structural basis for Marburg virus neutralization by a cross-reactive human antibody. *Cell* **160**, 904-912 (2015).
40. M. L. Fusco *et al.*, Protective mAbs and cross-reactive mAbs raised by immunization with engineered Marburg virus GPs. *PLoS Pathog.* **11**, e1005016 (2015).
41. A. I. Flyak *et al.*, Mechanism of human antibody-mediated neutralization of Marburg virus. *Cell* **160**, 893-903 (2015).
42. J. Pallesen *et al.*, Structures of Ebola virus GP and sGP in complex with therapeutic antibodies. *Nat. Microbiol.* **1**, 16128 (2016).
43. Z. Y. Keck *et al.*, Macaque monoclonal antibodies targeting novel conserved epitopes within filovirus glycoprotein. *J. Virol.* **90**, 279-291 (2016).

44. F. W. Holtsberg *et al.*, Pan-ebolavirus and pan-filovirus mouse monoclonal antibodies: protection against Ebola and Sudan viruses. *J. Virol.* **90**, 266-278 (2016).
45. K. A. Howell *et al.*, Antibody treatment of Ebola and Sudan virus infection via a uniquely exposed epitope within the glycoprotein receptor-binding site. *Cell Rep.* **15**, 1514-1526 (2016).
46. X. L. Zhao *et al.*, Immunization-elicited broadly protective antibody reveals ebolavirus fusion loop as a site of vulnerability. *Cell* **169**, 891-904.e15 (2017).
47. A. Z. Wec *et al.*, Antibodies from a human survivor define sites of vulnerability for broad protection against ebolaviruses. *Cell* **169**, 878-890.e15 (2017).
48. L. B. King *et al.*, The marburgvirus-neutralizing human monoclonal antibody MR191 targets a conserved site to block virus receptor binding. *Cell Host Microbe* **23**, 101-109.e4 (2018).
49. P. Gilchuk *et al.*, Analysis of a therapeutic antibody cocktail reveals determinants for cooperative and broad ebolavirus neutralization. *Immunity* **52**, 388-403.e12 (2020).
50. P. Gilchuk *et al.*, Multifunctional pan-ebolavirus antibody recognizes a site of broad vulnerability on the ebolavirus glycoprotein. *Immunity* **49**, 363-374.e10 (2018).
51. C. D. Murin *et al.*, Convergence of a common solution for broad ebolavirus neutralization by glycan cap-directed human antibodies. *Cell Rep.* **35**, 108984 (2021).
52. A. I. Flyak *et al.*, Broadly neutralizing antibodies from human survivors target a conserved site in the Ebola virus glycoprotein HR2-MPER region. *Nat. Microbiol.* **3**, 670-677 (2018).
53. K. A. Howell *et al.*, Cooperativity enables non-neutralizing antibodies to neutralize ebolavirus. *Cell Rep.* **19**, 413-424 (2017).
54. E. O. Saphire *et al.*, Systematic analysis of monoclonal antibodies against Ebola virus GP defines features that contribute to protection. *Cell* **174**, 938-952.e13 (2018).
55. Y. G. Zhao *et al.*, Toremifene interacts with and destabilizes the Ebola virus glycoprotein. *Nature* **535**, 169-172 (2016).
56. F. Shaikh *et al.*, Structure-based in silico screening identifies a potent ebolavirus inhibitor from a traditional Chinese medicine library. *J. Med. Chem.* **62**, 2928-2937 (2019).
57. J. S. Ren, Y. G. Zhao, E. E. Fry, D. I. Stuart, Target identification and mode of action of four chemically divergent drugs against ebolavirus infection. *J. Med. Chem.* **61**, 724-733 (2018).
58. J. M. Dias *et al.*, A shared structural solution for neutralizing ebolaviruses. *Nat. Struct. Mol. Biol.* **18**, 1424-1427 (2011).
59. J. E. Lee *et al.*, Structure of the Ebola virus glycoprotein bound to an antibody from a human survivor. *Nature* **454**, 177-182 (2008).
60. C. D. Murin, P. Gilchuk, J. E. Crowe, A. B. Ward, Structural biology illuminates molecular determinants of broad ebolavirus neutralization by human antibodies for pan-ebolavirus therapeutic development. *Front. Immunol.* **12**, 808047 (2022).
61. A. Hargreaves *et al.*, Filovirus neutralising antibodies: mechanisms of action and therapeutic application. *Pathog.* **10**, 1201 (2021).
62. A. M. Henao-Restrepo *et al.*, Efficacy and effectiveness of an rVSV-vectored vaccine in preventing Ebola virus disease: final results from the Guinea ring vaccination, open-label, cluster-randomised trial (Ebola Ca Suffit!). *Lancet* **389**, 505-518 (2017).

63. I. D. Milligan *et al.*, Safety and immunogenicity of novel adenovirus type 26- and modified vaccinia Ankara-vectored Ebola vaccines: a randomized clinical trial. *J. Am. Med. Assoc.* **315**, 1610-1623 (2016).
64. U. N. Sarwar *et al.*, Safety and immunogenicity of DNA vaccines encoding ebolavirus and marburgvirus wild-type glycoproteins in a phase I clinical trial. *J. Infect. Dis.* **211**, 549-557 (2015).
65. J. E. Ledgerwood *et al.*, Chimpanzee adenovirus vector Ebola vaccine. *N. Engl. J. Med.* **376**, 928-938 (2017).
66. K. Ewer *et al.*, A monovalent chimpanzee adenovirus Ebola vaccine boosted with MVA. *N. Engl. J. Med.* **374**, 1635-1646 (2016).
67. F. C. Zhu *et al.*, Safety and immunogenicity of a recombinant adenovirus type-5 vector-based Ebola vaccine in healthy adults in Sierra Leone: a single-centre, randomised, double-blind, placebo-controlled, phase 2 trial. *Lancet* **389**, 621-628 (2017).
68. F. C. Zhu *et al.*, Safety and immunogenicity of a novel recombinant adenovirus type-5 vector-based Ebola vaccine in healthy adults in China: preliminary report of a randomised, double-blind, placebo-controlled, phase 1 trial. *Lancet* **385**, 2272-2279 (2015).
69. M. J. Hamer *et al.*, Safety, tolerability, and immunogenicity of the chimpanzee adenovirus type 3-vectored Marburg virus (cAd3-Marburg) vaccine in healthy adults in the USA: a first-in-human, phase 1, open-label, dose-escalation trial. *Lancet* **401**, 294-302 (2023).
70. M. D. Tapia *et al.*, Safety, reactogenicity, and immunogenicity of a chimpanzee adenovirus vectored Ebola vaccine in adults in Africa: a randomised, observer-blind, placebo-controlled, phase 2 trial. *Lancet Infect. Dis.* **20**, 707-718 (2020).
71. A. To *et al.*, Thermostable bivalent filovirus vaccine protects against severe and lethal Sudan ebolavirus and marburgvirus infection. *Vaccine* **42**, 598-607 (2024).
72. K. B. Preston *et al.*, Single-vial filovirus glycoprotein vaccines: biophysical characteristics and immunogenicity after co-lyophilization with adjuvant. *Vaccine* **39**, 5650-5657 (2021).
73. D. Xu *et al.*, Design of universal Ebola virus vaccine candidates via immunofocusing. *Proc. Natl. Acad. Sci. U. S. A.* **121**, e2316960121 (2024).
74. M. Meyer *et al.*, Modified mRNA-based vaccines elicit robust immune responses and protect guinea pigs from Ebola virus disease. *J. Infect. Dis.* **217**, 451-455 (2018).
75. L. A. Parish, E. J. Stavale, C. R. Houchens, D. N. Wolfe, Developing vaccines to improve preparedness for filovirus outbreaks: the perspective of the USA biomedical advanced research and development authority (BARDA). *Vaccines* **11**, 1120 (2023).
76. M. Meyer, D. C. Malherbe, A. Bukreyev, Can Ebola virus vaccines have universal immune correlates of protection? *Trends Microbiol.* **27**, 8-16 (2019).
77. S. A. Ehrhardt *et al.*, Polyclonal and convergent antibody response to Ebola virus vaccine rVSV-ZEBOV. *Nat. Med.* **25**, 1589-1600 (2019).
78. H. Cohen-Dvashi *et al.*, Structural basis for a convergent immune response against Ebola virus. *Cell Host Microbe* **27**, 418-427.e4 (2020).
79. B. F. Haynes, J. R. Mascola, The quest for an antibody-based HIV vaccine. *Immunol. Rev.* **275**, 5-10 (2017).
80. P. D. Kwong, J. R. Mascola, G. J. Nabel, Broadly neutralizing antibodies and the search for an HIV-1 vaccine: the end of the beginning. *Nat. Rev. Immunol.* **13**, 693-701 (2013).

81. B. F. Haynes, G. Kelsoe, S. C. Harrison, T. B. Kepler, B-cell-lineage immunogen design in vaccine development with HIV-1 as a case study. *Nat. Biotechnol.* **30**, 423-433 (2012).
82. L. M. Walker, D. R. Burton, Rational antibody-based HIV-1 vaccine design: current approaches and future directions. *Curr. Opin. Immunol.* **22**, 358-366 (2010).
83. B. S. Graham, M. S. A. Gilman, J. S. McLellan, Structure-based vaccine antigen design. *Annu. Rev. Med.* **70**, 91-104 (2019).
84. R. W. Sanders *et al.*, A next-generation cleaved, soluble HIV-1 Env trimer, BG505 SOSIP.664 gp140, expresses multiple epitopes for broadly neutralizing but not non-neutralizing antibodies. *PLoS Pathog.* **9**, e1003618 (2013).
85. S. K. Sharma *et al.*, Cleavage-independent HIV-1 Env trimers engineered as soluble native spike mimetics for vaccine design. *Cell Rep.* **11**, 539-550 (2015).
86. L. Kong *et al.*, Uncleaved prefusion-optimized gp140 trimers derived from analysis of HIV-1 envelope metastability. *Nat. Commun.* **7**, 12040 (2016).
87. J. S. McLellan *et al.*, Structure-based design of a fusion glycoprotein vaccine for respiratory syncytial virus. *Science* **342**, 592-598 (2013).
88. M. G. Joyce *et al.*, Iterative structure-based improvement of a fusion-glycoprotein vaccine against RSV. *Nat. Struct. Mol. Biol.* **23**, 811-820 (2016).
89. A. Krarup *et al.*, A highly stable prefusion RSV F vaccine derived from structural analysis of the fusion mechanism. *Nat. Commun.* **6**, 8143 (2015).
90. Y. Che *et al.*, Rational design of a highly immunogenic prefusion- stabilized F glycoprotein antigen for a respiratory syncytial virus vaccine. *Sci. Transl. Med.* **15**, eade6422 (2023).
91. K. V. Houser *et al.*, Safety and immunogenicity of an HIV-1 prefusion-stabilized envelope trimer (Trimer 4571) vaccine in healthy adults: A first-in-human open-label, randomized, dose-escalation, phase 1 clinical trial. *Eclinicalmedicine* **48**, 101477 (2022).
92. G. Papazisis *et al.*, Respiratory syncytial virus vaccines: analysis of pre-marketing clinical trials for immunogenicity in the population over 50 years of age. *Vaccines* **12**, 353 (2024).
93. M. Melgar *et al.*, Use of respiratory syncytial virus vaccines in older adults: recommendations of the advisory committee on immunization practices - United States, 2023. *Morb. Mortal. Wkly. Rep.* **72**, 793-801 (2023).
94. L. Rutten *et al.*, Structure-based design of prefusion-stabilized filovirus glycoprotein trimers. *Cell Rep.* **30**, 4540-4550.e3 (2020).
95. L. He *et al.*, Single-component multilayered self-assembling nanoparticles presenting rationally designed glycoprotein trimers as Ebola virus vaccines. *Nat. Commun.* **12**, 2633 (2021).
96. J. J. Suschak, C. S. Schmaljohn, Vaccines against Ebola virus and Marburg virus: recent advances and promising candidates. *Hum. Vaccin. Immunother.* **15**, 2359-2377 (2019).
97. O. Reynard *et al.*, Ebolavirus glycoprotein GP masks both its own epitopes and the presence of cellular surface proteins. *J. Virol.* **83**, 9596-9601 (2009).
98. J. R. Francica *et al.*, Steric shielding of surface epitopes and impaired immune recognition induced by the Ebola virus glycoprotein. *PLoS Pathog.* **6**, e1001098 (2010).
99. N. Chaudhary, D. Weissman, K. A. Whitehead, mRNA vaccines for infectious diseases: principles, delivery and clinical translation. *Nat. Rev. Drug Discov.* **20**, 817-838 (2021).
100. D. S. Khoury *et al.*, Neutralizing antibody levels are highly predictive of immune protection from symptomatic SARS-CoV-2 infection. *Nat. Med.* **27**, 1205-1211 (2021).

101. B. Nguyen, N. H. Tolia, Protein-based antigen presentation platforms for nanoparticle vaccines. *NPJ Vaccines* **6**, 70 (2021).
102. D. J. Irvine, B. J. Read, Shaping humoral immunity to vaccines through antigen-displaying nanoparticles. *Curr. Opin. Immunol.* **65**, 1-6 (2020).
103. R. Rappuoli, D. Serruto, Self-assembling nanoparticles usher in a new era of vaccine design. *Cell* **176**, 1245-1247 (2019).
104. P. J. M. Brouwer, R. W. Sanders, Presentation of HIV-1 envelope glycoprotein trimers on diverse nanoparticle platforms. *Curr. Opin. HIV AIDS* **14**, 302-308 (2019).
105. M. Brinkkemper, K. Sliepen, Nanoparticle vaccines for inducing HIV-1 neutralizing antibodies. *Vaccines* **7**, 76 (2019).
106. B. Asbach, R. Wagner, Particle-based delivery of the HIV envelope protein. *Curr. Opin. HIV AIDS* **12**, 265-271 (2017).
107. H. Y. Huang *et al.*, Vaccination with SARS-CoV-2 spike protein lacking glycan shields elicits enhanced protective responses in animal models. *Sci. Transl. Med.* **14**, eabm0899 (2022).
108. Y.-N. Zhang *et al.*, Single-component multilayered self-assembling protein nanoparticles presenting glycan-trimmed uncleaved prefusion optimized envelope trimers as HIV-1 vaccine candidates. *Nat. Commun.* **14**, 1985 (2023).
109. C. C. Wang *et al.*, Glycans on influenza hemagglutinin affect receptor binding and immune response. *Proc. Natl. Acad. Sci. U. S. A.* **106**, 18137-18142 (2009).
110. S. C. Wang, H. Y. Liao, J. Y. Zhang, T. J. R. Cheng, C. H. Wong, Development of a universal influenza vaccine using hemagglutinin stem protein produced from Pichia pastoris. *Virol.* **526**, 125-137 (2019).
111. B. R. West *et al.*, Structural basis of pan-ebolavirus neutralization by a human antibody against a conserved, yet cryptic epitope. *mBio* **9**, e01674-18 (2018).
112. C. D. Murin *et al.*, Structural basis of pan-ebolavirus neutralization by an antibody targeting the glycoprotein fusion loop. *Cell Rep.* **24**, 2723-2732.e4 (2018).
113. B. M. Janus *et al.*, Structural basis for broad neutralization of ebolaviruses by an antibody targeting the glycoprotein fusion loop. *Nat. Commun.* **9**, 3934 (2018).
114. B. R. West *et al.*, Structural basis of broad ebolavirus neutralization by a human survivor antibody. *Nat. Struct. Mol. Biol.* **26**, 204-212 (2019).
115. D. Lyumkis *et al.*, Cryo-EM structure of a fully glycosylated soluble cleaved HIV-1 envelope trimer. *Science* **342**, 1484-1490 (2013).
116. S. Bangaru *et al.*, Structural analysis of full-length SARS-CoV-2 spike protein from an advanced vaccine candidate. *Science* **370**, 1089-1094 (2020).
117. H. L. Turner *et al.*, Potent anti-influenza H7 human monoclonal antibody induces separation of hemagglutinin receptor-binding head domains. *PLoS Biol.* **17**, e3000139 (2019).
118. S. Bale *et al.*, Structural basis for differential neutralization of ebolaviruses. *Viruses* **4**, 447-470 (2012).
119. A. Punjani, J. L. Rubinstein, D. J. Fleet, M. A. Brubaker, cryoSPARC: algorithms for rapid unsupervised cryo-EM structure determination. *Nat. Methods* **14**, 290-296 (2017).
120. K. Braz Gomes *et al.*, Single-component multilayered self-assembling protein nanoparticles displaying extracellular domains of matrix protein 2 as a pan-influenza A vaccine. *ACS Nano* **17**, 23545-23567 (2023).

121. Y.-N. Zhang *et al.*, Mechanism of a COVID-19 nanoparticle vaccine candidate that elicits a broadly neutralizing antibody response to SARS-CoV-2 variants. *Sci. Adv.* **7**, eabj3107 (2021).
122. R. Rappuoli, Glycoconjugate vaccines: principles and mechanisms. *Sci. Transl. Med.* **10**, eaat4615 (2018).
123. J. G. Cyster, B cell follicles and antigen encounters of the third kind. *Nat. Immunol.* **11**, 989-996 (2010).
124. B. A. Heesters, R. C. Myers, M. C. Carroll, Follicular dendritic cells: dynamic antigen libraries. *Nat. Rev. Immunol.* **14**, 495-504 (2014).
125. J. G. Cyster, P. C. Wilson, Antibody modulation of B cell responses-Incorporating positive and negative feedback. *Immunity* **57**, 1466-1481 (2024).
126. J. Misasi *et al.*, Structural and molecular basis for Ebola virus neutralization by protective human antibodies. *Science* **351**, 1343-1346 (2016).
127. A. Martínez-Riaño *et al.*, Long-term retention of antigens in germinal centers is controlled by the spatial organization of the follicular dendritic cell network. *Nat. Immunol.* **24**, 1281-1294 (2023).
128. G. D. Victora, M. C. Nussenzweig, Germinal centers. *Annu. Rev. Immunol.* **30**, 429-457 (2012).
129. C. D. Allen, J. G. Cyster, Follicular dendritic cell networks of primary follicles and germinal centers: phenotype and function. *Semin. Immunol.* **20**, 14-25 (2008).
130. B. A. Heesters, C. E. van der Poel, A. Das, M. C. Carroll, Antigen presentation to B cells. *Trends Immunol.* **37**, 844-854 (2016).
131. M. E. M. El Shikh, R. M. El Sayed, S. Sukumar, A. K. Szakal, J. G. Tew, Activation of B cells by antigens on follicular dendritic cells. *Trends Immunol.* **31**, 205-211 (2010).
132. G. A. Roth *et al.*, Designing spatial and temporal control of vaccine responses. *Nat. Rev. Mater.* **7**, 174-195 (2022).
133. P. Yousefpour, K. Ni, D. J. Irvine, Targeted modulation of immune cells and tissues using engineered biomaterials. *Nat. Rev. Bioeng.* **1**, 107-124 (2023).
134. Y. R. Carrasco, F. D. Batista, B cells acquire particulate antigen in a macrophage-rich area at the boundary between the follicle and the subcapsular sinus of the lymph node. *Immunity* **27**, 160-171 (2007).
135. T. Junt *et al.*, Subcapsular sinus macrophages in lymph nodes clear lymph-borne viruses and present them to antiviral B cells. *Nature* **450**, 110-114 (2007).
136. T. G. Phan, I. Grigorova, T. Okada, J. G. Cyster, Subcapsular encounter and complement-dependent transport of immune complexes by lymph node B cells. *Nat. Immunol.* **8**, 992-1000 (2007).
137. T. G. Phan, J. A. Green, E. E. Gray, Y. Xu, J. G. Cyster, Immune complex relay by subcapsular sinus macrophages and noncognate B cells drives antibody affinity maturation. *Nat. Immunol.* **10**, 786-793 (2009).
138. S. F. Gonzalez *et al.*, Capture of influenza by medullary dendritic cells via SIGN-R1 is essential for humoral immunity in draining lymph nodes. *Nat. Immunol.* **11**, 427-434 (2010).
139. C. D. Allen, T. Okada, J. G. Cyster, Germinal-center organization and cellular dynamics. *Immunity* **27**, 190-202 (2007).
140. J. G. Cyster, C. D. C. Allen, B cell responses: cell interaction dynamics and decisions. *Cell* **177**, 524-540 (2019).

141. F. D. Batista, N. E. Harwood, The who, how and where of antigen presentation to B cells. *Nat. Rev. Immunol.* **9**, 15-27 (2009).
142. Z. Shulman *et al.*, T follicular helper cell dynamics in germinal centers. *Science* **341**, 673-677 (2013).
143. S. Crotty, T follicular helper cell differentiation, function, and roles in disease. *Immunity* **41**, 529-542 (2014).
144. L. He *et al.*, Single-component, self-assembling, protein nanoparticles presenting the receptor binding domain and stabilized spike as SARS-CoV-2 vaccine candidates. *Sci. Adv.* **7**, eabf1591 (2021).
145. L. He *et al.*, Proof of concept for rational design of hepatitis C virus E2 core nanoparticle vaccines. *Sci. Adv.* **6**, eaaz6225 (2020).
146. R. W. Cross *et al.*, An introduction to the Marburg virus vaccine consortium, MARVAC. *PLoS Pathog.* **18**, e1010805 (2022).
147. D. N. Wolfe *et al.*, Selection of filovirus isolates for vaccine development programs. *Vaccines* **9**, 1045 (2021).
148. Y.-N. Zhang *et al.*, A single-component multilayered self-assembling protein nanoparticle vaccine based on extracellular domains of matrix protein 2 against both influenza A and B. *Vaccines* **12**, 975 (2024).
149. Y. Z. Lee *et al.*, Rational design of uncleaved prefusion-closed trimer vaccines for human respiratory syncytial virus and metapneumovirus. *Nat. Commun.* **15**, 9939 (2024).
150. L. He *et al.*, HIV-1 vaccine design through minimizing envelope metastability. *Sci. Adv.* **4**, aau6769 (2018).
151. L. He *et al.*, Presenting native-like trimeric HIV-1 antigens with self-assembling nanoparticles. *Nat. Commun.* **7**, 12041 (2016).
152. M. Gonzalez-Hernandez *et al.*, Preclinical immunogenicity and protective efficacy of a SARS-CoV-2 RBD-based vaccine produced with the thermophilic filamentous fungal expression system Thermothelomyces heterothallica C1. *Front. Immunol.* **14**, 1204834 (2023).
153. L. Lazo *et al.*, A recombinant SARS-CoV-2 receptor-binding domain expressed in an engineered fungal strain of Thermothelomyces heterothallica induces a functional immune response in mice. *Vaccine* **40**, 1162-1169 (2022).
154. J. Korn *et al.*, Baculovirus-free insect cell expression system for high yield antibody and antigen production. *Sci. Rep.* **10**, 21393 (2020).
155. M.-A. Elsliger *et al.*, The JCSG high-throughput structural biology pipeline. *Acta Crystallogr. Sect. F Struct. Biol. Cryst. Commun.* **66**, 1137-1142 (2010).
156. Z. Otwinowski, W. Minor, Processing of X-ray diffraction data collected in oscillation mode. *Methods Enzymol.* **276**, 307-326 (1997).
157. P. Emsley, B. Lohkamp, W. G. Scott, K. Cowtan, Features and development of Coot. *Acta Crystallogr. D Biol. Crystallogr.* **66**, 486-501 (2010).
158. D. Liebschner *et al.*, Macromolecular structure determination using X-rays, neutrons and electrons: recent developments in Phenix. *Acta Crystallogr. D: Struct. Biol.* **75**, 861-877 (2019).
159. H. Berman, K. Henrick, H. Nakamura, Announcing the worldwide Protein Data Bank. *Nat. Struct. Biol.* **10**, 980 (2003).
160. E. Potterton, P. Briggs, M. Turkenburg, E. Dodson, A graphical user interface to the CCP4 program suite. *Acta Crystallogr. D Biol. Crystallogr.* **59**, 1131-1137 (2003).

161. G. Tang *et al.*, EMAN2: An extensible image processing suite for electron microscopy. *J. Struct. Biol.* **157**, 38-46 (2007).
162. E. F. Pettersen *et al.*, UCSF chimera - A visualization system for exploratory research and analysis. *J. Comput. Chem.* **25**, 1605-1612 (2004).
163. E. C. Meng *et al.*, UCSF ChimeraX: Tools for structure building and analysis. *Protein Sci.* **32**, e4792 (2023).
164. E. F. Pettersen *et al.*, UCSF ChimeraX: Structure visualization for researchers, educators, and developers. *Protein Sci.* **30**, 70-82 (2021).
165. T. D. Goddard *et al.*, UCSF ChimeraX: Meeting modern challenges in visualization and analysis. *Protein Sci.* **27**, 14-25 (2018).
166. J. Zhu, L. Xie, B. Honig, Structural refinement of protein segments containing secondary structure elements: Local sampling, knowledge-based potentials, and clustering. *Proteins: Struct. Funct. Bioinf.* **65**, 463-479 (2006).
167. B. L. deGroot *et al.*, Prediction of protein conformational freedom from distance constraints. *Proteins: Struct. Funct. Genet.* **29**, 240-251 (1997).
168. R. Samudrala, J. Moult, An all-atom distance-dependent conditional probability discriminatory function for protein structure prediction. *J. Mol. Biol.* **275**, 895-916 (1998).
169. C. A. Schneider, W. S. Rasband, K. W. Eliceiri, NIH Image to ImageJ: 25 years of image analysis. *Nat. Methods* **9**, 671-675 (2012).

Figure Legends

Fig. 1. Rational design and in vitro characterization of ebolavirus GP trimers. (**a**) Schematic representation of GP construct design, including the MLD deletion (Δmuc) between G314 to N463, P^2 (T577P) or P^4 (L579P) mutation in HR1c, W615L mutation at the neck of the HR2 stalk, and C-terminal extension from D632 to D637. IFL: internal fusion loop. (**b**) Schematic representation of an ebolavirus GP trimer bound to NAb ADI-15878 (left) and SEC profiles of six ebolavirus GPΔmuc constructs following transient expression in 25 ml of ExpiCHO cells and IAC purification using an ADI-15878 column (right). Two major SEC peaks, aggregation (A) and trimer (T), are marked on the profile. (**c**) BN-PAGE of six ADI-15878/SEC-purified ebolaviruses GPΔmuc trimers. The gel bands are consistent with the expected trimer size and molecular weight. (**d**) DSC thermograms of six ADI-15878/SEC-purified ebolaviruses GPΔmuc trimers. The experimental data and Gaussian fitting are shown as black dots and red lines, respectively. Key parameters, such as thermal denaturation midpoint (T_m or T_{m1} and T_{m2}), onset temperature (T_{onset}), and half width of the peak ($\Delta T_{1/2}$) are labeled on the thermogram. (**e**) Site-specific glycan profiles for ADI-15878/SEC-purified EBOV, SUDV, and BDBV GPΔmuc-WL^2P^4 trimers. Glycan compositions are grouped into four types, including complex (solid pink), hybrid (pink lines), oligomannose (solid green), and unoccupied (solid gray). Glycan sites that could not be determined are denoted as "N.D." Sites that are not present are denoted as "N.P." (**f**) nsEM-derived 3D reconstructions of EBOV, SUDV, and BDBV GPΔmuc-WL^2P^4 trimers and their complexes with NAb ADI-15878. Crystal structures of EBOV GPΔmuc-WL^2P^2 (PDB ID: 7JPH) and ADI-15878 (PDB ID: 6DZN) were used in the density fitting, with GP1, GP2, and ADI-15878 Fab in the resulting molecular model colored in cyan, green, and pink, respectively. (**e**) ELISA-derived EC_{50} (μg/ml) values of six ebolaviruses GPΔmuc trimers binding to four pan-ebolavirus NAbs and a

marburgvirus NAb, MR-78. If absorbance at 450 nm is less than 0.5 at the starting and highest concentration (10 μg/ml), then the antigen has negligible binding to the tested antibody, and the EC_{50} value is set to 10 μg/ml. (**f**) BLI profiles of six ebolaviruses GPΔmuc trimers binding to the same NAbs. Sensorgrams were obtained from an Octet RED96 instrument using an antigen titration series of six concentrations (starting at 600 nM followed by 2-fold dilutions) and are shown in **Fig. S1i**. Peak values at the highest concentration are shown in a matrix, in which cells are colored in green (weak binding) to red (strong binding).

Fig. 2. Structural characterization of an unliganded EBOV GPΔmuc-WL^2P^4 trimer and a SUDV GPΔmuc-WL^2P^4 trimer in complex with NAb CA45. (**a**) Left: crystal structure of a stabilized EBOV GPΔmuc-WL^2P^4 trimer determined at a resolution of 3.2 Å, with GP1 shown in cyan, glycan cap shown in gray, IFL shown in pink, and GP2 shown in gold. Structural details could not be determined for regions R200-P209, K294-I301, and C-terminus (T634-D637). Right: comparative analysis of the HR1c bend and its local structure for three rationally designed EBOV GPΔmuc constructs bearing the WL^2 mutation (PDB ID: 7JPI), WL^2P^2 mutation (PDB ID: 7JPH), and WL^2P^4 mutation. Sidechains are shown for amino acids that form cross-protomer interactions, including L95, R130, L573, and T576. A cutoff of 3.3 Å is used to define the donor-acceptor distance within a hydrogen bond. (**b**) Cryo-EM-derived 3D reconstruction of a SUDV GPΔmuc-WL^2P^4 trimer in complex with CA45 Fab determined at 3.13 Å, with GP1 shown in orange, GP2 shown in green, CA45 heavy chain shown in blue, and CA45 light chain shown in pink. The glycan cap and HR2 stalk are missing in the density map at this resolution and can only be seen partially when the resolution is relaxed beyond 4.0 Å, as shown in **Fig. S2e**. (**c**) Ribbon representation of the cryo-EM structure of the SUDV GPΔmuc-WL^2P^4 trimer in complex with CA45 Fab. The same color-coding scheme is adopted for GP1, GP2, and CA45 heavy and light chains. Atomic details

of the glycan cap and HR2 stalk cannot be reliably resolved due to low resolution of the density map for these regions. The left panel shows atomic details of hydrogen bonds and salt bridges between SUDV GPΔmuc and NAb CA45 heavy chain (top) and light chain (bottom), whereas the right panel overlaps the HR1c bend of SUDV GPΔmuc-WL^{2}P^4 with that of BDBV GPΔmuc (cryo-EM structure, top) and that of EBOV GPΔmuc-WL^{2}P^4 (crystal structure, bottom).

Fig. 3. Rational design and in vitro characterization of ebolaviruses GP-presenting SApNPs. (**a**) Rational design of a 60-mer SApNP for the optimal surface display of trimeric antigens with a narrow stalk. Twenty I3-01v9a trimers assemble into an I3-01v9a SApNP (left), with the N-termini forming a triangle of 50.5 Å (middle). Using computational design, the *N*-terminus of I3-01v9a was extended by engineering a helix that packs against the protein core with the first residue forming a triangle of 12.9 Å, resulting in I3-01v9b/c. (**b**) nsEM analysis of EBOV GPΔmuc-WL^{2}P^4-I3-01v9b-T, in which I3-01v9b-T is a trimeric version of I3-01v9b with mutations to interrupt the particle-forming interface. Top: examples of 2D classification images; Bottom: side and top views of nsEM-derived 3D model. (**c**) Schematic representation of EBOV GPΔmuc-WL^{2}P^4-presenting I3-01v9b/c SApNP. The calculated particle size is 49.1 nm measured for GP1-T269. (**d**) SEC profiles of six ebolavirus GPΔmuc-WL^{2}P^4-presenting SApNPs following transient expression in ExpiCHO cells and IAC purification using an ADI-15878 column. The NP peak is labeled on the SEC profile, along with partially assembled NP (pNP) and trimer (T) peaks. (**e**) nsEM images of six SEC-purified ebolaviruses of GPΔmuc-WL^{2}P^4-presenting SApNPs. The scale (50 nm) is labeled on the nsEM images. (**f**) Particle size distribution of six SEC-purified ebolavirus GPΔmuc-WL^{2}P^4-presenting SApNPs. The hydrodynamic diameter (D_h) was measured by DLS. Three measurements are reported for each SUDV GPΔmuc SApNP, with the particle size range labeled on the plot. (**g**) Site-specific glycan profile of SUDV GPΔmuc-WL^{2}P^4-presenting E2p and

I3-01v9b SApNPs, with the same labeling scheme of glycan types as in **Fig. 1e**. (**h**) ELISA-derived EC_{50} (μg/ml) values of six ebolaviruses GPΔmuc-WL^2P^4-presenting SApNPs binding to five NAbs, with the same cutoff (0.5) used for absorbance at 450 nm as in **Fig. 1f**. (**i**) BLI profiles of six ebolaviruses GPΔmuc-WL^2P^4-presenting SApNPs binding to five NAbs. Sensorgrams were obtained using the same protocol as in **Fig. 1g** and are shown in **Fig. S3k**. Peak values at the highest concentration are shown in a matrix, with the same color-coding as in **Fig. 1g**.

Fig. 4. Glycan modification of EBOV and SUDV GPΔmuc-WL^2P^4 trimers and SApNPs. (**a**) SEC profiles of EBOV and SUDV GPΔmuc-WL^2P^4 constructs following transient expression in HEK293F cells and IAC purification using an ADI-15878 column, each construct with two glycan modifications: kifunensine (Kif) treatment and kifunensine plus endo H (Kif/endo H) treatment. While HEK293F expression in the presence of Kif produces oligomannose-type glycans, further treatment with endo H results in a monolayer of GlcNAc cores. The SEC peak around 14.7 ml corresponds to endo H. (**b**) DSC thermograms of ADI-15878/SEC-purified EBOV and SUDV GPΔmuc-WL^2P^4 trimers after glycan treatment. The experimental data and Gaussian fitting are shown as black dots and red lines, respectively. Key parameters, such as thermal denaturation midpoint (T_m or T_{m1} and T_{m2}), onset temperature (T_{onset}), and half width of the peak ($\Delta T_{1/2}$) are labeled on the thermogram. (**c**) ELISA-derived EC_{50} (μg/ml) values of glycan-modified EBOV and SUDV GPΔmuc-WL^2P^4 trimers binding to five NAbs, with the same cutoff (0.5) used for absorbance at 450 nm as in **Fig. 1f**. (**d**) BLI profiles of glycan-modified EBOV and SUDV GPΔmuc-WL^2P^4 trimers binding to five NAbs. Sensorgrams were obtained using the same protocol as in **Fig. 1g** and are shown in **Fig. S4c**. Peak values at the highest concentration are shown in a matrix, with the same color-coding as in **Fig. 1g**. (**e**) SEC profiles (top) and nsEM images (bottom) of glycan-modified EBOV and SUDV GPΔmuc-WL^2P^4-presenting SApNPs.

Glycan modification was performed as described in **Fig. 4a**, with the results for EBOV GPΔmuc I3-01v9b not shown due to its low expression yield. The scale (50 nm) is labeled on the nsEM images. (**f**) Site-specific glycan profile of SUDV GPΔmuc-WL^{2}P^4-presenting E2p and I3-01v9b SApNPs after kifunensine treatment, with the same glycan type labeling as in **Fig. 1e**. (**g**) ELISA-derived EC_{50} (μg/ml) values of glycan-modified SUDV GPΔmuc-WL^{2}P^4-presenting E2p and I3-01v9b SApNPs binding to five NAbs, as in **Fig. 1f**. (**h**) BLI profiles of glycan-modified SUDV GPΔmuc-WL^{2}P^4-presenting E2p and I3-01v9b SApNPs binding to five NAbs. Sensorgrams were obtained using the same protocol as in **Fig. 1g** and are shown in **Fig. S4h**. Peak values at the highest concentration are shown in a matrix, with the same color-coding as in **Fig. 1g**.

Fig. 5. Rational design and in vitro characterization of marburgvirus GP trimers. (**a**) Schematic representation of GP construct design, including MLD deletion (Δmuc) between T256 to T424, P^2 (T578P) or P^4 (E580P) mutation in HR1c, and double mutation E631F/Q632V at the C-terminus, all based on the RAVV backbone. (**b**) SEC profiles of four RAVV GP constructs following transient expression in 16 ml of ExpiCHO cells and Nickel purification. Aggregation (A), trimer (T), and GP subunit (S) peaks are marked on the SEC profile. (**c**) BN-PAGE of RAVV GPΔmuc-P^{2}CT trimer fractions from SEC purification. (**d**) DSC thermograms of Nickel/SEC-purified RAVV GPΔmuc-P^2-foldon and GPΔmuc-P^{2}CT-foldon trimers. The experimental data and Gaussian fitting are shown as black dots and red lines, respectively. Thermal denaturation midpoint (T_{m1}, T_{m2}, and T_{m3}) values are labeled. (**e**) nsEM analysis of RAVV GPΔmuc-P^{2}CT-foldon/MR-78 Fab complex. Left: crystal structure (PDB ID: 5UQY) of RAVV GPΔmuc/MR-78 Fab complex fitted into the nsEM density map (left). Right: nsEM-derived 3D density map of RAVV GPΔmuc/MR-78 Fab complex (EMDB: 6233, shown in orange surface) overlaid with the nsEM density map. (**f**) Site-specific glycan profile of RAVV GPΔmuc-P^{2}CT trimer, with the same

glycan type labeling as in **Fig. 1e**. (**g**) ELISA-derived EC_{50} (μg/ml) values of RAVV GPΔmuc-P^2 and GPΔmuc-P^2CT trimer binding to marburgvirus NAbs MR-78 and MR-191, with the same cutoff (0.5) used for absorbance at 450 nm as in **Fig. 1f**. (**h**) BLI profiles of RAVV GPΔmuc-P^2 and GPΔmuc-P^2CT trimer binding to marburgvirus NAbs MR-78 and MR-191. Sensorgrams were obtained using the same protocol as in **Fig. 1g** and are shown in **Fig. S5h**. Peak values at the highest concentration are shown in a matrix, with the same color-coding as in **Fig. 1g**.

Fig. 6. Retention of SUDV GPΔmuc-presenting SApNPs in lymph node follicles. Distribution of (**a**) E2p and (**b**) I3-01v9b SApNPs displaying SUDV GPΔmuc-WL^2P^4 trimers in a lymph node 12 h after a single-dose injection (10 μg/injection, 40 μg/mouse, left). A pan-ebolavirus NAb, CA45, was used to stain the sentinel lymph node tissue sections. Right: schematic illustration of SUDV SApNP accumulation in lymph node follicles. (**c**) Trafficking and retention of the SUDV GPΔmuc trimer and SApNPs in lymph node follicles 2 h to 8 weeks after a single-dose injection. Scale bar = 50 μm for each image. (**d**) Time-dependent curve and (**e**) Area under the curve (AUC) of the CA45-stained area in immunohistological images of SUDV vaccine retention in lymph node follicles over 8 weeks. (**f**) Quantification of SUDV vaccine accumulation in lymph node follicles 48 h after a single-dose injection. Data were collected from more than 10 lymph node follicles (*n* = 3-5 mice/group). (**g**) Interaction of SUDV GPΔmuc trimer and trimer-presenting SApNPs with FDC networks in lymph node follicles 48 h after a single-dose injection. Both E2p and I3-01v9b SApNPs colocalized with FDC networks. Immunofluorescent images are pseudo-color-coded ($CD21^+$, green; $CD169^+$, red; CA45, white). Scale bars = 500 and 100 μm for a complete lymph node and the enlarged image of a follicle, respectively. The data points are expressed as the mean ± SEM for (d) and SD for (e and f). The data were analyzed using one-way ANOVA followed by Tukey's multiple comparison *post hoc* test. **p < 0.01, ****p < 0.0001.

Fig. 7. Interaction of SUDV GPΔmuc-presenting SApNPs with FDCs and phagocytic cells in lymph nodes. (a-c) TEM images of (**a**) E2p SApNPs (yellow arrows) and (**b, c**) I3-01v9b SApNPs presenting SUDV GPΔmuc-WL^{2}P^4 trimers aligned on FDC dendrites in lymph node follicles (**a, b**) 12 h and (**c**) 48 h after a single-dose injection (2 footpads, 50 μg/footpad). The administered dose was 200 μl of antigen/aluminum phosphate (AP) adjuvant mix containing 100 μg of SApNP and 100 μl of AP adjuvant into two hind footpads. Fresh popliteal lymph nodes were collected. No AP adjuvant was observed on FDC dendrites. (**d, e**) TEM images of (**d**) E2p and (**e**) I3-01v9b SApNPs (yellow arrows) presenting SUDV GPΔmuc-WL^{2}P^4 trimers observed on the surface and inside endolysosomes of phagocytic cells 12 h after a single-dose injection. (**f**) TEM images of AP adjuvant (green arrows) aggregated in the extracellular matrix (ECM) 2 h after the injection. (**g**) TEM images of Sudan GPΔmuc-presenting I3-01v9b SApNPs and AP adjuvants observed inside endolysosomes of phagocytic cells 48 h after the injection.

Fig. 8. Induction of germinal center reactions by SUDV GPΔmuc-presenting SApNPs in lymph nodes. (**a**) Top: representative immunofluorescent images of germinal centers (GCs) induced by the SUDV GPΔmuc-presenting SApNP vaccine 2 weeks after a single-dose injection (10 μg/injection, 40 μg/mouse). The administered dose was 80 μl of antigen/aluminum phosphate (AP) adjuvant mix. Bottom: robust GC formation with well-organized light zone (LZ) and dark zone (DZ) compartments in lymph node follicles. GC B cells (GL7$^+$, red) attached to FDCs (CD21$^+$, green) and T_{fh} cells located in LZ of GCs. Scale bars = 500 and 100 μm for a complete lymph node and the enlarged image of a follicle, respectively. (**b**, **c**) Assessment of GCs in immunofluorescent images 2, 5, and 8 weeks after a single-dose injection or 2 and 5 weeks after the boost, which occurred 3 weeks after the prime (n = 5 mice/group). The GC/FDC ratio and GC size were measured and plotted. (**d**, **e**) Representative GC immunofluorescent images generated by Sudan

GP vaccine constructs at 8 weeks using a single-dose or prime-boost regimen. Scale bar = 50 μm for an enlarged lymph node follicle. (**f, g**) Quantification of GCs using flow cytometry after single-dose or prime-boost injections (n = 5 mice/group). Frequency and number of GC B cells and T_{fh} cells were characterized and plotted. The data points are shown as the mean ± SD. The data were analyzed using one-way ANOVA followed by Tukey's multiple comparison *post hoc* test for each timepoint. ns (not significant), *p < 0.05, **p < 0.01, ***p < 0.001, ****p < 0.0001.

Fig. 9. **Antibody responses to rationally designed filovirus vaccines in mice.** (a) Schematic illustration of the mouse immunization regimen for EBOV, SUDV, and RAVV GPΔmuc vaccines (n = 8 mice/group). The administered dose was 200 μl of antigen/AH + CpG adjuvant mix containing 10 μg of immunogen and 100 μl of adjuvant. Mice were immunized at weeks 0, 3, 9 and 15 with an extended interval of 6 weeks between the 2nd and 3rd doses and 3rd and 4th doses via the intraperitoneal route. (**b-d**) EBOV vaccine-induced binding antibody (bAb) responses against (**b**) EBOV GPΔmuc-WL^2P^4(1TD0), (**c**) SUDV GPΔmuc-WL^2P^4(1TD0), and (**d**) RAVV GPΔmuc-P^2CT(1TD0). (**e-g**) EBOV vaccine-induced NAb responses against (**e**) EBOV Makona, (**f**) SUDV Gulu, and (**g**) BDBV Uganda pseudoviruses. (**h-j**) SUDV vaccine-induced bAb responses against (**h**) SUDV GPΔmuc-WL^2P^4(1TD0), (**i**) EBOV GPΔmuc-WL^2P^4(1TD0), and (**j**) RAVV GPΔmuc-P^2CT(1TD0). (**k-m**) SUDV vaccine-induced NAb responses against (**k**) SUDV Gulu, (**l**) EBOV Makona, and (**m**) BDBV Uganda pseudoviruses. (**n-p**) RAVV vaccine-induced bAb responses against (**n**) RAVV GPΔmuc-P^2CT(1TD0), (**o**) EBOV GPΔmuc-WL^2P^4(1TD0), and (**p**) SUDV GPΔmuc-WL^2P^4(1TD0). (**q**) RAVV vaccine-induced NAb responses against MARV Angola pseudovirus and pseudotyped ebolaviruses using purified IgG and serum, respectively. Notably, EC_{50} titers were derived from serum ELISA against coating antigens, with geometric means labeled on the plots. ID_{50}/IC_{50} titers were derived from pseudovirus neutralization assays,

with geometric means labeled on the plots. The ID_{50}/IC_{50} values were derived by setting % neutralization to be 0.0-100.0%. Color coding indicates the level of ID_{50} values (green to red: low to high neutralization). The data points are shown as the mean ± SD. The data were analyzed using one-way ANOVA, followed by Tukey's multiple comparison *post hoc* test for each timepoint. Statistical significance is indicated as the following: ns (not significant), *$p < 0.05$, **$p < 0.01$, ***$p < 0.001$, and ****$p < 0.0001$. The schematic illustration of the mouse immunization protocol was created with BioRender.com.

Fig. 10. Effect of glycan modification on antibody responses elicited by filovirus vaccines. Schematic illustration of the mouse immunization regimen for glycan-modified EBOV, SUDV, and RAVV vaccines (n = 8 mice/group). The administered dose was 200 µl of antigen/AH + CpG adjuvant mix containing 10 µg of glycan-modified immunogen and 100 µl of adjuvant. Mice were injected at weeks 0, 3, 6 and 9 with an interval of 3 weeks between each immunization via the intraperitoneal route. The immunogenicity of filovirus vaccine antigens was compared between glycan modifications (expressed in the presence of kifunensine [Kif] *vs.* Kif treatment followed by glycan trimming using endo H) and wildtype. (**b**-**d**) Glycan-modified EBOV vaccine-induced bAb responses against EBOV GPΔmuc-WL^2P^4(1TD0). (**e**-**g**) Glycan-modified EBOV vaccine-induced NAb responses against EBOV Makona pseudovirus. (**h**-**j**) Glycan-modified SUDV vaccine-induced bAb responses against SUDV GPΔmuc-WL^2P^4(1TD0). (**k**-**m**) Glycan-modified SUDV vaccine-induced NAb responses against Gulu pseudovirus. (**n**) Glycan-trimmed RAVV vaccine-induced bAb responses against RAVV GPΔmuc-P^2CT(1TD0). (**o**) Glycan-trimmed RAVV vaccine-induced NAb responses against MARV Angola and pseudotyped ebolaviruses, both using purified IgG. EC_{50} titers were derived from serum ELISA against coating antigens, with geometric means labeled on the plots. ID_{50}/IC_{50} titers were derived from the pseudovirus neutralization assays,

with geometric means labeled on the plots. The ID_{50}/IC_{50} values were derived by setting % neutralization to 0.0-100.0%. Color coding indicates the level of IC_{50} values (green to red: low to high neutralization). Of note, the immunogenicity data for wildtype EBOV GPΔmuc trimer/SApNPs, SUDV GPΔmuc trimer, and RAVV GPΔmuc trimer from the prior long-interval immunization study were included for comparison, for which the boost timepoints (W11 and W17) were labeled but not used for the statistical analysis. The data points are shown as the mean ± SD. The data were analyzed using one-way ANOVA, followed by Tukey's multiple comparison *post hoc* test for each timepoint. Statistical significance is indicated as the following: ns (not significant), $*p < 0.05$, $**p < 0.01$, $***p < 0.001$, and $****p < 0.0001$. The schematic illustration of the mouse immunization protocol was created with BioRender.com.

Figure 1

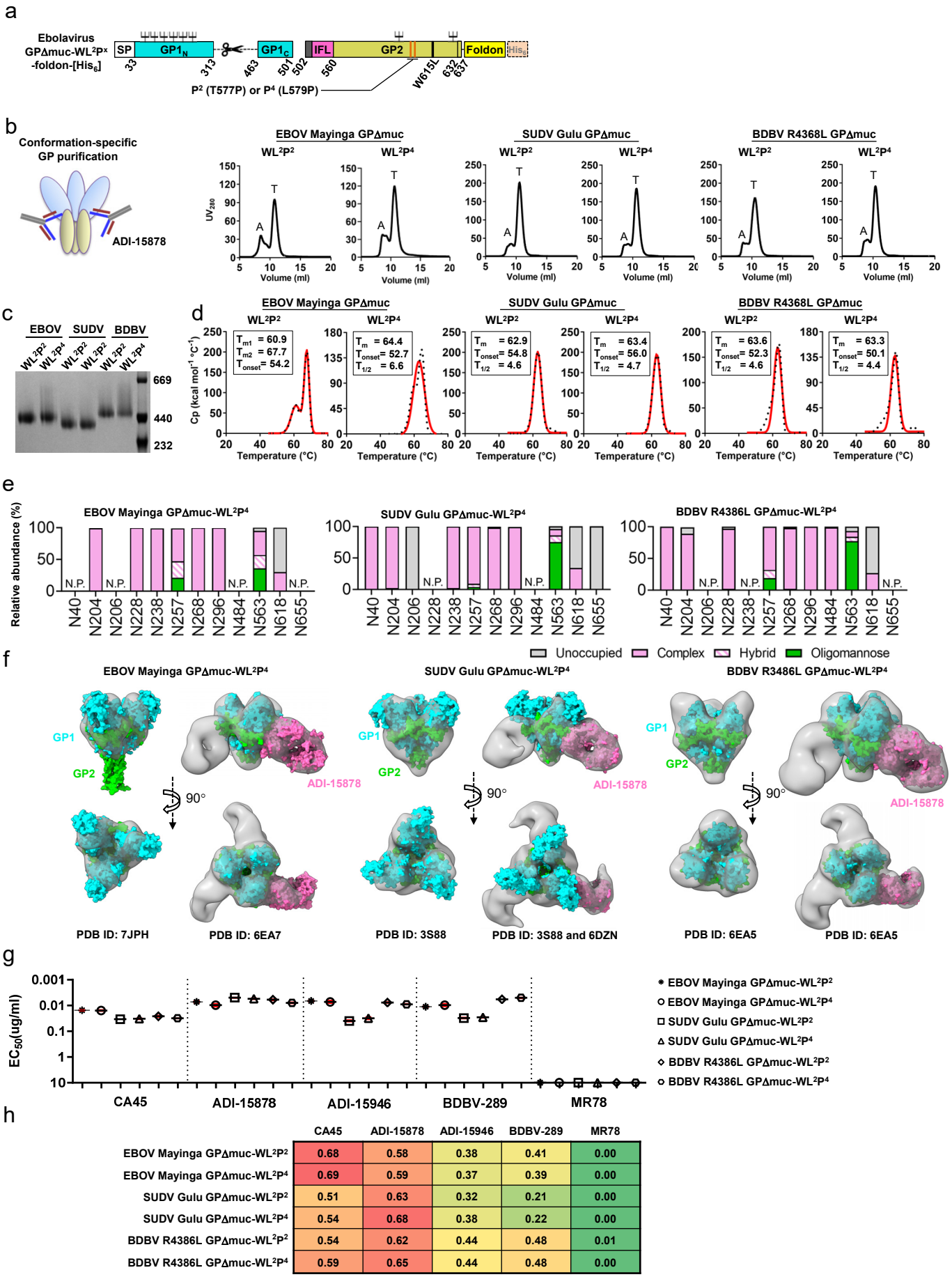

	CA45	ADI-15878	ADI-15946	BDBV-289	MR78
EBOV Mayinga GPΔmuc-WL^{2}P^2	0.68	0.58	0.38	0.41	0.00
EBOV Mayinga GPΔmuc-WL^{2}P^4	0.69	0.59	0.37	0.39	0.00
SUDV Gulu GPΔmuc-WL^{2}P^2	0.51	0.63	0.32	0.21	0.00
SUDV Gulu GPΔmuc-WL^{2}P^4	0.54	0.68	0.38	0.22	0.00
BDBV R4386L GPΔmuc-WL^{2}P^2	0.54	0.62	0.44	0.48	0.01
BDBV R4386L GPΔmuc-WL^{2}P^4	0.59	0.65	0.44	0.48	0.00

Figure 2

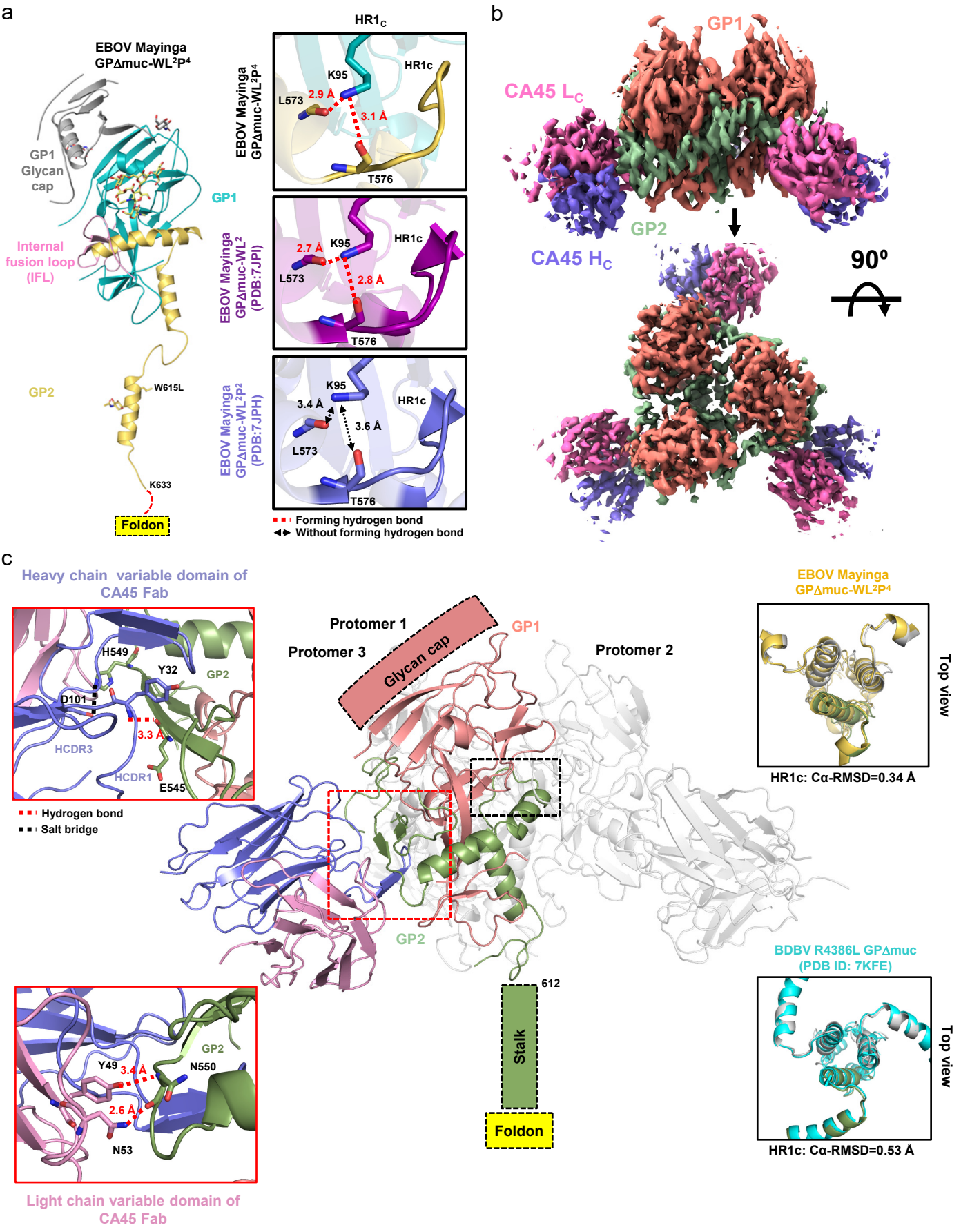

Figure 3

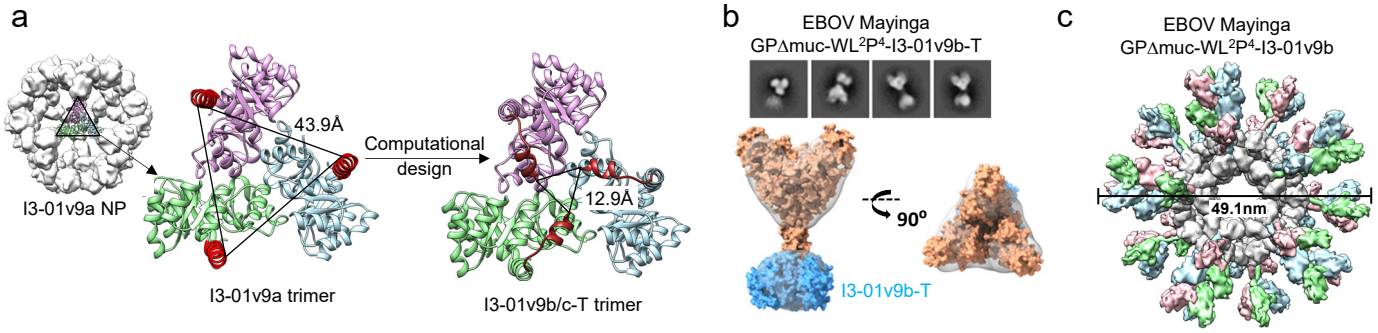

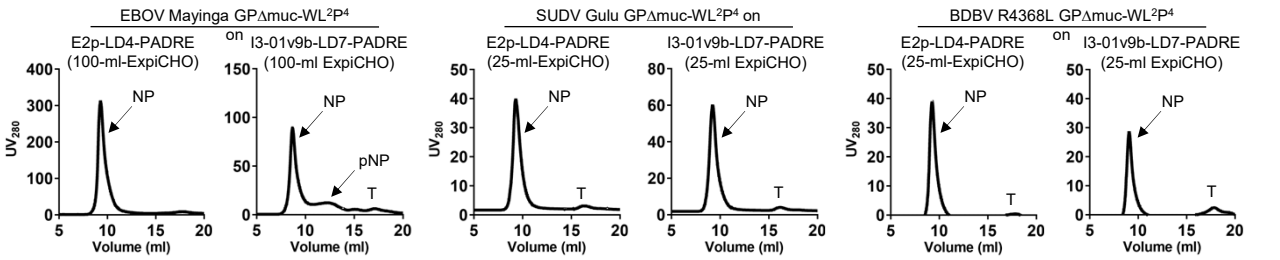

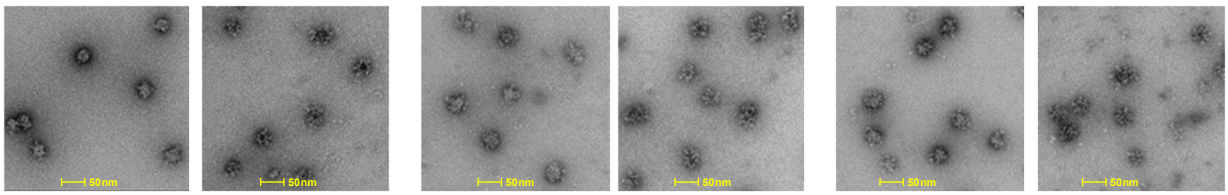

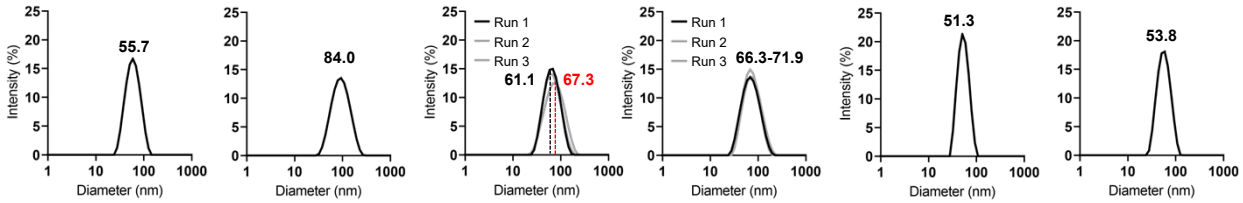

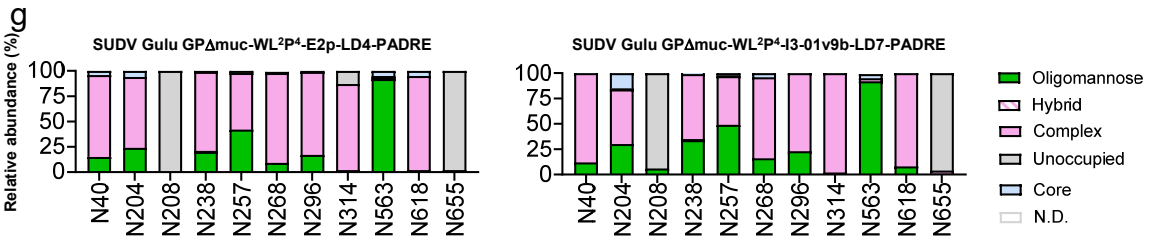

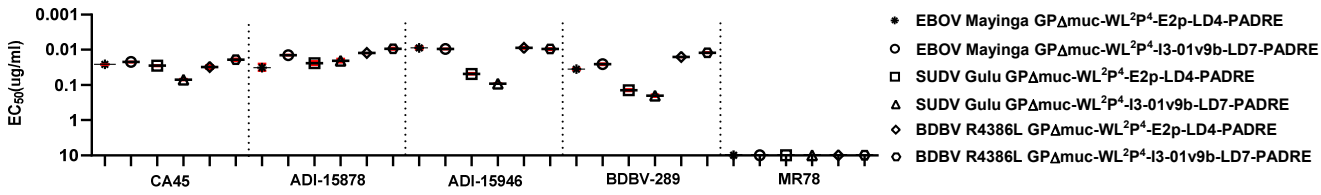

i

	CA45	ADI-15878	ADI-15946	BDBV-289	MR78
EBOV Mayinga GPΔmuc-WL^{2}P^4-E2p-LD4-PADRE	0.71	0.90	0.73	0.79	0.01
EBOV Mayinga GPΔmuc-WL^{2}P^4-I3-01v9b-LD7-PADRE	0.90	0.83	0.66	0.68	0.03
SUDV Gulu GPΔmuc-WL^{2}P^4-E2p-LD4-PADRE	1.37	1.60	1.37	0.51	0.00
SUDV Gulu GPΔmuc-WL^{2}P^4-I3-01v9b-LD7-PADRE	0.72	1.44	1.06	0.39	0.01
BDBV R4386L GPΔmuc-WL^{2}P^4-E2p-LD4-PADRE	0.95	1.68	1.24	2.03	0.01
BDBV R4386L GPΔmuc-WL^{2}P^4-I3-01v9b-LD7-PADRE	0.50	1.21	1.24	0.87	0.00

Figure 4

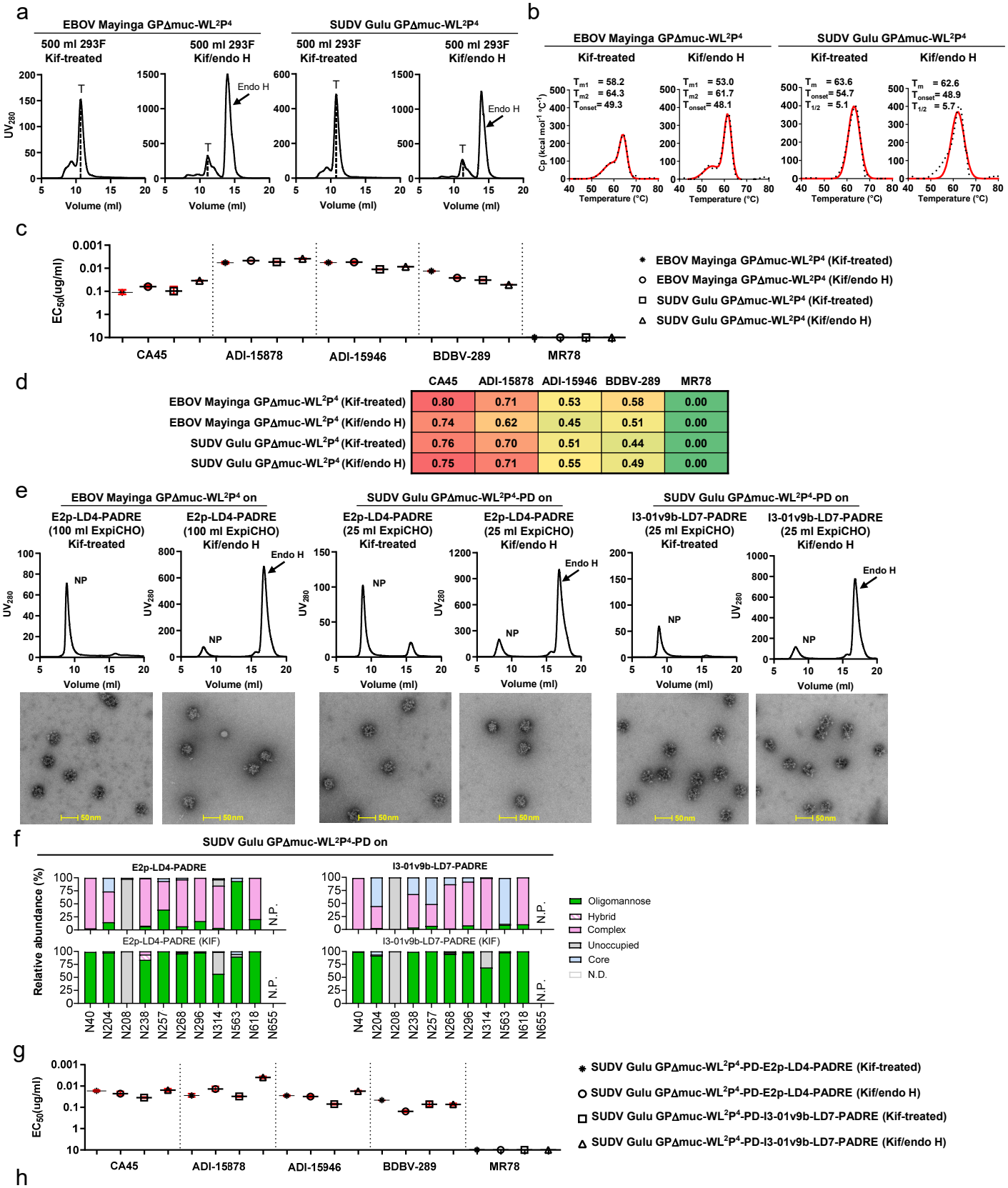

	CA45	ADI-15878	ADI-15946	BDBV-289	MR78
EBOV Mayinga GPΔmuc-WL^{2}P^4 (Kif-treated)	0.80	0.71	0.53	0.58	0.00
EBOV Mayinga GPΔmuc-WL^{2}P^4 (Kif/endo H)	0.74	0.62	0.45	0.51	0.00
SUDV Gulu GPΔmuc-WL^{2}P^4 (Kif-treated)	0.76	0.70	0.51	0.44	0.00
SUDV Gulu GPΔmuc-WL^{2}P^4 (Kif/endo H)	0.75	0.71	0.55	0.49	0.00

	CA45	ADI-15878	ADI-15946	BDBV-289	MR78
SUDV Gulu GPΔmuc-WL^{2}P^4-PD-E2p-LD4-PADRE (Kif-treated)	1.29	1.46	1.44	0.48	0.01
SUDV Gulu GPΔmuc-WL^{2}P^4-PD-E2p-LD4-PADRE (Kif/endo H)	1.63	2.23	1.78	0.58	0.00
SUDV Gulu GPΔmuc-WL^{2}P^4-PD-I3-01v9b-LD7-PADRE (Kif-treated)	0.89	1.43	1.20	0.42	0.01
SUDV Gulu GPΔmuc-WL^{2}P^4-PD-I3-01v9b-LD7-PADRE (Kif/endo H)	1.00	1.60	1.35	0.64	0.00

Figure 5

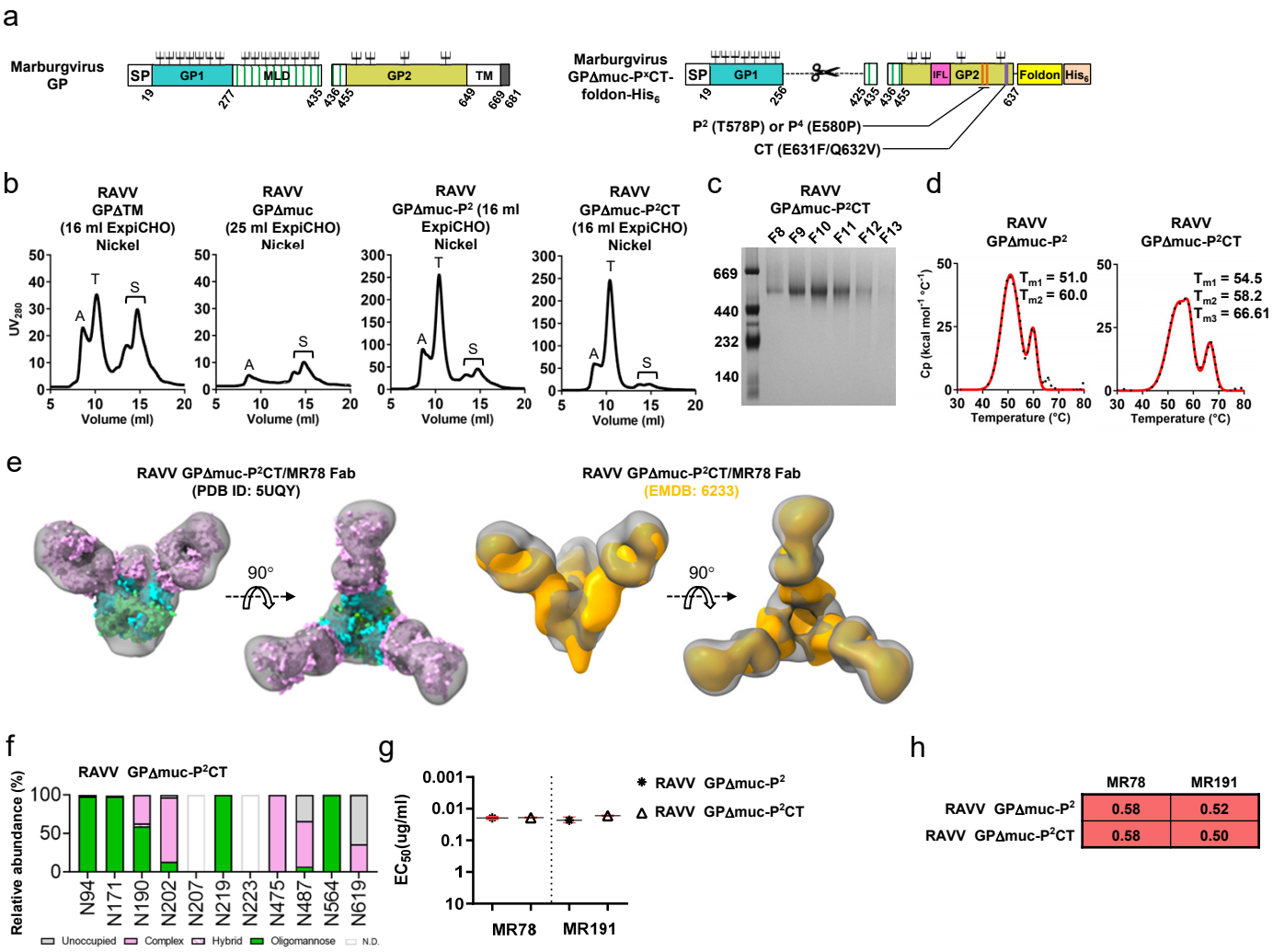

Figure 6

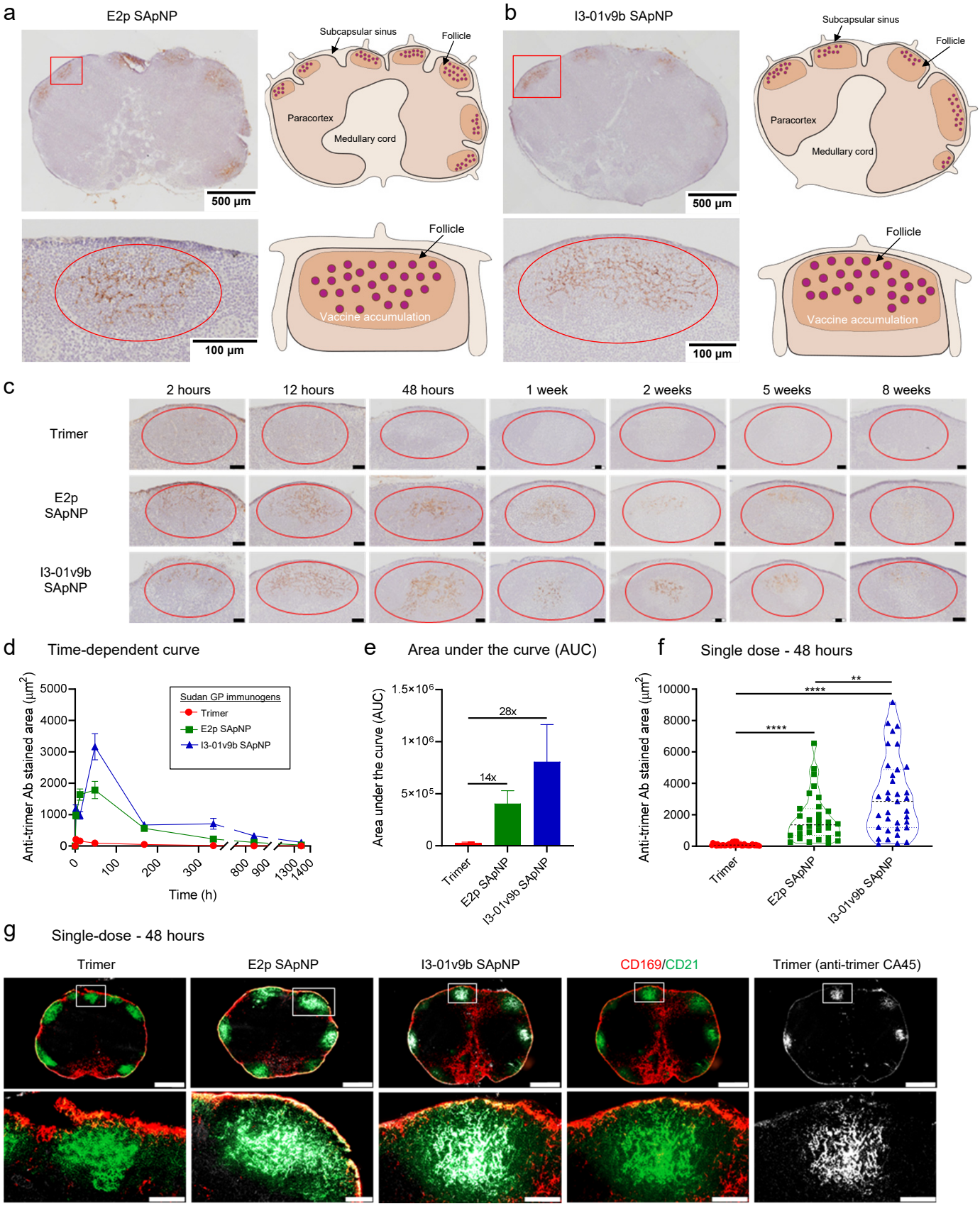

Figure 7

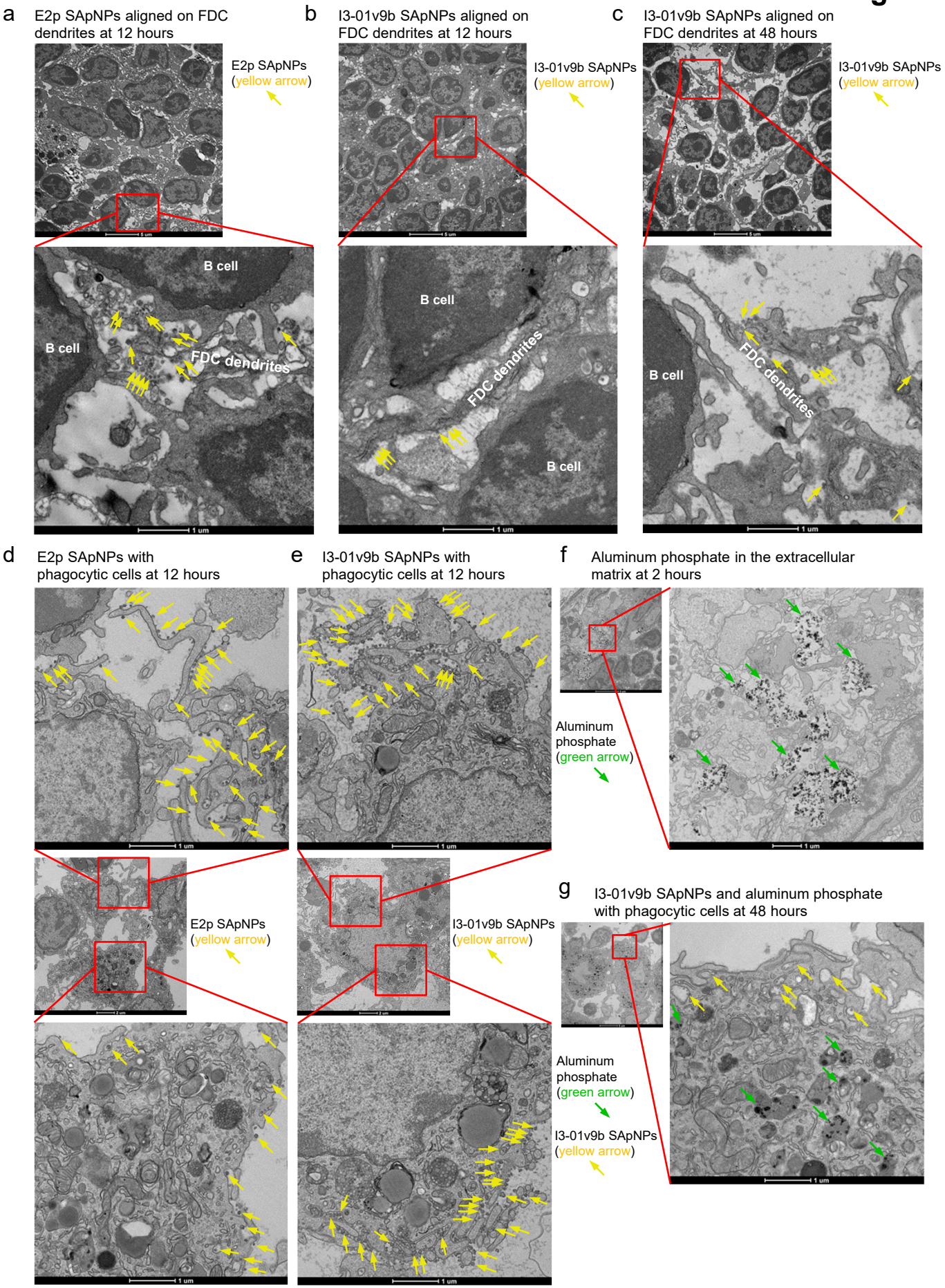

Figure 8

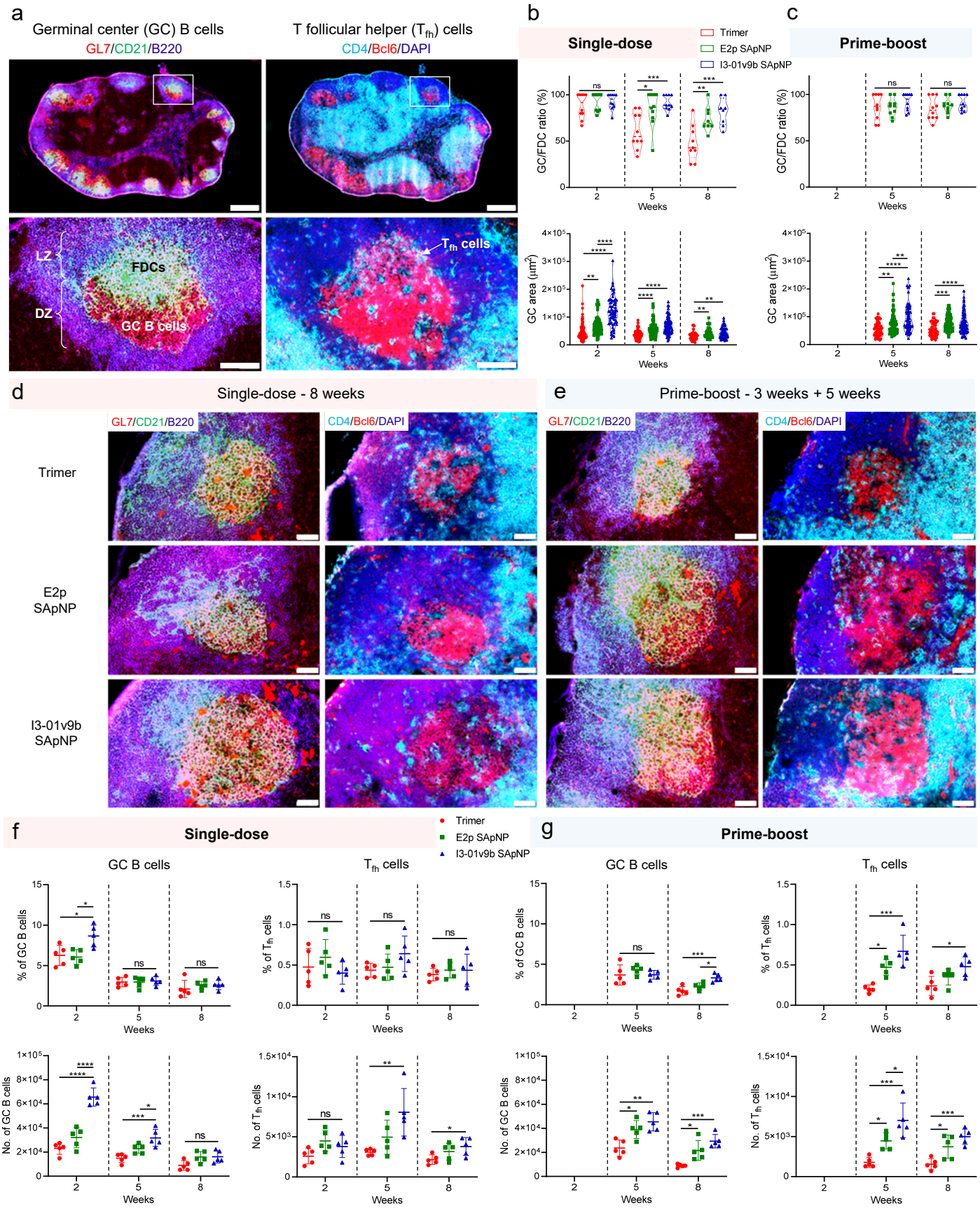

Figure 9

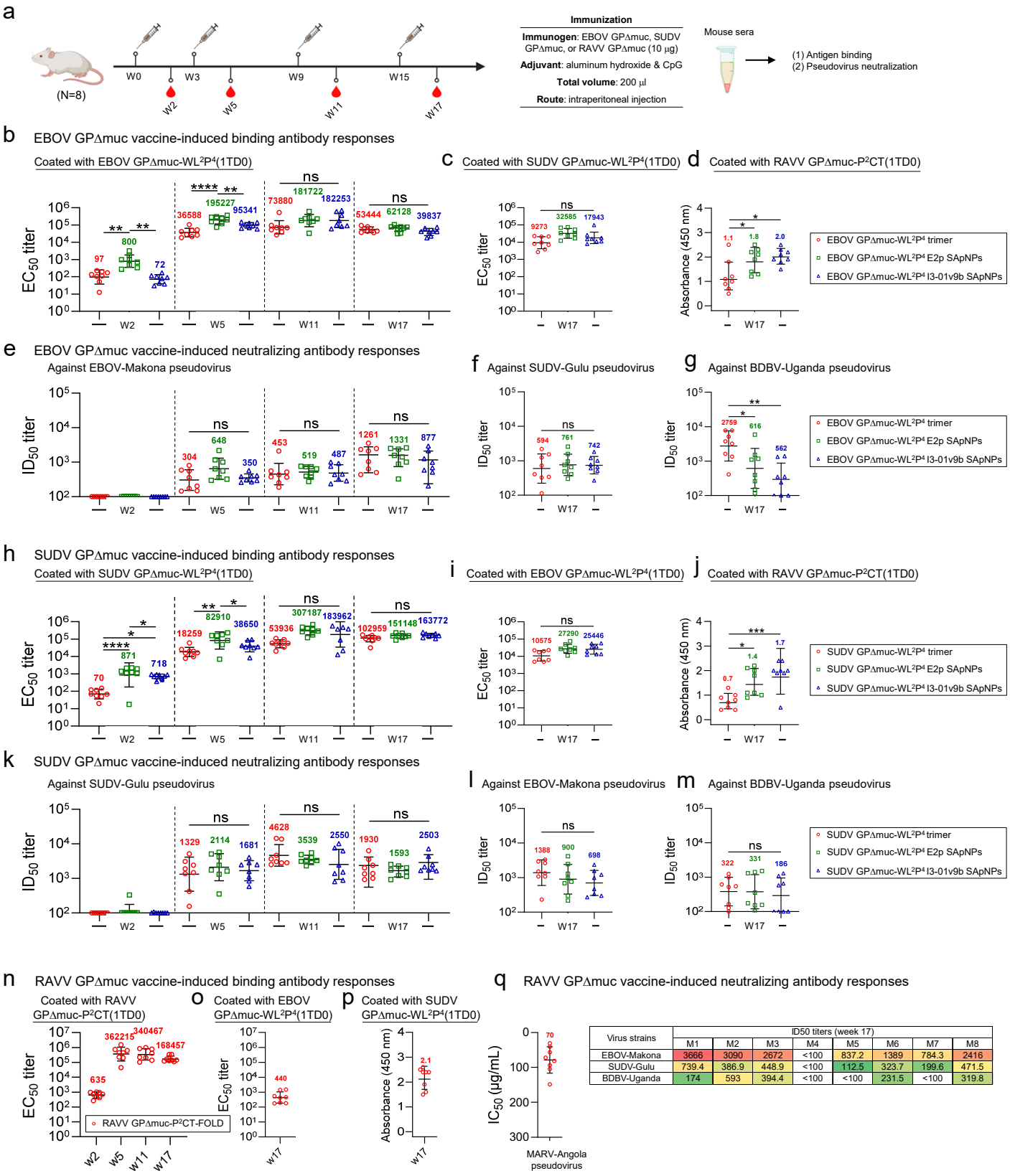

Virus strains	ID50 titers (week 17)							
	M1	M2	M3	M4	M5	M6	M7	M8
EBOV-Makona	3666	3090	2672	<100	837.2	1389	784.3	2416
SUDV-Gulu	739.4	386.9	448.9	<100	112.5	323.7	199.6	471.5
BDBV-Uganda	174	593	394.4	<100	<100	231.5	<100	319.8

Figure 10

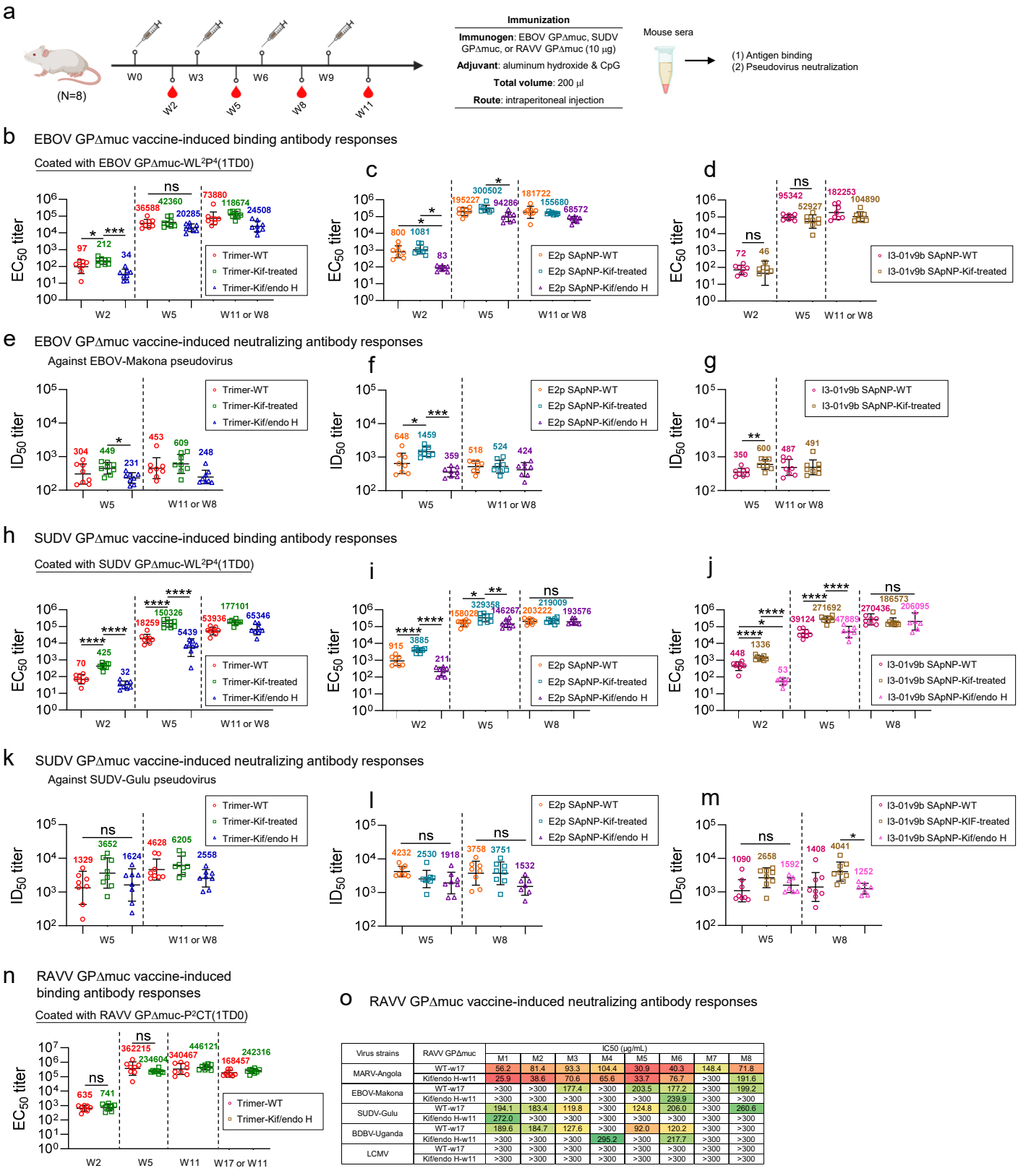

Virus strains	RAVV GPΔmuc	IC50 (μg/mL)							
		M1	M2	M3	M4	M5	M6	M7	M8
MARV-Angola	WT-w17	56.2	81.4	93.3	104.4	30.9	40.3	148.4	71.8
	Kif/endo H-w11	25.9	38.6	70.6	65.6	33.7	76.7	>300	191.6
EBOV-Makona	WT-w17	>300	>300	177.4	>300	203.5	177.2	>300	199.2
	Kif/endo H-w11	>300	>300	>300	>300	>300	239.9	>300	>300
SUDV-Gulu	WT-w17	194.1	183.4	119.8	>300	124.8	206.0	>300	260.6
	Kif/endo H-w11	272.0	>300	>300	>300	>300	>300	>300	>300
BDBV-Uganda	WT-w17	189.6	184.7	127.6	>300	92.0	120.2	>300	>300
	Kif/endo H-w11	>300	>300	>300	295.2	>300	217.7	>300	>300
LCMV	WT-w17	>300	>300	>300	>300	>300	>300	>300	>300
	Kif/endo H-w11	>300	>300	>300	>300	>300	>300	>300	>300

Fig. S1

a

>EBOV Mayinga GPΔmuc-WL²P²-foldon-[His₆]

MGVTGILQLPRDRFKRTSFFLWVIILFQRTFSIPLGVIHNSALQVSDVDKLVCRDKLSSTNQLRSVGLNLEGNGVATDVPSATKRWGFRSGVPPKVVNYEAGEWAENC
YNLEIKKPDGSECLPAAPDGIRGFPRCRYVHKVSGTGPCAGDFAFHKEGAFFLYDRLASTVIYRGTTFAEGVVAFLILPQAKKDFFSSHPLREPVNATEDPSSGYYST
TIRYQATGFGTNETEYLFEVDNLTYVQLESRFTPQFLLQLNETIYTSGKRSNTTGKLIWKVNPEIDTTIGEWAFWETKKNLTRKIRSEELSFTVVSTHHQDTGEESAS
SGKLGLITNTIAGVAGLITGGRRTRREAIVNAQPKCNPNLHYWTTQDEGAAIGLAWIPYFGPAAEGIYIEGLMHNQDGLICGLRQLANETTQALQLFLRATPELRTFS
ILNRKAIDFLLQRWGGTCHILGPDCCIEPHDLTKNITDKIDQIIHDFVDKTLPDASGYIPEAPRDGQAYVRKDGEWVLLSTFL[GSHHHHHH]

>EBOV Mayinga GPΔmuc-WL²P⁴-foldon-[His₆]

MGVTGILQLPRDRFKRTSFFLWVIILFQRTFSIPLGVIHNSALQVSDVDKLVCRDKLSSTNQLRSVGLNLEGNGVATDVPSATKRWGFRSGVPPKVVNYEAGEWAENC
YNLEIKKPDGSECLPAAPDGIRGFPRCRYVHKVSGTGPCAGDFAFHKEGAFFLYDRLASTVIYRGTTFAEGVVAFLILPQAKKDFFSSHPLREPVNATEDPSSGYYST
TIRYQATGFGTNETEYLFEVDNLTYVQLESRFTPQFLLQLNETIYTSGKRSNTTGKLIWKVNPEIDTTIGEWAFWETKKNLTRKIRSEELSFTVVSTHHQDTGEESAS
SGKLGLITNTIAGVAGLITGGRRTRREAIVNAQPKCNPNLHYWTTQDEGAAIGLAWIPYFGPAAEGIYIEGLMHNQDGLICGLRQLANETTQALQLFLRATTEPRTFS
ILNRKAIDFLLQRWGGTCHILGPDCCIEPHDLTKNITDKIDQIIHDFVDKTLPDASGYIPEAPRDGQAYVRKDGEWVLLSTFL[GSHHHHHH]

>SUDV Gulu GPΔmuc-WL²P²-foldon-[His₆]

MGILPSPGMPALLSLVSLLSVLLMGCVAEMPLGVVTNSTLEVTEIDQLVCKDHLASTDQLKSVGLNLEGSGVSTDIPSATKRWGFRSGVPPKVVSYEAGEWAENCYNL
EIKKPDGSECLPPPPDGVRGFPRCRYVHKAQGTGPCPGDYAFHKDGAFFLYDRLASTVIYRGVNFAEGVIAFLILAKPKETFLQSPPIREAVNYTENTSSYYATSYLE
YEIENFGAQHSTTLFKIDNNTFVRLDRPHTPQFLFQLNDTIHLHQQLSNTTGRLIWTLDANINADIGEWAFWENKKNLSEQLRGEELSFEALSLNETEDDDAASSSTS
NGLITSTVTGILGSLGLRKRSRRQTNTKATGKCNPNLHYWTAQEQHNAAGIAWIPYFGPGAEGIYTEGLMHNQNALVCGLRQLANETTQALQLFLRATPELRTYTILN
RKAIDFLLRRWGGTCRILGPDCCIEPHDLTKNITDKINQIIHDFIDNPLPNASGYIPEAPRDGQAYVRKDGEWVLLSTFL[GSHHHHHH]

>SUDV Gulu GPΔmuc-WL²P⁴-foldon-[His₆]

MGILPSPGMPALLSLVSLLSVLLMGCVAEMPLGVVTNSTLEVTEIDQLVCKDHLASTDQLKSVGLNLEGSGVSTDIPSATKRWGFRSGVPPKVVSYEAGEWAENCYNL
EIKKPDGSECLPPPPDGVRGFPRCRYVHKAQGTGPCPGDYAFHKDGAFFLYDRLASTVIYRGVNFAEGVIAFLILAKPKETFLQSPPIREAVNYTENTSSYYATSYLE
YEIENFGAQHSTTLFKIDNNTFVRLDRPHTPQFLFQLNDTIHLHQQLSNTTGRLIWTLDANINADIGEWAFWENKKNLSEQLRGEELSFEALSLNETEDDDAASSSTS
NGLITSTVTGILGSLGLRKRSRRQTNTKATGKCNPNLHYWTAQEQHNAAGIAWIPYFGPGAEGIYTEGLMHNQNALVCGLRQLANETTQALQLFLRATTEPRTYTILN
RKAIDFLLRRWGGTCRILGPDCCIEPHDLTKNITDKINQIIHDFIDNPLPNASGYIPEAPRDGQAYVRKDGEWVLLSTFL[GSHHHHHH]

>BDBV R4386L GPΔmuc-WL²P²-foldon-[His₆]

MGILPSPGMPALLSLVSLLSVLLMGCVAEIPLGVVHNNTLQVSDIDKLVCRDKLSSTSQLKSVGLNLEGNGVATDVPTATKRWGFRAGVPPKVVNYEAGEWAENCYNL
DIKKADGSECLPEAPEGVRGFPRCRYVHKVSGTGPCPEGYAFHKEGAFFLYDRLASTIIYRSTTFSEGVVAFLILPETKKDFFQSPPLHEPANMTTDPSSYYHTVTLN
YVADNFGTNMTNFLFQVDHLTYVQLEPRFTPQFLVQLNETIYTNGRRSNTTGTLIWKVNPTVDTGVGEWAFWENKKNFTKTLSSEELSVIFVPRAQDPGSNDISESTE
PGPLTNTTRGAANLLTGSRRTRREITLRTQAKCNPNLHYWTTQDEGAAIGLAWIPYFGPAAEGIYTEGIMHNQNGLICGLRQLANETTQALQLFLRATPELRTFSILN
RKAIDFLLQRWGGTCHILGPDCCIEPHDLTKNITDKIDQIIHDFIDKPLPDASGYIPEAPRDGQAYVRKDGEWVLLSTFL[GSHHHHHH]

>BDBV R4386L GPΔmuc-WL²P⁴-foldon-[His₆]

MGILPSPGMPALLSLVSLLSVLLMGCVAEIPLGVVHNNTLQVSDIDKLVCRDKLSSTSQLKSVGLNLEGNGVATDVPTATKRWGFRAGVPPKVVNYEAGEWAENCYNL
DIKKADGSECLPEAPEGVRGFPRCRYVHKVSGTGPCPEGYAFHKEGAFFLYDRLASTIIYRSTTFSEGVVAFLILPETKKDFFQSPPLHEPANMTTDPSSYYHTVTLN
YVADNFGTNMTNFLFQVDHLTYVQLEPRFTPQFLVQLNETIYTNGRRSNTTGTLIWKVNPTVDTGVGEWAFWENKKNFTKTLSSEELSVIFVPRAQDPGSNDISESTE
PGPLTNTTRGAANLLTGSRRTRREITLRTQAKCNPNLHYWTTQDEGAAIGLAWIPYFGPAAEGIYTEGIMHNQNGLICGLRQLANETTQALQLFLRATTEPRTFSILN
RKAIDFLLQRWGGTCHILGPDCCIEPHDLTKNITDKIDQIIHDFIDKPLPDASGYIPEAPRDGQAYVRKDGEWVLLSTFL[GSHHHHHH]

b **SEC profile of 6 ebolavirus GPΔmuc constructs expressed in HEK293F cells and purified by Nickel and IAC columns**

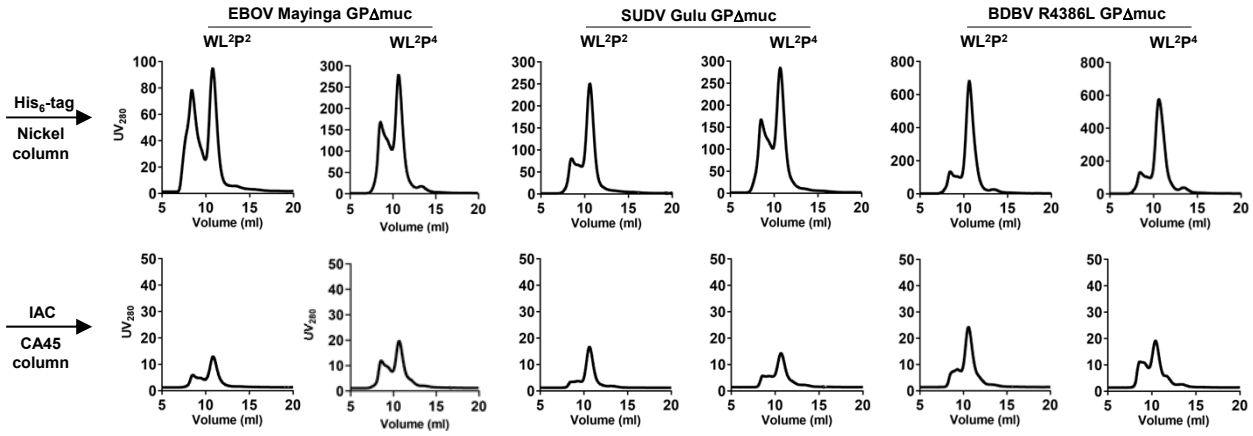

Fig. S1

C

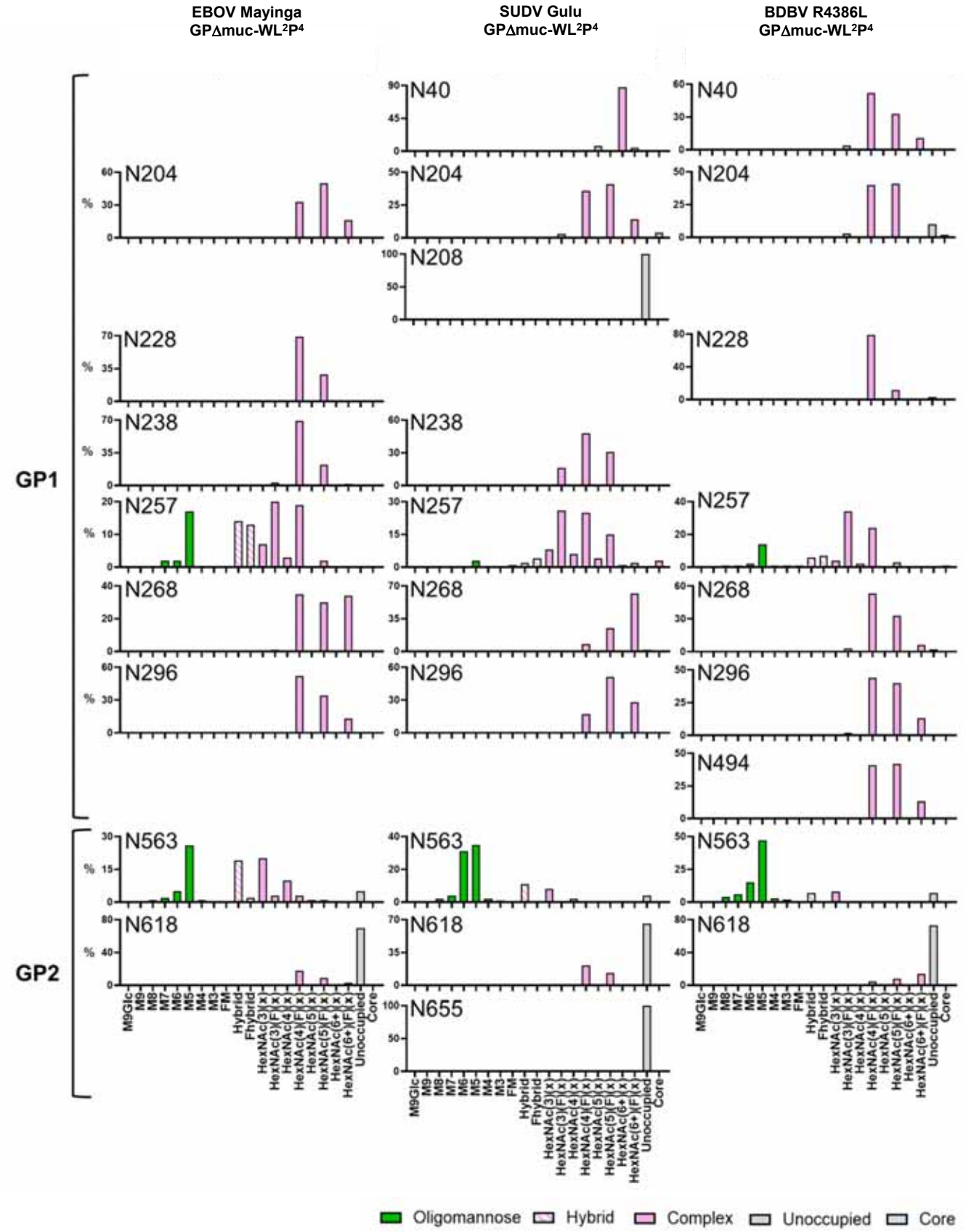

Fig. S1

d Flowchart of image processing and model building protocol

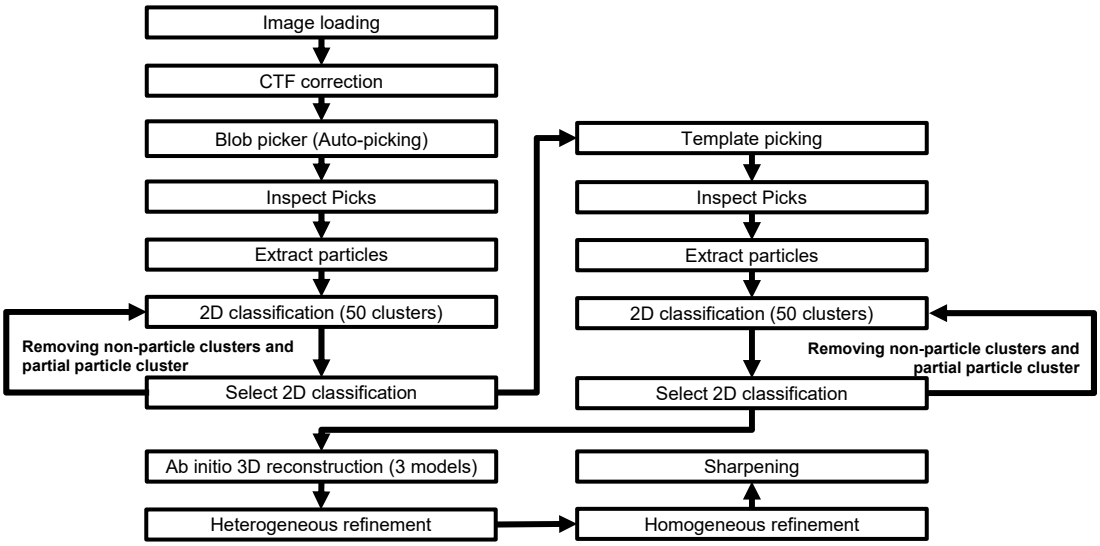

e **Selected 2D classifications for 3D modeling of EBOV Mayinga GPΔmuc**

GPΔmuc-WL²P⁴ trimer/ADI-15878 Fab complex

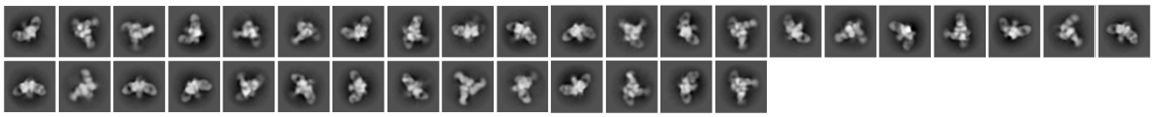

GPΔmuc-WL²P⁴ trimer

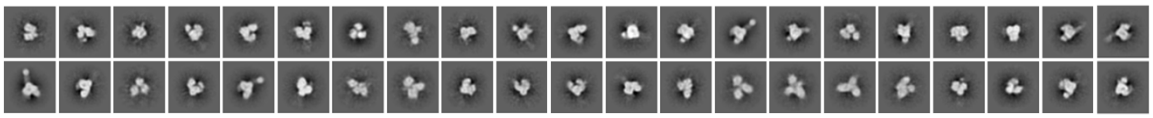

f **Selected 2D classifications for 3D modeling of SUDV Gulu GPΔmuc**

GPΔmuc-WL²P⁴ trimer/ADI-15878 Fab complex

GPΔmuc-WL²P⁴ trimer

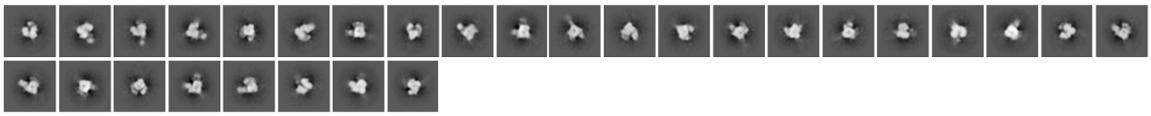

g **Selected 2D classifications for 3D modeling of BDBV R3486L GPΔmuc**

GPΔmuc-WL²P⁴ trimer/ADI-15878 Fab complex

GPΔmuc-WL²P⁴ trimer

Fig. S1

h ELISA analysis of 6 rationally designed ebolavirus GPΔmuc trimers binding to 5 filovirus NAbs

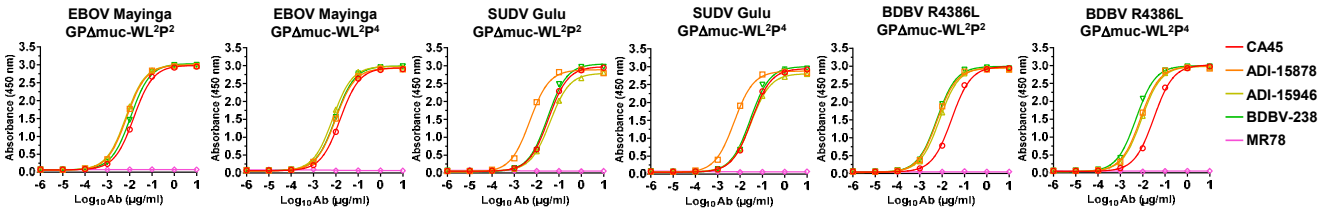

EBOV Mayinga GPΔmuc-WL^{2}P^2									
CA45		ADI-15878		ADI-15946		BDBV-289		MR78	
EC50	STD	EC50	STD	EC50	STD	EC50	STD	EC50	STD
0.01520	0.00023	0.00727	0.00072	0.00669	0.00017	0.01109	0.00029	N.D.	N.D.

EBOV Mayinga GPΔmuc-WL^{2}P^4									
CA45		ADI-15878		ADI-15946		BDBV-289		MR78	
EC50	STD	EC50	STD	EC50	STD	EC50	STD	EC50	STD
0.015639	0.000587	0.009683	0.001136	0.007233	0.000747	0.009632	0.00102	N.D.	N.D.

SUDV Gulu GPΔmuc-WL^{2}P^2									
CA45		ADI-15878		ADI-15946		BDBV-289		MR78	
EC50	STD	EC50	STD	EC50	STD	EC50	STD	EC50	STD
0.0338	2.83E-05	0.004959	7.07E-06	0.039574	0.002213	0.030734	0.000834	N.D.	N.D.

SUDV Gulu GPΔmuc-WL^{2}P^4									
CA45		ADI-15878		ADI-15946		BDBV-289		MR78	
EC50	STD	EC50	STD	EC50	STD	EC50	STD	EC50	STD
0.032764	0.001209	0.005461	0.000156	0.031179	0.002638	0.028805	0.000792	N.D.	N.D.

BDBV R4386L GPΔmuc-WL^{2}P^2									
CA45		ADI-15878		ADI-15946		BDBV-289		MR78	
EC50	STD	EC50	STD	EC50	STD	EC50	STD	EC50	STD
0.026339	0.001499	0.005969	0.000224	0.007626	0.000158	0.005773	3.39E-05	N.D.	N.D.

BDBV R4386L GPΔmuc-WL^{2}P^4									
CA45		ADI-15878		ADI-15946		BDBV-289		MR78	
EC50	STD	EC50	STD	EC50	STD	EC50	STD	EC50	STD
0.031360	0.000170	0.007866	0.000318	0.008934	0.000208	0.005026	0.000132	N.D.	N.D.

i BLI analysis of 6 rationally designed ebolavirus GPΔmuc trimers binding to 5 filovirus NAbs

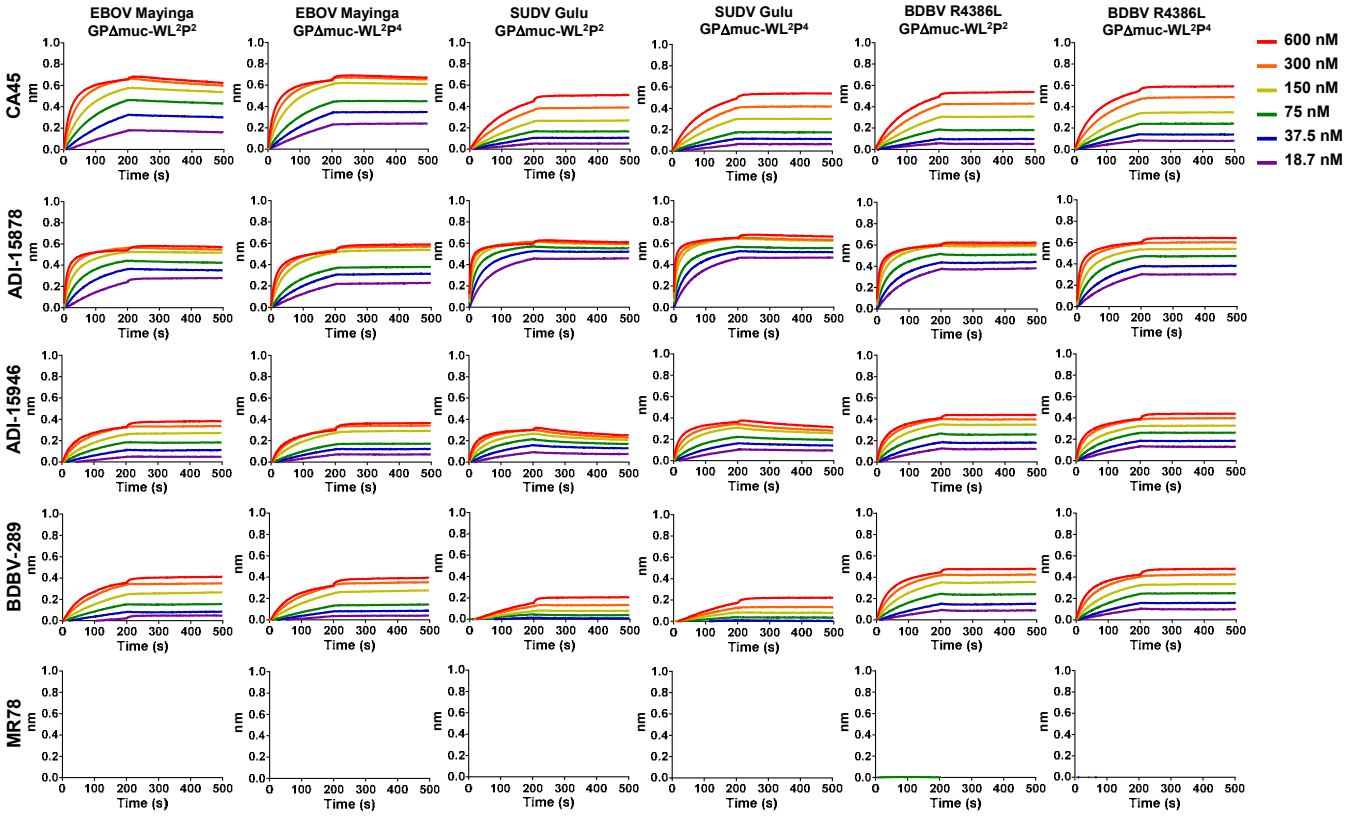

***K_D* values for 6 rationally designed ebolavirus GPΔmuc trimers binding to 5 filovirus NAbs (nM) [a]**

	CA45	ADI-15878	ADI-15946	BDBV-289	MR78
EBOV Mayinga GPΔmuc-WL^{2}P^2	2.62	<1.0E-3	<1.0E-3	<1.0E-3	— [b]
EBOV Mayinga GPΔmuc-WL^{2}P^4	<1.0E-3	<1.0E-3	<1.0E-3	<1.0E-3	— [b]
SUDV Gulu GPΔmuc-WL^{2}P^2	<1.0E-3	<1.0E-3	7.22	<1.0E-3	— [b]
SUDV Gulu GPΔmuc-WL^{2}P^4	<1.0E-3	<1.0E-3	4.89	<1.0E-3	— [b]
BDBV R4386L GPΔmuc-WL^{2}P^2	<1.0E-3	<1.0E-3	<1.0E-3	<1.0E-3	— [b]
BDBV R4386L GPΔmuc-WL^{2}P^4	<1.0E-3	<1.0E-3	<1.0E-3	<1.0E-3	— [b]

[a] K_D values were derived from biolayer interferometry (BLI) using the binding equations describing a 1:1 interaction.
[b] "—" indicates cases where the peak signal value at the highest ebolavirus antigen concentration is 0.2 or lower.

Fig. S1. Construct design and in vitro characterization of ebolavirus GPΔmuc trimers. (**a**) Amino acid sequences of EBOV Mayinga , SUDV Gulu, and BDBV R3486L GPΔmuc-WL^{2}P^x-foldon-[His$_6$] constructs containing P^2 and P^4 mutations. Signal peptide, GP, restriction site (AS), foldon, linker (GS), and His$_6$ tag are highlighted in yellow, grey, green, orange, pink, and teal, respectively. The WL^{2}P^x mutations are colored in red. Notably, foldon is a C-terminal trimerization motif used in all ebolavirus GPΔmuc constructs and therefore will not be included in the construct names (except here in the sequence definition) to avoid redundancy. The GS linker and His$_6$ tag are shown in [ ] to indicate that they are only included in a set of GPΔmuc constructs generated for testing the Nickel purification method. (**b**) SEC profiles of EBOV Mayinga , SUDV Gulu, and BDBV R3486L GPΔmuc produced in 165 ml HEK293F cells and purified using either a Nickel column or a CA45 antibody column. (**c**) Compositional site-specific glycan analysis of three ebolavirus GPΔmuc-WL^{2}P^4 trimers. The graphs summarize quantitative mass spectrometric analysis of the glycan population present at individual N-linked glycosylation sites simplified into categories of glycans. The oligomannose-type glycan series (M9 to M5; Man$_9$GlcNAc$_2$ to Man$_5$GlcNAc$_2$) is colored green, afucosylated and fucosylated hybrid-type glycans (hybrid and F hybrid) are dashed pink, and complex glycans are grouped according to the number of antennae and presence of core fucosylation and are colored pink. Unoccupancy of an N-linked glycan site is represented in gray. Glycan sites that could not be determined are denoted as “N.D.”. (**d**) Flowchart of image processing, 2D classification, and 3D reconstruction of negative stain EM (nsEM) data obtained for EBOV, SUDV, and BDBV GPΔmuc trimers and their complexes with ADI-15878 Fab using CryoSPARC. (**e**)-(**f**) Representative 2D classification images of EBOV, SUDV, and BDBV GPΔmuc-WL^{2}P^4 trimers and their complexes with ADI-15878 Fab. (**g**) ELISA analysis of EBOV, SUDV, and BDBV GPΔmuc trimers binding to 5 filovirus NAbs in the IgG form. Briefly, each well was coated with 0.1 μg of the appropriate antigen, and IgG was diluted in a 10-fold dilution series from a starting concentration of 10 μg/ml for all tested antibodies. Error bars represent the difference between these duplicate values at each concentration tested for each sample. (**h**) BLI analysis of EBOV, SUDV, and BDBV GPΔmuc trimers binding to 5 filovirus NAbs in the IgG form. Sensorgrams were obtained from an Octet RED96 instrument using the AHC biosensor. A two-fold concentration gradient of antigen, starting at 600 nM, was used in a dilution series of six. K_D values derived from a 1:1 fitting model are summarized in a table.

Fig. S2

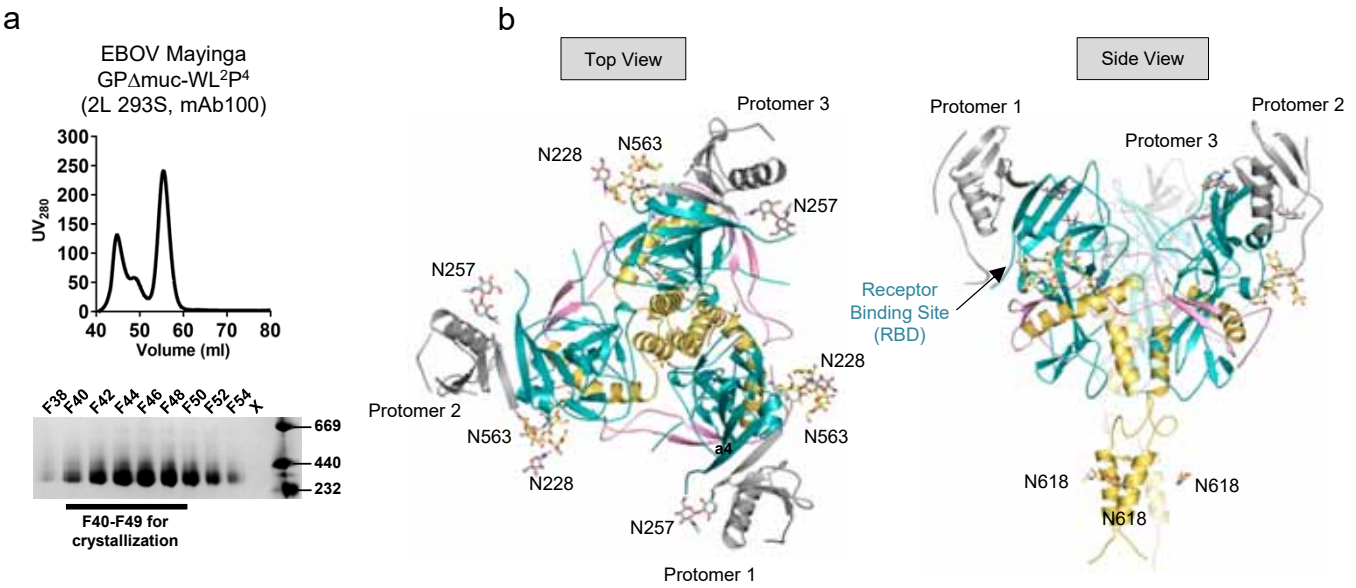

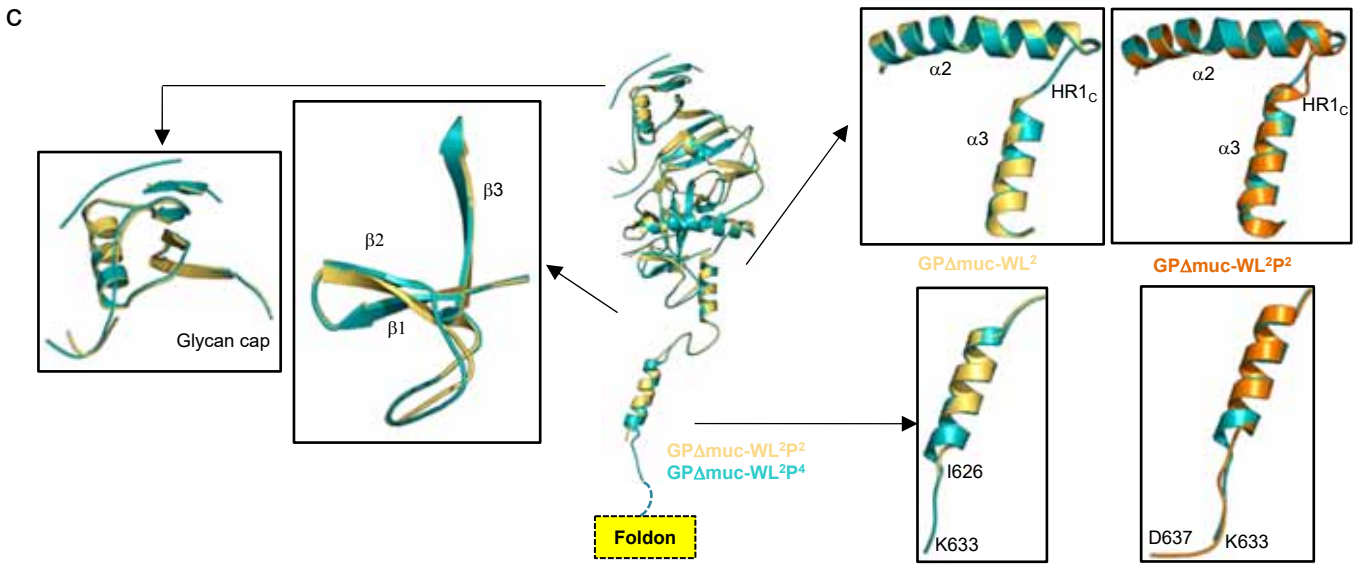

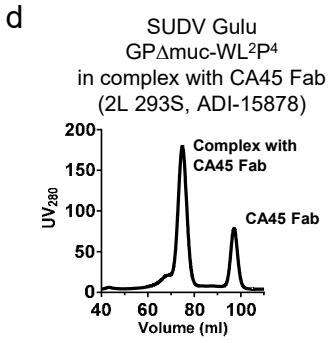

Fig. S2

e

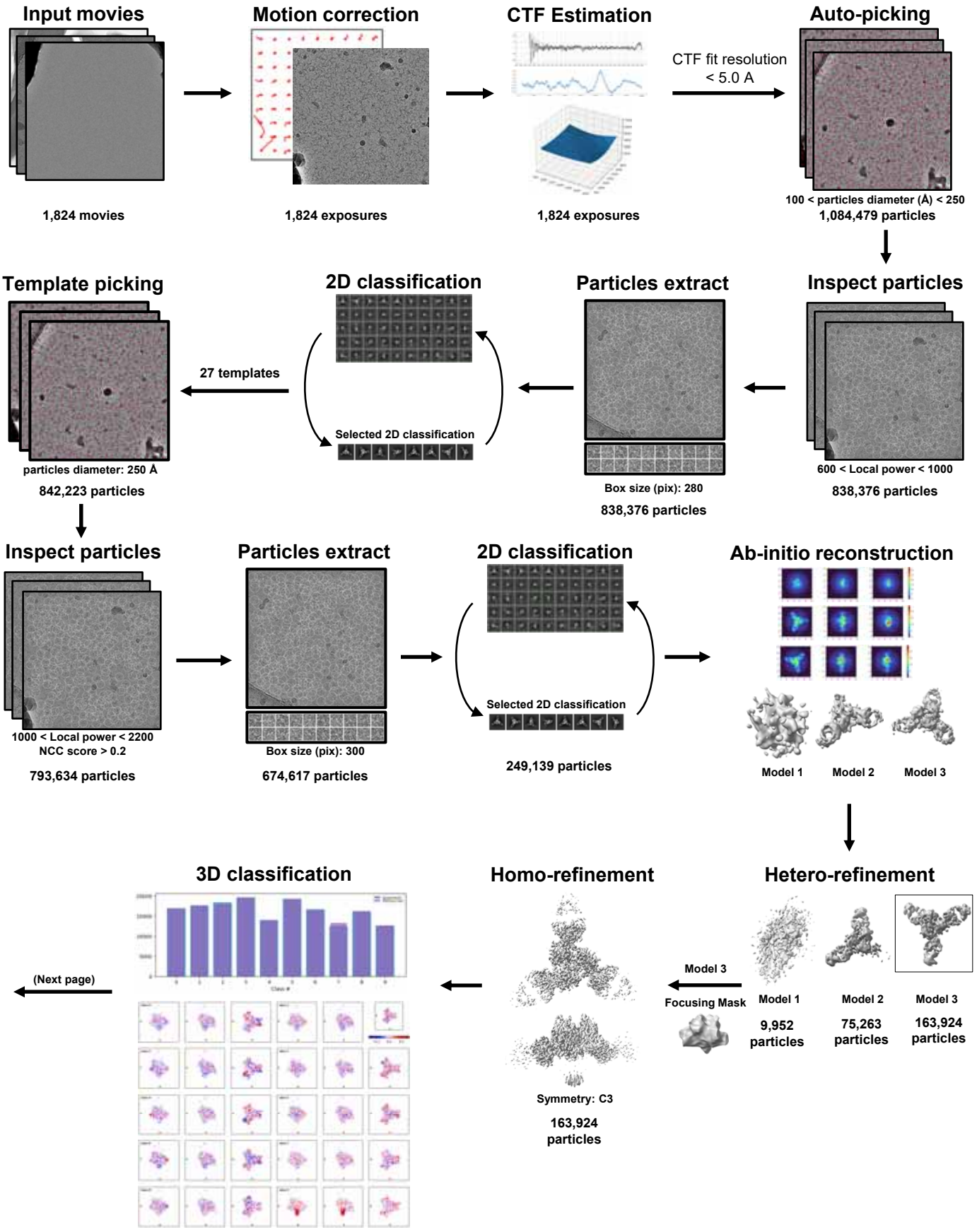

Fig. S2

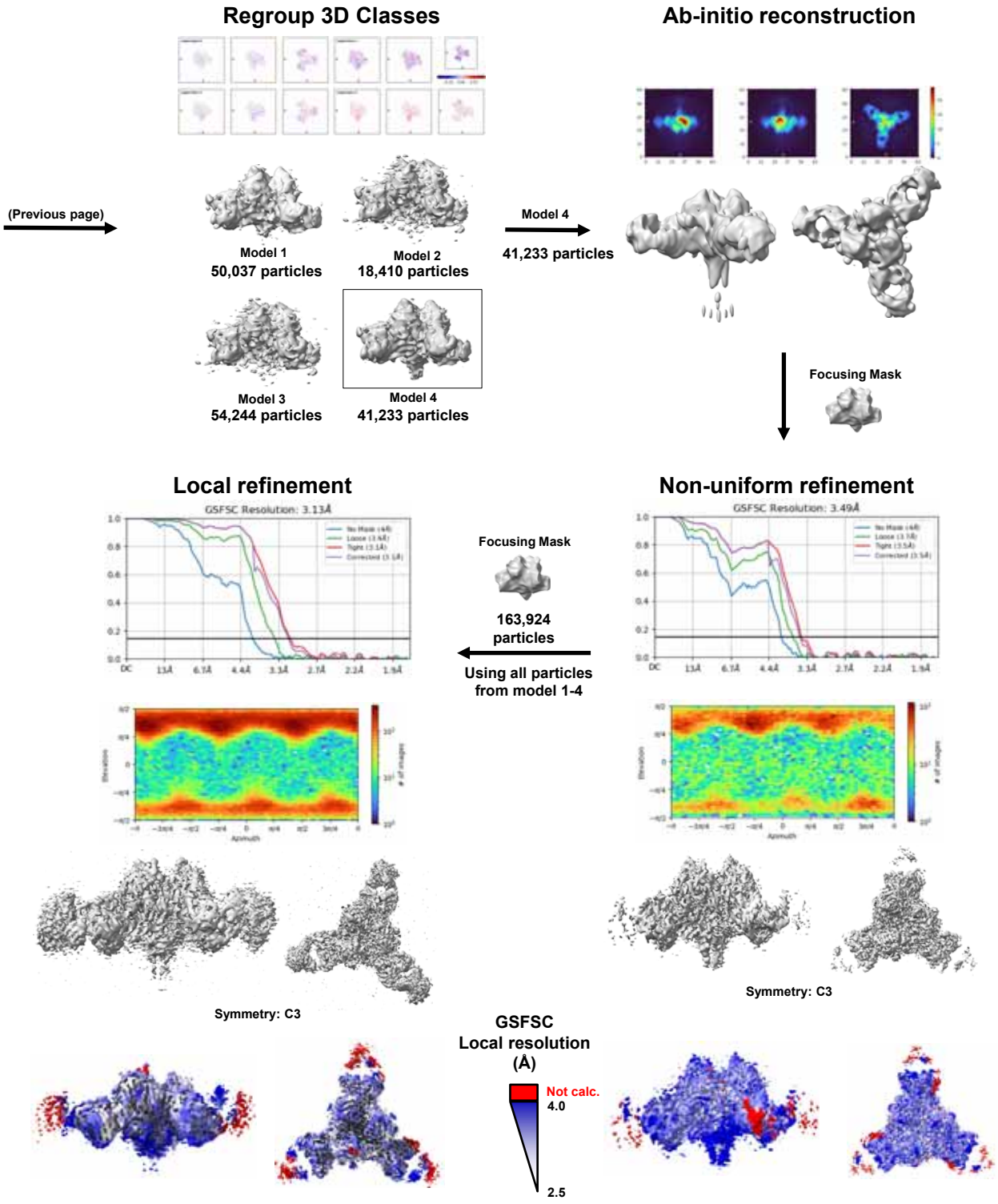

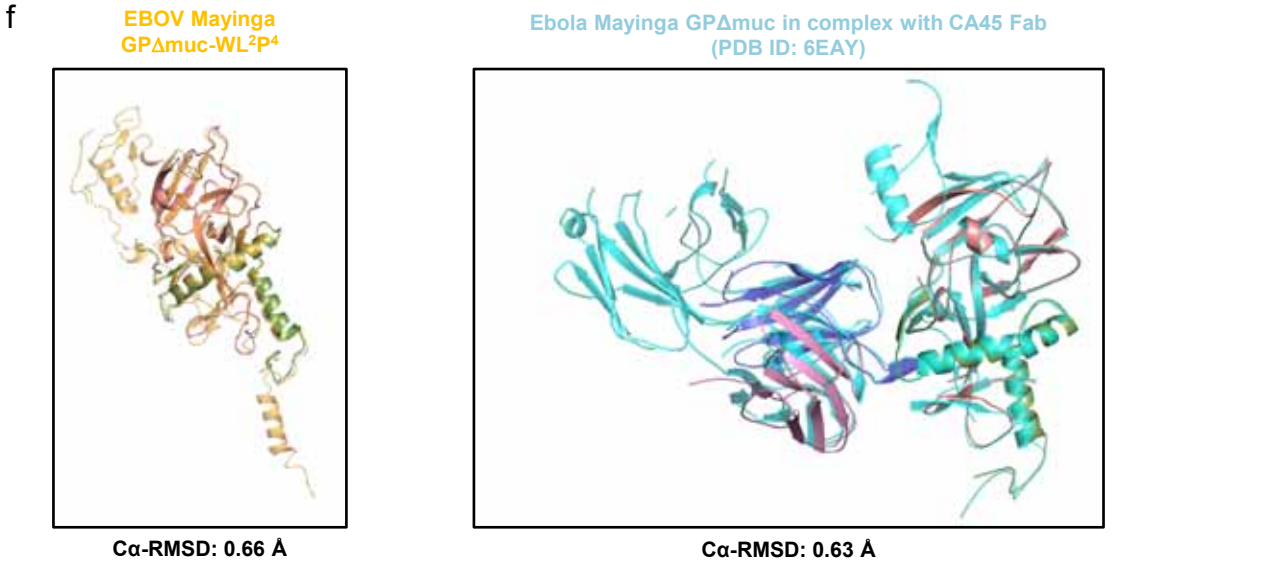

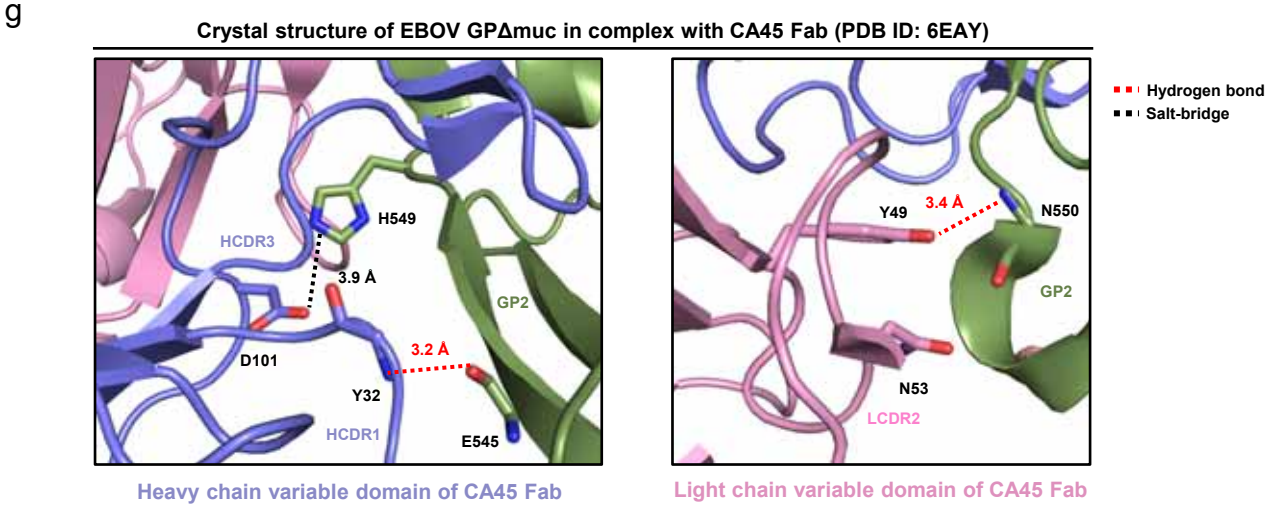

Fig. S2. Structural analysis for EBOV GPΔmuc-WL²P⁴ trimer and CA45 Fab-bound SUDV GPΔmuc-WL²P⁴ trimer. (**a**) SEC profile of EBOV GPΔmuc-WL²P⁴ trimer expressed in 2L HEK293S cells and BN-PAGE of ADI-15878/SEC-purified EBOV GPΔmuc-WL²P⁴ trimer. Fractions F40 to F49 were used for crystallization screening. The SEC profile was generated from a HiLoad Superdex 200 16/600 PG column (Cytiva). (**b**) Ribbon representation of EBOV GPΔmuc-WL²P⁴ trimer structure (Left: top view; Right: side view). The structure is colored as follows: glycan cap (gray), RBS (cyan), GP2 (yellow), and IFL (pink). *N*-linked glycans at N228, N257, N563, and N618 are shown as color-coded (by atom type) sticks. (**c**) Structural comparison of GPΔmuc-WL²P⁴ and previously reported GPΔmuc-WL² and GPΔmuc-WL²P² trimers. The ribbon models of three GPΔmuc trimers containing WL²P⁴, WL², and WL²P² mutations are shown in cyan, gold, and orange, respectively. Regions that are critical to the GP structure and exhibit appreciable differences in structure are superposed and shown as enlarged insects. (**d**) SEC profile of ADI-15878/SEC-purified SUDV GPΔmuc-WL²P⁴ trimer expressed in 2L HEK293S cells and complexed with ADI-15878 Fab. The SEC profile was generated from a Superose 6 10/300 increase column. (**e**) Schematic representation of image processing, 2D classification, and 3D reconstruction of cryo-EM data obtained for SUDV GPΔmuc-WL²P⁴ trimer in complex with ADI-15878 Fab using CryoSPARC. (**f**) Left: cryo-EM structure of SUDV GPΔmuc-WL²P⁴ superposed with the crystal structure of EBOV GPΔmuc-WL²P⁴ for comparison at the monomer level. The Cα root mean square deviation (Cα-RMSD) is 0.66 Å for 154 matching Cα atoms. Right: cryo-EM structure of SUDV GPΔmuc-WL²P⁴ in complex with ADI-15878 Fab superposed with the previously reported crystal structure of EBOV GPΔmuc in complex with CA45 Fab (PDB ID: 6EAY). Cα-RMSD is 0.63 Å for 149 matching Cα atoms. (**g**) Structural details illustrated for the GP-CA45 interface in the crystal structure of EBOV GPΔmuc in complex with CA45 Fab (PDB ID: 6EAY). Hydrogen bonds are shown in red dashed line and salt bridge shown in black dashed line with distances labeled.

Fig. S3

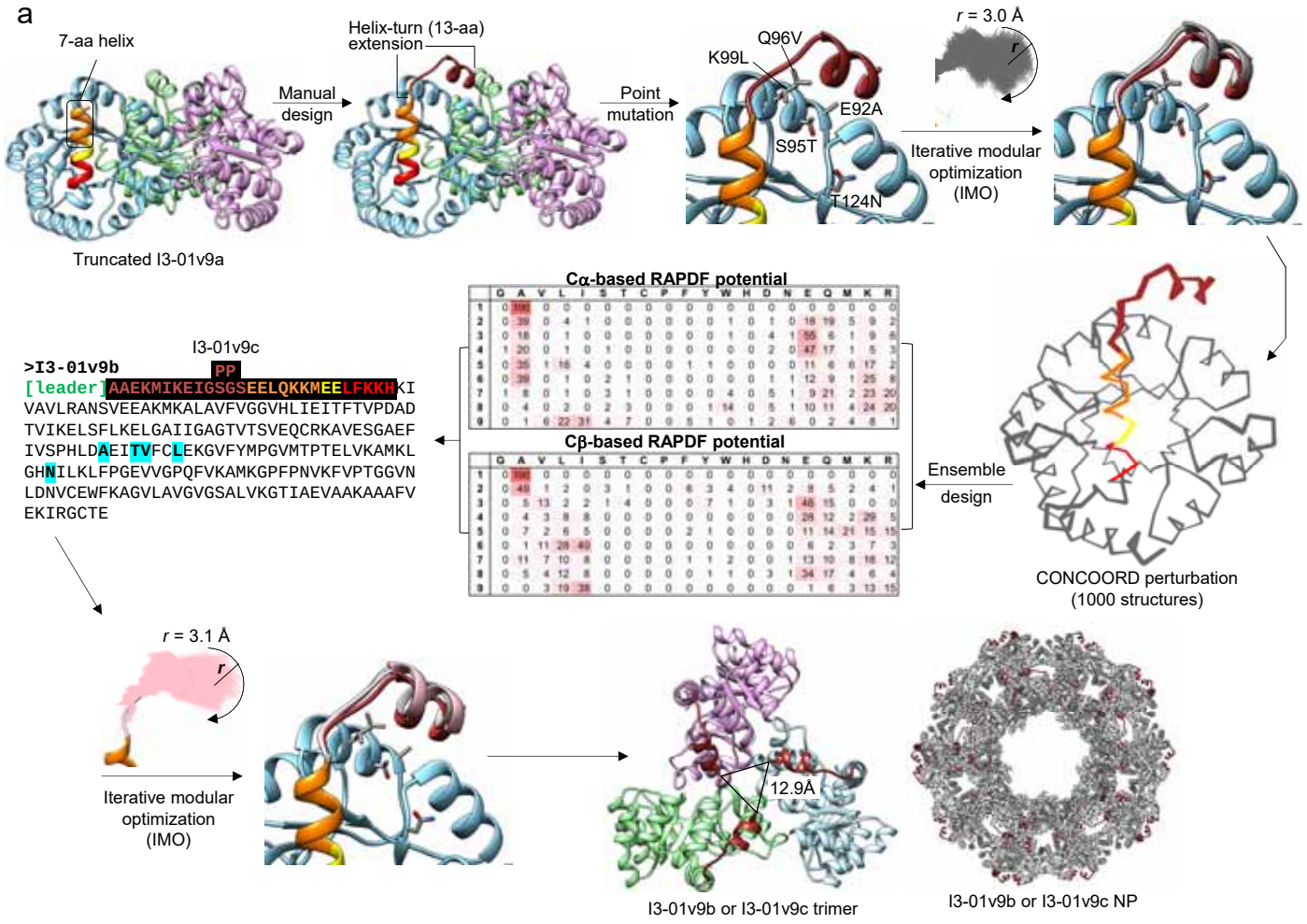

Fig. S3

b

>EBOV Mayinga GPΔmuc-WL²P⁴-I3-01v9b-T

MGVTGILQLPRDRFKRTSFFLWVIILFQRTFSIPLGVIHNSALQVSDVDKLVCRDKLSSTNQLRSVGLNLEGNGVATDVPSATKRWGFRSGVPPKVVNYEAGEWAENCYNLEI
KKPDGSECLPAAPDGIRGFPRCRYVHKVSGTGPCAGDFAFHKEGAFFLYDRLASTVIYRGTTFAEGVVAFLILPQAKKDFFSSHPLREPVNATEDPSSGYYSTTIRYQATGFG
TNETEYLFEVDNLTYVQLESRFTPQFLLQLNETIYTSGKRSNTTGKLIWKVNPEIDTTIGEWAFWETKKNLTRKIRSEELSFTVVSTHHQDTGEESASSGKLGLITNTIAGVA
GLITGGRRTRREAIVNAQPKCNPNLHYWTTQDEGAAIGLAWIPYFGPAAEGIYIEGLMHNQDGLICGLRQLANETTQALQLFLRATTEPRTFSILNRKAIDFLLQRWGGTCHI
LGPDCCIEPHDLTKNITDKIDQIIHDFVDKTLPDASGAEKMIKEIGSGSEELQKKMEELFKKHKIVAVLRANSVEEAKEKALAVFEGGVHLIEITFTVPDADTVIKELSFLKE
KGAIIGAGTVTSVEQCRKAVESGAEFIVSPHLDAEITVFCLEKGVFYMPGVMTPTELVKAMKLGHNILKLFPGEVVGPQFVKAMKGPFPNVKFVPTGGVNLDNVCEWFKAGVL
AVGVGSALVKGTPDEVREKAKAFVEKIRGCTE

>EBOV Mayinga GPΔmuc-WL²P⁴-I3-01v9c-T

MGVTGILQLPRDRFKRTSFFLWVIILFQRTFSIPLGVIHNSALQVSDVDKLVCRDKLSSTNQLRSVGLNLEGNGVATDVPSATKRWGFRSGVPPKVVNYEAGEWAENCYNLEI
KKPDGSECLPAAPDGIRGFPRCRYVHKVSGTGPCAGDFAFHKEGAFFLYDRLASTVIYRGTTFAEGVVAFLILPQAKKDFFSSHPLREPVNATEDPSSGYYSTTIRYQATGFG
TNETEYLFEVDNLTYVQLESRFTPQFLLQLNETIYTSGKRSNTTGKLIWKVNPEIDTTIGEWAFWETKKNLTRKIRSEELSFTVVSTHHQDTGEESASSGKLGLITNTIAGVA
GLITGGRRTRREAIVNAQPKCNPNLHYWTTQDEGAAIGLAWIPYFGPAAEGIYIEGLMHNQDGLICGLRQLANETTQALQLFLRATTEPRTFSILNRKAIDFLLQRWGGTCHI
LGPDCCIEPHDLTKNITDKIDQIIHDFVDKTLPDASGAEKMIKEIGPPSEELQKKMEELFKKHKIVAVLRANSVEEAKEKALAVFEGGVHLIEITFTVPDADTVIKELSFLKE
KGAIIGAGTVTSVEQCRKAVESGAEFIVSPHLDAEITVFCLEKGVFYMPGVMTPTELVKAMKLGHNILKLFPGEVVGPQFVKAMKGPFPNVKFVPTGGVNLDNVCEWFKAGVL
AVGVGSALVKGTPDEVREKAKAFVEKIRGCTE

c

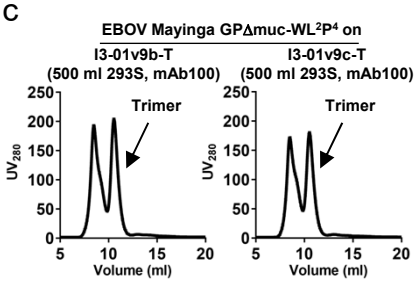

d

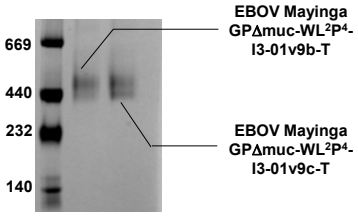

e

2D classes of EBOV Mayinga GPΔmuc-WL²P⁴-I3-01v9b-T

Selected 2D classification for modeling

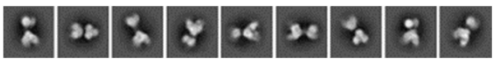

f

2D classes of EBOV Mayinga GPΔmuc-WL²P⁴-I3-01v9c-T

Selected 2D classification for modeling

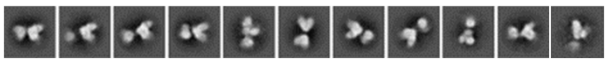

g

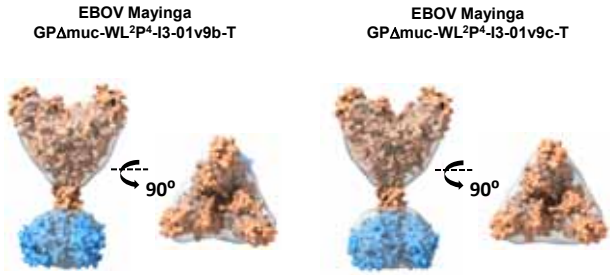

h

>EBOV Mayinga GPΔmuc-WL²P⁴-E2p-LD4-PADRE

MGVTGILQLPRDRFKRTSFFLWVIILFQRTFSIPLGVIHNSALQVSDVDKLVCRDKLSSTNQLRSVGLNLEGNGVATDVPSATKRWGFRSGVPPKVVNYEAGEWAENCYNLEI
KKPDGSECLPAAPDGIRGFPRCRYVHKVSGTGPCAGDFAFHKEGAFFLYDRLASTVIYRGTTFAEGVVAFLILPQAKKDFFSSHPLREPVNATEDPSSGYYSTTIRYQATGFG
TNETEYLFEVDNLTYVQLESRFTPQFLLQLNETIYTSGKRSNTTGKLIWKVNPEIDTTIGEWAFWETKKNLTRKIRSEELSFTVVSTHHQDTGEESASSGKLGLITNTIAGVA
GLITGGRRTRREAIVNAQPKCNPNLHYWTTQDEGAAIGLAWIPYFGPAAEGIYIEGLMHNQDGLICGLRQLANETTQALQLFLRATTEPRTFSILNRKAIDFLLQRWGGTCHI
LGPDCCIEPHDLTKNITDKIDQIIHDFVDKTLPDASGAAAKPATTEGEFPETREKMSGIRRAIAKAMVHSKHTAPHVTLMDEADVKLVAHRKKFKAIAAEKGIKLTFLPYVVK
ALVSALREYPVLNTAIDDETEEIIQKHYYNIGIAADTDRGLLVPVIKHADRKPIFALAQEINELAEKARDGKLTPGEMKGASCTITNIGSAGGQWFTPVINHPEVAILGIGRI
AEKPIVRDGEIVAAPMLALSLSFDHRMIDGATAQKALNHIKRLLSDPELLLMGGGGSFSEEQKKALDLAFYFDRRLTPEWRRYLSQRLGLNEEQIERWFRRKEQQIGWSHPQF
EKGSAKFVAAWTLKAAA

>EBOV Mayinga GPΔmuc-WL²P⁴-I3-01v9b-LD7-PADRE

MGVTGILQLPRDRFKRTSFFLWVIILFQRTFSIPLGVIHNSALQVSDVDKLVCRDKLSSTNQLRSVGLNLEGNGVATDVPSATKRWGFRSGVPPKVVNYEAGEWAENCYNLEI
KKPDGSECLPAAPDGIRGFPRCRYVHKVSGTGPCAGDFAFHKEGAFFLYDRLASTVIYRGTTFAEGVVAFLILPQAKKDFFSSHPLREPVNATEDPSSGYYSTTIRYQATGFG
TNETEYLFEVDNLTYVQLESRFTPQFLLQLNETIYTSGKRSNTTGKLIWKVNPEIDTTIGEWAFWETKKNLTRKIRSEELSFTVVSTHHQDTGEESASSGKLGLITNTIAGVA
GLITGGRRTRREAIVNAQPKCNPNLHYWTTQDEGAAIGLAWIPYFGPAAEGIYIEGLMHNQDGLICGLRQLANETTQALQLFLRATTEPRTFSILNRKAIDFLLQRWGGTCHI
LGPDCCIEPHDLTKNITDKIDQIIHDFVDKTLPDASGAEKMIKEIGSGSEELQKKMEELFKKHKIVAVLRANSVEEAKMKALAVFVGGVHLIEITFTVPDADTVIKELSFLKE
LGAIIGAGTVTSVEQCRKAVESGAEFIVSPHLDAEITVFCLEKGVFYMPGVMTPTELVKAMKLGHNILKLFPGEVVGPQFVKAMKGPFPNVKFVPTGGVNLDNVCEWFKAGVL
AVGVGSALVKGTIAEVAAKAAAFVEKIRGCTEGGGGSSPAVDIGDRLDELEKALEALSAEDGHDDVGQRLESLLRRWNSRRADGSAKFVAAWTLKAAA

>SUDV Gulu GPΔmuc-WL²P⁴-E2p-LD4-PADRE

MGILPSPGMPALLSLVSLLSVLLMGCVAEMPLGVVTNSTLEVTEIDQLVCKDHLASTDQLKSVGLNLEGSGVSTDIPSATKRWGFRSGVPPKVVSYEAGEWAENCYNLEIKKP
DGSECLPPPPDGVRGFPRCRYVHKAQGTGPCPGDYAFHKDGAFFLYDRLASTVIYRGVNFAEGVIAFLILAKPKETFLQSPPIREAVNYTENTSSYYATSYLEYEIENFGAQH
STTLFKIDNNTFVRLDRPHTPQFLFQLNDTIHLHQQLSNTTGRLIWTLDANINADIGEWAFWENKKNLSEQLRGEELSFEALSLNETEDDDAASSSTSNGLITSTVTGILGSL
GLRKRSRRQTNTKATGKCNPNLHYWTAQEQHNAAGIAWIPYFGPGAEGIYTEGLMHNQNALVCGLRQLANETTQALQLFLRATTEPRTYTILNRKAIDFLLRRWGGTCRILGP
DCCIEPHDLTKNITDKINQIIHDFIDNPLPNASGAAAKPATTEGEFPETREKMSGIRRAIAKAMVHSKHTAPHVTLMDEADVTKLVAHRKKFKAIAAEKGIKLTFLPYVVKAL
VSALREYPVLNTAIDDETEEIIQKHYYNIGIAADTDRGLLVPVIKHADRKPIFALAQEINELAEKARDGKLTPGEMKGASCTITNIGSAGGQWFTPVINHPEVAILGIGRIAE
KPIVRDGEIVAAPMLALSLSFDHRMIDGATAQKALNHIKRLLSDPELLLMGGGGSFSEEQKKALDLAFYFDRRLTPEWRRYLSQRLGLNEEQIERWFRRKEQQIGWSHPQFEK
GSAKFVAAWTLKAAA

>SUDV Gulu GPΔmuc-WL²P⁴-I3-01v9b-LD7-PADRE

MGILPSPGMPALLSLVSLLSVLLMGCVAEMPLGVVTNSTLEVTEIDQLVCKDHLASTDQLKSVGLNLEGSGVSTDIPSATKRWGFRSGVPPKVVSYEAGEWAENCYNLEIKKP
DGSECLPPPPDGVRGFPRCRYVHKAQGTGPCPGDYAFHKDGAFFLYDRLASTVIYRGVNFAEGVIAFLILAKPKETFLQSPPIREAVNYTENTSSYYATSYLEYEIENFGAQH
STTLFKIDNNTFVRLDRPHTPQFLFQLNDTIHLHQQLSNTTGRLIWTLDANINADIGEWAFWENKKNLSEQLRGEELSFEALSLNETEDDDAASSSTSNGLITSTVTGILGSL
GLRKRSRRQTNTKATGKCNPNLHYWTAQEQHNAAGIAWIPYFGPGAEGIYTEGLMHNQNALVCGLRQLANETTQALQLFLRATTEPRTYTILNRKAIDFLLRRWGGTCRILGP
DCCIEPHDLTKNITDKINQIIHDFIDNPLPNASGAEKMIKEIGSGSEELQKKMEELFKKHKIVAVLRANSVEEAKMKALAVFVGGVHLIEITFTVPDADTVIKELSFLKELGA
IIGAGTVTSVEQCRKAVESGAEFIVSPHLDAEITVFCLEKGVFYMPGVMTPTELVKAMKLGHNILKLFPGEVVGPQFVKAMKGPFPNVKFVPTGGVNLDNVCEWFKAGVLAVG
VGSALVKGTIAEVAAKAAAFVEKIRGCTEGGGGSSPAVDIGDRLDELEKALEALSAEDGHDDVGQRLESLLRRWNSRRADGSAKFVAAWTLKAAA

Fig. S3

>BDBV R4386L GPΔmuc-WL²P⁴-E2p-LD4-PADRE

MGILPSPGMPALLSLVSLLSVLLMGCVAEIPLGVVHNNTLQVSDIDKLVCRDKLSSTSQLKSVGLNLEGNGVATDVPTATKRWGFRAGVPPKVVNYEAGEWAENCYNLDIKKA
DGSECLPEAPEGVRGFPRCRYVHKVSGTGPCPEGYAFHKEGAFFLYDRLASTIIYRSTTFSEGVVAFLILPETKKDFFQSPPLHEPANMTTDPSSYYHTVTLNYVADNFGTNM
TNFLFQVDHLTYVQLEPRFTPQFLVQLNETIYTNGRRSNTTGTLIWKVNPTVDTGVGEWAFWENKKNFTKTLSSEELSVIFVPRAQDPGSNDISESTEPGPLTNTTRGAANLL
TGSRRTRREITLRTQAKCNPNLHYWTTQDEGAAIGLAWIPYFGPAAEGIYTEGIMHNQNGLICGLRQLANETTQALQLFLRATTEPRTFSILNRKAIDFLLQRWGGTCHILGP
DCCIEPHDLTKNITDKIDQIIHDFIDKPLPDASGAAAKPATTEGEFPETREKMSGIRRAIAKAMVHSKHTAPHVTLMDEADVTKLVAHRKKFKAIAAEKGIKLTFLPYVVKAL
VSALREYPVLNTAIDDETEEIIQKHYYNIGIAADTDRGLLVPVIKHADRKPIFALAQEINELAEKARDGKLTPGEMKGASCTITNIGSAGGQWFTPVINHPEVAILGIGRIAE
KPIVRDGEIVAAPMLALSLSFDHRMIDGATAQKALNHIKRLLSDPELLLMGGGGSFSEEQKKALDLAFYFDRRLTPEWRRYLSQRLGLNEEQIERWFRRKEQQIGWSHPQFEK
GSAKFVAAWTLKAAA

>BDBV R4386L GPΔmuc-WL²P⁴-I3-01v9b-LD7-PADRE

MGILPSPGMPALLSLVSLLSVLLMGCVAEIPLGVVHNNTLQVSDIDKLVCRDKLSSTSQLKSVGLNLEGNGVATDVPTATKRWGFRAGVPPKVVNYEAGEWAENCYNLDIKKA
DGSECLPEAPEGVRGFPRCRYVHKVSGTGPCPEGYAFHKEGAFFLYDRLASTIIYRSTTFSEGVVAFLILPETKKDFFQSPPLHEPANMTTDPSSYYHTVTLNYVADNFGTNM
TNFLFQVDHLTYVQLEPRFTPQFLVQLNETIYTNGRRSNTTGTLIWKVNPTVDTGVGEWAFWENKKNFTKTLSSEELSVIFVPRAQDPGSNDISESTEPGPLTNTTRGAANLL
TGSRRTRREITLRTQAKCNPNLHYWTTQDEGAAIGLAWIPYFGPAAEGIYTEGIMHNQNGLICGLRQLANETTQALQLFLRATTEPRTFSILNRKAIDFLLQRWGGTCHILGP
DCCIEPHDLTKNITDKIDQIIHDFIDKPLPDASGAEKMIKEIGSGSEELQKKMEELFKKHKIVAVLRANSVEEAKMKALAVFVGGVHLIEITFTVPDADTVIKELSFLKELGA
IIGAGTVTSVEQCRKAVESGAEFIVSPHLDAEITVFCLEKGVFYMPGVMTPTELVKAMKLGHNILKLFPGEVVGPQFVKAMKGPFPNVKFVPTGGVNLDNVCEWFKAGVLAVG
VGSALVKGTIAEVAAKAAAFVEKIRGCTEGGGGSSPAVDIGDRLDELEKALEALSAEDGHDDVGQRLESLLRRWNSRRADGSAKFVAAWTLKAAA

i

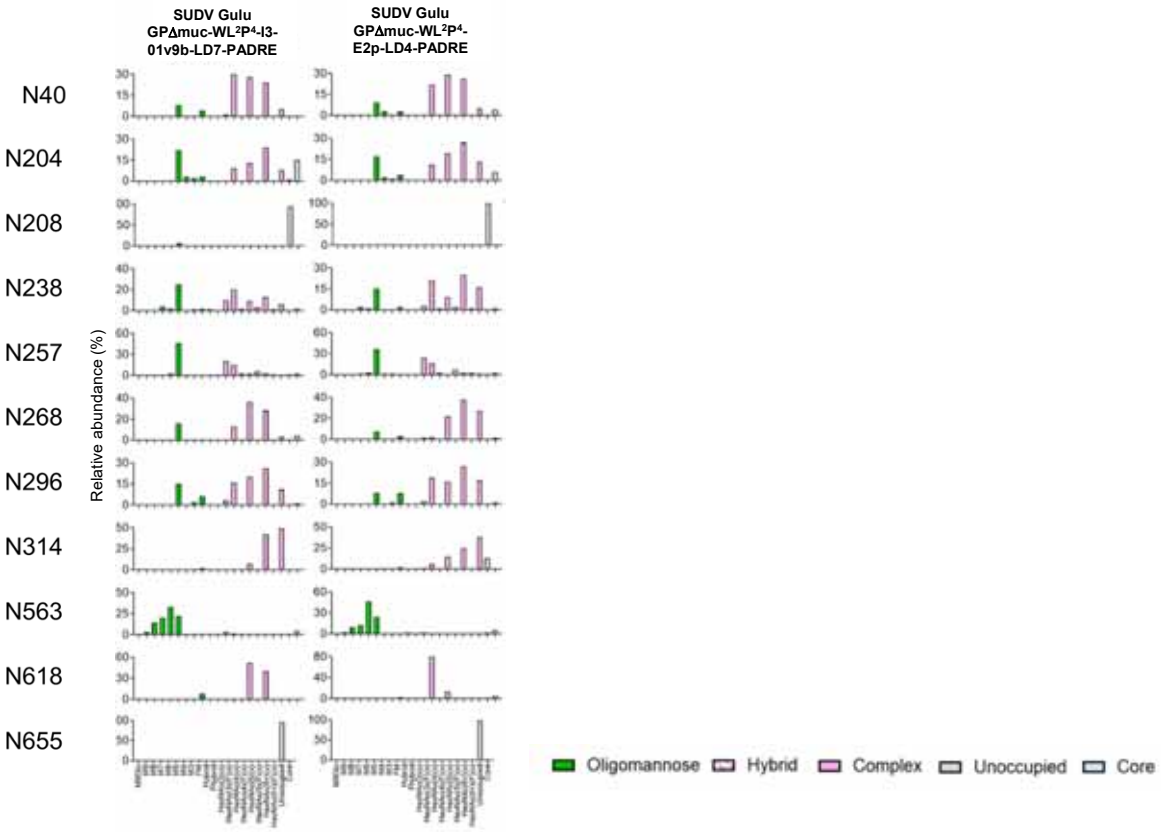

j **ELISA analysis of 6 rationally designed ebolavirus GPΔmuc SApNPs binding to 5 filovirus NAbs**

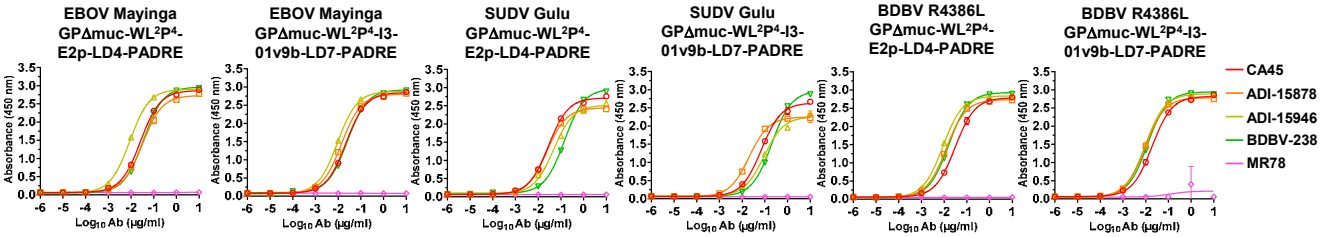

EBOV Mayinga GPΔmuc-WL²P⁴ E2p-LD4-PADRE									
CA45		ADI-15878		ADI-15946		BDBV-289		MR78	
EC50	STD	EC50	STD	EC50	STD	EC50	STD	EC50	STD
0.02593	0.00030	0.03197	0.00696	0.00879	0.00075	0.03550	0.00212	N.D.	N.D.

EBOV Mayinga GPΔmuc-WL²P⁴ I3-01v9b-LD7-PADRE									
CA45		ADI-15878		ADI-15946		BDBV-289		MR78	
EC50	STD	EC50	STD	EC50	STD	EC50	STD	EC50	STD
0.022141	0.000587	0.014095	0.000148	0.009384	0.000164	0.025555	0.00123	N.D.	N.D.

SUDV Gulu GPΔmuc-WL²P⁴ E2p-LD4-PADRE									
CA45		ADI-15878		ADI-15946		BDBV-289		MR78	
EC50	STD	EC50	STD	EC50	STD	EC50	STD	EC50	STD
0.02819	0.00070	0.02407	0.00284	0.04811	0.00204	0.14057	0.00849	N.D.	N.D.

SUDV Gulu GPΔmuc-WL²P⁴ I3-01v9b-LD7-PADRE									
CA45		ADI-15878		ADI-15946		BDBV-289		MR78	
EC50	STD	EC50	STD	EC50	STD	EC50	STD	EC50	STD
0.0699	0.0024	0.0204	0.0024	0.0910	0.0007	0.2017	0.0139	N.D.	N.D.

BDBV R4386L GPΔmuc-WL²P⁴ E2p-LD4-PADRE									
CA45		ADI-15878		ADI-15946		BDBV-289		MR78	
EC50	STD	EC50	STD	EC50	STD	EC50	STD	EC50	STD
0.0307	0.0035	0.0123	0.0002	0.0087	0.0004	0.0159	0.0002	N.D.	N.D.

BDBV R4386L GPΔmuc-WL²P⁴ I3-01v9b-LD7-PADRE									
CA45		ADI-15878		ADI-15946		BDBV-289		MR78	
EC50	STD	EC50	STD	EC50	STD	EC50	STD	EC50	STD
0.0191	0.0014	0.0093	0.0005	0.0095	0.0005	0.0120	0.0003	N.D.	N.D.

Fig. S3

k BLI analysis of 6 rationally designed ebolavirus GPΔmuc SApNPs binding to 5 filovirus NAbs

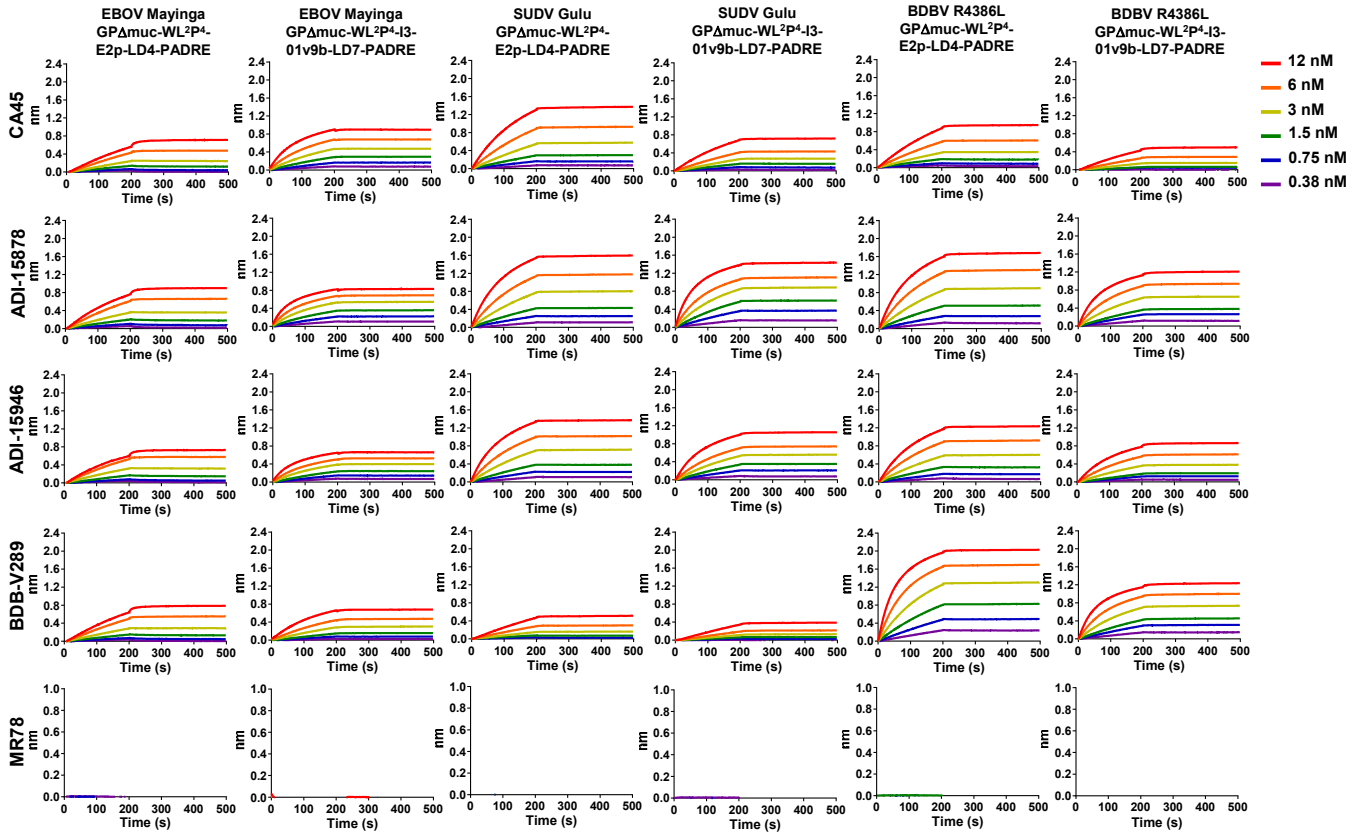

***K_D* values for 6 redesigned Filo-virus GP NP binding to 5 representative antibodies (nM) [a]**

	CA45	ADI-15878	ADI-15946	BDBV-289	MR78
EBOV Mayinga GPΔmuc-WL²P⁴-E2p-LD4-PADRE	<1.0E-3	<1.0E-3	<1.0E-3	<1.0E-3	— [b]
EBOV Mayinga GPΔmuc-WL²P⁴-I3-01v9b-LD7-PADRE	<1.0E-3	<1.0E-3	<1.0E-3	<1.0E-3	— [b]
SUDV Gulu GPΔmuc-WL²P⁴-E2p-LD4-PADRE	<1.0E-3	<1.0E-3	<1.0E-3	<1.0E-3	— [b]
SUDV Gulu GPΔmuc-WL²P⁴-I3-01v9b-LD7-PADRE	<1.0E-3	<1.0E-3	<1.0E-3	<1.0E-3	— [b]
BDBV R4386L GPΔmuc-WL²P⁴-E2p-LD4-PADRE	<1.0E-3	<1.0E-3	<1.0E-3	<1.0E-3	— [b]
BDBV R4386L GPΔmuc-WL²P⁴-I3-01v9b-LD7-PADRE	<1.0E-3	<1.0E-3	<1.0E-3	<1.0E-3	— [b]

[a] K_D values were derived from biolayer interferometry (BLI) using the binding equations describing a 1:1 interaction.
[b] "—" indicates cases where the peak signal value at the highest ebolavirus antigen concentration is 0.2 or lower.

Fig. S3

Fig. S3. Rational design of I3-01v9b/c and in vitro characterization of ebolavirus GPΔmuc-presenting SApNPs. (**a**) Schematic representation of computational design of I3-01v9b/c. Top left: structural model of I3-01v9a with the 11-aa N-terminal helix truncated to 7 aa; Top middle left: a 13-aa helix-turn fragment (9-aa helix + 4-aa turn, all alanine) was fused to the 7-aa N-terminal helix of the truncated I3-01v9a in such a way the new 9-aa N-terminal helix from the fused fragment would pack within the groove of two helices that are part of the I3-01 core; Top middle right: four mutations, E92A, S95T, Q96V, and K99L, were introduced to the I3-01 core helices to remove their steric clashes with the new N-terminal helix; Top right: iterative modular optimization (IMO) of the helix-turn backbone, with a radius of 3.0 Å measured for the first amino acid at the N-terminus; Middle right: 1000 slightly perturbed backbone conformations generated by CONCOORD, a torsion-space sampling program; Middle middle: results from an ensemble-based protein design program used to predict the optimal sequence for the 9-aa N-terminal helix within the fragment using Cα and Cβ-based RAPDF potentials. The 4-aa turn was set to "GSGS"; Middle left: sequence of I3-01v9b designed by combining data from both RAPDF potentials, with the difference between I3-01v9b and I3-01v9c (the "PP" mutation) labeled on the sequence; Bottom left: further backbone relaxation using IMO with a minimum perturbation angle; Bottom right: a structural model of the trimeric I3-01v9b/c, termed I3-01v9b/c-T, in which the N-termini form a triangle of 12.9 Å, and a structural model of fully assembled I3-01v9b/c NP. (**b**) Amino acids sequences of EBOV GPΔmuc-WL2P4-I3-01v9b/c-T, which are EBOV Mayinga GPΔmuc-WL^{2}P^4 anchored to the trimeric I3-01v9b/c-T scaffolds. Signal peptide, GP, restriction site (AS), and I3-01v9b/c-T are highlighted in yellow, grey, green and pink, respectively. The double proline mutation in the N-terminus of I3-01v9c-T that differs from I3-01v9b-T is highlighted in red. (**c**) SEC profiles of EBOV GPΔmuc-WL2P4-I3-01v9b/c-T expressed in 500 ml HEK293S cells and purified using an ADI-15878 column. (**d**) BN-PAGE of ADI-15878/SEC-purified EBOV GPΔmuc-WL2P4-I3-01v9b/c-T. (**e**) and (**f**) Representative 2D classification images of ADI-15878/SEC-purified EBOV GPΔmuc-WL2P4-I3-01v9b/c-T trimers. (**g**) 3D reconstructions of ADI-15878/SEC-purified EBOV GPΔmuc-WL2P4-I3-01v9b/c-T trimers. Crystal structures of EBOV GPΔmuc-WL^{2}P^2 (PDB ID:7JPH) and the bacterial enzyme from which I3-01 was derived (PDB ID:1VLW) were fitted into the model and shown in orange and blue, respectively. (**h**) Amino acids sequences of EBOV, SUDV, and BDBV GPΔmuc-WL^{2}P^4-E2P-LD4-PADRE and -I3-01v9b-LD7-PADRE SApNP constructs. LD stands for locking domain (LD), which is fused to the C-terminus of the NP backbone and forms an inner layer to stabilize the NP shell from the inside. PADRE is a helper T-cell epitope and forms a hydrophobic core at the center of the assembled NP to further stabilize the NP structure and to induce a strong T-help response upon vaccination. (**i**) Compositional site-specific glycan analysis of SUDV GPΔmuc-WL^{2}P^4-E2P-LD4-PADRE and I3-01v9b-LD7-PADRE SApNPs, as in **Fig. S1c**. (**j**) ELISA analysis of EBOV, SUDV, and BDBV GPΔmuc-WL^{2}P^4-E2P-LD4-PADRE and I3-01v9b-LD7-PADRE SApNPs binding to 5 filovirus NAbs, as in **Fig. S1h**. (**k**) BLI analysis of EBOV, SUDV, and BDBV GPΔmuc-WL^{2}P^4-E2P-LD4-PADRE and I3-01v9b-LD7-PADRE SApNPs binding to 5 filovirus NAbs. A two-fold concentration gradient of antigen, starting at 12 nM, was used in a dilution series of six. K_D values derived from a 1:1 fitting model are summarized in a table.

Fig. S4

a

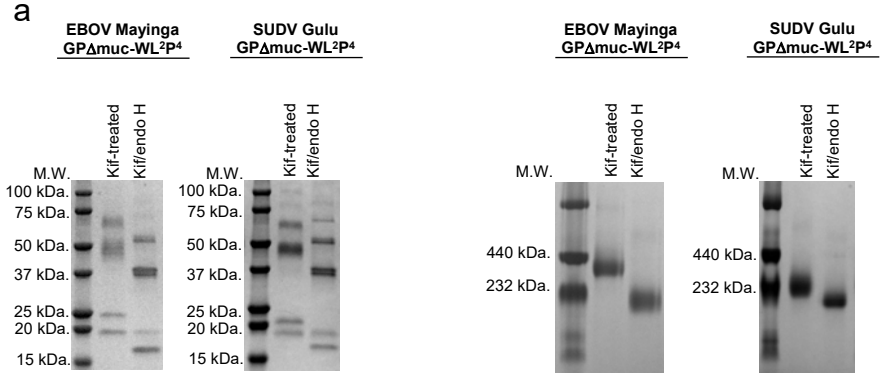

b **ELISA analysis of Kif-treated and glycan-trimmed EBOV and SUDV GPΔmuc-WL²P⁴ trimers binding to 5 filovirus NAbs**

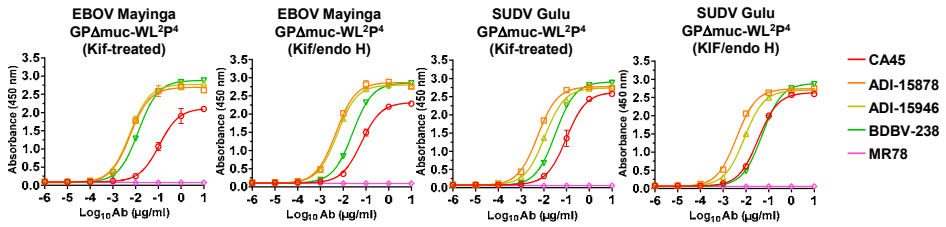

EBOV Mayinga GPΔmuc-WL²P⁴ (Kif-treated)									
CA45		ADI-15878		ADI-15946		BDBV-289		MR78	
EC50	STD	EC50	STD	EC50	STD	EC50	STD	EC50	STD
0.1110	0.0252	0.0058	0.0006	0.0057	0.0003	0.0133	0.0004	N.D.	N.D.

EBOV Mayinga GPΔmuc-WL²P⁴ (Kif/endo H)									
CA45		ADI-15878		ADI-15946		BDBV-289		MR78	
EC50	STD	EC50	STD	EC50	STD	EC50	STD	EC50	STD
0.0624	0.0093	0.0047	0.0001	0.0055	0.0006	0.0261	0.0021	N.D.	N.D.

SUDV Gulu GPΔmuc-WL²P⁴ (Kif-treated)									
CA45		ADI-15878		ADI-15946		BDBV-289		MR78	
EC50	STD	EC50	STD	EC50	STD	EC50	STD	EC50	STD
0.0973	0.0354	0.0054	0.0003	0.0111	0.0003	0.0325	0.0013	N.D.	N.D.

SUDV Gulu GPΔmuc-WL²P⁴ (Kif/endo H)									
CA45		ADI-15878		ADI-15946		BDBV-289		MR78	
EC50	STD	EC50	STD	EC50	STD	EC50	STD	EC50	STD
0.0347	0.0012	0.0039	0.0002	0.0086	0.0002	0.0518	0.0010	N.D.	N.D.

c **BLI analysis of Kif-treated and glycan-trimmed EBOV and SUDV GPΔmuc-WL²P⁴ trimers binding to 5 filovirus NAbs**

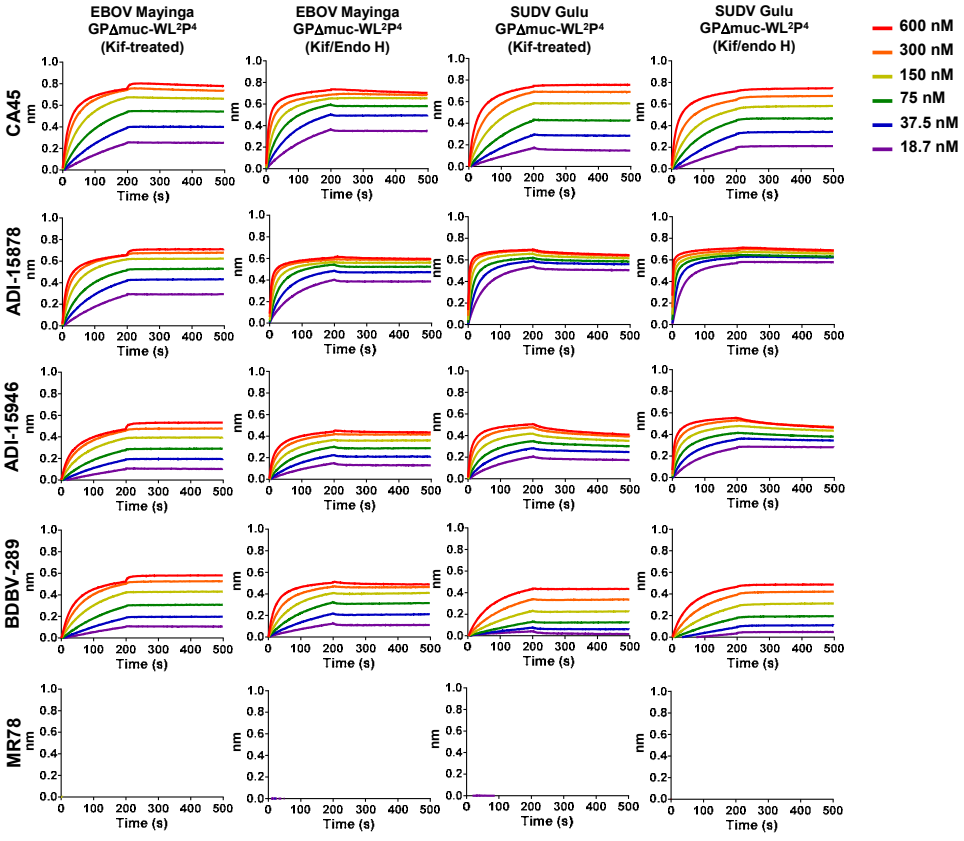

Fig. S4

K_D values for 4 glycan-modified ebolavirus GPΔmuc trimers binding to 5 filovirus NAbs (nM) [a]

	CA45	ADI-15878	ADI-15946	BDBV-289	MR78
EBOV Mayinga GPΔmuc-WL^{2}P^4 (Kif-treated)	<1.0E-3	<1.0E-3	<1.0E-3	<1.0E-3	— [b]
EBOV Mayinga GPΔmuc-WL^{2}P^4 (Kif/endo H)	<1.0E-3	<1.0E-3	<1.0E-3	<1.0E-3	— [b]
SUDV Gulu GPΔmuc-WL^{2}P^4 (Kif-treated)	<1.0E-3	2.99E-2	2.03	<1.0E-3	— [b]
SUDV Gulu GPΔmuc-WL^{2}P^4 (Kif/endo H)	<1.0E-3	<1.0E-3	9.52E-1	<1.0E-3	— [b]

[a] K_D values were derived from bio-layer interferometry (BLI) using the binding equations describing a 1:1 interaction.
[b] "—" indicates cases where the peak signal value at the highest ebolavirus antigen concentration is 0.2 or lower.

d

>SUDV Gulu GPΔmuc-WL^{2}P^4-PD-E2p-LD4-PADRE
MGILPSPGMPALLSLVSLLSVLLMGCVAEMPLGVVTNSTLEVTEIDQLVCKDHLASTDQLKSVGLNLEGSGVSTDIPSATKRWGFRSGVPPKVVSYEAGEWAENCYNLEIKKP
DGSECLPPPPDGVRGFPRCRYVHKAQGTGPCPGDYAFHKDGAFFLYDRLASTVIYRGVNFAEGVIAFLILAKPKETFLQSPPIREAVNYTENTSSYYATSYLEYEIENFGAQH
STTLFKIDNNTFVRLDRPHTPQFLFQLNDTIHLHQQLSNTTGRLIWTLDANINADIGEWAFWENKKNLSEQLRGEELSFEALSLNETEDDDAASSSTSNGLITSTVTGILGSL
GLRKRSRRQTNTKATGKCNPNLHYWTAQEQHNAAGIAWIPYFGPGAEGIYTEGLMHNQNALVCGLRQLANETTQALQLFLRATTEPRTYTILNRKAIDFLLRRWGGTCRILGP
DCCIEPHDLTKNITDKINQIIHDFIDNPLPDASGAAAKPATTEGEFPETREKMSGIRRAIAKAMVHSKHTAPHVTLMDEADVT
KLVAHRKKFKAIAAEKGIKLTFLPYVVKALVSALREYPVLNTAIDDETEEIIQKHYYNIGIAADTDRGLLVPVIKHADRKPIFALAQEINELAEKARDGKLTPGEMKGASCTI
TNIGSAGGQWFTPVINHPEVAILGIGRIAEKPIVRDGEIVAAPMLALSLSFDHRMIDGATAQKALNHIKRLLSDPELLLMGGGGSFSEEQKKALDLAFYFDRRLTPEWRRYLS
QRLGLNEEQIERWFRRKEQQIGWSHPQFEKGSAKFVAAWTLKAAA
>SUDV Gulu GPΔmuc-WL^{2}P^4-PD-I3-01v9b-LD7-PADRE
MGILPSPGMPALLSLVSLLSVLLMGCVAEMPLGVVTNSTLEVTEIDQLVCKDHLASTDQLKSVGLNLEGSGVSTDIPSATKRWGFRSGVPPKVVSYEAGEWAENCYNLEIKKP
DGSECLPPPPDGVRGFPRCRYVHKAQGTGPCPGDYAFHKDGAFFLYDRLASTVIYRGVNFAEGVIAFLILAKPKETFLQSPPIREAVNYTENTSSYYATSYLEYEIENFGAQH
STTLFKIDNNTFVRLDRPHTPQFLFQLNDTIHLHQQLSNTTGRLIWTLDANINADIGEWAFWENKKNLSEQLRGEELSFEALSLNETEDDDAASSSTSNGLITSTVTGILGSL
GLRKRSRRQTNTKATGKCNPNLHYWTAQEQHNAAGIAWIPYFGPGAEGIYTEGLMHNQNALVCGLRQLANETTQALQLFLRATTEPRTYTILNRKAIDFLLRRWGGTCRILGP
DCCIEPHDLTKNITDKINQIIHDFIDNPLPDASGAEKMIKEIGSGSEELQKKMEELFKKHKIVAVLRANSVEEAKEKALAVFEGGVHLIEITFTVPDADTVIKELSFLKEKGA
IIGAGTVTSVEQCRKAVESGAEFIVSPHLDAEITVFCLEKGVFYMPGVMTPTELVKAMKLGHNILKLFPGEVVGPQFVKAMKGPFPNVKFVPTGGVNLDNVCEWFKAGVLAVG
VGSALVKGTPDEVREKAKAFVEKIRGCTEGGGGSSPAVDIGDRLDELEKALEALSAEDGHDDVGQRLESLLRRWNSRRADGSAKFVAAWTLKAAA

e

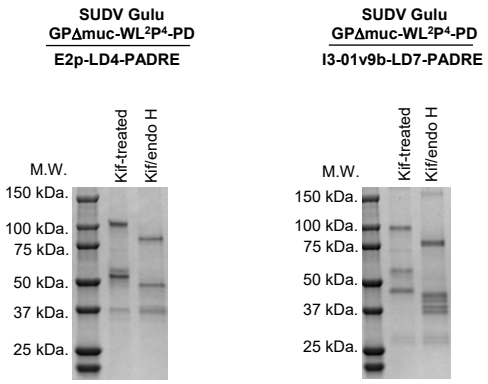

Fig. S4

f **Site-specific glycan profiles of wildtype and Kif-treated SUDV GPΔmuc-WL^{2}P^4-PD-presenting SApNPs**

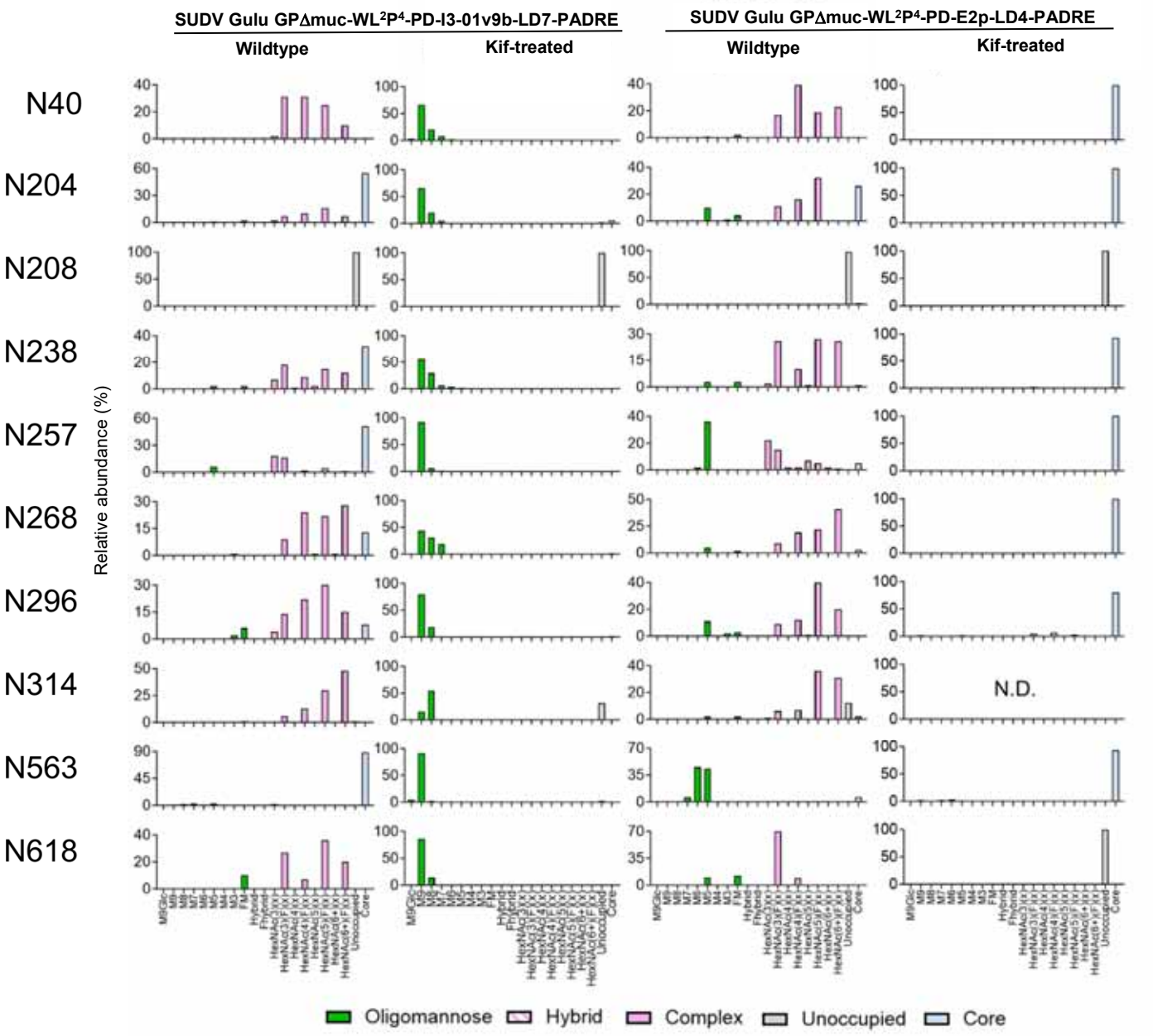

Fig. S4

g

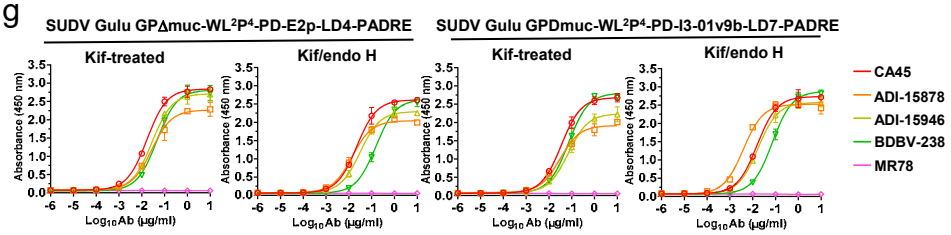

SUDV Gulu GPΔmuc-WL2P4-PD-E2p-LD4-PADRE (Kif-treated)									
CA45		ADI-15878		ADI-15946		BDBV-829		MR78	
EC50	STD	EC50	STD	EC50	STD	EC50	STD	EC50	STD
0.0168	0.0014	0.0277	0.0049	0.0283	0.0021	0.0462	0.0006	N.D.	N.D.

SUDV Gulu GPΔmuc-WL2P4-PD-E2p-LD4-PADRE (Kif/endo H)									
CA45		ADI-15878		ADI-15946		BDBV-829		MR78	
EC50	STD	EC50	STD	EC50	STD	EC50	STD	EC50	STD
0.0226	0.0048	0.0308	0.002	0.0312	0.0043	0.1550	0.0179	N.D.	N.D.

SUDV Gulu GPΔmuc-WL2P4-PD-I3-01v9b-LD7-PADRE (Kif-treated)									
CA45		ADI-15878		ADI-15946		BDBV-829		MR78	
EC50	STD	EC50	STD	EC50	STD	EC50	STD	EC50	STD
0.0348	0.0024	0.0254	0.0163	0.0708	0.0049	0.0718	0.0181	N.D.	N.D.

SUDV Gulu GPΔmuc-WL2P4-PD-I3-01v9b-LD7-PADRE (Kif/endo H)									
CA45		ADI-15878		ADI-15946		BDBV-829		MR78	
EC50	STD	EC50	STD	EC50	STD	EC50	STD	EC50	STD
0.0155	0.0023	0.0039	0.0004	0.0174	0.0011	0.0726	0.0083	N.D.	N.D.

h

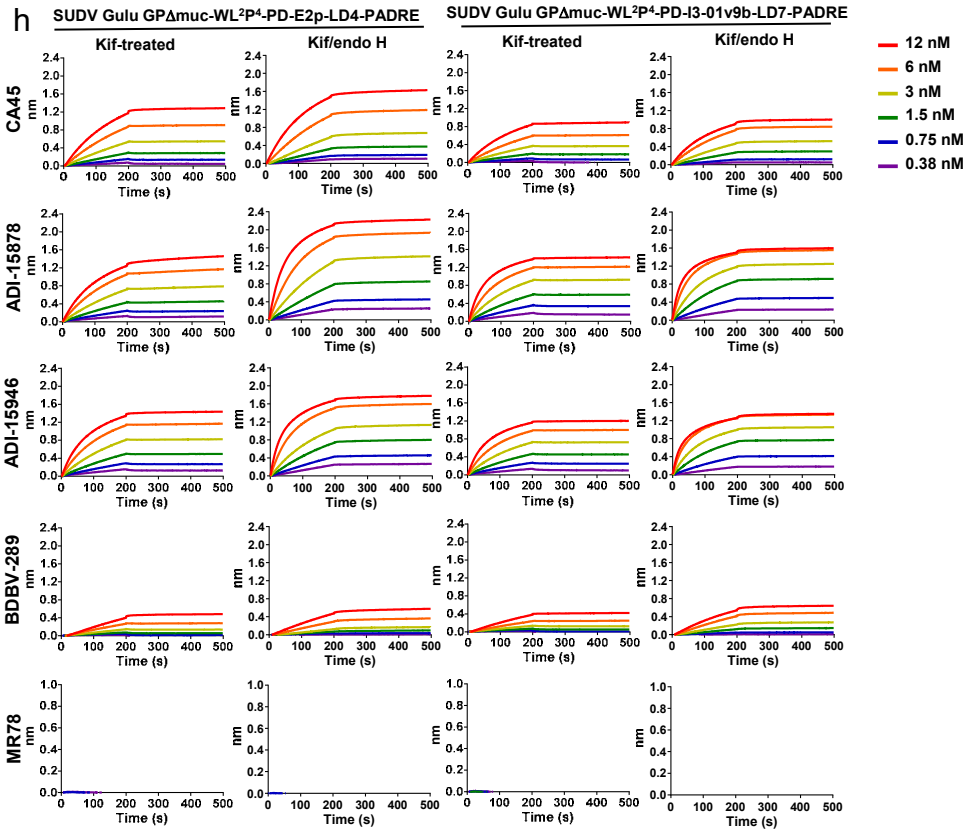

K_D values for 4 glycan-modified SUDVGPΔmuc-WL2P4-PD-presenting SApNPs binding to 5 filovirus NAbs (nM) [a]

	CA45	ADI-15878	ADI-15946	BDBV-289	MR78
SUDV Gulu GPΔmuc-WL2P4-PD-E2p-LD4-PADRE (Kif-treated)	<1.0E-3	<1.0E-3	<1.0E-3	<1.0E-3	— [b]
SUDV Gulu GPΔmuc-WL2P4-PD-E2p-LD4-PADRE (Kif/endo H)	<1.0E-3	<1.0E-3	<1.0E-3	<1.0E-3	— [b]
SUDV Gulu GPΔmuc-WL2P4-PD-I3-01v9b-LD7-PADRE (Kif-treated)	<1.0E-3	<1.0E-3	<1.0E-3	<1.0E-3	— [b]
SUDV Gulu GPΔmuc-WL2P4-PD-I3-01v9b-LD7-PADRE (Kif/endo H)	<1.0E-3	<1.0E-3	<1.0E-3	<1.0E-3	— [b]

[a] K_D values were derived from biolayer interferometry (BLI) using the binding equations describing a 1:1 interaction.
[b] "—" indicates cases where the peak signal value at the highest SUDV antigen concentration is 0.2 or lower.

Fig. S4. In vitro characterization for glycan-modified ebolavirus GPΔmuc trimers and SApNPs. (**a**) SDS-PAGE and BN-PAGE of glycan-modified EBOV Mayinga and SUDV Gulu GPΔmuc-WL^{2}P^4 trimers. They were either expressed in the presence of kifunensine (Kif-treated) to obtain oligomannose-only glycans or further trimmed using endo H (Kif/endo H) to obtain a mono-layer of GlcNAc stumps. (**b**) ELISA analysis of glycan-modified EBOV Mayinga and SUDV Gulu GPΔmuc-WL^{2}P^4 trimers binding to 5 filovirus NAbs in the IgG form, as in **Fig S1h.** (**c**) BLI analysis of glycan-modified EBOV Mayinga and SUDV Gulu GPΔmuc-WL^{2}P^4 trimers binding to 5 filovirus NAbs in the IgG form, as in **Fig S1i**. (**d**) Construct sequences for "multilayered" E2p (E2p-LD4-PADRE) and I3-01v9b (I3-0v9b-LD7-PADRE) SApNPs presenting 20 copies of a SUDV Gulu GPΔmuc-WL^{2}P^4-PD trimer, which contains a mutation (N637D) at the C-terminus to remove a potential glycosylation site between GP and NP. (**e**) SDS-PAGE of 3 glycan-modified SApNPs corresponding to EBOV Mayinga GPΔmuc-WL^{2}P^4 on the E2p-LD4-PADRE scaffold and SUDV Gulu GPΔmuc-WL^{2}P^4-PD on the E2p-LD4-PADRE and I3-01v9b-LD7-PADRE scaffolds. (**f**) Compositional site-specific glycan analysis of SUDV GPΔmuc-WL^{2}P^4-PD-presenting E2p and I3-01v9b SApNPs, as in **Fig. S1c**. (**g**) ELISA analysis of glycan-modified SUDV Gulu GPΔmuc-WL2P4-PD-presenting E2P and I3-01v9b SApNPs binding to 5 filovirus NAbs in the IgG form, as in **Fig S1h**. (**h**) BLI analysis of glycan-modified SUDV Gulu GPΔmuc-WL^{2}P^4-PD-presenting E2P and I3-01v9b SApNPs binding to 5 filovirus NAbs in the IgG form, as in **Fig S3k**.

Fig. S5

a

>RAVV GPΔTM-foldon-His$_6$

MGVTGILQLPRDRFKRTSFFLWVIILFQRTFSIKTLPVLEIASNSQPQDVDSVCSGTLQKTEDVHLMGFTLSGQKVADSPLEASKRWAFRTGVPPKNVEYTEGEEAKTCYNIS
VTDPSGKSLLLDPPSNIRDYPKCKTVHHIQGQNPHAQGIALHLWGAFFLYDRVASTTMYRGKVFTEGNIAAMIVNKTVHRMIFSRQGQGYRHMNLTSTNKYWTSSNETQRNDT
GCFGILQEYNSTNNQTCPPSLKPPSLPTVTPSIHSTNTQINTAK**SGT**MNPSSDDEDLMISGSGSGEQGPHTTLNVVTEQKQSSTILSTPSLHPSTSQHEQNSTNPSRHAVTEH
NGTDPTTQPATLLNNTNTTPTYNTLKYNLSTPSPPTRNITNNDTQRELAESEQTNAQLNTTLDPTENPTTGQDTNSTTNIIMTTSDITSKHPTNSSPDSSPTT**RPPI**YFRKKR
SIFWKEGDIFPFLDGLINTEIDFDPIPNTETIFDESPSFNTSTNEEQHTPPNISLTFSYFPDKNGDTAYSGENENDCDAELRIWSVQEDDLAAGLSWIPFFGPGIEGLYTAGL
IKNQNNLVCRLRRLANQTAKSLELLLRVTTEERTFSLINRHAIDFLLTRWGGTCKVLGPDCCIGIEDLSKNISEQIDKIRKDEQKEETGASGYIPEAPRDGQAYVRKDGEWVL
LSTFLGSHHHHHH

>RAVV GPΔmuc-foldon-His$_6$

MGVTGILQLPRDRFKRTSFFLWVIILFQRTFSIKTLPVLEIASNSQPQDVDSVCSGTLQKTEDVHLMGFTLSGQKVADSPLEASKRWAFRTGVPPKNVEYTEGEEAKTCYNIS
VTDPSGKSLLLDPPSNIRDYPKCKTVHHIQGQNPHAQGIALHLWGAFFLYDRVASTTMYRGKVFTEGNIAAMIVNKTVHRMIFSRQGQGYRHMNLTSTNKYWTSSNETQRNDT
GCFGILQEYNSTNNQTCPPSLKPPSLPTVTPSIHSTNTQINTAK**SGTRPP**IYFRKKRSIFWKEGDIFPFLDGLINTEIDFDPIPNTETIFDESPSFNTSTNEEQHTPPNISLT
FSYFPDKNGDTAYSGENENDCDAELRIWSVQEDDLAAGLSWIPFFGPGIEGLYTAGLIKNQNNLVCRLRRLANQTAKSLELLLRVTTEERTFSLINRHAIDFLLTRWGGTCKV
LGPDCCIGIEDLSKNISEQIDKIRKDEQKEETGASGYIPEAPRDGQAYVRKDGEWVLLSTFLGSHHHHHH

>RAVV GPΔmuc-P^2-foldon-His$_6$

MGVTGILQLPRDRFKRTSFFLWVIILFQRTFSIKTLPVLEIASNSQPQDVDSVCSGTLQKTEDVHLMGFTLSGQKVADSPLEASKRWAFRTGVPPKNVEYTEGEEAKTCYNIS
VTDPSGKSLLLDPPSNIRDYPKCKTVHHIQGQNPHAQGIALHLWGAFFLYDRVASTTMYRGKVFTEGNIAAMIVNKTVHRMIFSRQGQGYRHMNLTSTNKYWTSSNETQRNDT
GCFGILQEYNSTNNQTCPPSLKPPSLPTVTPSIHSTNTQINTAK**SGTRPP**IYFRKKRSIFWKEGDIFPFLDGLINTEIDFDPIPNTETIFDESPSFNTSTNEEQHTPPNISLT
FSYFPDKNGDTAYSGENENDCDAELRIWSVQEDDLAAGLSWIPFFGPGIEGLYTAGLIKNQNNLVCRLRRLANQTAKSLELLLRVT**P**EERTFSLINRHAIDFLLTRWGGTCKV
LGPDCCIGIEDLSKNISEQIDKIRKDEQKEETGASGYIPEAPRDGQAYVRKDGEWVLLSTFLGSHHHHHH

>RAVV GPΔmuc-P^4-foldon-His$_6$

MGVTGILQLPRDRFKRTSFFLWVIILFQRTFSIKTLPVLEIASNSQPQDVDSVCSGTLQKTEDVHLMGFTLSGQKVADSPLEASKRWAFRTGVPPKNVEYTEGEEAKTCYNIS
VTDPSGKSLLLDPPSNIRDYPKCKTVHHIQGQNPHAQGIALHLWGAFFLYDRVASTTMYRGKVFTEGNIAAMIVNKTVHRMIFSRQGQGYRHMNLTSTNKYWTSSNETQRNDT
GCFGILQEYNSTNNQTCPPSLKPPSLPTVTPSIHSTNTQINTAK**SGTRPP**IYFRKKRSIFWKEGDIFPFLDGLINTEIDFDPIPNTETIFDESPSFNTSTNEEQHTPPNISLT
FSYFPDKNGDTAYSGENENDCDAELRIWSVQEDDLAAGLSWIPFFGPGIEGLYTAGLIKNQNNLVCRLRRLANQTAKSLELLLRVTT**P**RTFSLINRHAIDFLLTRWGGTCKV
LGPDCCIGIEDLSKNISEQIDKIRKDEQKEETGASGYIPEAPRDGQAYVRKDGEWVLLSTFLGSHHHHHH

>RAVV GPΔmuc-P^{2}CT-foldon-His$_6$

MGVTGILQLPRDRFKRTSFFLWVIILFQRTFSIKTLPVLEIASNSQPQDVDSVCSGTLQKTEDVHLMGFTLSGQKVADSPLEASKRWAFRTGVPPKNVEYTEGEEAKTCYNIS
VTDPSGKSLLLDPPSNIRDYPKCKTVHHIQGQNPHAQGIALHLWGAFFLYDRVASTTMYRGKVFTEGNIAAMIVNKTVHRMIFSRQGQGYRHMNLTSTNKYWTSSNETQRNDT
GCFGILQEYNSTNNQTCPPSLKPPSLPTVTPSIHSTNTQINTAK**SGTRPP**IYFRKKRSIFWKEGDIFPFLDGLINTEIDFDPIPNTETIFDESPSFNTSTNEEQHTPPNISLT
FSYFPDKNGDTAYSGENENDCDAELRIWSVQEDDLAAGLSWIPFFGPGIEGLYTAGLIKNQNNLVCRLRRLANQTAKSLELLLRVT**P**EERTFSLINRHAIDFLLTRWGGTCKV
LGPDCCIGIEDLSKNISEQIDKIRKD**FV**KEETGASGYIPEAPRDGQAYVRKDGEWVLLSTFLGSHHHHHH

b

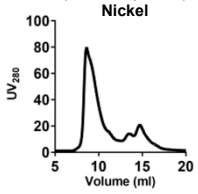

c

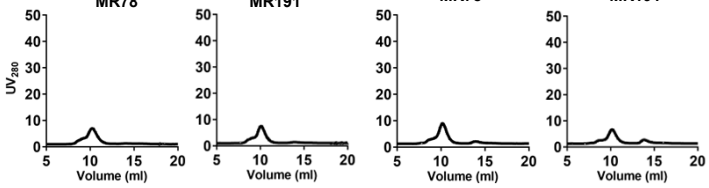

d

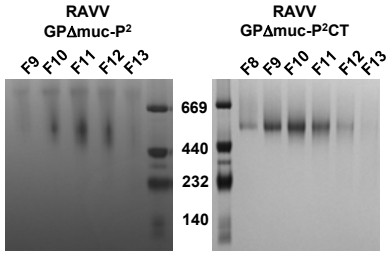

e

2D classes of RAVV GPΔmuc-P^{2}CT / MR78 Fab complex

Selected 2D classifications for 3D modeling

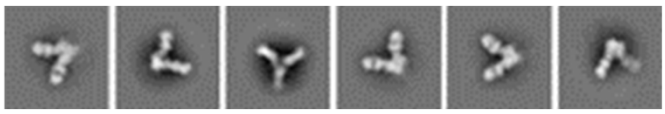

Fig. S5

f

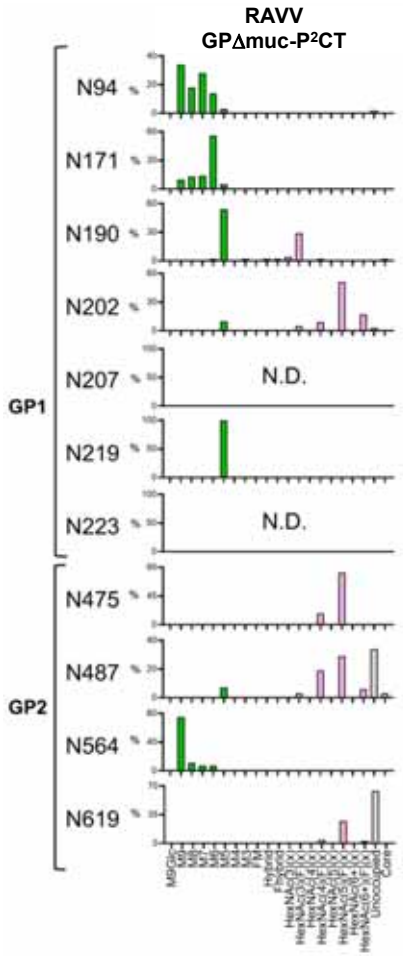

g

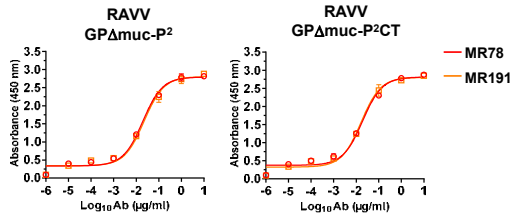

RAVV GPΔmuc-P²			
MR78		MR191	
EC50	STD	EC50	STD
0.0191	0.0007	0.0166	0.0007

RAVV GPΔmuc-P²CT			
MR78		MR191	
EC50	STD	EC50	STD
0.0196	0.0015	0.0230	0.0046

h

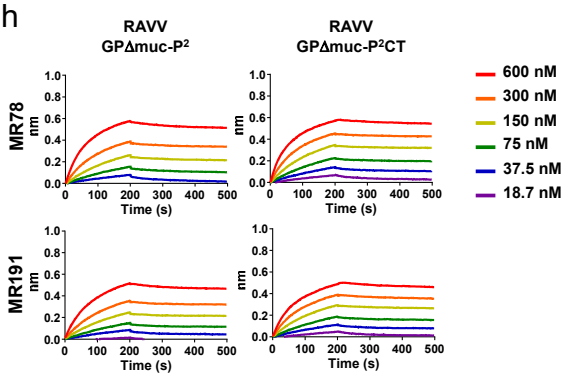

K_D values for two RAVV GPΔmuc trimers binding to 2 marburgvirus NAbs in the IgG form (nM) [a]

	MR78	MR191
RAVV GPΔmuc-P²	6.61E-1	1.55E+1
RAVV GPΔmuc-P²CT	8.06	1.30E+1

[a] K_D values were derived from bio-layer interferometry (BLI) using the binding equations describing a 1:1 interaction.
[b] "—" indicates cases where the peak signal value at the highest RSV-F concentration is 0.2 or lower.

i

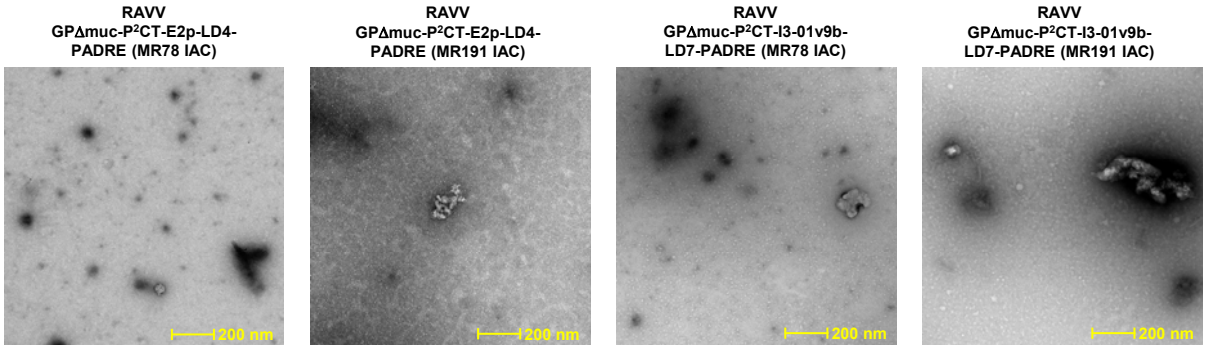

Fig. S5. Construct design and in vitro characterization of RAVV GP trimers. (**a**) Constructs sequences of RAVV GP designs. Signal peptide, mucin-like domain (MLD), HR1c, restriction site (AS), foldon, linker (GS), and His_6-tag are highlighted in yellow, gray, cyan, green, orange, light pink, and light sea green, respectively. The proline mutation on HR1c and CT are shown in red. Notably, the foldon motif, GS linker, and His_6 tag are present in all RAVV GP trimers tested in this study and will not be included in the construct names to avoid redundancy. (**b**) SEC profile of Nickel-purified RAVV GPΔmuc-P^4 expressed in 16 ml ExpiCHO cells. (**c**) SECs profile of NAb MR78/MR191-purified RAVV GPΔmuc-P^2 and GPΔmuc-P^2CT each expressed in 16 ml ExpiCHO cells. (**d**) BN-PAGE of the trimer fractions from the SEC analysis of Nickel-purified RAVV GPΔmuc-P^2 and GPΔmuc-P^2CT. (**e**) Representative 2D classification images of the RAVV GPΔmuc-P^2CT trimer in complex with MR78 Fab. (**f**) Compositional site-specific glycan analysis for RAVV GPΔmuc-P^2CT trimer, as in **Fig. S1c**. (**g**) ELISA analysis of RAVV GPΔmuc-P^2 and GPΔmuc-P^2CT trimers binding to NAbs MR78 and MR191 in the IgG form. Briefly, each well was coated with 0.1 μg of the appropriate antigen and IgG antibodies were diluted in a 10-fold dilution series from a starting concentration of 10 μg/ml for all antibodies. Error bars represent the difference between these duplicate values at each concentration tested for each sample. (**h**) BLI analysis of RAVV GPΔmuc-P^2 and GPΔmuc-P^2CT trimers binding to NAbs MR78 and MR191 in the IgG form, as in **Fig. S1i**. (i) nsEM analysis of RAVV GPΔmuc-P^2CT E2p and I3-01v9b constructs following ExpiCHO expression and MR78- or MR191-based IAC purification. Scale bar is labeled in yellow on the EM micrographs. No discernible protein NPs are shown in any of the EM micrographs.

Fig. S6

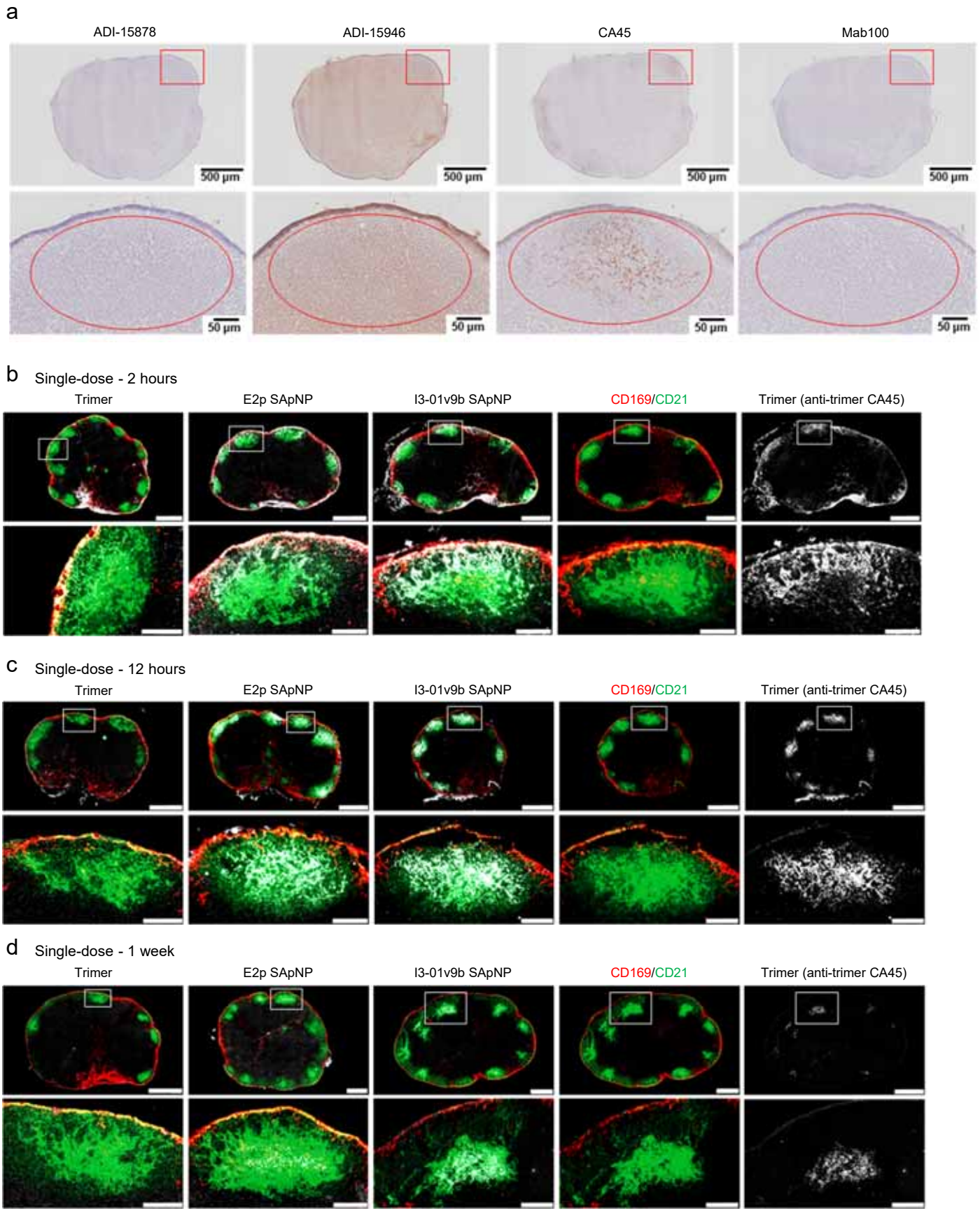

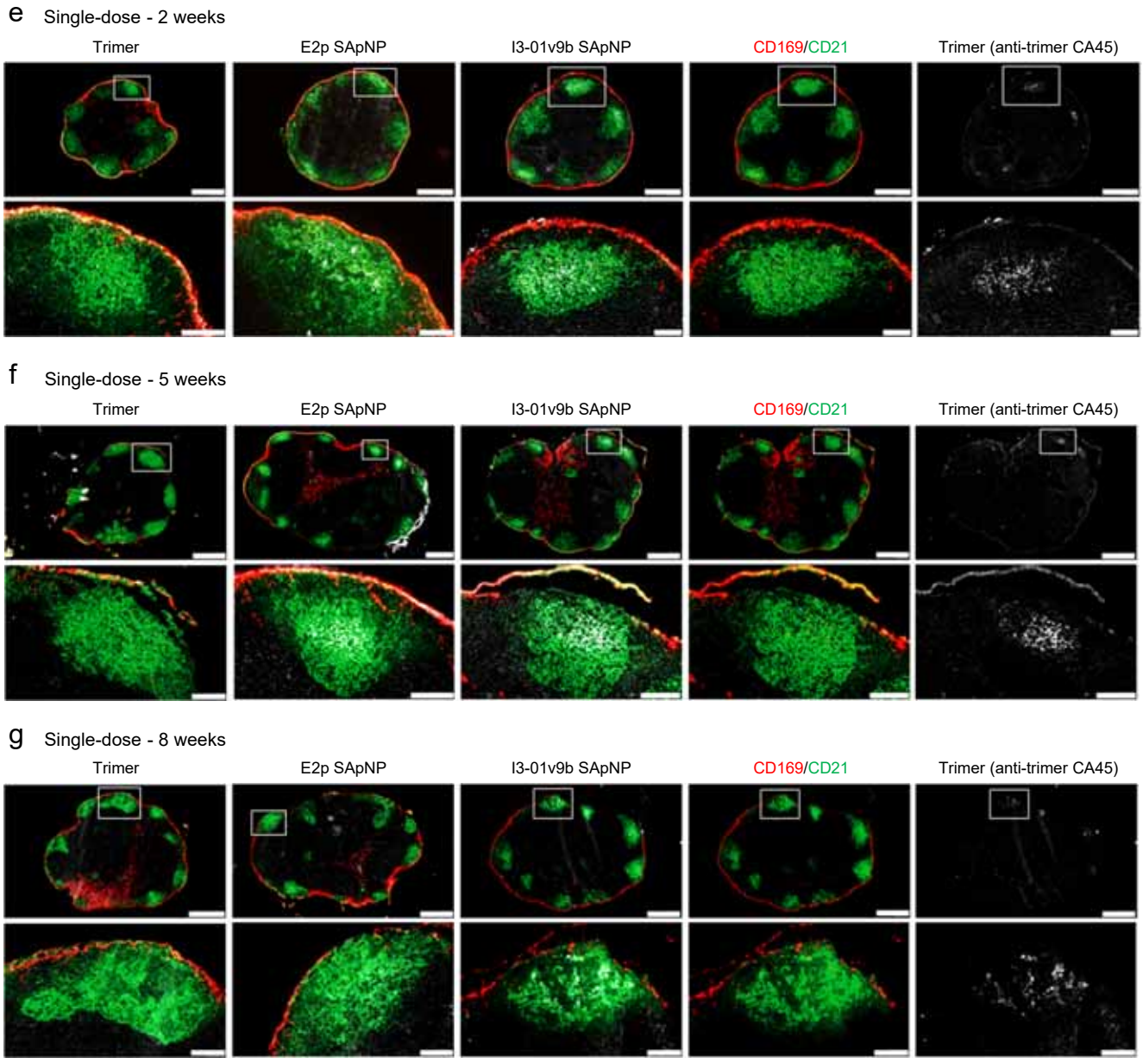

Fig. S6. Immunohistological images of SUDV GPΔmuc trimer and SApNPs in lymph nodes. (**a**) Immunostaining images of lymph node tissues from SUDV GPΔmuc trimer-presenting SApNP injected mice stained with four anti-trimer antibody ADI-15878, ADI-15946, CA45 and Mab100. SUDV vaccine constructs of GPΔmuc trimer and GPΔmuc trimer-presenting E2p and I3-01v9b SApNPs interaction with FDC networks in lymph node follicles (**b**) 2 hours, (**c**) 12 hours, (**d**) 1 week, (**e**) 2 weeks, (**f**) 5 weeks, and (**g**) 8 weeks after a single-dose injection (10 μg per injection, totaling 40 μg per mouse). Immunofluorescent images are pseudo color coded (CD21+, green; CD169+, red; anti-trimer CA45, white). Scale bars = 500 and 100 μm for complete lymph node and enlarged image of a follicle, respectively. Data were collected from more than 10 lymph node follicles (n = 3-5 mice/group).

Fig. S7

a E2p SApNPs (yellow arrow) are aligned on FDC dendrites after 2 hours of injection

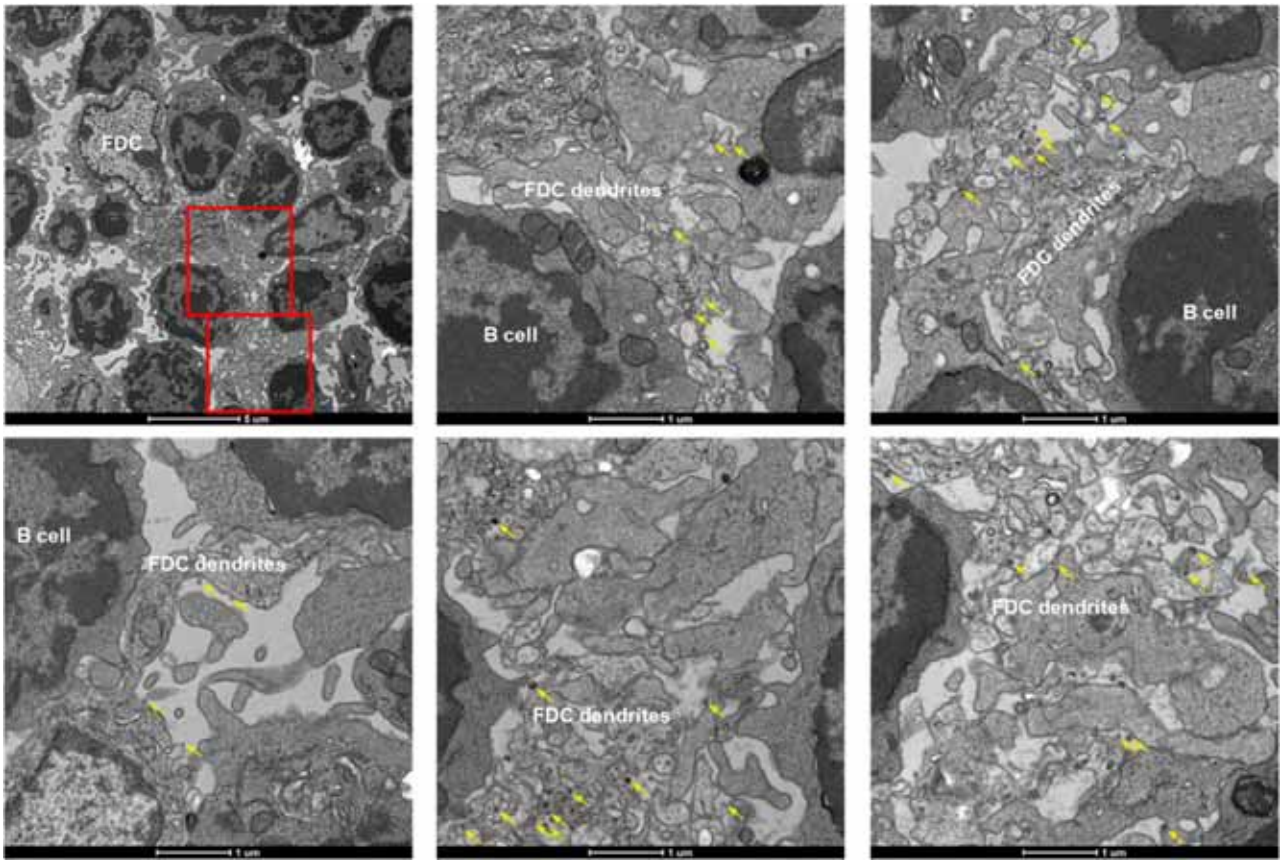

b E2p SApNPs (yellow arrow) are aligned on FDC dendrites after 12 hours of injection

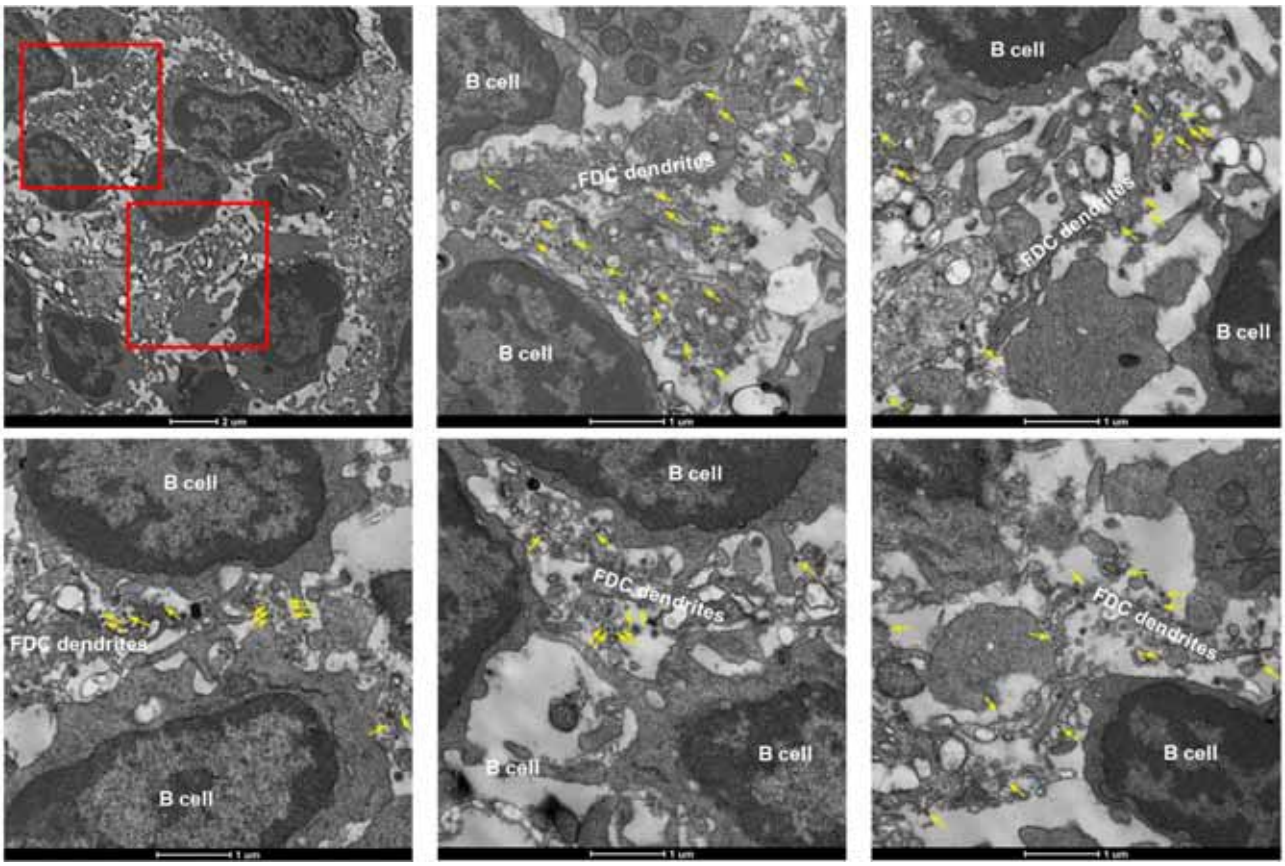

Fig. S7

c E2p SApNPs (yellow arrow) are aligned on FDC dendrites or taken up by B cells after 48 hours of injection

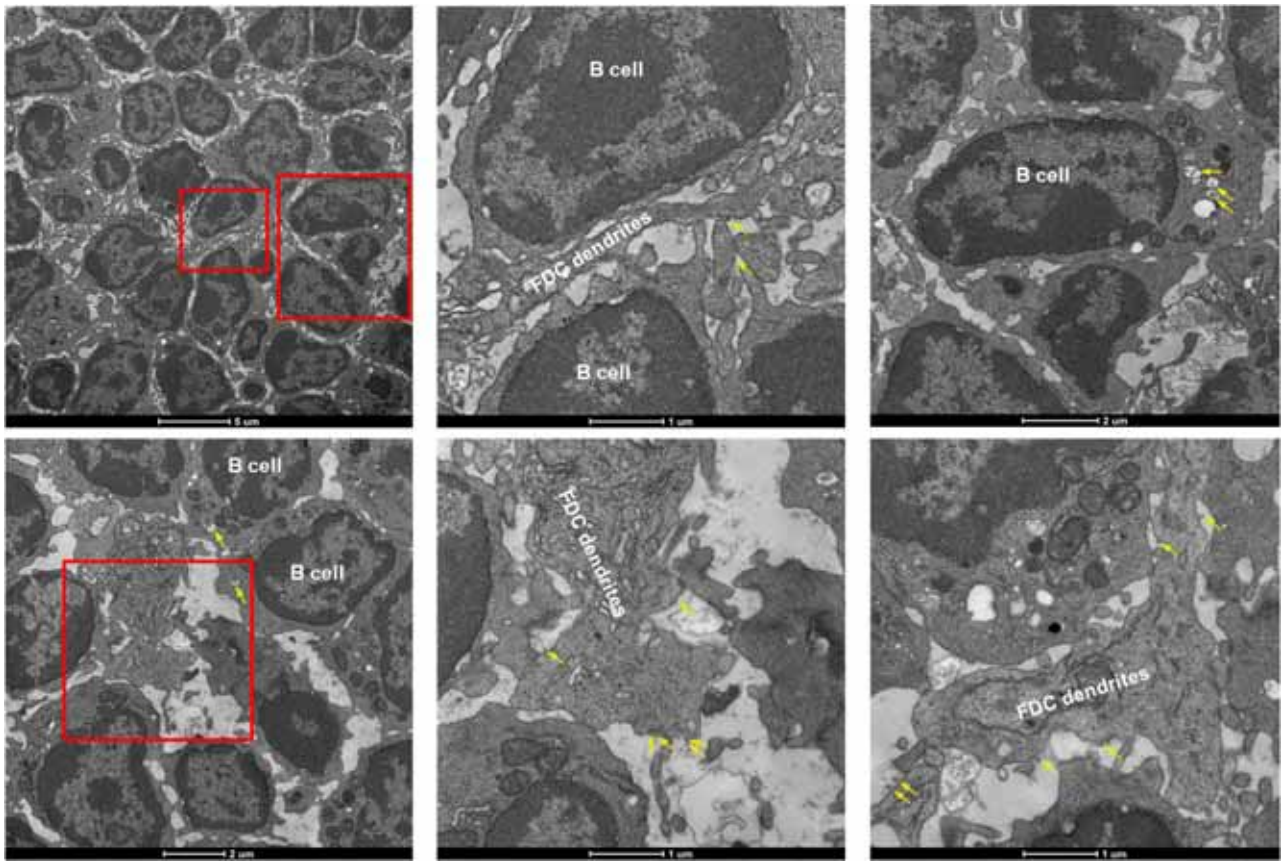

d I3-01v9b SApNPs (yellow arrow) are aligned on FDC dendrites or inside endolysosomes of FDC dendrities after 2 hours of injection

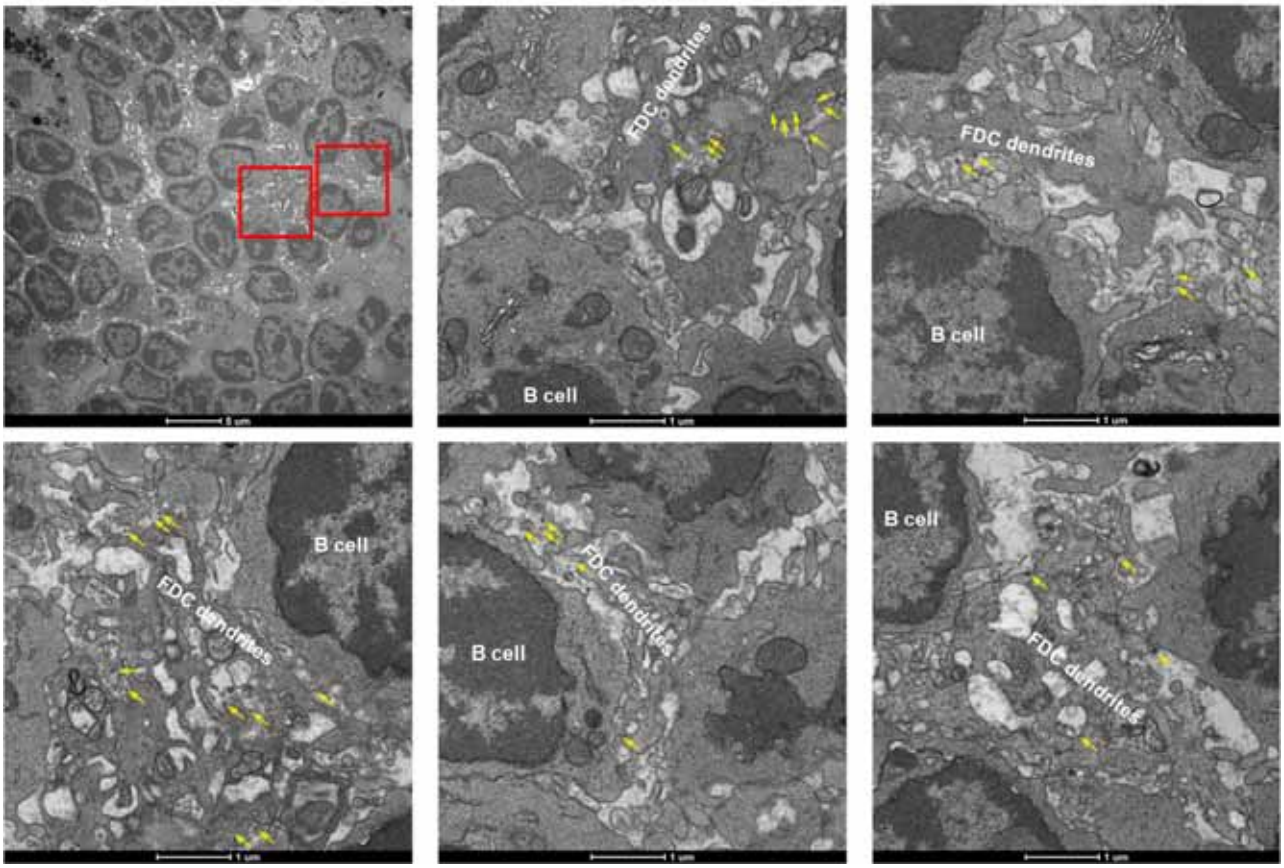

Fig. S7

e I3-01v9b SApNPs (yellow arrow) are aligned on FDC dendrites or taken up by B cells after 12 hours of injection

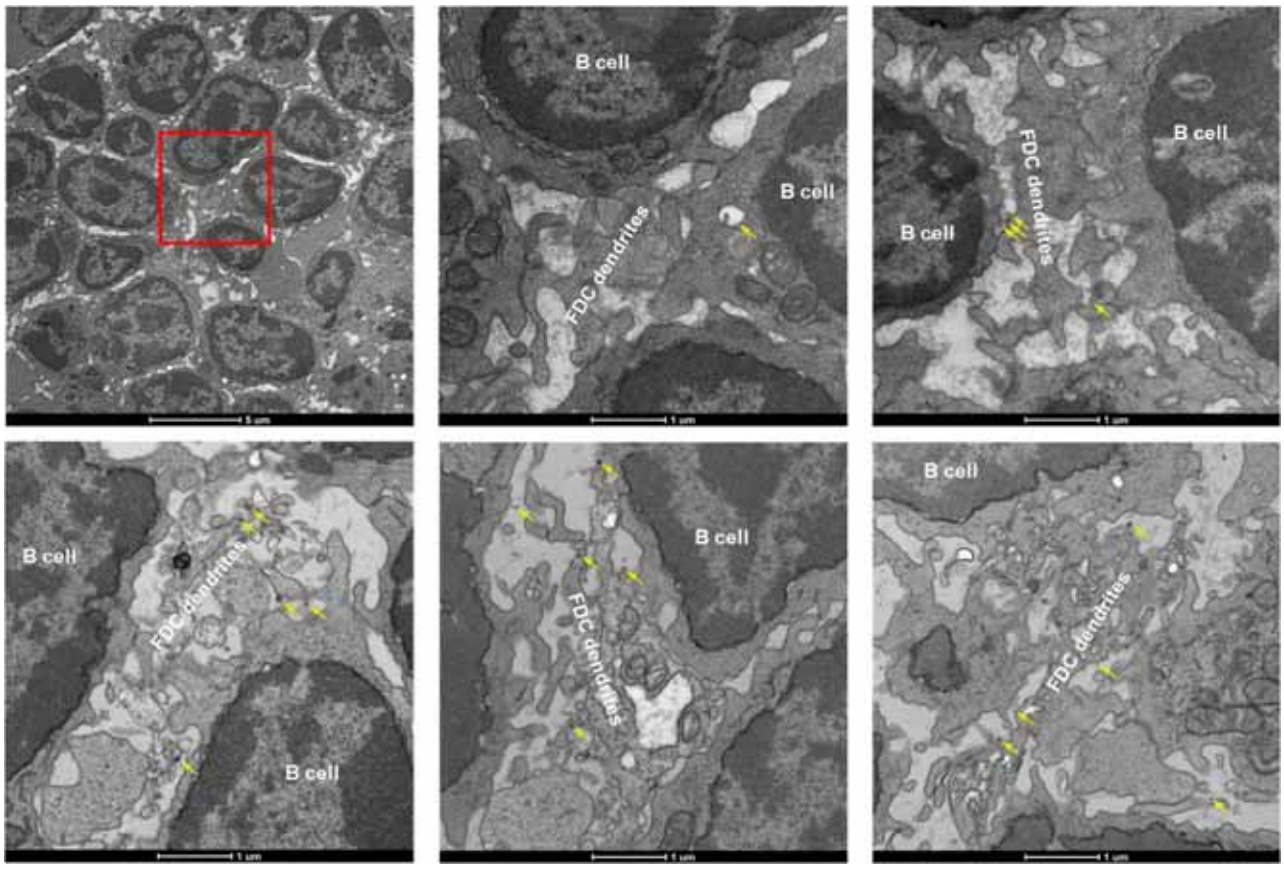

f I3-01v9b SApNPs (yellow arrow) are aligned on FDC dendrites after 48 hours of injection

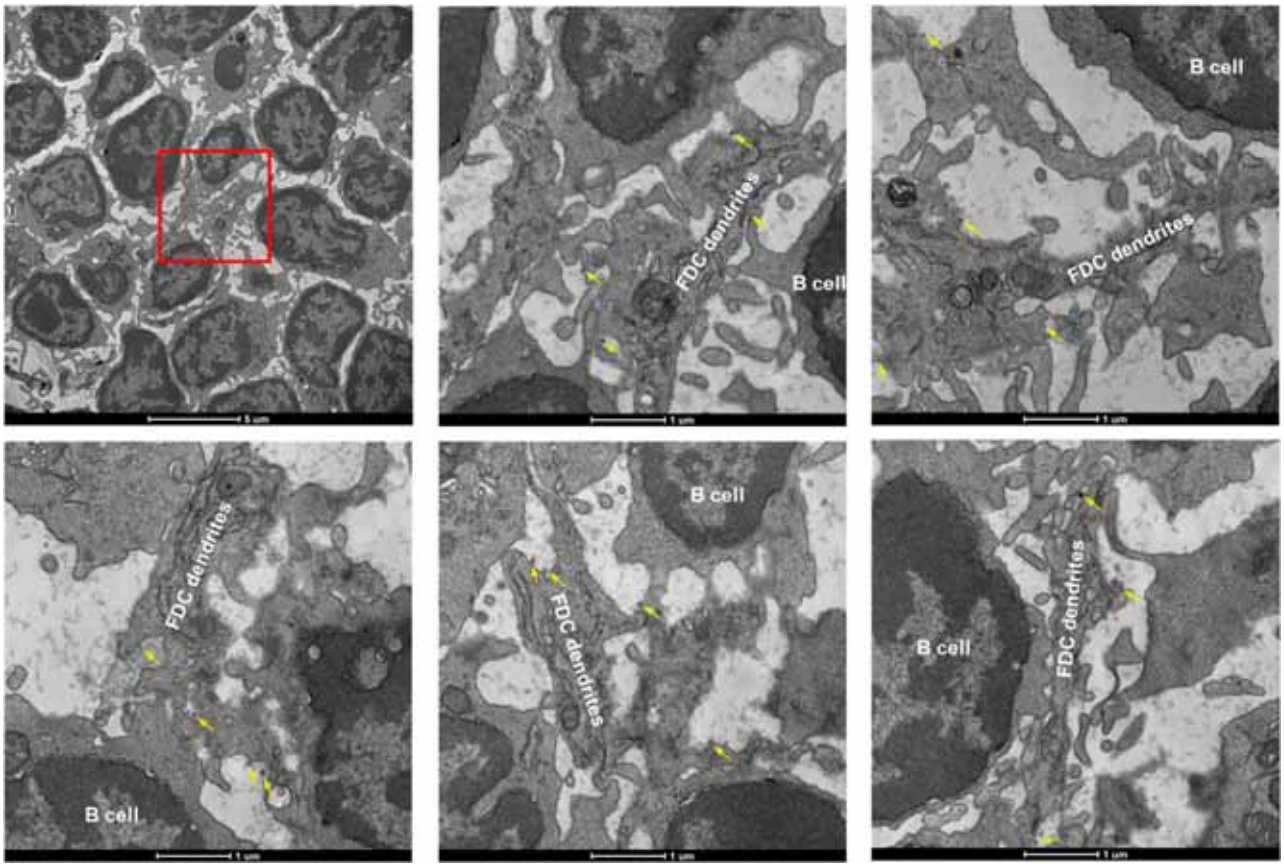

Fig. S7

g E2p SApNPs (yellow arrow) are associated with phagocytic cells after 2 hours of injection

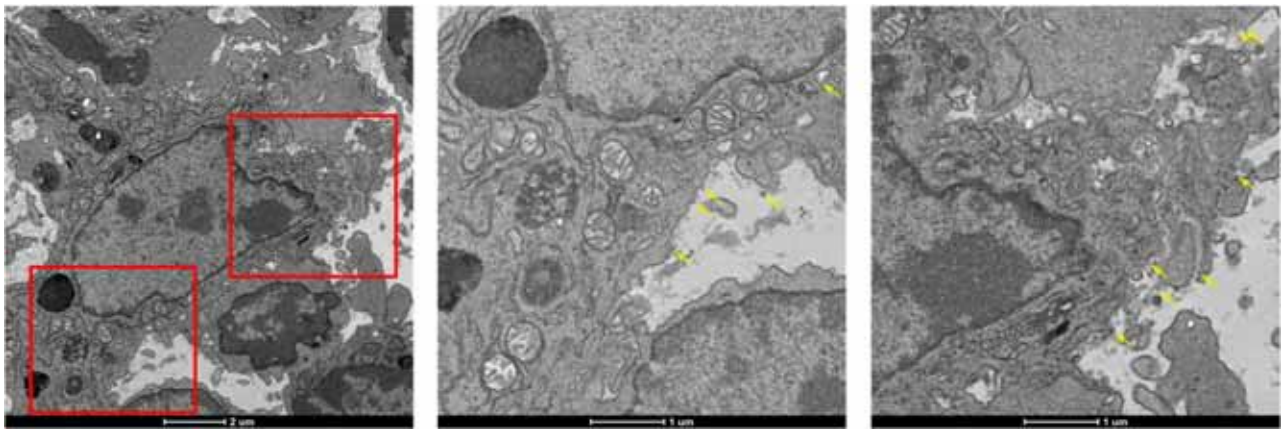

h E2p SApNPs (yellow arrow) are associated with phagocytic cells after 12 hours of injection

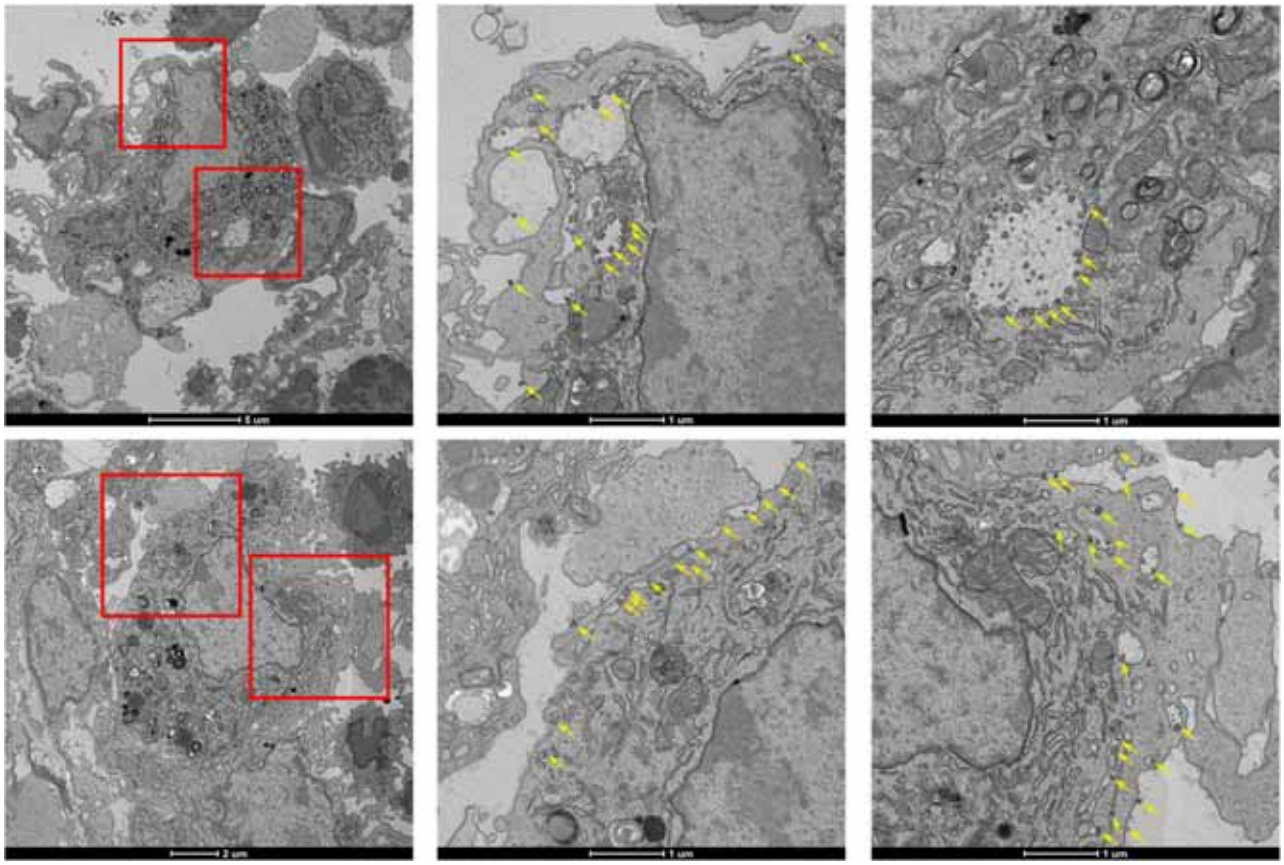

Fig. S7

i E2p SApNPs (yellow arrow) are associated with phagocytic cells after 48 hours of injection

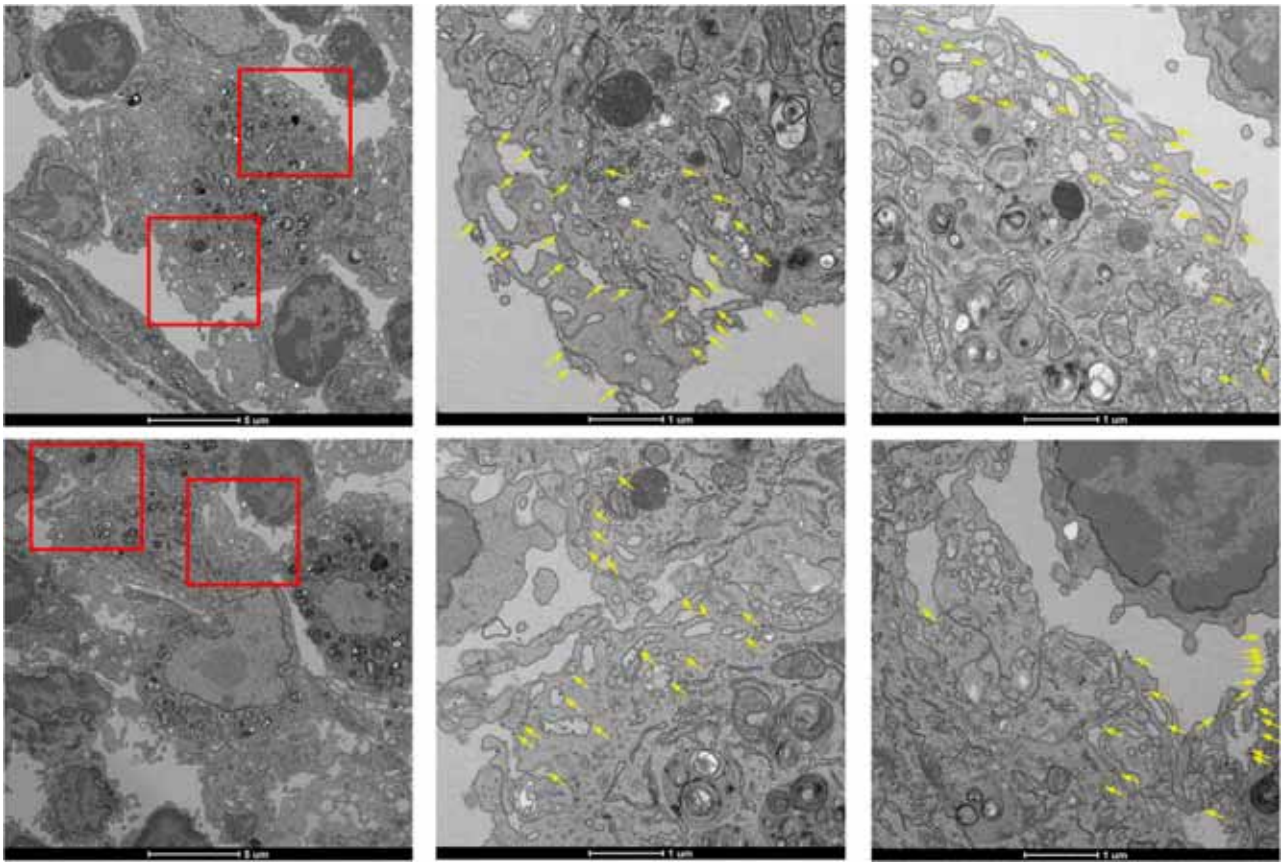

j I3-01v9b SApNPs (yellow arrow) are associated with phagocytic cells after 2 hours of injection

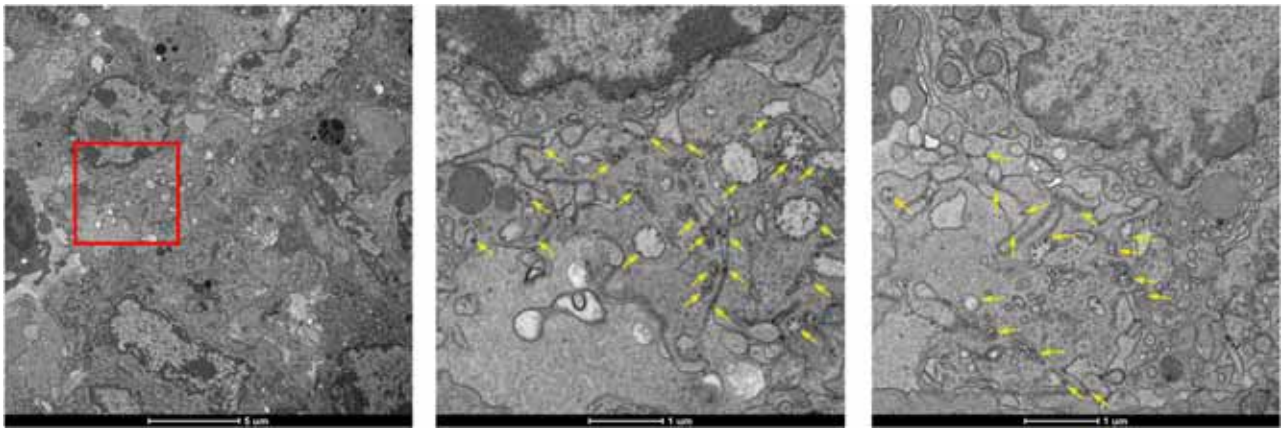

Fig. S7

k I3-01v9b SApNPs (yellow arrow) are associated with phagocytic cells after 12 hours of injection

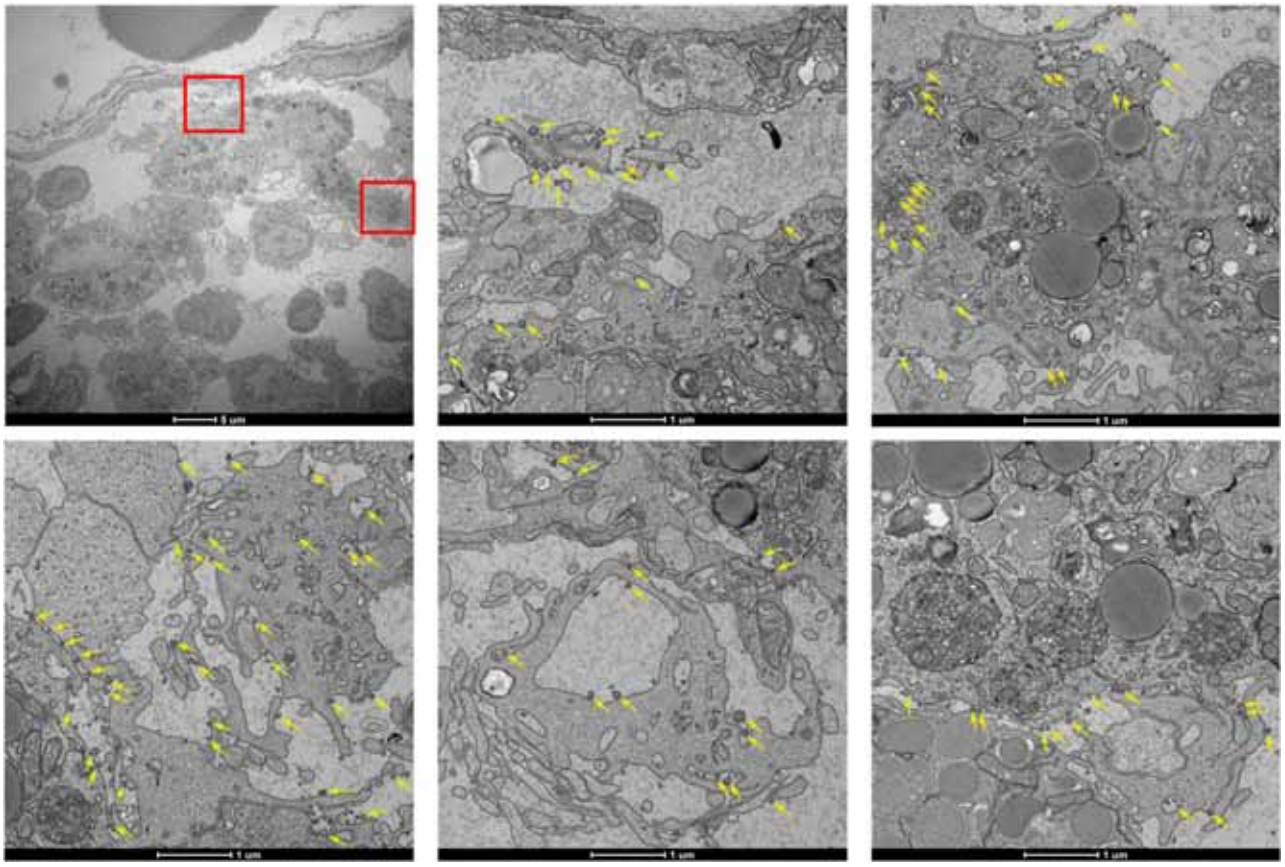

l I3-01v9b SApNPs (yellow arrow) are associated with phagocytic cells after 48 hours of injection

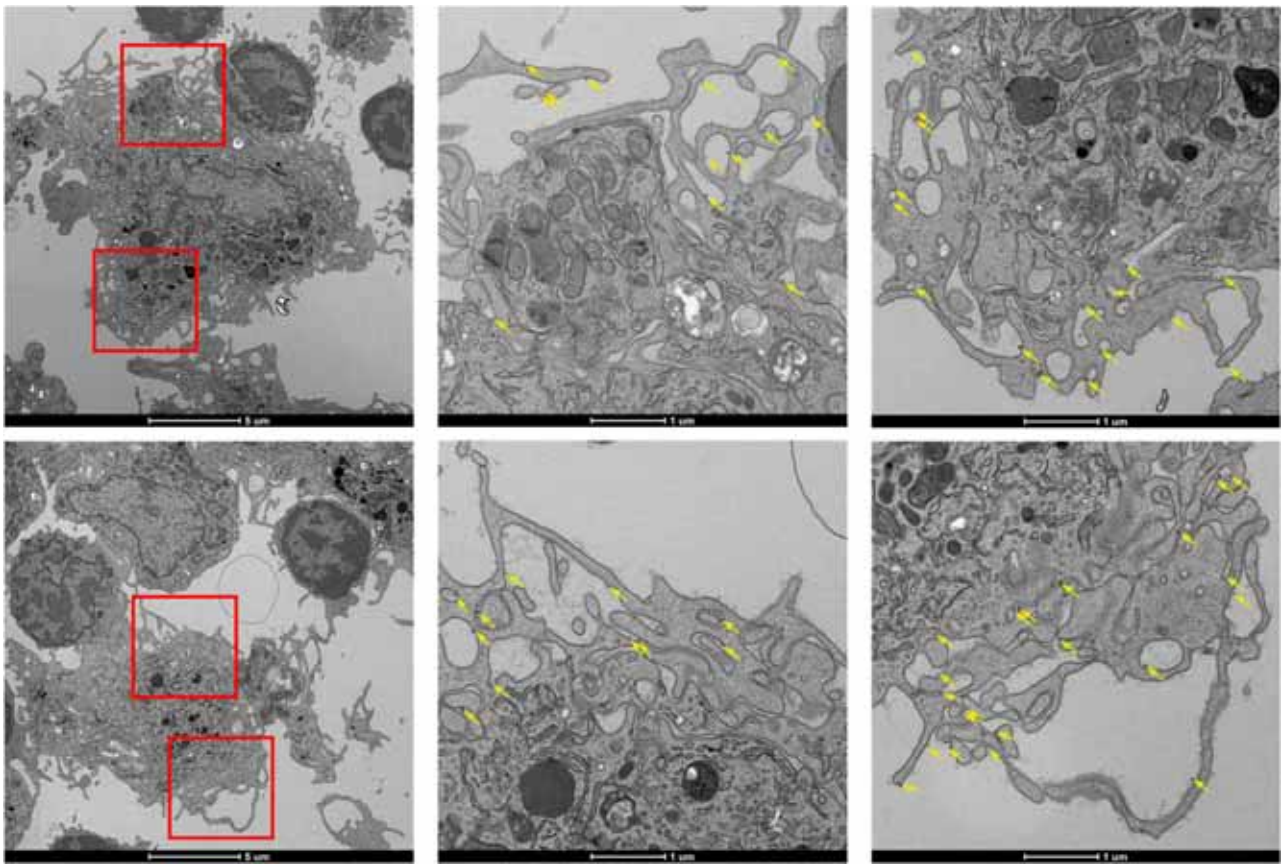

Fig. S7

m Aluminum phosphate (green arrow) tends to aggregate in the ECM after 2 hours of injection

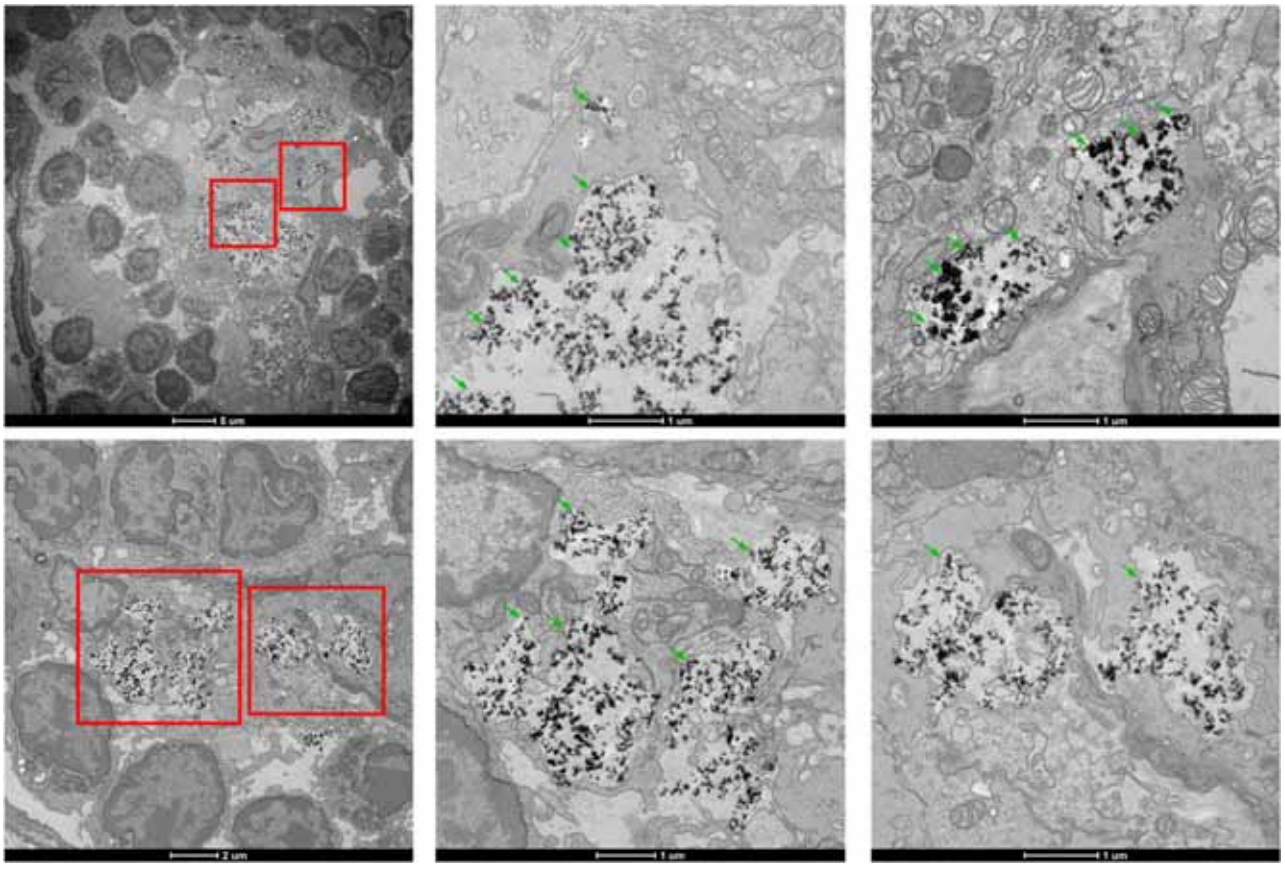

n I3-01v9b SApNPs (yellow arrow) and aluminum phosphate (green arrow) with phagocytic cells at 2 hours

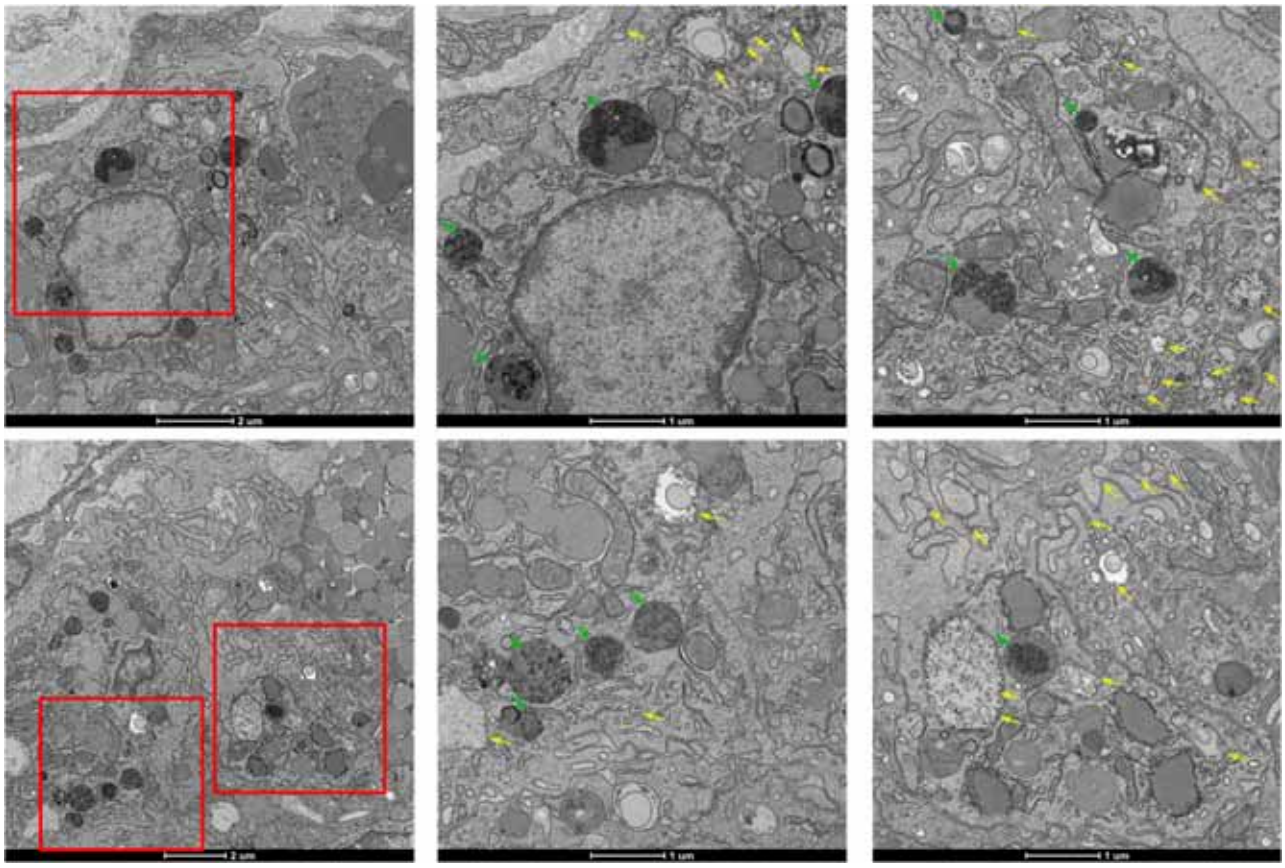

Fig. S7

o I3-01v9b SApNPs (yellow arrow) and aluminum phosphate (green arrow) with phagocytic cells at 12 hours

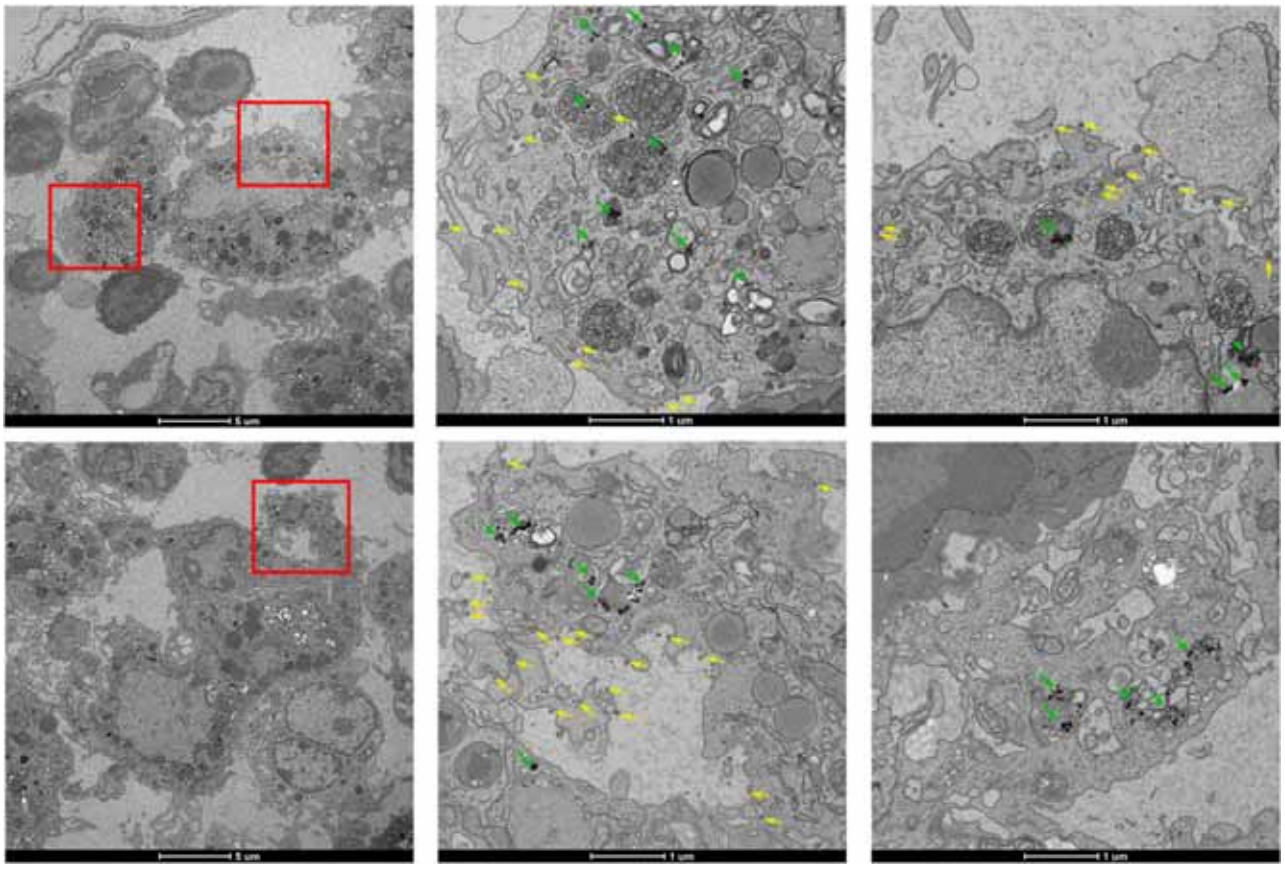

p I3-01v9b SApNPs (yellow arrow) and aluminum phosphate (green arrow) with phagocytic cells at 48 hours

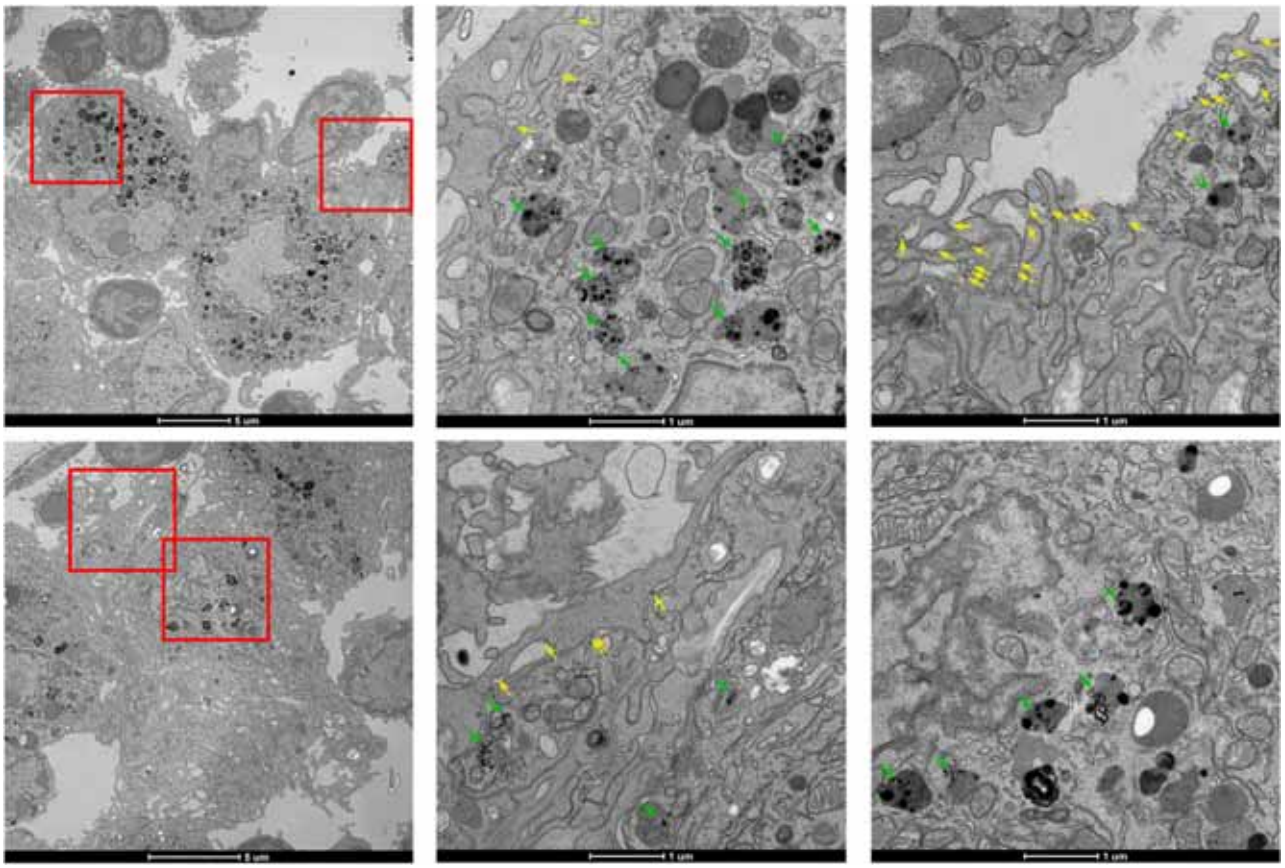

Fig. S7

Fig. S7. TEM images of Sudan GPΔmuc-presenting SApNPs interacting with FDCs and phagocytic cells in a lymph node. SUDV GPΔmuc trimer-presenting E2p SApNPs are aligned on FDC dendrites at (**a**) 2 hours, (**b**) 12 hours, and (**c**) 48 hours after a single-dose injection (2 footpads, 50 μg/footpad). SUDV GPΔmuc trimer-presenting I3-01v9b SApNPs are aligned on FDC dendrites at (**d**) 2 hours, (**e**) 12 hours, and (**f**) 48 hours after a single-dose injection. Aluminum phosphate (AP) particles are not associated with SApNPs on FDC dendrites. SUDV GPΔmuc trimer-presenting E2p SApNPs are aligned on the surface or inside endolysosomes of phagocytic cells at (**g**) 2 hours, (**h**) 12 hours, and (**i**) 48 hours after an injection. SUDV GPΔmuc trimer-presenting I3-01v9b SApNPs are associated with phagocytic cells after (**j**) 2 hours, (**k**) 12 hours, and (**l**) 48 hours after the injection. (**m**) AP particles aggregate in the extracellular matrix 2 hours after the injection. SUDV GPΔmuc trimer-presenting I3-01v9b SApNPs formulated with AP are associated with phagocytic cells at (**n**) 2 hours, (**o**) 12 hours, and (**p**) 48 hours after an injection. TEM images were performed on 2 popliteal lymph nodes for each SApNP construct. E2p or I3-01v9b SApNPs are pointed to by yellow arrows and AP adjuvants are pointed to by green arrows.

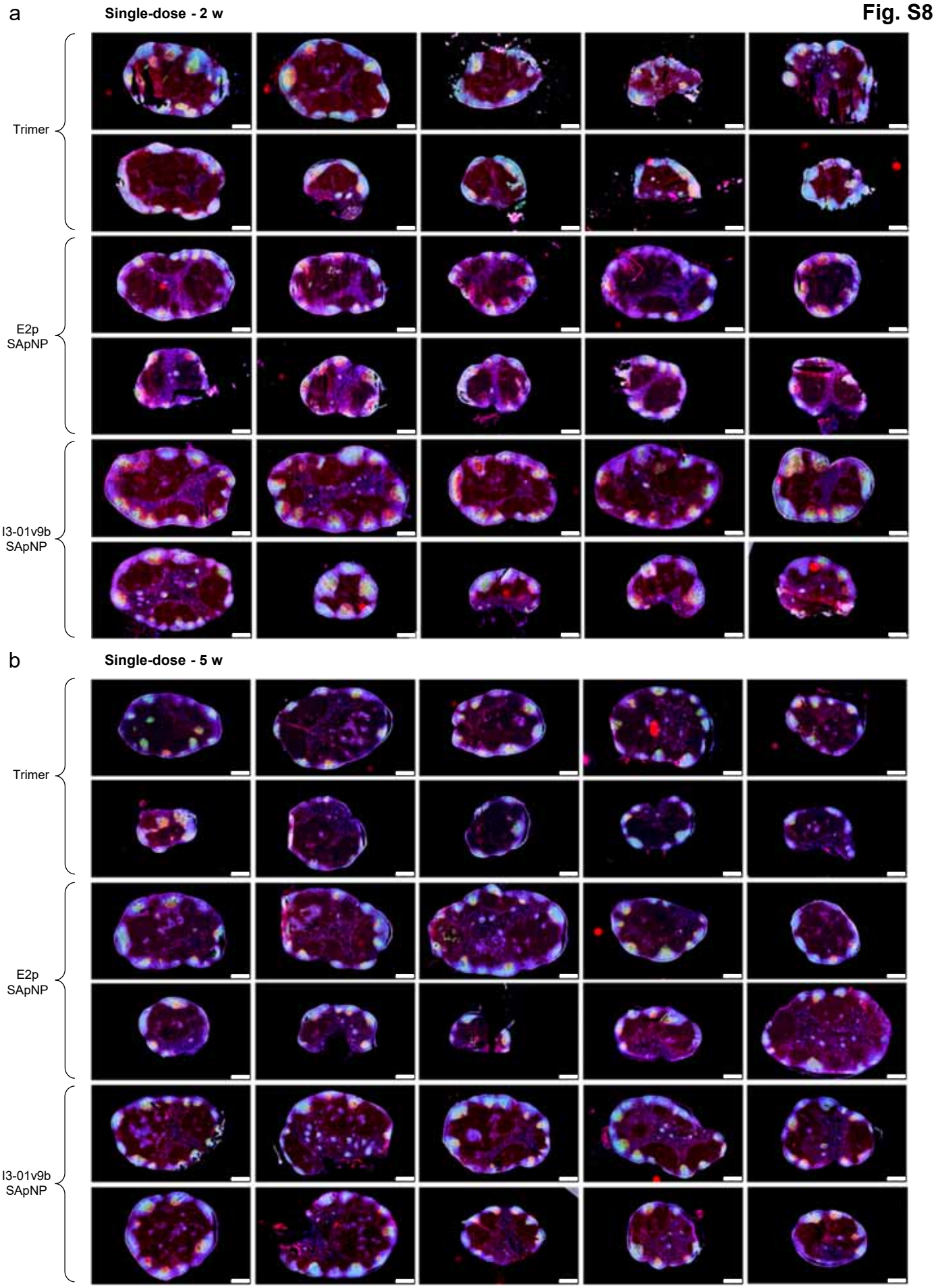

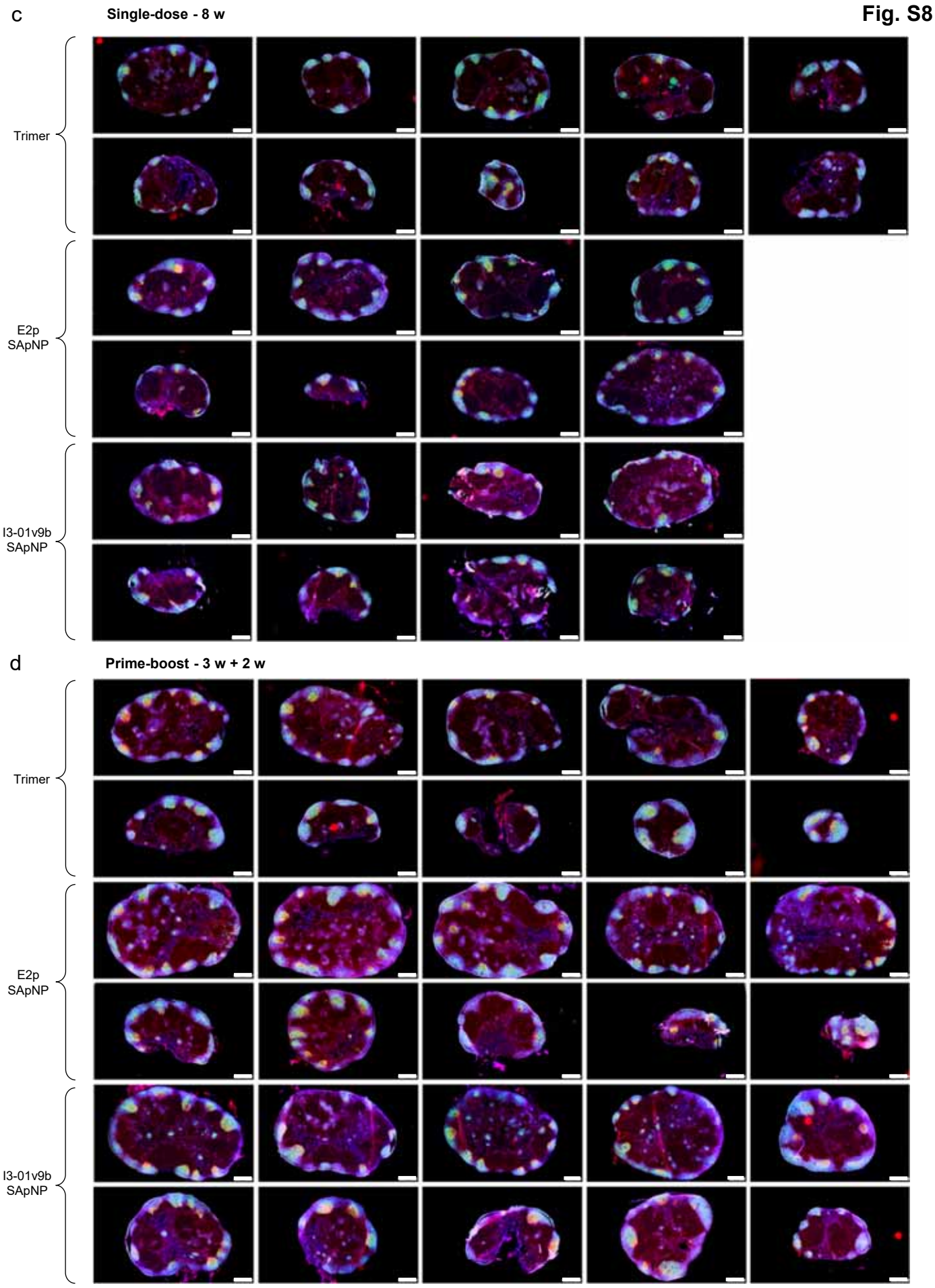

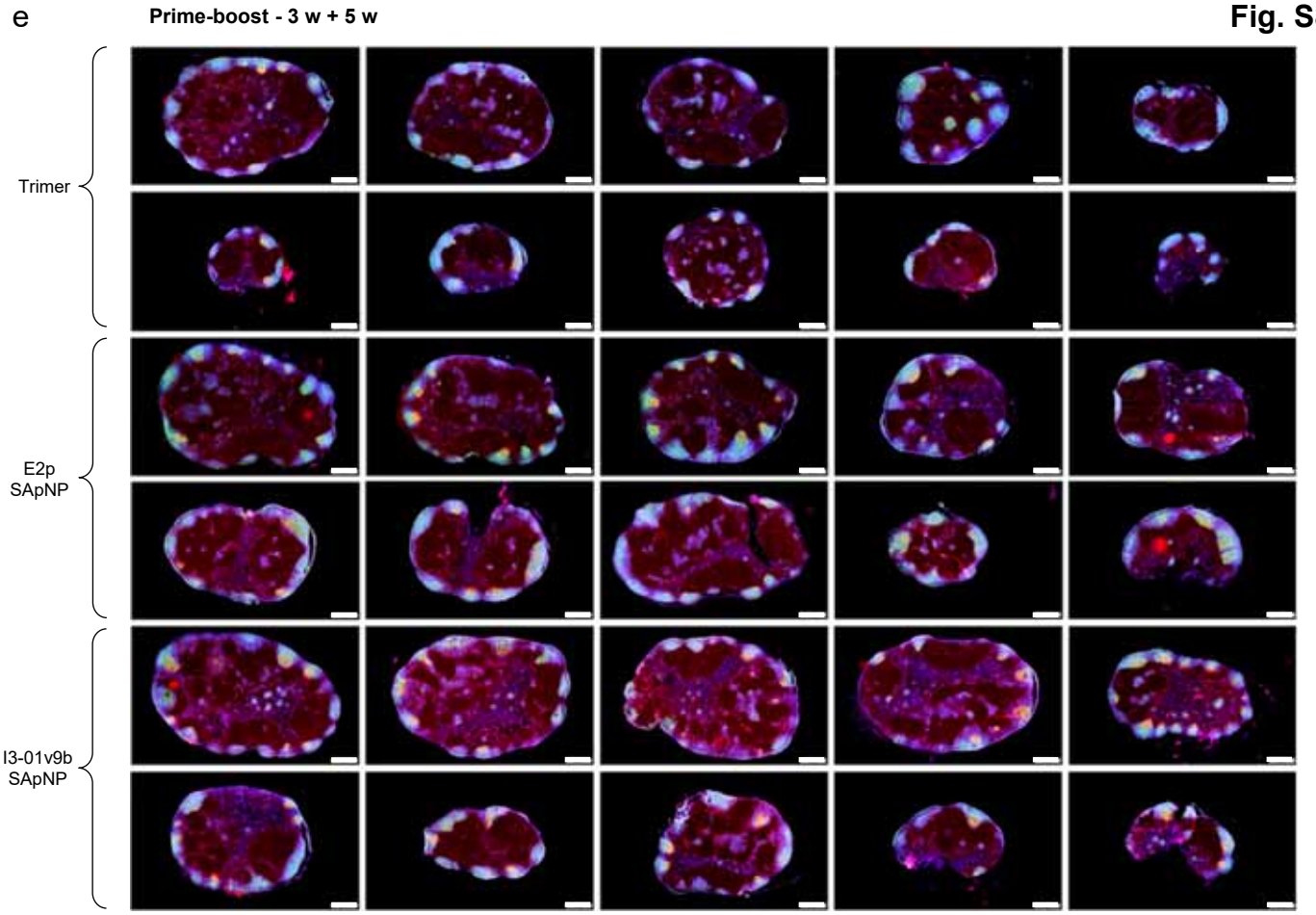

Fig. S8. Immunohistological analysis of SUDV GPΔmuc trimer and SApNP vaccine-induced GCs. Immunohistological images of GCs at (**a**) 2, (**b**) 5, and (**c**) 8 weeks after a single-dose injection of GPΔmuc trimer and GPΔmuc trimer-presenting E2p and I3-01v9b SApNPs (10 μg per injection, totaling 40 μg per mouse). Images of GCs at (**d**) 2 and (**e**) 5 weeks after the boost, which occurred at 3 weeks after the first dose (n = 5 mice/group). Immunofluorescent images are pseudo color coded (GL7+, red; CD21+, green; B220, blue). Scale bars = 500 μm for each image of a lymph node.

a

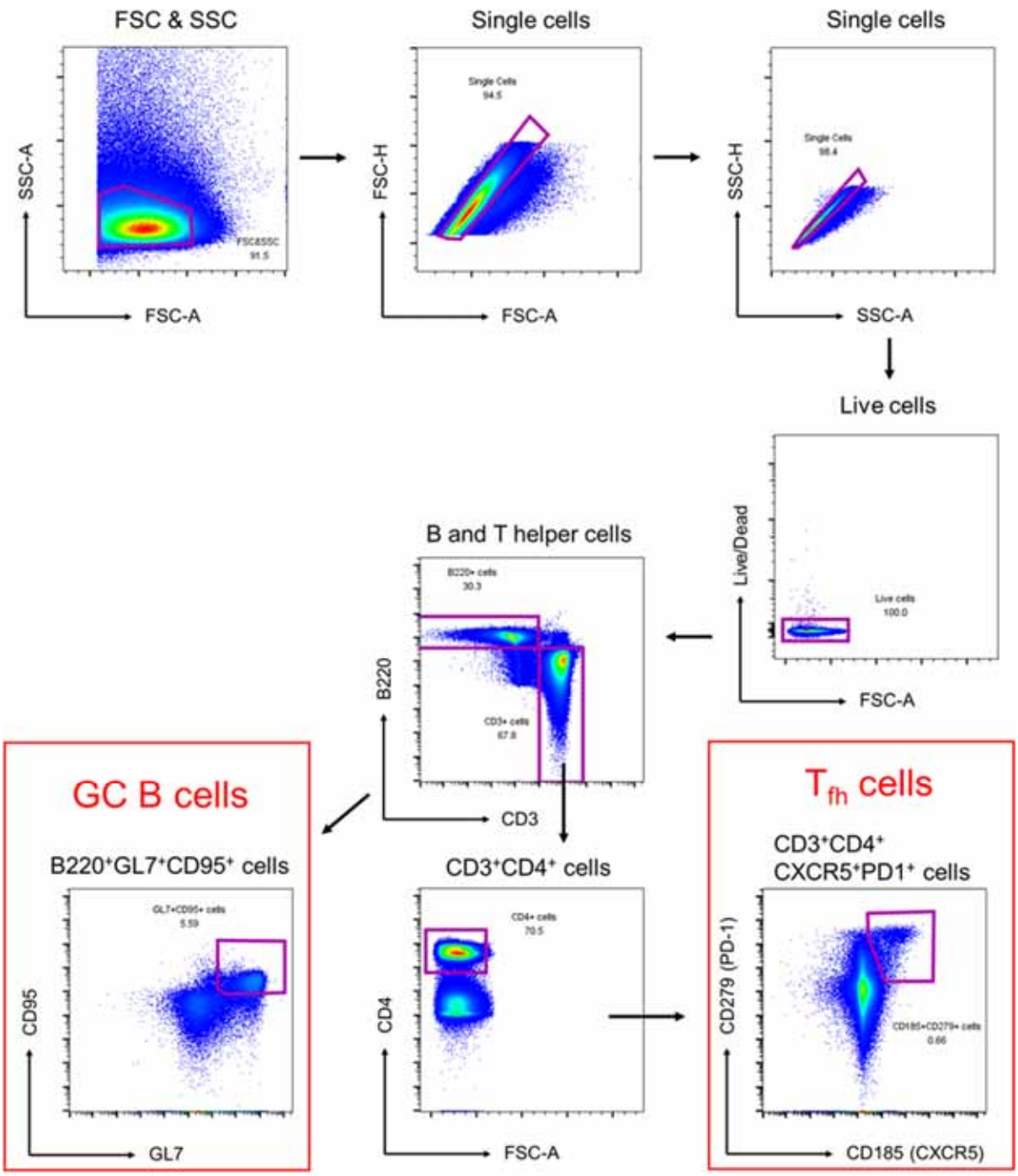

Fig. S9. Flow cytometry analysis of SUDV GPΔmuc trimer and SApNPs vaccine-induced GCs. Gating strategy for analyzing GCs (GC B cells and T follicular helper cells) using flow cytometry (*n* = 5 mice/group).

Fig. S10

a Sera of individual mice immunized with EBOV vaccines binding to EBOV GPΔmuc-WL^{2}P^4(1TD0) trimer

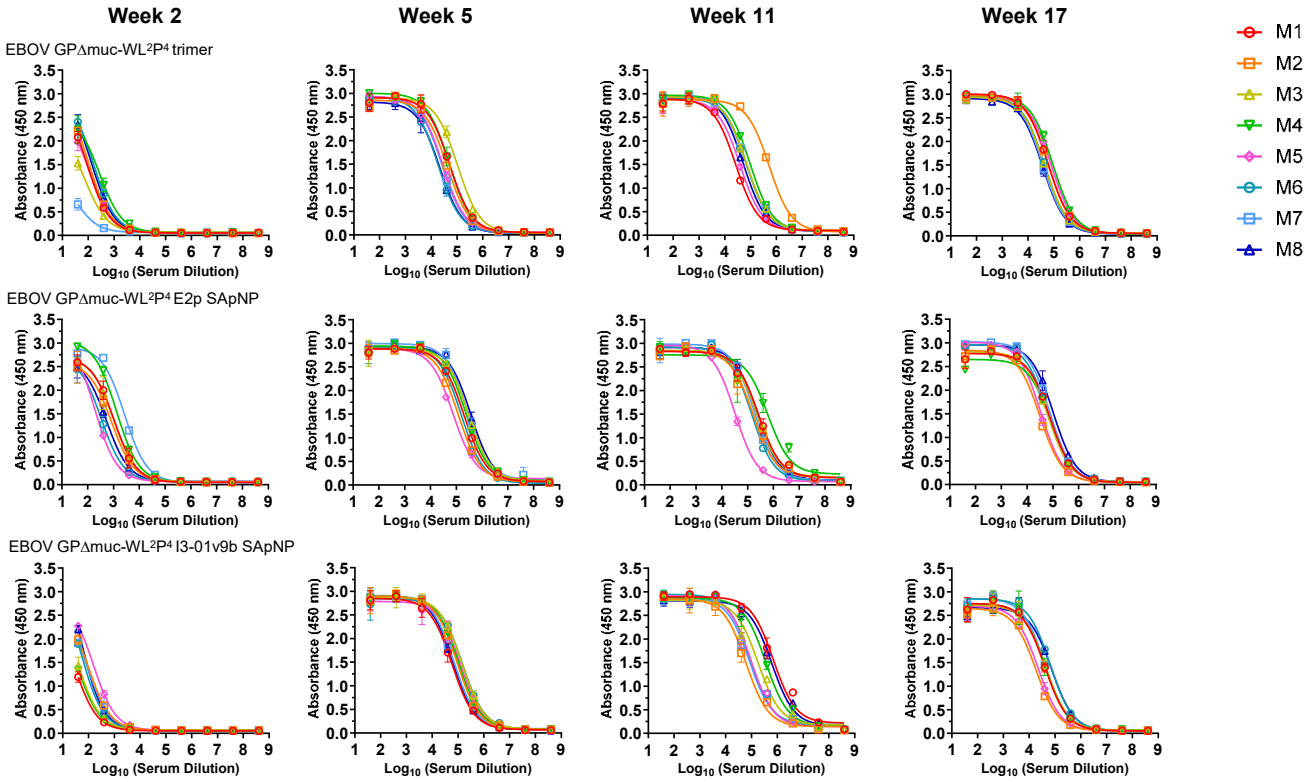

b Mouse serum ELISA EC_{50} titers

Week 2

Antigen	EC50 titers (week 2)								Geometric Mean
	M1	M2	M3	M4	M5	M6	M7	M8	
EBOV GPΔmuc-WL^{2}P^4 trimer	111.7	136.3	51.3	227.2	103.0	200.2	12.6	173.3	97.3
EBOV GPΔmuc-WL^{2}P^4 E2p SApNP	985.3	706.4	970.8	1772.0	271.5	336.1	3145.0	486.4	799.6
EBOV GPΔmuc-WL^{2}P^4 I3-01v9b SApNP	30.1	101.8	43.0	37.9	172.4	80.7	91.5	115.6	72.1

Week 5

Antigen	EC50 titers (week 5)								Geometric Mean
	M1	M2	M3	M4	M5	M6	M7	M8	
EBOV GPΔmuc-WL^{2}P^4 trimer	52545	41735	104914	48787	27947	18271	26144	21434	36588.3
EBOV GPΔmuc-WL^{2}P^4 E2p SApNP	199849	120954	303168	237335	74446	156667	282413	368341	195227.1
EBOV GPΔmuc-WL^{2}P^4 I3-01v9b SApNP	58458	93275	140476	104463	128829	148277	70114	63709	95341.8

Week 11

Antigen	EC50 titers (week 11)								Geometric Mean
	M1	M2	M3	M4	M5	M6	M7	M8	
EBOV GPΔmuc-WL^{2}P^4 trimer	26545	524033	69054	94400	39464	69865	68351	51944	73880.6
EBOV GPΔmuc-WL^{2}P^4 E2p SApNP	267135	163352	223491	606328	32762	143908	182928	233182	181721.7
EBOV GPΔmuc-WL^{2}P^4 I3-01v9b SApNP	703967	60730	178784	354031	97482	91294	82827	610293	182253.3

Week 17

Antigen	EC50 titers (week 17)								Geometric Mean
	M1	M2	M3	M4	M5	M6	M7	M8	
EBOV GPΔmuc-WL^{2}P^4-FOLD	59703	59841	42414	92526	80033	44111	36894	36448	53444.3
EBOV GPΔmuc-WL^{2}P^4 E2p SApNP	78072	31500	66659	79702	33830	63116	75359	105584	62128.2
EBOV GPΔmuc-WL^{2}P^4 I3-01v9b SApNP	40965	18206	43559	42711	22529	65820	41237	74760	39837.1

Statistical analysis

One-way ANOVA with Tukey's multiple comparisons test (w2)	Statistics	Adjusted P Value
EBOV GPΔmuc-WL^{2}P^4 trimer vs. EBOV GPΔmuc-WL^{2}P^4 E2p SApNP	**	0.0067
EBOV GPΔmuc-WL^{2}P^4 trimer vs. EBOV GPΔmuc-WL^{2}P^4 I3-01v9b SApNP	ns	0.9871
EBOV GPΔmuc-WL^{2}P^4 E2p SApNP vs. EBOV GPΔmuc-WL^{2}P^4 I3-01v9b SApNP	**	0.0047

One-way ANOVA with Tukey's multiple comparisons test (w5)	Statistics	Adjusted P Value
EBOV GPΔmuc-WL^{2}P^4 trimer vs. EBOV GPΔmuc-WL^{2}P^4 E2p SApNP	****	<0.0001
EBOV GPΔmuc-WL^{2}P^4 trimer vs. EBOV GPΔmuc-WL^{2}P^4 I3-01v9b SApNP	ns	0.1769
EBOV GPΔmuc-WL^{2}P^4 E2p SApNP vs. EBOV GPΔmuc-WL^{2}P^4 I3-01v9b SApNP	**	0.0034

One-way ANOVA with Tukey's multiple comparisons test (w11)	Statistics	Adjusted P Value
EBOV GPΔmuc-WL^{2}P^4 trimer vs. EBOV GPΔmuc-WL^{2}P^4 E2p SApNP	ns	0.5058
EBOV GPΔmuc-WL^{2}P^4 trimer vs. EBOV GPΔmuc-WL^{2}P^4 I3-01v9b SApNP	ns	0.2942
EBOV GPΔmuc-WL^{2}P^4 E2p SApNP vs. EBOV GPΔmuc-WL^{2}P^4 I3-01v9b SApNP	ns	0.9135

One-way ANOVA with Tukey's multiple comparisons test (w17)	Statistics	Adjusted P Value
EBOV GPΔmuc-WL^{2}P^4 trimer vs. EBOV GPΔmuc-WL^{2}P^4 E2p SApNP	ns	0.6171
EBOV GPΔmuc-WL^{2}P^4 trimer vs. EBOV GPΔmuc-WL^{2}P^4 I3-01v9b SApNP	ns	0.4761
EBOV GPΔmuc-WL^{2}P^4 E2p SApNP vs. EBOV GPΔmuc-WL^{2}P^4 I3-01v9b SApNP	ns	0.1078

Fig. S10

c Week-7 sera of individual mice immunized with EBOV vaccines binding to SUDV GPΔmuc-WL^{2}P^4(1TD0) trimer

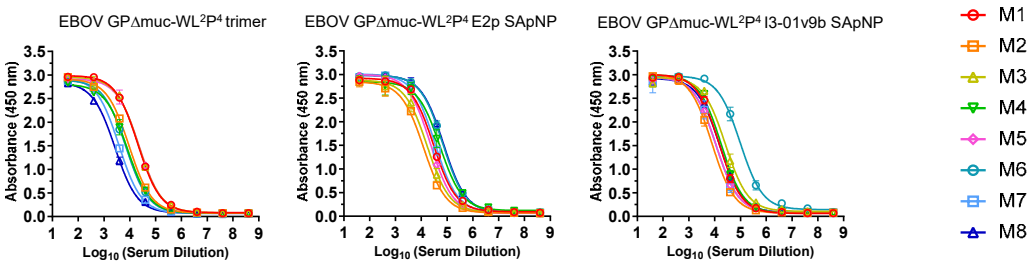

Mouse serum ELISA EC_{50} titers

	Antigen	EC50 titers (week 17)								Geometric Mean
		M1	M2	M3	M4	M5	M6	M7	M8	
Week 17	EBOV GPΔmuc-WL^{2}P^4 trimer	20545	9375	21603	8039	22891	7014	3805	2676	9273.3
	EBOV GPΔmuc-WL^{2}P^4 E2p SApNP	29973	12206	17018	52874	22735	68558	33997	72867	32585.3
	EBOV GPΔmuc-WL^{2}P^4 I3-01v9b SApNP	15023	7900	26186	17813	11241	97786	11184	15787	17943.0

Statistical analysis

One-way ANOVA with Tukey's multiple comparisons test (w17)	Statistics	Adjusted P Value
EBOV GPΔmuc-WL^{2}P^4 trimer vs. EBOV GPΔmuc-WL^{2}P^4 E2p SApNP	ns	0.0641
EBOV GPΔmuc-WL^{2}P^4 trimer vs. EBOV GPΔmuc-WL^{2}P^4 I3-01v9b SApNP	ns	0.4678
EBOV GPΔmuc-WL^{2}P^4 E2p SApNP vs. EBOV GPΔmuc-WL^{2}P^4 I3-01v9b SApNP	ns	0.4656

d Week-17 sera of individual mice immunized with EBOV vaccines binding to RAVV GPΔmuc-P^{2}CT(1TD0) trimer

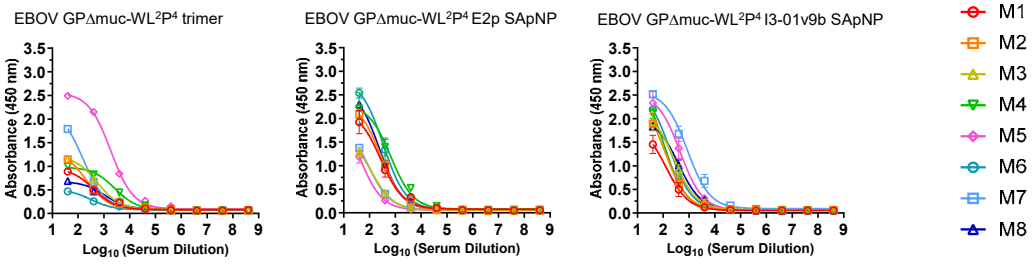

Mouse serum ELISA EC_{50} titers

	Antigen	Absorbance (450 nm) (week 17)								Geometric Mean
		M1	M2	M3	M4	M5	M6	M7	M8	
Week 17	EBOV GPΔmuc-WL^{2}P^4 trimer	0.9	1.1	1.2	1.0	2.5	0.5	1.8	0.7	1.1
	EBOV GPΔmuc-WL^{2}P^4 E2p SApNP	1.9	2.1	1.3	2.2	1.2	2.5	1.4	2.3	1.8
	EBOV GPΔmuc-WL^{2}P^4 I3-01v9b SApNP	1.5	1.9	1.9	2.1	2.3	2.2	2.5	1.8	2.0

Statistical analysis

One-way ANOVA with Tukey's multiple comparisons test (w17)	Statistics	Adjusted P Value
EBOV GPΔmuc-WL^{2}P^4 trimer vs. EBOV GPΔmuc-WL^{2}P^4 E2p SApNP	*	0.0449
EBOV GPΔmuc-WL^{2}P^4 trimer vs. EBOV GPΔmuc-WL^{2}P^4 I3-01v9b SApNP	*	0.0111
EBOV GPΔmuc-WL^{2}P^4 E2p SApNP vs. EBOV GPΔmuc-WL^{2}P^4 I3-01v9b SApNP	ns	0.7982

Fig. S10

e Sera of individual mice immunized with EBOV vaccines neutralizing an EBOV Makona strain

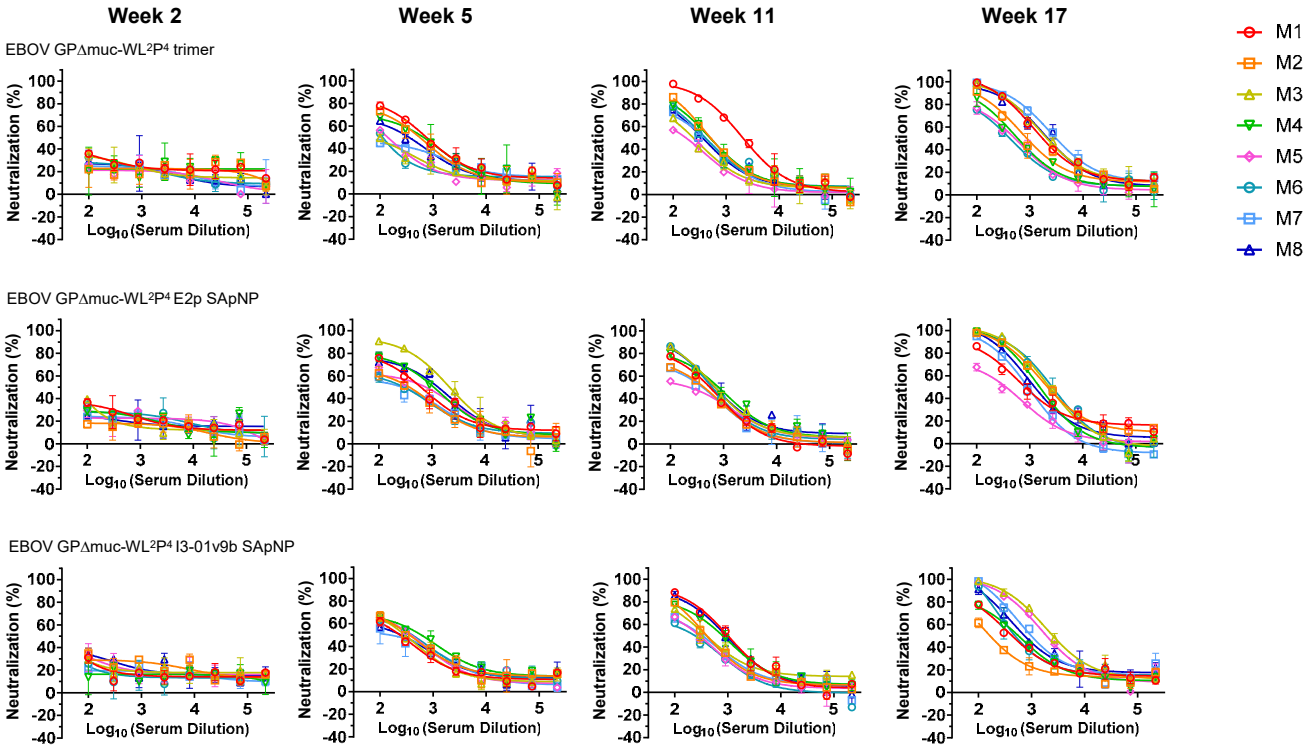

f Mouse serum neutralizing ID_{50} titers

Week 2

Antigen	ID50 titers (week 2)								Geometric Mean
	M1	M2	M3	M4	M5	M6	M7	M8	
EBOV GPΔmuc-WL²P⁴ trimer	<100	<100	<100	<100	<100	<100	<100	<100	N/A
EBOV GPΔmuc-WL²P⁴ E2p SApNP	<100	<100	<100	<100	<100	<100	<100	<100	N/A
EBOV GPΔmuc-WL²P⁴ I3-01v9b SApNP	<100	<100	<100	<100	<100	<100	<100	<100	N/A

Week 5

Antigen	ID50 titers (week 5)								Geometric Mean
	M1	M2	M3	M4	M5	M6	M7	M8	
EBOV GPΔmuc-WL²P⁴ trimer	805.4	559.3	149.3	588.2	174.1	145.1	203.2	360.5	304.1
EBOV GPΔmuc-WL²P⁴ E2p SApNP	636.9	358.8	2178.0	1002.0	555.2	322.9	299.4	1167.0	648.4
EBOV GPΔmuc-WL²P⁴ I3-01v9b SApNP	267.9	390.2	313.1	575.8	378.9	413.4	258.7	296.7	350.3

Week 11

Antigen	ID50 titers (week 11)								Geometric Mean
	M1	M2	M3	M4	M5	M6	M7	M8	
EBOV GPΔmuc-WL²P⁴ trimer	2117.0	560.6	254.4	521.5	188.7	430.2	369.3	377.3	453.2
EBOV GPΔmuc-WL²P⁴ E2p SApNP	494.5	392.0	734.2	747.4	275.3	643.8	365.2	759.9	518.6
EBOV GPΔmuc-WL²P⁴ I3-01v9b SApNP	1006.0	434.9	454.1	766.3	289.4	237.7	327.0	928.5	487.3

Week 17

Antigen	ID50 titers (week 17)								Geometric Mean
	M1	M2	M3	M4	M5	M6	M7	M8	
EBOV GPΔmuc-WL²P⁴ trimer	2106.0	1038.0	2482.0	641.1	505.0	437.0	3537.0	2352.0	1260.8
EBOV GPΔmuc-WL²P⁴ E2p SApNP	1000.0	2501.0	2393.0	1580.0	329.2	2587.0	875.5	1415.0	1333.1
EBOV GPΔmuc-WL²P⁴ I3-01v9b SApNP	513.1	205.2	2961.0	592.6	2154.0	693.4	1272.0	994.0	876.7

Statistical analysis

One-way ANOVA with Tukey's multiple comparisons test (w5)	Statistics	Adjusted P Value
EBOV GPΔmuc-WL²P⁴ trimer vs. EBOV GPΔmuc-WL²P⁴ E2p SApNP	ns	0.0919
EBOV GPΔmuc-WL²P⁴ trimer vs. EBOV GPΔmuc-WL²P⁴ I3-01v9b SApNP	ns	0.9982
EBOV GPΔmuc-WL²P⁴ E2p SApNP vs. EBOV GPΔmuc-WL²P⁴ I3-01v9b SApNP	ns	0.0824

One-way ANOVA with Tukey's multiple comparisons test (w11)	Statistics	Adjusted P Value
EBOV GPΔmuc-WL²P⁴ trimer vs. EBOV GPΔmuc-WL²P⁴ E2p SApNP	ns	0.9676
EBOV GPΔmuc-WL²P⁴ trimer vs. EBOV GPΔmuc-WL²P⁴ I3-01v9b SApNP	ns	0.9724
EBOV GPΔmuc-WL²P⁴ E2p SApNP vs. EBOV GPΔmuc-WL²P⁴ I3-01v9b SApNP	ns	0.9998

One-way ANOVA with Tukey's multiple comparisons test (w17)	Statistics	Adjusted P Value
EBOV GPΔmuc-WL²P⁴ trimer vs. EBOV GPΔmuc-WL²P⁴ E2p SApNP	ns	0.9938
EBOV GPΔmuc-WL²P⁴ trimer vs. EBOV GPΔmuc-WL²P⁴ I3-01v9b SApNP	ns	0.618
EBOV GPΔmuc-WL²P⁴ E2p SApNP vs. EBOV GPΔmuc-WL²P⁴ I3-01v9b SApNP	ns	0.6831

Fig. S10

g Week-17 sera of individual mice immunized with EBOV vaccines neutralizing a SUDV Gulu strain

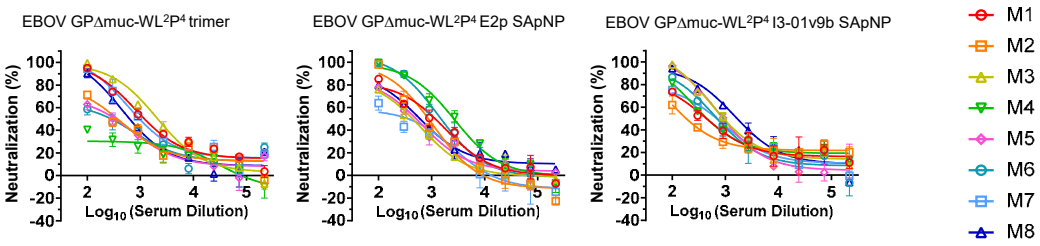

Mouse serum neutralizing ID_{50} titers

	Antigen	ID50 titers (week 17)								Geometric Mean
		M1	M2	M3	M4	M5	M6	M7	M8	
Week 17	EBOV GPΔmuc-WL^{2}P^4 trimer	1530.0	407.3	2200.0	113.8	341.2	323.2	1236.0	726.5	593.8
	EBOV GPΔmuc-WL^{2}P^4 E2p SApNP	956.0	759.0	403.8	2580.0	489.0	1564.0	301.3	647.6	761.3
	EBOV GPΔmuc-WL^{2}P^4 I3-01v9b SApNP	512.3	265.2	1198.0	608.8	1006.0	765.2	662.5	1824.0	742.3

Statistical analysis

One-way ANOVA with Tukey's multiple comparisons test (w17)	Statistics	Adjusted P Value
EBOV GPΔmuc-WL^{2}P^4 trimer vs. EBOV GPΔmuc-WL^{2}P^4 E2p SApNP	ns	0.9497
EBOV GPΔmuc-WL^{2}P^4 trimer vs. EBOV GPΔmuc-WL^{2}P^4 I3-01v9b SApNP	ns	>0.9999
EBOV GPΔmuc-WL^{2}P^4 E2p SApNP vs. EBOV GPΔmuc-WL^{2}P^4 I3-01v9b SApNP	ns	0.9453

h Week-17 sera of individual mice immunized with EBOV vaccines neutralizing a BDBV Uganda strain

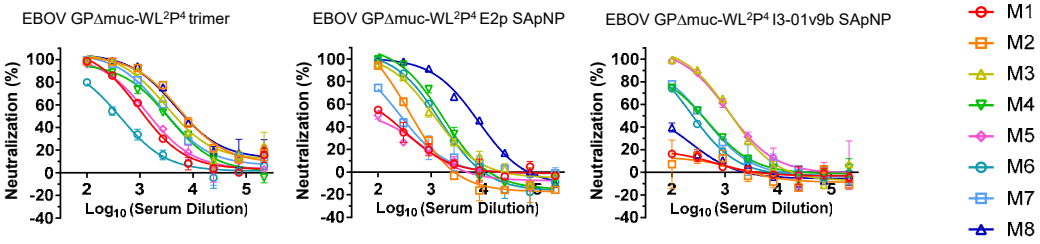

Mouse serum neutralizing ID_{50} titers

	Antigen	ID50 titers (week 17)								Geometric Mean
		M1	M2	M3	M4	M5	M6	M7	M8	
Week 17	EBOV GPΔmuc-WL^{2}P^4 trimer	1344.0	7809.0	5137.0	3217.0	1631.0	411.3	3729.0	7747.0	2759.4
	EBOV GPΔmuc-WL^{2}P^4 E2p SApNP	149.6	394.3	1109.0	1525.0	115.1	1174.0	261.1	5895.0	616.1
	EBOV GPΔmuc-WL^{2}P^4 I3-01v9b SApNP	<100	<100	1332.0	356.1	1397.0	240.1	352.0	<100	561.9

Statistical analysis

One-way ANOVA with Tukey's multiple comparisons test (w17)	Statistics	Adjusted P Value
EBOV GPΔmuc-WL^{2}P^4 trimer vs. EBOV GPΔmuc-WL^{2}P^4 E2p SApNP	*	0.0469
EBOV GPΔmuc-WL^{2}P^4 trimer vs. EBOV GPΔmuc-WL^{2}P^4 I3-01v9b SApNP	**	0.0076
EBOV GPΔmuc-WL^{2}P^4 E2p SApNP vs. EBOV GPΔmuc-WL^{2}P^4 I3-01v9b SApNP	ns	0.6882

Fig. S10

i Sera of individual mice immunized with SUDV vaccines binding to SUDV GPΔmuc-WL^{2}P^4(1TD0) trimer

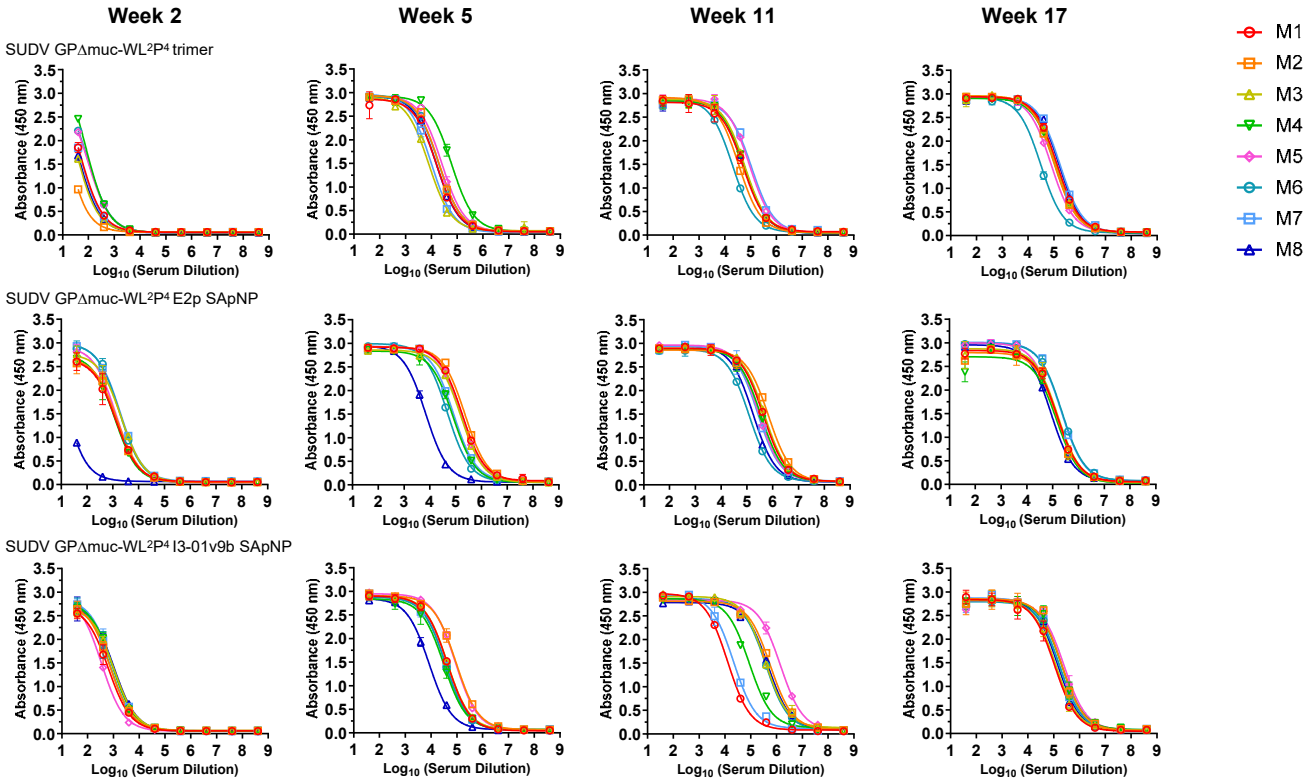

j Mouse serum ELISA EC_{50} titers

Week 2

Antigen	EC50 titers (week 2)								Geometric Mean
	M1	M2	M3	M4	M5	M6	M7	M8	
SUDV GPΔmuc-WL^{2}P^4 trimer	69.8	20.2	50.0	149.7	116.9	122.4	68.1	55.0	69.8
SUDV GPΔmuc-WL^{2}P^4 E2p SApNP	1058.0	1223.0	1977.0	1062.0	1419.0	2123.0	2262.0	17.9	871.0
SUDV GPΔmuc-WL^{2}P^4 I3-01v9b SApNP	550.3	700.2	876.2	893.5	373.7	741.1	903.2	940.0	718.4

Week 5

Antigen	EC50 titers (week 5)								Geometric Mean
	M1	M2	M3	M4	M5	M6	M7	M8	
SUDV GPΔmuc-WL^{2}P^4 trimer	16436	19941	7907	60277	25656	19754	9992	15619	18259.2
SUDV GPΔmuc-WL^{2}P^4 E2p SApNP	177305	230404	159220	79353	157784	47895	82714	6921	82910.4
SUDV GPΔmuc-WL^{2}P^4 I3-01v9b SApNP	42731	93470	42715	31125	87027	36180	35115	8482	38650.3

Week 11

Antigen	EC50 titers (week 11)								Geometric Mean
	M1	M2	M3	M4	M5	M6	M7	M8	
SUDV GPΔmuc-WL^{2}P^4 trimer	51852	34819	59219	58035	92570	20182	108658	56856	53935.6
SUDV GPΔmuc-WL^{2}P^4 E2p SApNP	427238	688825	479499	349324	289258	121660	264183	173015	307186.5
SUDV GPΔmuc-WL^{2}P^4 I3-01v9b SApNP	12804	573418	373590	88061	1405850	379235	21591	471753	183962.3

Week 17

Antigen	EC50 titers (week 17)								Geometric Mean
	M1	M2	M3	M4	M5	M6	M7	M8	
SUDV GPΔmuc-WL^{2}P^4 trimer	132375	104284	117314	112501	78562	31328	174100	161747	102958.9
SUDV GPΔmuc-WL^{2}P^4 E2p SApNP	150503	150658	156743	142867	124345	229353	218325	86164	151148.0
SUDV GPΔmuc-WL^{2}P^4 I3-01v9b SApNP	108351	204158	120591	200895	248727	170555	157838	144221	163771.7

Statistical analysis

One-way ANOVA with Tukey's multiple comparisons test (w2)	Statistics	Adjusted P Value
SUDV GPΔmuc-WL^{2}P^4 trimer vs. SUDV GPΔmuc-WL^{2}P^4 E2p SApNP	****	<0.0001
SUDV GPΔmuc-WL^{2}P^4 trimer vs. SUDV GPΔmuc-WL^{2}P^4 I3-01v9b SApNP	*	0.0169
SUDV GPΔmuc-WL^{2}P^4 E2p SApNP vs. SUDV GPΔmuc-WL^{2}P^4 I3-01v9b SApNP	*	0.0207

One-way ANOVA with Tukey's multiple comparisons test (w5)	Statistics	Adjusted P Value
SUDV GPΔmuc-WL^{2}P^4 trimer vs. SUDV GPΔmuc-WL^{2}P^4 E2p SApNP	**	0.0016
SUDV GPΔmuc-WL^{2}P^4 trimer vs. SUDV GPΔmuc-WL^{2}P^4 I3-01v9b SApNP	ns	0.5472
SUDV GPΔmuc-WL^{2}P^4 E2p SApNP vs. SUDV GPΔmuc-WL^{2}P^4 I3-01v9b SApNP	*	0.0187

One-way ANOVA with Tukey's multiple comparisons test (w11)	Statistics	Adjusted P Value
SUDV GPΔmuc-WL^{2}P^4 trimer vs. SUDV GPΔmuc-WL^{2}P^4 E2p SApNP	ns	0.1259
SUDV GPΔmuc-WL^{2}P^4 trimer vs. SUDV GPΔmuc-WL^{2}P^4 I3-01v9b SApNP	ns	0.0502
SUDV GPΔmuc-WL^{2}P^4 E2p SApNP vs. SUDV GPΔmuc-WL^{2}P^4 I3-01v9b SApNP	ns	0.885

One-way ANOVA with Tukey's multiple comparisons test (w17)	Statistics	Adjusted P Value
SUDV GPΔmuc-WL^{2}P^4 trimer vs. SUDV GPΔmuc-WL^{2}P^4 E2p SApNP	ns	0.1724
SUDV GPΔmuc-WL^{2}P^4 trimer vs. SUDV GPΔmuc-WL^{2}P^4 I3-01v9b SApNP	ns	0.0653
SUDV GPΔmuc-WL^{2}P^4 E2p SApNP vs. SUDV GPΔmuc-WL^{2}P^4 I3-01v9b SApNP	ns	0.8627

Fig. S10

k Week-17 sera of individual mice immunized with SUDV vaccines binding to EBOV GPΔmuc-WL^{2}P^4(1TD0) trimer

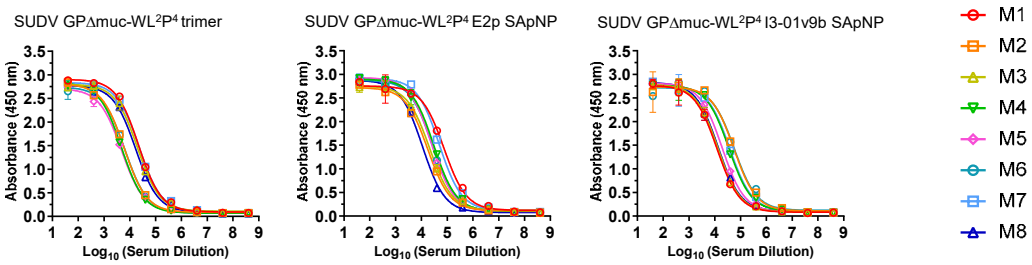

Mouse serum ELISA EC_{50} titers

	Antigen	EC50 titers (week 17)								Geometric Mean
		M1	M2	M3	M4	M5	M6	M7	M8	
Week 17	SUDV GPΔmuc-WL^{2}P^4 trimer	22131	6105	19939	4814	4809	6529	22832	16822	10574.9
	SUDV GPΔmuc-WL^{2}P^4 E2p SApNP	74857	17696	20913	30182	25142	26898	49408	11012	27290.2
	SUDV GPΔmuc-WL^{2}P^4 I3-01v9b SApNP	12210	55319	13273	35138	19190	57302	38054	13336	25446.4

Statistical analysis

One-way ANOVA with Tukey's multiple comparisons test (w17)	Statistics	Adjusted P Value
SUDV GPΔmuc-WL^{2}P^4 trimer vs. SUDV GPΔmuc-WL^{2}P^4 E2p SApNP	ns	0.0832
SUDV GPΔmuc-WL^{2}P^4 trimer vs. SUDV GPΔmuc-WL^{2}P^4 I3-01v9b SApNP	ns	0.1177
SUDV GPΔmuc-WL^{2}P^4 E2p SApNP vs. SUDV GPΔmuc-WL^{2}P^4 I3-01v9b SApNP	ns	0.9817

l Week-17 sera of individual mice immunized with SUDV vaccines binding to RAVV GPΔmuc-P^{2}CT(1TD0) trimer

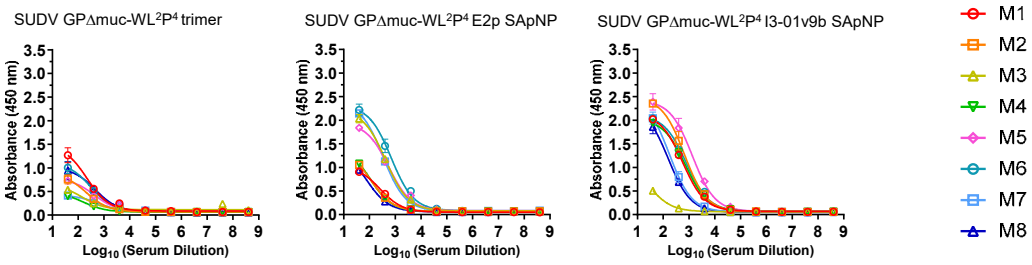

Mouse serum ELISA EC_{50} titers

	Antigen	Absorbance (450 nm) (week 17)								Geometric Mean
		M1	M2	M3	M4	M5	M6	M7	M8	
Week 17	SUDV GPΔmuc-WL^{2}P^4 trimer	1.3	0.8	0.5	0.4	0.7	1.0	0.4	0.9	0.7
	SUDV GPΔmuc-WL^{2}P^4 E2p SApNP	0.9	1.1	2.0	1.1	1.8	2.2	2.1	1.0	1.4
	SUDV GPΔmuc-WL^{2}P^4 I3-01v9b SApNP	2.0	2.4	0.5	1.9	2.4	2.0	2.0	1.9	1.7

Statistical analysis

One-way ANOVA with Tukey's multiple comparisons test (w17)	Statistics	Adjusted P Value
SUDV GPΔmuc-WL^{2}P^4 trimer vs. SUDV GPΔmuc-WL^{2}P^4 E2p SApNP	*	0.0149
SUDV GPΔmuc-WL^{2}P^4 trimer vs. SUDV GPΔmuc-WL^{2}P^4 I3-01v9b SApNP	***	0.0005
SUDV GPΔmuc-WL^{2}P^4 E2p SApNP vs. SUDV GPΔmuc-WL^{2}P^4 I3-01v9b SApNP	ns	0.338

Fig. S10

m Sera of individual mice immunized with SUDV vaccines neutralizing a SUDV Gulu strain

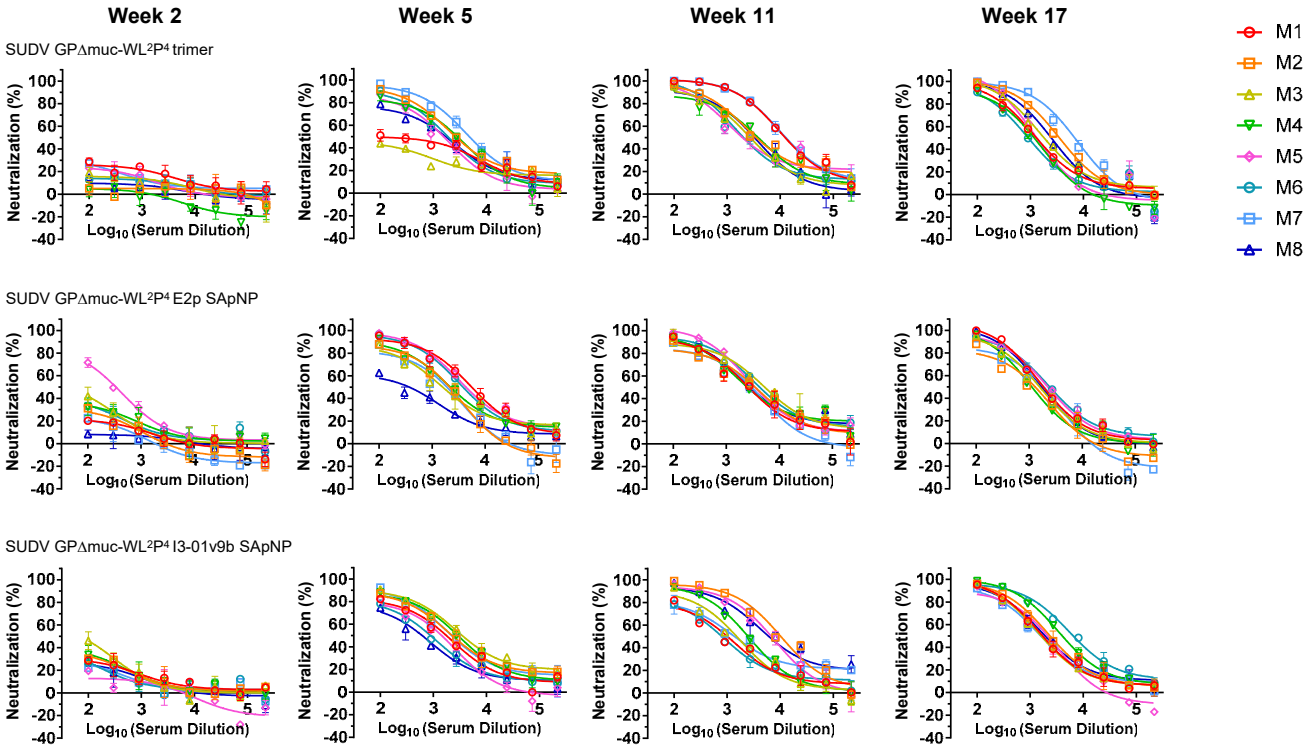

n Mouse serum neutralizing ID_{50} titers

Week 2

Antigen	ID50 titers (week 2)								Geometric Mean
	M1	M2	M3	M4	M5	M6	M7	M8	
SUDV GPΔmuc-WL^{2}P^4 trimer	<100	<100	<100	<100	<100	<100	<100	<100	N/A
SUDV GPΔmuc-WL^{2}P^4 E2p SApNP	<100	<100	<100	<100	331.1	<100	<100	<100	N/A
SUDV GPΔmuc-WL^{2}P^4 I3-01v9b SApNP	<100	<100	107.2	<100	<100	<100	<100	<100	N/A

Week 5

Antigen	ID50 titers (week 5)								Geometric Mean
	M1	M2	M3	M4	M5	M6	M7	M8	
SUDV GPΔmuc-WL^{2}P^4 trimer	420	3076	156.6	2417	1377	1896	5149	1477	1328.6
SUDV GPΔmuc-WL^{2}P^4 E2p SApNP	5677	1634	1754	2420	5081	4212	1332	355.5	2114.1
SUDV GPΔmuc-WL^{2}P^4 I3-01v9b SApNP	1582	2485	4102	2862	1119	843.6	2506	584.4	1681.2

Week 11

Antigen	ID50 titers (week 11)								Geometric Mean
	M1	M2	M3	M4	M5	M6	M7	M8	
SUDV GPΔmuc-WL^{2}P^4 trimer	13810	4694	2805	3670	2858	2497	14410	3069	4628.4
SUDV GPΔmuc-WL^{2}P^4 E2p SApNP	2835	3130	5528	3311	3940	4935	2323	3352	3538.7
SUDV GPΔmuc-WL^{2}P^4 I3-01v9b SApNP	889.3	10154	1391	2424	6257	808.9	1524	7608	2549.8

Week 17

Antigen	ID50 titers (week 17)								Geometric Mean
	M1	M2	M3	M4	M5	M6	M7	M8	
SUDV GPΔmuc-WL^{2}P^4 trimer	1389	3550	2017	1006	1354	931.1	6329	2409	1929.8
SUDV GPΔmuc-WL^{2}P^4 E2p SApNP	2035	928.9	1546	1147	2291	2536	1215	1753	1593.1
SUDV GPΔmuc-WL^{2}P^4 I3-01v9b SApNP	1853	2507	1746	4395	1648	7166	1695	2160	2503.1

Statistical analysis

One-way ANOVA with Tukey's multiple comparisons test (w5)	Statistics	Adjusted P Value
SUDV GPΔmuc-WL^{2}P^4 trimer vs. SUDV GPΔmuc-WL^{2}P^4 E2p SApNP	ns	0.5769
SUDV GPΔmuc-WL^{2}P^4 trimer vs. SUDV GPΔmuc-WL^{2}P^4 I3-01v9b SApNP	ns	0.9998
SUDV GPΔmuc-WL^{2}P^4 E2p SApNP vs. SUDV GPΔmuc-WL^{2}P^4 I3-01v9b SApNP	ns	0.5879

One-way ANOVA with Tukey's multiple comparisons test (w11)	Statistics	Adjusted P Value
SUDV GPΔmuc-WL^{2}P^4 trimer vs. SUDV GPΔmuc-WL^{2}P^4 E2p SApNP	ns	0.4294
SUDV GPΔmuc-WL^{2}P^4 trimer vs. SUDV GPΔmuc-WL^{2}P^4 I3-01v9b SApNP	ns	0.4956
SUDV GPΔmuc-WL^{2}P^4 E2p SApNP vs. SUDV GPΔmuc-WL^{2}P^4 I3-01v9b SApNP	ns	0.9925

One-way ANOVA with Tukey's multiple comparisons test (w17)	Statistics	Adjusted P Value
SUDV GPΔmuc-WL^{2}P^4 trimer vs. SUDV GPΔmuc-WL^{2}P^4 E2p SApNP	ns	0.6592
SUDV GPΔmuc-WL^{2}P^4 trimer vs. SUDV GPΔmuc-WL^{2}P^4 I3-01v9b SApNP	ns	0.7862
SUDV GPΔmuc-WL^{2}P^4 E2p SApNP vs. SUDV GPΔmuc-WL^{2}P^4 I3-01v9b SApNP	ns	0.2916

Fig. S10

o Week-17 sera of individual mice immunized with SUDV vaccines neutralizing an EBOV Makona strain

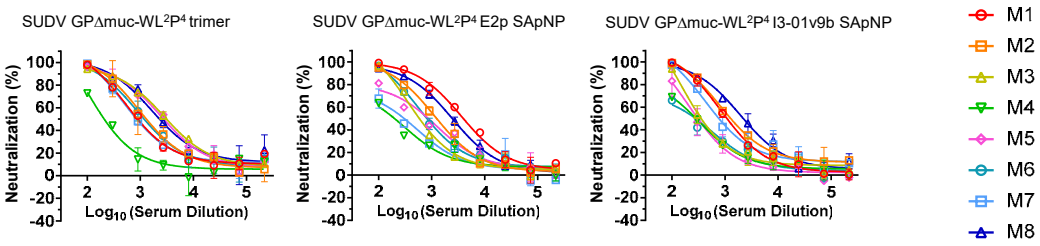

Mouse serum neutralizing ID_{50} titers

	Antigen	ID50 titers (week 17)								Geometric Mean
		M1	M2	M3	M4	M5	M6	M7	M8	
Week 17	SUDV GPΔmuc-WL^{2}P^4 trimer	1073	1510	3312	230.5	2932	1345	1075	2621	1387.6
	SUDV GPΔmuc-WL^{2}P^4 E2p SApNP	4144	1304	687.5	217	758.8	964.7	297	2453	899.9
	SUDV GPΔmuc-WL^{2}P^4 I3-01v9b SApNP	1214	1567	467.4	296.9	336.4	271	990.7	2370	698.3

Statistical analysis

One-way ANOVA with Tukey's multiple comparisons test (w17)	Statistics	Adjusted P Value
SUDV GPΔmuc-WL^{2}P^4 trimer vs. SUDV GPΔmuc-WL^{2}P^4 E2p SApNP	ns	0.7312
SUDV GPΔmuc-WL^{2}P^4 trimer vs. SUDV GPΔmuc-WL^{2}P^4 I3-01v9b SApNP	ns	0.2983
SUDV GPΔmuc-WL^{2}P^4 E2p SApNP vs. SUDV GPΔmuc-WL^{2}P^4 I3-01v9b SApNP	ns	0.7257

p Week-17 sera of individual mice immunized with SUDV vaccines neutralizing a BDBV Uganda strain

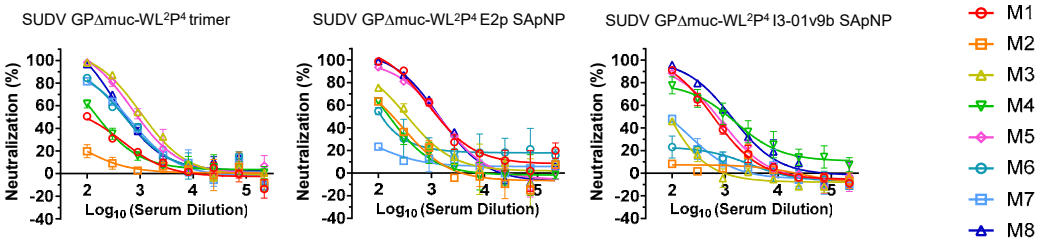

Mouse serum neutralizing ID_{50} titers

	Antigen	ID50 titers (week 17)								Geometric Mean
		M1	M2	M3	M4	M5	M6	M7	M8	
Week 17	SUDV GPΔmuc-WL^{2}P^4 trimer	126.7	26.1	1237.0	165.3	985.6	518.9	543.9	613.3	322.0
	SUDV GPΔmuc-WL^{2}P^4 E2p SApNP	1504.0	174.5	356.0	156.5	1298.0	151.8	35.5	1393.0	330.6
	SUDV GPΔmuc-WL^{2}P^4 I3-01v9b SApNP	580.4	9.7	69.0	1085.0	656.4	<100	<100	1280.0	185.5

Statistical analysis

One-way ANOVA with Tukey's multiple comparisons test (w17)	Statistics	Adjusted P Value
SUDV GPΔmuc-WL^{2}P^4 trimer vs. SUDV GPΔmuc-WL^{2}P^4 E2p SApNP	ns	0.913
SUDV GPΔmuc-WL^{2}P^4 trimer vs. SUDV GPΔmuc-WL^{2}P^4 I3-01v9b SApNP	ns	0.9893
SUDV GPΔmuc-WL^{2}P^4 E2p SApNP vs. SUDV GPΔmuc-WL^{2}P^4 I3-01v9b SApNP	ns	0.8492

Fig. S10

q Sera of individual mice immunized with RAVV vaccines binding to RAVV GPΔmuc-P²CT(1TD0) trimer

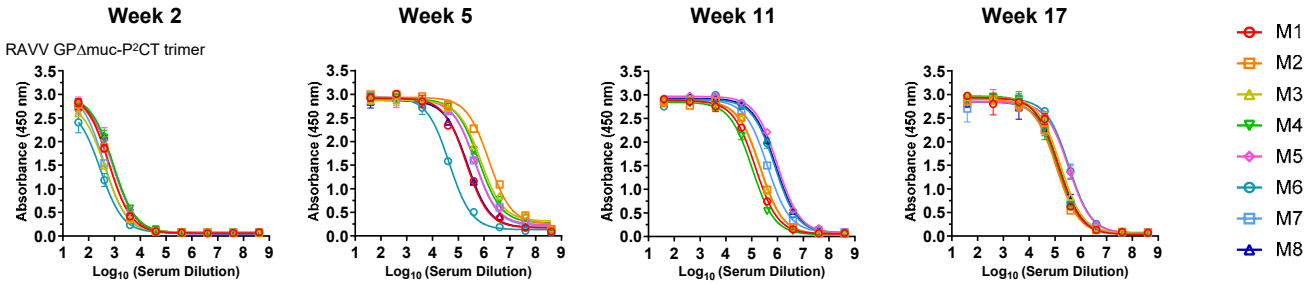

Mouse serum ELISA EC_{50} titers

Antigen	EC50 titers								Geometric Mean
	M1	M2	M3	M4	M5	M6	M7	M8	
RAVV GPΔmuc-P²CT trimer-w2	718.9	721.9	432.3	1030.0	946.3	262.3	481.5	958.5	635.1
RAVV GPΔmuc-P²CT trimer-w5	202735	1544554	746406	628189	447117	44771	446178	225949	362215.2
RAVV GPΔmuc-P²CT trimer-w11	139135	218951	208199	104125	998580	786127	408247	853062	340466.6
RAVV GPΔmuc-P²CT trimer-w17	140811	110900	164905	119990	336478	344895	127509	141835	168457.1

r Week-17 sera of individual mice immunized with RAVV vaccines binding to EBOV GPΔmuc-WL²P⁴(1TD0) trimer

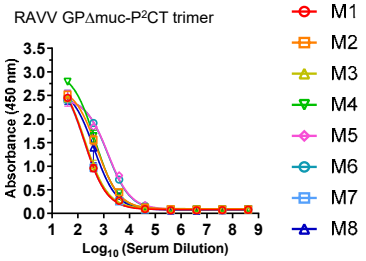

Mouse serum ELISA EC_{50} titers

Antigen	EC50 titers (week 17)								Geometric Mean
	M1	M2	M3	M4	M5	M6	M7	M8	
RAVV GPΔmuc-P²CT trimer	177.5	537.5	197.8	459.9	1477.0	1430.0	182.7	422.8	440.4

s Week-17 sera of individual mice immunized with RAVV vaccines binding to SUDV GPΔmuc-WL²P⁴(1TD0) trimer

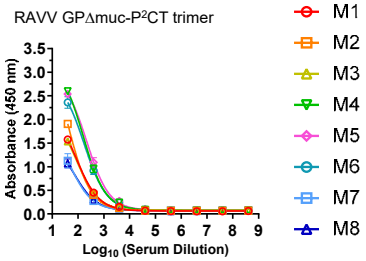

Mouse serum ELISA EC_{50} titers

Antigen	Absorbance (450 nm) (week 17)								Geometric Mean
	M1	M2	M3	M4	M5	M6	M7	M8	
RAVV GPΔmuc-P²CT trimer	1.6	1.9	1.5	2.6	2.5	2.4	2.4	2.4	2.1

t Week-17 IgG samples of individual mice immunized with RAVV vaccines neutralizing a MARV Angola strain

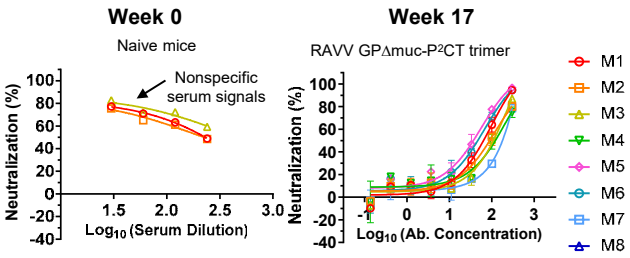

Week 17 mouse IgG neutralization

Virus strains	IC50 (μg/mL)								Geometric Mean
	M1	M2	M3	M4	M5	M6	M7	M8	
MARV-Angola	56.2	81.4	93.3	104.4	30.9	40.3	148.4	71.8	70.2

u Week-17 sera of individual mice immunized with RAVV vaccines neutralizing three ebolavirus strains

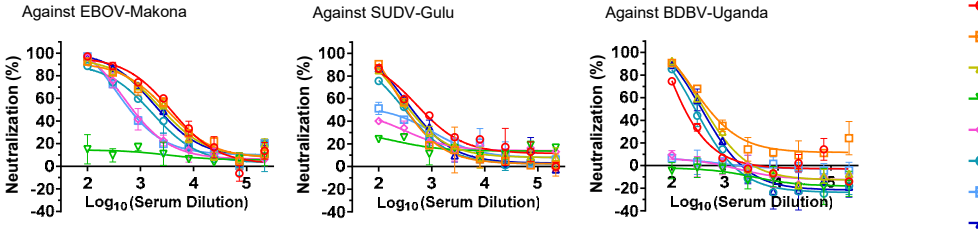

Fig. S10. Immunogenicity of EBOV, SUDV, and RAVV GPΔmuc vaccines in mice. (**a**) ELISA curves of mouse sera from EBOV GPΔmuc trimer and SApNP vaccine groups (n = 8 mice/group) binding to the coating antigen, EBOV GPΔmuc-WL^{2}P^4(1TD0) trimer (**b**) (Top) Summary of geometric means of EC_{50} titers measured for Ebola GPΔmuc vaccine groups against EBOV GPΔmuc-WL^{2}P^4(1TD0) trimer. Color coding indicates the level of EC_{50} titers (green to red: low to high binding). (Bottom) Summary of statistical analysis performed for each timepoint. Of note, the EC_{50} values at week 2 were derived by setting the minimum/maximum OD_{450} values to 0.0/2.8. (**c**) ELISA curves of mouse sera from EBOV GPΔmuc vaccine groups at week 17 after four immunizations binding to SUDV GPΔmuc-WL^{2}P^4(1TD0) trimer. Summary of geometric means of EC_{50} titers and statistical analysis. (**d**) ELISA curves of mouse sera from Ebola GPΔmuc vaccine groups at week 17 after four immunizations binding to RAVV GPΔmuc-P^{2}CT(1TD0) trimer. Summary of absorbance at 450 nm (A450) values was included. (**e**) Neutralization curves of mouse sera from EBOV GPΔmuc trimer and SApNP vaccine groups against EBOV Makona pseudovirus. (**f**) (Top) Summary of geometric means of ID_{50} titers measured for EBOV GPΔmuc vaccine groups against EBOV Makona pseudovirus. Color coding indicates the level of ID_{50} titers (white: no neutralization; green to red: low to high neutralization). Of note, the ID_{50} values were derived by setting the minimum/maximum %neutralization to 0.0/100.0 as constraints. (Bottom) Summary of statistical analysis as in (**b**). (**g**) Neutralization curves of mouse sera from EBOV GPΔmuc vaccine groups at week 17 against SUDV Gulu pseudovirus. Summary of geometric means of ID_{50} values and statistical analysis. (**h**) Neutralization curves of mouse sera from EBOV GPΔmuc vaccine groups at week 17 against BDBV Uganda pseudovirus. Summary of geometric means of ID_{50} values and statistical analysis. (**i**) ELISA curves of mouse sera from SUDV GPΔmuc trimer and SApNP vaccine groups binding to SUDV GPΔmuc-WL^{2}P^4(1TD0) trimer. (**j**) (Top) Summary of geometric means of EC_{50} titers measured for SUDV GPΔmuc vaccine groups against SUDV GPΔmuc-WL^{2}P^4(1TD0) trimer. (Bottom) Summary of statistical analysis as in (**b**). Of note, the EC_{50} values at week 2 were derived by setting the minimum/maximum OD_{450} values to 0.0/2.9. (**k**) ELISA curves of mouse sera from SUDV GPΔmuc vaccine groups at week 17 after four immunizations binding to EBOV GPΔmuc-WL^{2}P^4(1TD0) trimer. Summary of geometric means of EC_{50} titers and statistical analysis. (**l**) ELISA curves of mouse sera from SUDV GPΔmuc vaccine groups at week 17 after four immunizations binding to RAVV GPΔmuc-P^{2}CT(1TD0) trimer. Summary of A450 values was included. (**m**) Neutralization curves of mouse sera from SUDV GPΔmuc trimer and SApNP vaccine groups against SUDV Gulu pseudovirus. (**n**) (Top) Summary of geometric means of ID_{50} titers measured for EBOV GPΔmuc vaccine groups against EBOV Makona pseudovirus. (Bottom) Summary of statistical analysis as in (**b**). (**o**) Neutralization curves of mouse sera from EBOV GPΔmuc vaccine groups at week 17 against EBOV Makona pseudovirus. Summary of geometric means of ID_{50} values and statistical analysis. (**p**) Neutralization curves of mouse sera from EBOV GPΔmuc vaccine groups at week 17 against BDBV Uganda pseudovirus. Summary of geometric means of ID_{50} values and statistical analysis. (**q**) (Top) ELISA curves of mouse sera from RAVV GPΔmuc trimer vaccine groups binding to RAVV GPΔmuc-P^{2}CT(1TD0) trimer. (Bottom) Summary of geometric means of EC_{50} values. Of note, the EC_{50} values at week 2 were derived by setting the minimum/maximum OD_{450} values to 0.0/2.9. (**r**) ELISA curves of mouse sera from RAVV GPΔmuc vaccine groups at week 17 after four immunizations binding to EBOV GPΔmuc-WL^{2}P^4(1TD0) trimer. Summary of geometric means of EC_{50} titers. (**s**) ELISA curves of mouse sera from RAVV GPΔmuc vaccine groups at week 17 after four immunizations binding to SUDV GPΔmuc-WL^{2}P^4(1TD0) trimer. Summary of A450 values was included. (**t**) Neutralization curves of purified IgG from RAVV GPΔmuc vaccine groups at week 17 against MARV Angola pseudovirus. Summary of IC_{50} values. Left panel: sera from three naive mice showed nonspecific background in MARV Angola pseudovirus assays, suggesting that IgG purification is required to eliminate the nonspecific serum reactivity. (**u**) Neutralization curves of mouse sera from RAVV GPΔmuc vaccine groups at week 17 against various ebolavirus strains. Error bars represent the difference between these duplicate values at each concentration tested for each sample. EC_{50}, ID_{50}, and IC_{50} values were calculated in GraphPad Prism 10.3.1. Data were analyzed using one-way ANOVA, followed by Tukey's multiple comparison post hoc test for each timepoint. For significance, ns (not significant), *$p < 0.05$, **$p < 0.01$, ***$p < 0.001$, and ****$p < 0.0001$.

Figure S11

a **Sera of individual mice immunized with glycan-modified EBOV vaccines binding to EBOV GPΔmuc-WL^{2}P^4(1TD0) trimer**

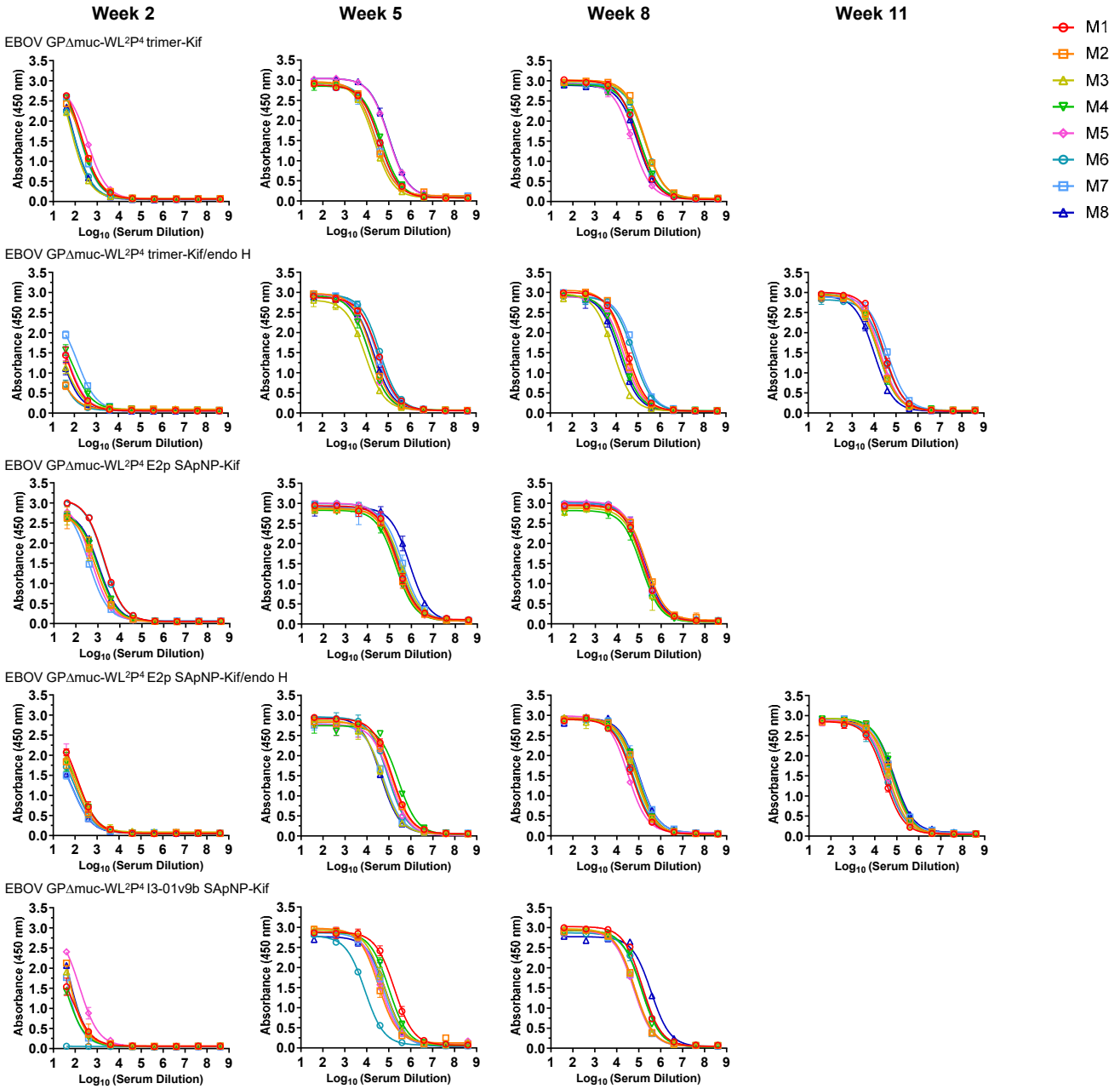

Figure S11

b Mouse serum ELISA EC_{50} titers

Week 2

Antigen	EC50 titers (week 2)								Geometric Mean
	M1	M2	M3	M4	M5	M6	M7	M8	
EBOV GPΔmuc-WL^{2}P^4 trimer	111.7	136.3	51.3	227.2	103.0	200.2	12.6	173.3	97.3
EBOV GPΔmuc-WL^{2}P^4 trimer-Kif	283.7	255.1	119.5	248.0	423.8	133.4	239.1	141.3	212.1
EBOV GPΔmuc-WL^{2}P^4 trimer-Kif/endo H	43.1	13.4	28.4	56.2	46.5	14.1	106.9	26.8	33.8
EBOV GPΔmuc-WL^{2}P^4 E2p SApNP	985.3	706.4	970.8	1772.0	271.5	336.1	3145.0	486.4	799.6
EBOV GPΔmuc-WL^{2}P^4 E2p SApNP-Kif	2721.0	813.3	815.7	1046.0	678.3	2584.0	482.5	1166.0	1080.8
EBOV GPΔmuc-WL^{2}P^4 E2p SApNP-Kif/endo H	126.0	84.5	104.9	95.8	122.8	69.1	50.0	51.4	83.4
EBOV GPΔmuc-WL^{2}P^4 I3-01v9b SApNP	30.1	101.8	43.0	37.9	172.4	80.7	91.5	115.6	72.1
EBOV GPΔmuc-WL^{2}P^4 I3-01v9b SApNP-Kif	51.8	97.6	80.2	41.8	201.5	0.9	62.9	95.3	45.5

Week 5

Antigen	EC50 titers (week 5)								Geometric Mean
	M1	M2	M3	M4	M5	M6	M7	M8	
EBOV GPΔmuc-WL^{2}P^4 trimer	52545	41735	104914	48787	27947	18271	26144	21434	36588
EBOV GPΔmuc-WL^{2}P^4 trimer-Kif	38706	25086	21695	47634	99875	36855	27014	103907	42360
EBOV GPΔmuc-WL^{2}P^4 trimer-Kif/endo H	35186	18238	8909	13634	13630	41752	29227	22113	20285
EBOV GPΔmuc-WL^{2}P^4 E2p SApNP	199849	120954	303168	237335	74446	156667	282413	368341	195227
EBOV GPΔmuc-WL^{2}P^4 E2p SApNP-Kif	241215	224657	335618	192147	216173	258075	406613	838779	300502
EBOV GPΔmuc-WL^{2}P^4 E2p SApNP-Kif/endo H	141920	136153	48617	265817	117352	88543	56725	42434	94286
EBOV GPΔmuc-WL^{2}P^4 I3-01v9b SApNP	58458	93275	140476	104463	128829	148277	70114	63709	95342
EBOV GPΔmuc-WL^{2}P^4 I3-01v9b SApNP-Kif	180905	34224	63566	102618	42941	8255	57374	74974	52927

Week 11 or 8

Antigen	EC50 titers (week 11 or 8)								Geometric Mean
	M1	M2	M3	M4	M5	M6	M7	M8	
EBOV GPΔmuc-WL^{2}P^4 trimer-w11	26545	524033	69054	94400	39464	69865	68351	51944	73881
EBOV GPΔmuc-WL^{2}P^4 trimer-Kif-w8	93214	195305	183599	116631	50918	193472	114590	89398	118674
EBOV GPΔmuc-WL^{2}P^4 trimer-Kif/endo H-w8	31571	25030	7454	16954	21834	59045	72580	13927	24508
EBOV GPΔmuc-WL^{2}P^4 E2p SApNP-w11	267135	163352	223491	606328	32762	143908	182928	233182	181722
EBOV GPΔmuc-WL^{2}P^4 E2p SApNP-Kif-w8	153387	211525	149619	126857	158759	131151	152440	176520	155680
EBOV GPΔmuc-WL^{2}P^4 E2p SApNP-Kif/endo H-w8	50455	81205	73372	89472	32112	55202	99817	102711	68571
EBOV GPΔmuc-WL^{2}P^4 I3-01v9b SApNP-w11	703967	60730	178784	354031	97482	91294	82827	610293	182253
EBOV GPΔmuc-WL^{2}P^4 I3-01v9b SApNP-Kif-w8	146649	66233	62594	129059	58475	142777	61089	366113	104890

Statistical analysis

One-way ANOVA with Tukey's multiple comparisons test (w2)	Statistics	Adjusted P Value
EBOV GPΔmuc-WL^{2}P^4 trimer vs. EBOV GPΔmuc-WL^{2}P^4 trimer-Kif	*	0.0276
EBOV GPΔmuc-WL^{2}P^4 trimer vs. EBOV GPΔmuc-WL^{2}P^4 trimer-Kif/endo H	ns	0.0775
EBOV GPΔmuc-WL^{2}P^4 trimer-Kif vs. EBOV GPΔmuc-WL^{2}P^4 trimer-Kif/endo H	***	0.0001

One-way ANOVA with Tukey's multiple comparisons test (w5)	Statistics	Adjusted P Value
EBOV GPΔmuc-WL^{2}P^4 trimer vs. EBOV GPΔmuc-WL^{2}P^4 trimer-Kif	ns	0.8381
EBOV GPΔmuc-WL^{2}P^4 trimer vs. EBOV GPΔmuc-WL^{2}P^4 trimer-Kif/endo H	ns	0.2962
EBOV GPΔmuc-WL^{2}P^4 trimer-Kif vs. EBOV GPΔmuc-WL^{2}P^4 trimer-Kif/endo H	ns	0.1137

One-way ANOVA with Tukey's multiple comparisons test (w2)	Statistics	Adjusted P Value
EBOV GPΔmuc-WL^{2}P^4 E2p SApNP vs. EBOV GPΔmuc-WL^{2}P^4 E2p SApNP-Kif	ns	0.8496
EBOV GPΔmuc-WL^{2}P^4 E2p SApNP vs. EBOV GPΔmuc-WL^{2}P^4 E2p SApNP-Kif/endo H	*	0.0371
EBOV GPΔmuc-WL^{2}P^4 E2p SApNP-Kif vs. EBOV GPΔmuc-WL^{2}P^4 E2p SApNP-Kif/endo H	*	0.0112

One-way ANOVA with Tukey's multiple comparisons test (w5)	Statistics	Adjusted P Value
EBOV GPΔmuc-WL^{2}P^4 E2p SApNP vs. EBOV GPΔmuc-WL^{2}P^4 E2p SApNP-Kif	ns	0.2278
EBOV GPΔmuc-WL^{2}P^4 E2p SApNP vs. EBOV GPΔmuc-WL^{2}P^4 E2p SApNP-Kif/endo H	ns	0.3186
EBOV GPΔmuc-WL^{2}P^4 E2p SApNP-Kif vs. EBOV GPΔmuc-WL^{2}P^4 E2p SApNP-Kif/endo H	*	0.0119

Unpaired t test (w2)	Statistics	P Value
EBOV GPΔmuc-WL^{2}P^4 I3-01v9b SApNP vs. EBOV GPΔmuc-WL^{2}P^4 I3-01v9b SApNP-Kif	ns	0.8507

Unpaired t test (w5)	Statistics	P Value
EBOV GPΔmuc-WL^{2}P^4 I3-01v9b SApNP vs. EBOV GPΔmuc-WL^{2}P^4 I3-01v9b SApNP-Kif	ns	0.1978

Figure S11

C Sera of individual mice immunized with EBOV vaccines neutralizing an EBOV Makona strain

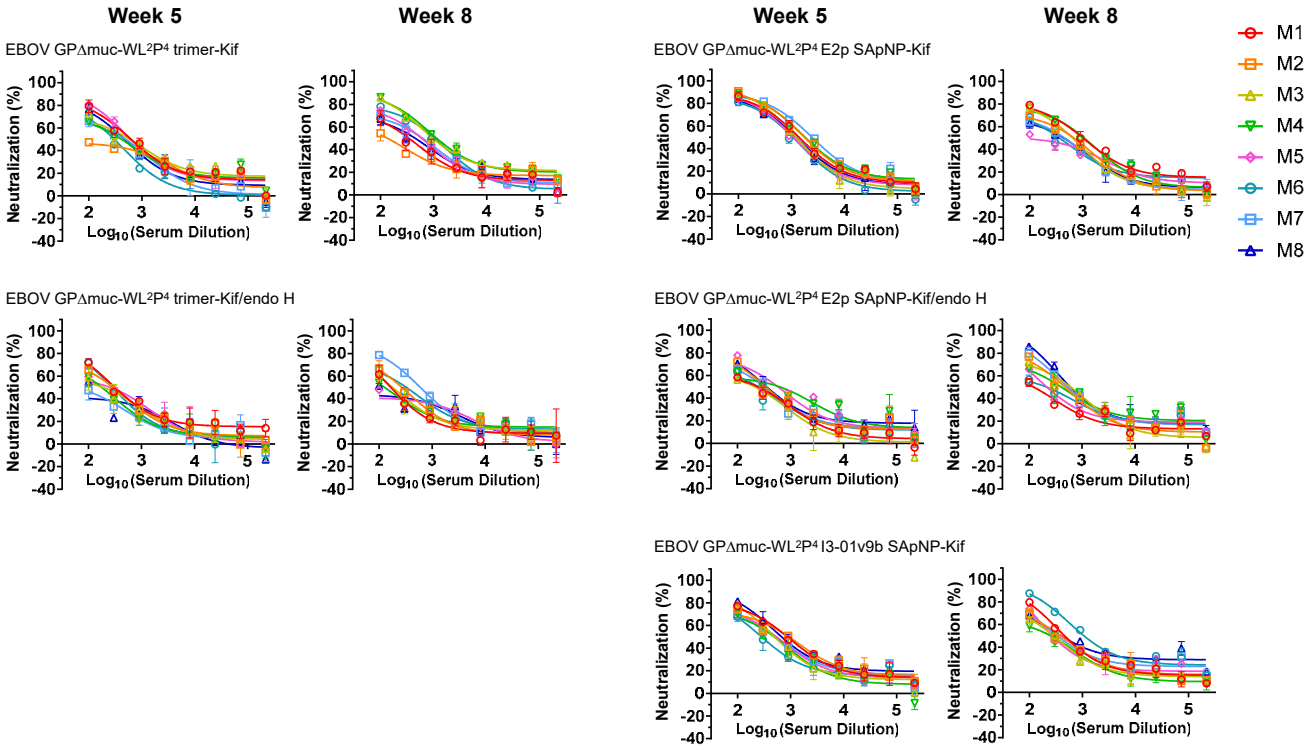

d Mouse serum neutralizing ID_{50} titers

Week 5

Antigen	ID50 titers (week 5)								Geometric Mean
	M1	M2	M3	M4	M5	M6	M7	M8	
EBOV GPΔmuc-WL²P⁴ trimer	805.4	559.3	149.3	588.2	174.1	145.1	203.2	360.5	304.1
EBOV GPΔmuc-WL²P⁴ trimer-Kif	685.5	234.7	577.4	443.0	708.5	285.4	407.7	489.1	449.3
EBOV GPΔmuc-WL²P⁴ trimer-Kif/endo H	383.7	299.7	227.6	199.9	271.6	298.0	132.4	145.5	231.2
EBOV GPΔmuc-WL²P⁴ E2p SApNP	636.9	358.8	2178.0	1002.0	555.2	322.9	299.4	1167.0	648.4
EBOV GPΔmuc-WL²P⁴ E2p SApNP-Kif	1414.0	1867.0	1249.0	1961.0	1107.0	963.3	2480.0	1201.0	1459.0
EBOV GPΔmuc-WL²P⁴ E2p SApNP-Kif/endo H	263.2	376.3	232.9	513.0	559.4	273.6	353.0	430.4	358.9
EBOV GPΔmuc-WL²P⁴ I3-01v9b SApNP	881.2	850.8	555.5	452.4	550.2	340.8	548.8	865.0	599.9
EBOV GPΔmuc-WL²P⁴ I3-01v9b SApNP-Kif	267.9	390.2	313.1	575.8	378.9	413.4	258.7	296.7	350.3

Week 11 or 8

Antigen	ID50 titers (week 11 or 8)								Geometric Mean
	M1	M2	M3	M4	M5	M6	M7	M8	
EBOV GPΔmuc-WL²P⁴ trimer-w11	2117.0	560.6	254.4	521.5	188.7	430.2	369.3	377.3	453.2
EBOV GPΔmuc-WL²P⁴ trimer-Kif-w8	370.3	204.5	1305	1425	578	911.8	569.1	448.8	609.1
EBOV GPΔmuc-WL²P⁴ trimer-Kif/endo H-w8	192.8	287.4	217.4	178.6	171.6	351.1	636.2	175.4	248.3
EBOV GPΔmuc-WL²P⁴ E2p SApNP-w11	494.5	392.0	734.2	747.4	275.3	643.8	365.2	759.9	518.6
EBOV GPΔmuc-WL²P⁴ E2p SApNP-Kif-w8	1031	562.3	594.7	902.2	273	393.9	416.3	408.9	524.1
EBOV GPΔmuc-WL²P⁴ E2p SApNP-Kif/endo H-w8	179.2	499.6	538.7	486.6	301.2	292.4	649.2	772.1	423.6
EBOV GPΔmuc-WL²P⁴ I3-01v9b SApNP-w11	1006.0	434.9	454.1	766.3	289.4	237.7	327.0	928.5	487.3
EBOV GPΔmuc-WL²P⁴ I3-01v9b SApNP-Kif-w8	562.9	429.3	326.9	281.2	376.1	1462	459.4	603.8	491.2

Statistical analysis

One-way ANOVA with Tukey's multiple comparisons test (w5)	Statistics	Adjusted P Value
EBOV GPΔmuc-WL²P⁴ trimer vs. EBOV GPΔmuc-WL²P⁴ trimer-Kif	ns	0.489
EBOV GPΔmuc-WL²P⁴ trimer vs. EBOV GPΔmuc-WL²P⁴ trimer-Kif/endo H	ns	0.3549
EBOV GPΔmuc-WL²P⁴ trimer-Kif vs. EBOV GPΔmuc-WL²P⁴ trimer-Kif/endo H	*	0.0453

One-way ANOVA with Tukey's multiple comparisons test (w5)	Statistics	Adjusted P Value
EBOV GPΔmuc-WL²P⁴ E2p SApNP vs. EBOV GPΔmuc-WL²P⁴ E2p SApNP-Kif	*	0.02
)V GPΔmuc-WL²P⁴ E2p SApNP vs. EBOV GPΔmuc-WL²P⁴ E2p SApNP-Kif/endo H	ns	0.1792
' GPΔmuc-WL²P⁴ E2p SApNP-Kif vs. EBOV GPΔmuc-WL²P⁴ E2p SApNP-Kif/endo H	***	0.0003

Unpaired t test (w5)	Statistics	P Value
V GPΔmuc-WL²P⁴ I3-01v9b SApNP vs. EBOV GPΔmuc-WL²P⁴ I3-01v9b SApNP-Kif	**	0.0055

Figure S11

e Sera of individual mice immunized with wildtype/glycan-modified SUDV vaccines binding to SUDV GPΔmuc-WL^{2}P^4(1TD0) trimer

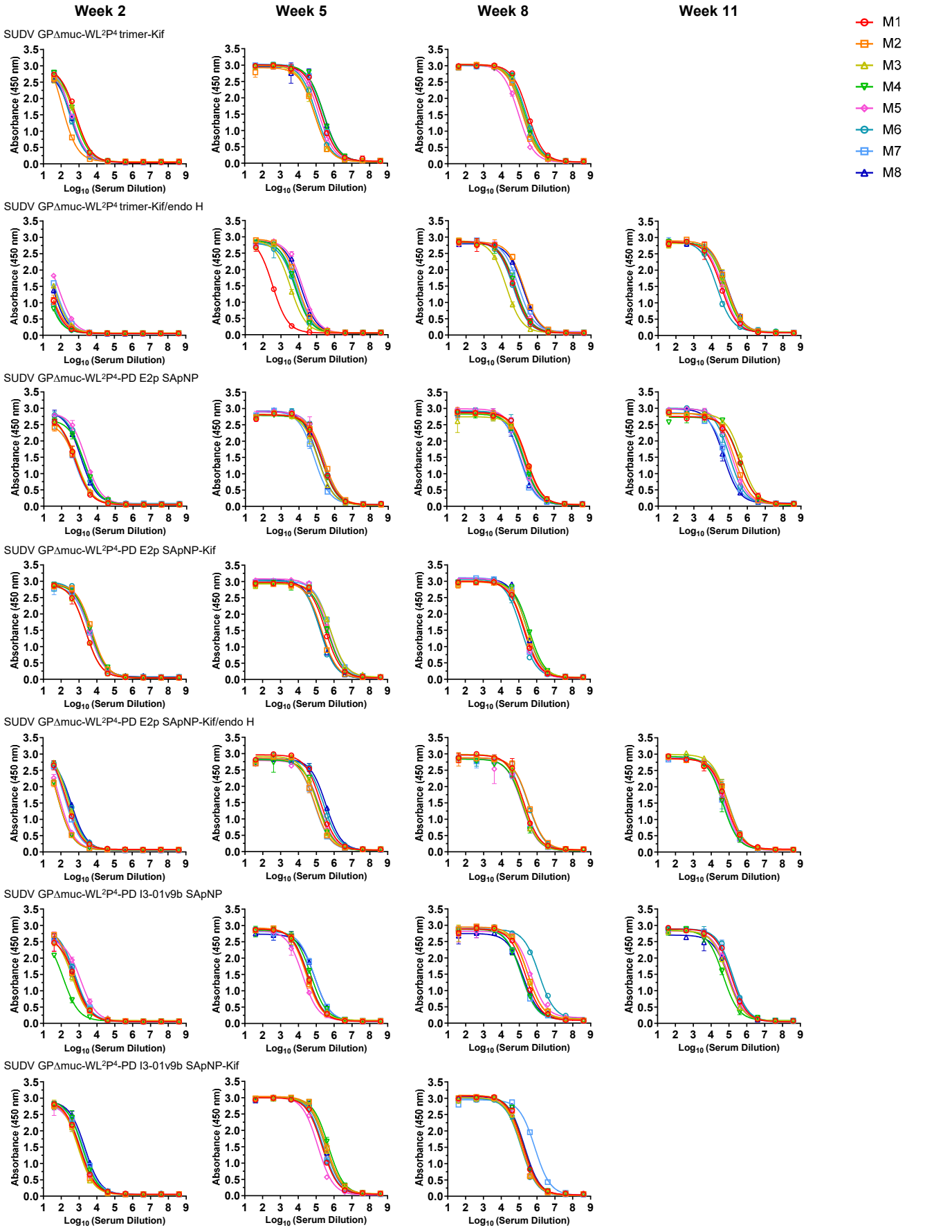

Figure S11

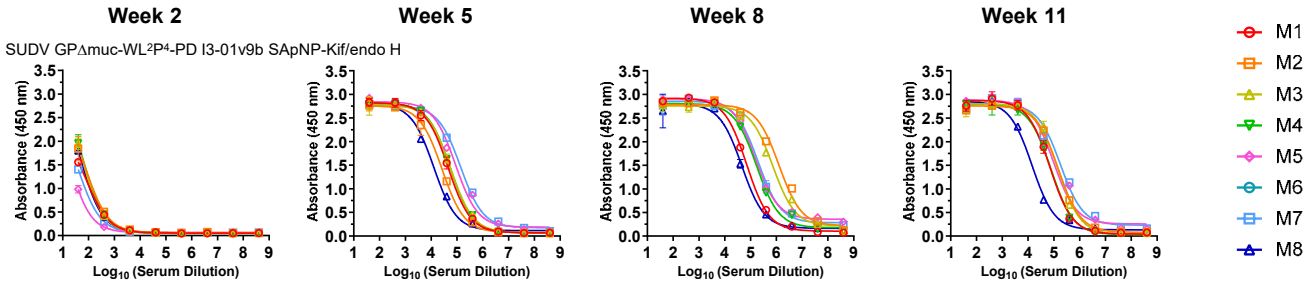

f Mouse serum ELISA EC_{50} titers

Week 2

Antigen	EC50 titers (week 2)								Geometric Mean
	M1	M2	M3	M4	M5	M6	M7	M8	
SUDV GPΔmuc-WL^{2}P^4 trimer	69.8	20.2	50.0	149.7	116.9	122.4	68.1	55.0	69.8
SUDV GPΔmuc-WL^{2}P^4 trimer-Kif	714.8	192.9	605.3	591.0	412.8	343.0	419.8	362.8	425.0
SUDV GPΔmuc-WL^{2}P^4 trimer-Kif/endo H	23.3	24.5	44.7	15.7	72.2	19.6	50.5	36.9	31.8
SUDV GPΔmuc-WL^{2}P^4-PD E2p SApNP	527.1	474.8	583.8	1483.0	2336.0	1545.0	475.4	1316.0	914.5
SUDV GPΔmuc-WL^{2}P^4-PD E2p SApNP-Kif	2482.0	5568.0	2483.0	4798.0	4273.0	4408.0	3878.0	4312.0	3884.6
SUDV GPΔmuc-WL^{2}P^4-PD E2p SApNP-Kif/endo H	271.0	99.3	330.9	99.8	124.0	375.7	234.7	410.6	211.4
SUDV GPΔmuc-WL^{2}P^4-PD I3-01v9b SApNP	469.6	479.9	387.3	115.2	890.0	616.4	586.8	503.1	448.2
SUDV GPΔmuc-WL^{2}P^4-PD I3-01v9b SApNP-Kif	1206.0	1067.0	961.1	1644.0	1098.0	1237.0	1839.0	2248.0	1355.8
SUDV GPΔmuc-WL^{2}P^4-PD I3-01v9b SApNP-Kif/endo H	49.8	73.8	77.8	80.5	20.8	N/A	38.4	65.2	53.1

Week 5

Antigen	EC50 titers (week 5)								Geometric Mean
	M1	M2	M3	M4	M5	M6	M7	M8	
SUDV GPΔmuc-WL^{2}P^4 trimer	16436	19941	7907	60277	25656	19754	9992	15619	18259.2
SUDV GPΔmuc-WL^{2}P^4 trimer-Kif	187796	83838	82374	256237	143796	100245	199748	272537	150326.2
SUDV GPΔmuc-WL^{2}P^4 trimer-Kif/endo H	337	8926	3406	6542	16601	6364	8124	13307	5439.3
SUDV GPΔmuc-WL^{2}P^4-PD E2p SApNP	194403	254967	120302	189915	195340	209194	72385	116111	158028.4
SUDV GPΔmuc-WL^{2}P^4-PD E2p SApNP-Kif	328808	203797	637646	429942	440079	160965	596309	178438	329358.5
SUDV GPΔmuc-WL^{2}P^4-PD E2p SApNP-Kif/endo H	174902	82685	108551	129398	143808	261848	79238	345641	146267.1
SUDV GPΔmuc-WL^{2}P^4-PD I3-01v9b SApNP	32933	27405	30608	50359	17406	34313	79188	83439	39124.1
SUDV GPΔmuc-WL^{2}P^4-PD I3-01v9b SApNP-Kif	213630	375263	331165	484567	123702	233165	246351	324809	271692.3
SUDV GPΔmuc-WL^{2}P^4-PD I3-01v9b SApNP-Kif/endo H	45679	26310	57270	55138	87196	N/A	138210	12630	47889.1

Week 11 or 8

Antigen	EC50 titers (week 11,8)								Geometric Mean
	M1	M2	M3	M4	M5	M6	M7	M8	
SUDV GPΔmuc-WL^{2}P^4 trimer-w11	51852	34819	59219	58035	92570	20182	108658	56856	53935.6
SUDV GPΔmuc-WL^{2}P^4 trimer-Kif-w8	302797	144377	177306	198140	88084	235081	164275	185242	177101.1
SUDV GPΔmuc-WL^{2}P^4 trimer-Kif/endo H-w8	50453	172980	18107	59100	58943	44125	87452	156514	65346.1
SUDV GPΔmuc-WL^{2}P^4-PD E2p SApNP-w8	299781	269350	317854	207812	165230	208403	120522	131427	203221.8
SUDV GPΔmuc-WL^{2}P^4-PD E2p SApNP-Kif-w8	192720	218683	292392	372944	179861	130425	179178	274004	219008.7
SUDV GPΔmuc-WL^{2}P^4-PD E2p SApNP-Kif/endo H-w8	180099	336638	152272	156367	145160	325977	149103	N/A	193576.0
SUDV GPΔmuc-WL^{2}P^4-PD I3-01v9b SApNP-w8	219021	293708	296644	131589	450528	1270551	122274	162786	270436.4
SUDV GPΔmuc-WL^{2}P^4-PD I3-01v9b SApNP-Kif-w8	166508	138485	135652	171299	143035	129149	754862	196507	186573.4
SUDV GPΔmuc-WL^{2}P^4-PD I3-01v9b SApNP-Kif/endo H-w8	71039	1261224	728092	170130	156138	N/A	198137	45999	206095.4

Statistical analysis

One-way ANOVA with Tukey's multiple comparisons test (w2)	Statistics	Adjusted P Value
SUDV GPΔmuc-WL^{2}P^4 trimer vs. SUDV GPΔmuc-WL^{2}P^4 trimer-Kif	****	<0.0001
SUDV GPΔmuc-WL^{2}P^4 trimer vs. SUDV GPΔmuc-WL^{2}P^4 trimer-Kif/endo H	ns	0.6485
SUDV GPΔmuc-WL^{2}P^4 trimer-Kif vs. SUDV GPΔmuc-WL^{2}P^4 trimer-Kif/endo H	****	<0.0001

One-way ANOVA with Tukey's multiple comparisons test (w5)	Statistics	Adjusted P Value
SUDV GPΔmuc-WL^{2}P^4 trimer vs. SUDV GPΔmuc-WL^{2}P^4 trimer-Kif	****	<0.0001
SUDV GPΔmuc-WL^{2}P^4 trimer vs. SUDV GPΔmuc-WL^{2}P^4 trimer-Kif/endo H	ns	0.8066
SUDV GPΔmuc-WL^{2}P^4 trimer-Kif vs. SUDV GPΔmuc-WL^{2}P^4 trimer-Kif/endo H	****	<0.0001

One-way ANOVA with Tukey's multiple comparisons test (w2)	Statistics	Adjusted P Value
SUDV GPΔmuc-WL^{2}P^4-PD E2p SApNP vs. SUDV GPΔmuc-WL^{2}P^4-PD E2p SApNP-Kif	****	<0.0001
SUDV GPΔmuc-WL^{2}P^4-PD E2p SApNP vs. SUDV GPΔmuc-WL^{2}P^4-PD E2p SApNP-Kif/endo H	ns	0.0778
SUDV GPΔmuc-WL^{2}P^4-PD E2p SApNP-Kif vs. SUDV GPΔmuc-WL^{2}P^4-PD E2p SApNP-Kif/endo H	****	<0.0001

One-way ANOVA with Tukey's multiple comparisons test (w5)	Statistics	Adjusted P Value
SUDV GPΔmuc-WL^{2}P^4-PD E2p SApNP vs. SUDV GPΔmuc-WL^{2}P^4-PD E2p SApNP-Kif	*	0.0103
SUDV GPΔmuc-WL^{2}P^4-PD E2p SApNP vs. SUDV GPΔmuc-WL^{2}P^4-PD E2p SApNP-Kif/endo H	ns	0.9984
SUDV GPΔmuc-WL^{2}P^4-PD E2p SApNP-Kif vs. SUDV GPΔmuc-WL^{2}P^4-PD E2p SApNP-Kif/endo H	**	0.0091

One-way ANOVA with Tukey's multiple comparisons test (w2)	Statistics	Adjusted P Value
SUDV GPΔmuc-WL^{2}P^4-PD I3-01v9b SApNP vs. SUDV GPΔmuc-WL^{2}P^4-PD I3-01v9b SApNP-Kif	****	<0.0001
IDV GPΔmuc-WL^{2}P^4-PD I3-01v9b SApNP vs. SUDV GPΔmuc-WL^{2}P^4-PD I3-01v9b SApNP-Kif/endo H	*	0.0224
V GPΔmuc-WL^{2}P^4-PD I3-01v9b SApNP-Kif vs. SUDV GPΔmuc-WL^{2}P^4-PD I3-01v9b SApNP-Kif/endo H	****	<0.0001

One-way ANOVA with Tukey's multiple comparisons test (w5)	Statistics	Adjusted P Value
SUDV GPΔmuc-WL^{2}P^4-PD I3-01v9b SApNP vs. SUDV GPΔmuc-WL^{2}P^4-PD I3-01v9b SApNP-Kif	****	<0.0001
SUDV GPΔmuc-WL^{2}P^4-PD I3-01v9b SApNP vs. SUDV GPΔmuc-WL^{2}P^4-PD I3-01v9b SApNP-Kif/endo H	ns	0.903
SUDV GPΔmuc-WL^{2}P^4-PD I3-01v9b SApNP-Kif vs. SUDV GPΔmuc-WL^{2}P^4-PD I3-01v9b SApNP-Kif/endo H	****	<0.0001

Figure S11

g Sera of individual mice immunized with wildtype/glycan-modified SUDV vaccines neutralizing a SUDV Gulu strain

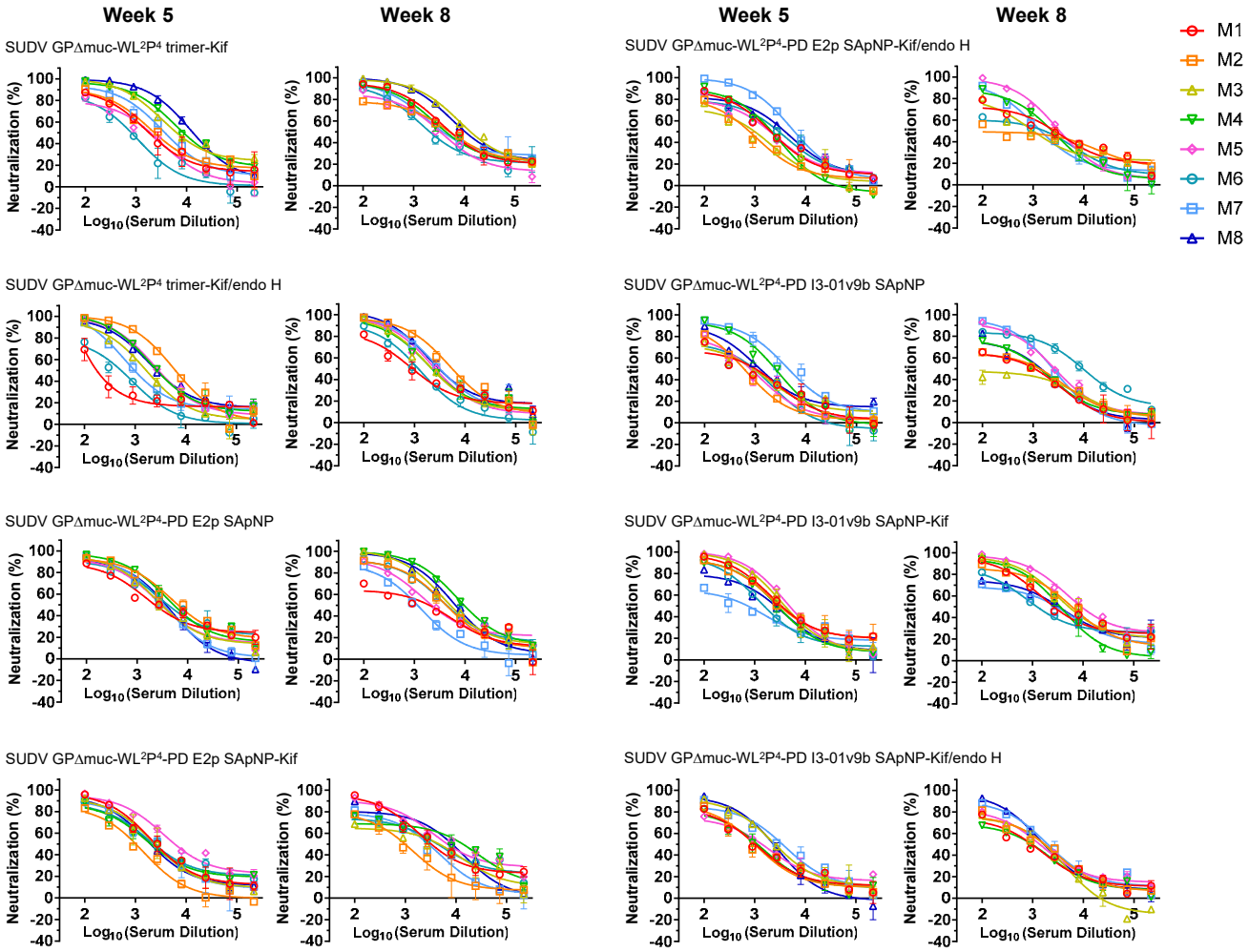

h Mouse serum neutralizing ID_{50} titers

Week 5

Antigen	ID50 titers (week 5) M1	M2	M3	M4	M5	M6	M7	M8	Geometric Mean
SUDV GPΔmuc-WL²P⁴ trimer	420	3076	156.6	2417	1377	1896	5149	1477	1328.6
SUDV GPΔmuc-WL²P⁴ trimer-Kif	1986	2709	8760	10520	1522	736.6	4016	14183	3652.3
SUDV GPΔmuc-WL²P⁴ trimer-Kif/endo H	243.4	6460	1691	3127	3197.0	463.3	1201.0	3265.0	1623.6
SUDV GPΔmuc-WL²P⁴-PD E2p SApNP	3142	7835	3520	6205	3431	5382	3249	3187	4231.6
SUDV GPΔmuc-WL²P⁴-PD E2p SApNP-Kif	2877	873.4	2512	2311	7871	2706	2473	2186	2530.2
SUDV GPΔmuc-WL²P⁴-PD E2p SApNP-Kif/endo H	2075	721.3	713.9	1791	1742	2481	6384	3462	1917.5
SUDV GPΔmuc-WL²P⁴-PD I3-01v9b SApNP	662.4	592.3	758.7	2268	682.9	642.8	4778	1402	1089.5
SUDV GPΔmuc-WL²P⁴-PD I3-01v9b SApNP-Kif	4252	3819	4262	2863	5193	1734	651.4	2141	2657.6
SUDV GPΔmuc-WL²P⁴-PD I3-01v9b SApNP-Kif/endo H	1023	1000	2652	1043	1287	N/A	3262	2177	1591.5

Week 11 or 8

Antigen	ID50 titers (week 11,8) M1	M2	M3	M4	M5	M6	M7	M8	Geometric Mean
SUDV GPΔmuc-WL²P⁴ trimer-w11	13810	4694	2805	3670	2858	2497	14410	3069	4628.4
SUDV GPΔmuc-WL²P⁴ trimer-Kif-w8	6582	5258	16937	5674	3316	2649	5681	13235	6204.7
SUDV GPΔmuc-WL²P⁴ trimer-Kif/endo H-w8	1035	6006	2560	2543	2847	1139	3639	3835	2557.7
SUDV GPΔmuc-WL²P⁴-PD E2p SApNP-w8	1224	4430	6202	11133	2887	4953	1083	6855	3757.6
SUDV GPΔmuc-WL²P⁴-PD E2p SApNP-Kif-w8	4414	880.9	2466	7047	10493	4060	2235	6092	3751.0
SUDV GPΔmuc-WL²P⁴-PD E2p SApNP-Kif/endo H-w8	2234	555.2	1224	2211	3512	1040	1615	N/A	1531.9
SUDV GPΔmuc-WL²P⁴-PD I3-01v9b SApNP-w8	739.1	911.5	343.7	1130	2675	9196	2305	1040	1407.8
SUDV GPΔmuc-WL²P⁴-PD I3-01v9b SApNP-Kif-w8	3830	5923	6805	3469	12386	1653	2090	3103	4041.0
SUDV GPΔmuc-WL²P⁴-PD I3-01v9b SApNP-Kif/endo H-w8	810.8	1367	1095	777.2	1388	N/A	2057	1791	1252.0

Statistical analysis

One-way ANOVA with Tukey's multiple comparisons test (w5)	Statistics	Adjusted P Value
SUDV GPΔmuc-WL²P⁴ trimer vs. SUDV GPΔmuc-WL²P⁴ trimer-Kif	ns	0.0934
SUDV GPΔmuc-WL²P⁴ trimer vs. SUDV GPΔmuc-WL²P⁴ trimer-Kif/endo H	ns	0.9563
SUDV GPΔmuc-WL²P⁴ trimer-Kif vs. SUDV GPΔmuc-WL²P⁴ trimer-Kif/endo H	ns	0.1577

One-way ANOVA with Tukey's multiple comparisons test (w5)	Statistics	Adjusted P Value
SUDV GPΔmuc-WL²P⁴-PD E2p SApNP vs. SUDV GPΔmuc-WL²P⁴-PD E2p SApNP-Kif	ns	0.2678
SUDV GPΔmuc-WL²P⁴-PD E2p SApNP vs. SUDV GPΔmuc-WL²P⁴-PD E2p SApNP-Kif/endo H	ns	0.0973
SUDV GPΔmuc-WL²P⁴-PD E2p SApNP-Kif vs. SUDV GPΔmuc-WL²P⁴-PD E2p SApNP-Kif/endo H	ns	0.8296

One-way ANOVA with Tukey's multiple comparisons test (w8)	Statistics	Adjusted P Value
SUDV GPΔmuc-WL²P⁴-PD E2p SApNP vs. SUDV GPΔmuc-WL²P⁴-PD E2p SApNP-Kif	ns	0.9947
SUDV GPΔmuc-WL²P⁴-PD E2p SApNP vs. SUDV GPΔmuc-WL²P⁴-PD E2p SApNP-Kif/endo H	ns	0.1006
SUDV GPΔmuc-WL²P⁴-PD E2p SApNP-Kif vs. SUDV GPΔmuc-WL²P⁴-PD E2p SApNP-Kif/endo H	ns	0.1201

One-way ANOVA with Tukey's multiple comparisons test (w5)	Statistics	Adjusted P Value
SUDV GPΔmuc-WL²P⁴-PD I3-01v9b SApNP vs. SUDV GPΔmuc-WL²P⁴-PD I3-01v9b SApNP-Kif	ns	0.0604
SUDV GPΔmuc-WL²P⁴-PD I3-01v9b SApNP vs. SUDV GPΔmuc-WL²P⁴-PD I3-01v9b SApNP-Kif/endo H	ns	0.9009
SUDV GPΔmuc-WL²P⁴-PD I3-01v9b SApNP-Kif vs. SUDV GPΔmuc-WL²P⁴-PD I3-01v9b SApNP-Kif/endo H	ns	0.1599

One-way ANOVA with Tukey's multiple comparisons test (w8)	Statistics	Adjusted P Value
SUDV GPΔmuc-WL²P⁴-PD I3-01v9b SApNP vs. SUDV GPΔmuc-WL²P⁴-PD I3-01v9b SApNP-Kif	ns	0.1544
SUDV GPΔmuc-WL²P⁴-PD I3-01v9b SApNP vs. SUDV GPΔmuc-WL²P⁴-PD I3-01v9b SApNP-Kif/endo H	ns	0.7712
SUDV GPΔmuc-WL²P⁴-PD I3-01v9b SApNP-Kif vs. SUDV GPΔmuc-WL²P⁴-PD I3-01v9b SApNP-Kif/endo H	*	0.0468

Figure S11

i Sera of individual mice immunized with glycan-modified RAVV vaccines binding to RAVV GPΔmuc-P²CT(1TD0) trimer

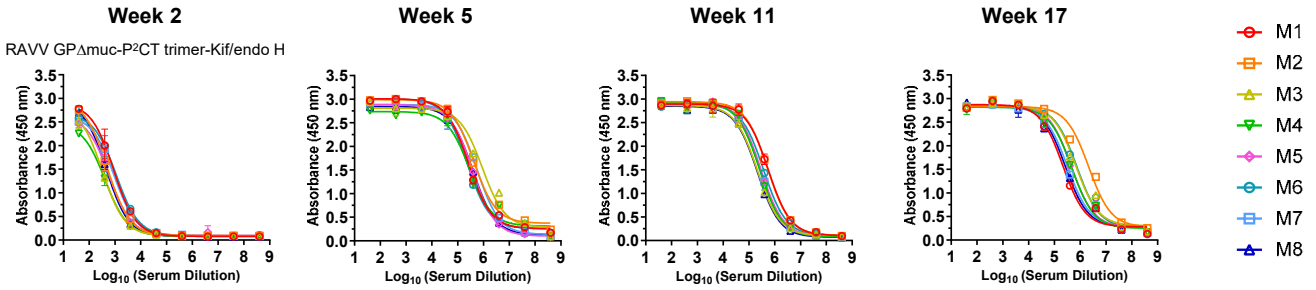

j Mouse serum ELISA EC_{50} titers

Week 2

Antigen	EC50 titers (week 2)								Geometric Mean
	M1	M2	M3	M4	M5	M6	M7	M8	
RAVV GPΔmuc-P²CT trimer	718.9	721.9	432.3	1030.0	946.3	262.3	481.5	958.5	635.1
RAVV GPΔmuc-P²CT trimer-Kif/endo H	1088.0	842.6	372.8	326.6	773.6	1455.0	1260.0	571.6	740.6

Week 5

Antigen	EC50 titers (week 5)								Geometric Mean
	M1	M2	M3	M4	M5	M6	M7	M8	
RAVV GPΔmuc-P²CT trimer	202735	1544554	746406	628189	447117	44771	446178	225949	362215.2
RAVV GPΔmuc-P²CT trimer-Kif/endo H	208318	261241	222068	150370	267446	198233	450054	211636	234603.9

Week 11 or 8

Antigen	EC50 titers (week 11,8)								Geometric Mean
	M1	M2	M3	M4	M5	M6	M7	M8	
RAVV GPΔmuc-P²CT trimer-w11	139135	218951	208199	104125	998580	786127	408247	853062	340466.6
RAVV GPΔmuc-P²CT trimer-Kif/endo H-w8	770620	683058	388118	292655	294767	621323	524297	273292	446120.6

Week 17 or 11

Antigen	EC50 titers (week 17,11)								Geometric Mean
	M1	M2	M3	M4	M5	M6	M7	M8	
RAVV GPΔmuc-P²CT trimer-w17	140811	110900	164905	119990	336478	344895	127509	141835	168457
RAVV GPΔmuc-P²CT trimer-Kif/endo H-w11	125144	295308	212027	173036	313400	398840	295603	237268	242316

Statistical analysis

Unpaired t test (w2)	Statistics	P Value
RAVV GPΔmuc-P²CT trimer vs. RAVV GPΔmuc-P²CT trimer-Kif/endo H	ns	0.4307

Unpaired t test (w5)	Statistics	P Value
RAVV GPΔmuc-P²CT trimer vs. RAVV GPΔmuc-P²CT trimer-Kif/endo H	ns	0.1079

k Purified IgG of individual mice immunized with RAVV vaccines neutralizing a MARV Angola strain

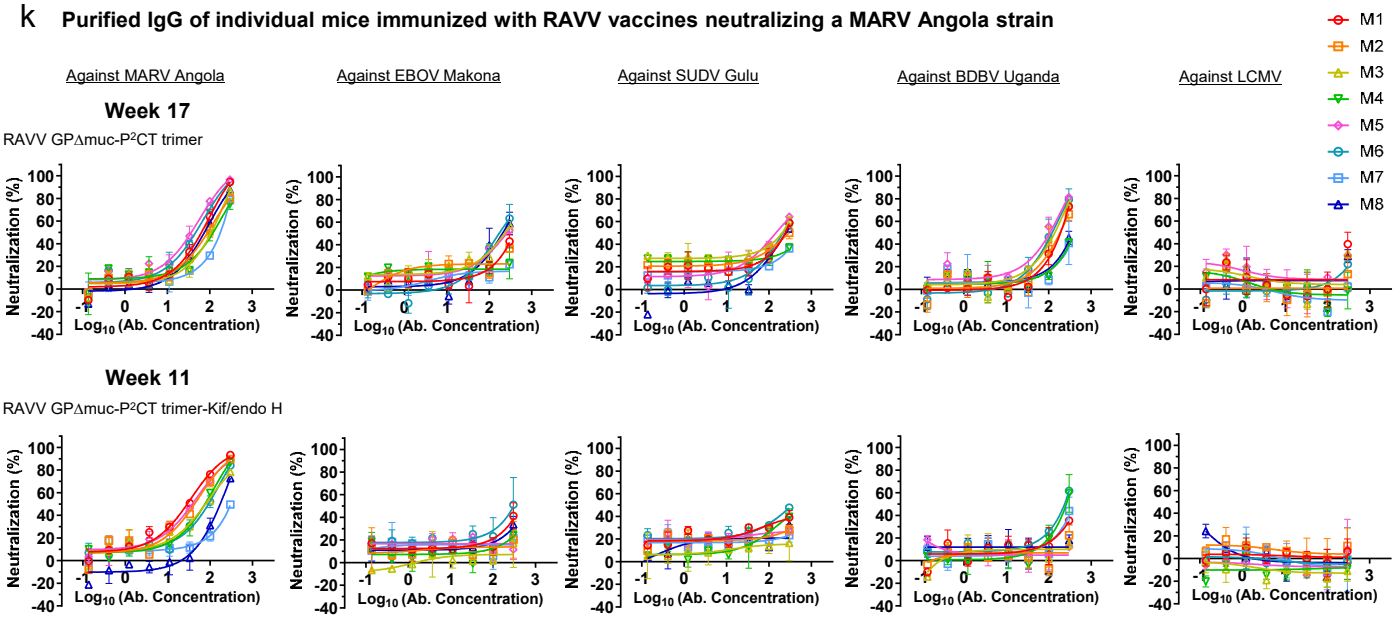

Figure S11

Fig. S11. Immunogenicity of glycan-modified EBOV, SUDV, and RAVV GPΔmuc vaccines in mice. (**a**) ELISA curves of mouse sera from glycan-modified EBOV GPΔmuc trimer and SApNP vaccine groups (n = 8 mice/group) binding to EBOV GPΔmuc-WL^{2}P^4(1TD0) trimer. (**b**) (Top) Summary of geometric means of EC_{50} titers measured for glycan-modified EBOV GPΔmuc vaccine groups against EBOV GPΔmuc-WL^{2}P^4(1TD0) trimer. Color coding indicates the level of EC_{50} titers (green to red: low to high binding). (Bottom) Summary of statistical analysis performed for each timepoint. Of note, the EC_{50} values at week 2 were derived by setting the minimum/maximum OD_{450} values to 0.0/2.8. (**c**) Neutralization curves of mouse sera from glycan-modified EBOV GPΔmuc trimer and SApNP vaccine groups against EBOV Makona pseudovirus. (**d**) (Top) Summary of geometric means of ID_{50} titers measured for EBOV GPΔmuc vaccine groups against EBOV Makona pseudovirus. Color coding indicates the level of ID_{50} titers (white: no neutralization; green to red: low to high neutralization). Of note, the ID_{50} values were derived by setting the minimum/maximum %neutralization to 0.0/100.0 as constraints. (Bottom) Summary of statistical analysis. (**e**) ELISA curves of mouse sera from glycan-modified SUDV GPΔmuc trimer and SApNP vaccine groups binding to SUDV GPΔmuc-WL^{2}P^4(1TD0) trimer. (**f**) (Top) Summary of geometric means of EC_{50} titers measured for glycan-modified SUDV GPΔmuc vaccine groups against SUDV GPΔmuc-WL^{2}P^4(1TD0) trimer. (Bottom) Summary of statistical analysis. Of note, the EC_{50} values at week 2 were derived by setting the minimum/maximum OD_{450} values to 0.0/2.9. (**g**) Neutralization curves of mouse sera from glycan-modified SUDV GPΔmuc trimer and SApNP vaccine groups against SUDV Gulu pseudovirus. (**h**) (Top) Summary of geometric means of ID_{50} titers measured for SUDV GPΔmuc vaccine groups against SUDV Gulu pseudovirus. (Bottom) Summary of statistical analysis. (**i**) ELISA curves of mouse sera from glycan modified RAVV GPΔmuc trimer vaccine groups binding to RAVV GPΔmuc-P^{2}CT(1TD0) trimer. (**j**) (Top) Summary of geometric means of EC_{50} titers measured for glycan-modified RAVV GPΔmuc vaccine groups against RAVV GPΔmuc-P^{2}CT(1TD0) trimer. (Bottom) Summary of statistical analysis. Of note, the EC_{50} values at week 2 were derived by setting the minimum/maximum OD_{450} values to 0.0/2.9. (**k**) Neutralization curves of purified mouse IgG from glycan-modified RAVV GPΔmuc vaccine groups after four immunizations at week 17 or week 11 against MARV Angola or various ebolavirus strains. Lymphocytic choriomeningitis virus (LCMV) was included as a negative control to confirm the cross-NAb responses measured using purified IgG. Error bars represent the difference between these duplicate values at each concentration tested for each sample. EC_{50} and ID_{50} values were calculated in GraphPad Prism 10.3.1. Data were analyzed using one-way ANOVA, followed by Tukey's multiple comparison post hoc test for each timepoint. For significance, ns (not significant), *p < 0.05, **p < 0.01, ***p < 0.001, and ****p < 0.0001.

Table S1. Data collection and refinement statistics for EBOV Mayinga GPΔmuc-WL^{2}P^4.

Data Collection	**EBOV Mayinga GPΔmuc-WL^{2}P^4**
Beamline	SSRL 12-1
Wavelength (Å)	0.97946
Resolution (Å)[a]	40.6 - 3.20 (3.29 - 3.20)
Space group	P321
Unit cell (Å)	114.47,114.47,133.38
(°)	90 90 120
Total reflections	189,316 (12,886)
Unique reflections	17,104 (815)
Multiplicity	11.1 (9.6)
Completeness (%)	99.8 (98.2)
Mean (I)/ σ_I	22.2 (1.2)
R_{merge} (%)	6.1 (>100)
R_{meas}[c] (%)	12.3 (>100)
R_{pim}[d] (%)	3.7 (69.3)
$CC_{1/2}$[e] (%)	99.8 (30.3)
Refinement	
Refinement resolution (Å)[a]	40.6 - 3.20 (3.29 - 3.20)
# reflections in refinement (work/free)	17,082 (1,323)
R_{work} (%)	21.5 (36.1)
R_{free} (%)	22.2 (33.0)
# Protein atoms	3,119
# Carbohydrate atoms	128
# Waters	0
# Protein residues	398
Bond r.m.s. deviation (Å)	0.013
Angle r.m.s. deviation (º)	1.60
Wilson B (Å^2)	114
Average B protein (Å^2)	119
carbohydrate (Å^2)	156
Ramachandran favored, allowed, outliers (%)	96.1, 3.9, 0.0, 0.0
Clashscore[f]	8.2
PDB ID	9N8E

[a]Numbers in parentheses are for highest resolution shell
[b]$R_{merge} = \Sigma_{hkl} \Sigma_{i=1,n}|I_i(hkl) - \langle I(hkl)\rangle| / \Sigma_{hkl} \Sigma_{i=1,n} I_i(hkl)$
[c]$R_{meas} = \Sigma_{hkl} \sqrt{(n/n-1)} \Sigma_{i=1,n}|I_i(hkl) - \langle I(hkl)\rangle| / \Sigma_{hkl} \Sigma_{i=1,n} I_i(hkl)$
[d]$R_{pim} = \Sigma_{hkl} \sqrt{(1/n-1)} \Sigma_{i=1,n}|I_i(hkl) - \langle I(hkl)\rangle| / \Sigma_{hkl} \Sigma_{i=1,n} I_i(hkl)$
[e]$CC_{1/2}$ = Pearson correlation coefficient between two random half datasets
[f]Number of unfavorable all-atom steric overlaps ≥ 0.4 Å per 1000 atoms

Table S2. Cryo-EM data collection information, model building, and refinement statistics.

Data collection information	**SUDV Gulu GPΔmuc-WL^{2}P^4/CA45 Fab**
Microscope	Titan Krios G4
Voltage (keV)	200
Detector	Falcon 4 camera with a Selectris-X energy filter
Recording mode	Counting
Magnification	130,000 x
Movie micrograph pixel size	0.89
Total dose (e–/Å^2)	50
Under focus range (μm)	-1.0 to -2.0 um
Number of movie micrographs	1,824
Model building and refinement statistics	
Map Resolution (Å)	3.13
Residues	
Amino-acids	1473
Carbohydrates	9
RMSD Bonds (Å)	0.003
RMSD Angles (º)	0.746
Ramachandran	
Outliers (%)	0.00
Allowed (%)	7.21
Favored (%)	92.8
Rotamer outliers	1.67
Clash score	8.98
Molprobity score	2.10
PDB ID	9N8F
EMDB ID	EMD-49127